



UNIVERSITY OF SILESIA  
IN KATOWICE

Institute of Physics  
Faculty of Science and Technology  
Doctoral School

DOCTORAL THESIS

**The Liquid-Liquid Phase Transition in Ionic Liquids  
at Ambient and Elevated Pressure**

Beibei Yao

Supervisor: Dr hab. Żaneta Wojnarowska

Chorzów 2023

# Acknowledgments

My doctoral studies are coming to an end, and the three-year journey has passed by in a flash. Looking back on my time at the University of Silesia in Katowice, I cherish every little moment and experience. This academic journey has been challenging yet rewarding, and I could not have achieved this milestone without the help of many people.

First and foremost, I would like to express my sincere gratitude to my supervisor, Dr hab. Żaneta Wojnarowska, for her encouragement, support, and mentorship throughout my doctoral studies. I am greatly honored to be the Ph.D. student of Żaneta. Her expertise, enthusiasm, flexible mind, and rigorous attitude toward science inspire me and have been invaluable in shaping my research trajectory and helping me develop into a scholar. Moreover, she is very kind, I am touched by her friendly help in my daily life, and she cares for me like family.

I wish to express my special thanks to Professor Marian Paluch for his guidance, insights, and recommendation. His ability to effortlessly blend his vast knowledge and experience with his natural wisdom and humor left a lasting impression on me.

I would like to thank the physics group of scholars, specifically Dr. inż. Justyna Knapik-Kowalczyk for her patient teaching in calorimetry and high-frequency equipment, Dr. Marzena Rams-Baron, Dr hab. Magdalena Tarnacka, and Dr. inż. Anna Szeremeta for helping me overcome obstacles and willingness to share their knowledge. And also thank my Polish colleagues for their help and friendship in my study and daily life, particularly Dr. Małgorzata Musiał, Mgr. Kinga Łucak, Mgr. Daniel Kramarczyk, and Mgr. Alfred Błażytko. I am also grateful to the staff and faculty in the Doctoral School and Chorzów campus for their administrative support, technical assistance, and intellectual community. I am pleased to have had the opportunity to work in such a productive and enjoyable cooperative environment.

I would like to acknowledge the financial support from National Science Centre, Poland [Opus 21, 2021/41/B/ST5/00840], which made this research possible. Their generous support has enabled me to pursue my academic goals and attend conferences.

I am grateful to my family and friends for their love and encouragement throughout my studies. Their unwavering belief in me, even during times of self-doubt, has been a constant source of motivation and inspiration. Finally, I would like to thank my partner, Dr. Shinian Cheng, for his steadfast support, patience, and understanding during this demanding time. This achievement would not have been possible without his love, support, and humor.

In conclusion, I would like to express my deepest appreciation to everyone who has contributed to my academic journey.

# Abstract

As one of the most intriguing physical phenomena, liquid-liquid phase transition (LLT) between two liquid states of single-component material is strategically significant in the field of condensed matter physics. It has attracted considerable attention recently due to its potential applications in various areas. The present thesis investigates the LLT phenomenon in a series of phosphonium ionic liquids (ILs) using calorimetry, dielectric spectroscopy, and other techniques (rheology, Raman measurements, small-angle X-Ray scattering). The effects of different IL structures on LLT are analyzed, focusing on both cation and anion variations. By tailoring the alkyl chain of trihexyl-tetradecylphosphonium ( $[P_{666,14}]^+$ ) cation, it demonstrates that the  $C_{14}$  alkyl chain is the critical length driving the generation of nonpolar local domains and thus observing two distinct supercooled states in the single-component system (LLT). In contrast, although there is no calorimetric evidence of LLT in the case of ILs with  $[P_{666,m}]^+$  ( $m=2,6,8,12$ ), their ion dynamics show similar changes to LLT in Stickel analysis near the liquid-glass transition, and the nanoscale ordering still occurs.

On the other hand, anions change in  $[P_{666,14}]^+$ -based ILs subtly affects the LLT behavior. Specifically, the ion dynamics reveal anomalous behavior during LLT for all examined ILs, i.e., the conductivity relaxation times  $\tau_\sigma$  are significantly longer, and their distribution gets broader; however, this signature of LLT occurs at slightly different  $\tau_\sigma$  being anion specific. However, when  $[P_{666,14}]^+$  was combined with bulky anions (i.e.,  $V_{vdW} > 0.2 \text{ nm}^3$ ), the LLT was prevented and could not be directly detected by calorimetry scanning and dielectric spectroscopy. Furthermore, ion dynamics follows the typical behavior of ion glass-formers in a supercooled liquid state, i.e., the temperature dependence of the conductivity relaxation time ( $\log \tau_\sigma (1000/T)$ ) obeys the Vogel–Fulcher–Tammann (VFT) law, and the shape of the conductivity relaxation process satisfies the time-temperature superposition (TTS) rule.

Furthermore, the decoupling between ion diffusion and structural dynamics has been detected for the first time in neat aprotic ionic liquids due to the occurrence of LLT. The self-assembly of liquid 2 is suggested as the physical origin behind this phenomenon and can be tuned by pressure. Pressure-induced nanostructure of liquid 2 depends on anion size leading to different pressure effects on ion transport. In addition, the time scale of relaxation dynamics of examined aprotic ILs under high pressure is sample-dependent; however, it exhibits an isochronal behavior at LLT, i.e.,  $\tau_\sigma (T_{LL}, P_{LL})$  remains constant for a given system. The pressure sensitivity and enthalpy fluctuations offer the possibility to estimate specific volume changes during LLT and suggest that the order parameter controlling LLT may not be density. It is worth mentioning that some other interesting

physical phenomena were also found to exist in the studied ILs, such as polyamorphism, indicating two or more amorphous states, and the inflection point in pressure dependence of relaxation dynamics. These results provide insight into the nature of LLT phenomenon and diverse opportunities for designing highly effective electrolytes that utilize ionic liquids with self-assembly properties.

The results presented in this dissertation have been presented in the following publications:

1. Beibei Yao, Marian Paluch, Mateusz Dulski, Courtney Quinn, Shannon McLaughlin, Anne McGrogan, Malgorzata Swadzba-Kwasny, and Zaneta Wojnarowska, *Tailoring Phosphonium Ionic Liquids for a Liquid–Liquid Phase Transition*, *J. Phys. Chem. Lett.*, 14, 2958-2964 (2023)
2. Zaneta Wojnarowska, Shinian Cheng, Beibei Yao, Malgorzata Swadzba-Kwasny, Shannon McLaughlin, Anne McGrogan, Yoan Delavoux, and Marian Paluch, *Pressure-induced liquid-liquid transition in a family of ionic materials*, *Nat. Commun.*, 13, 1342 (2022)
3. Beibei Yao, Marian Paluch, and Zaneta Wojnarowska, *Effect of bulky anions on the liquid-liquid phase transition in phosphonium ionic liquids: Ambient and high-pressure dielectric studies*, *Sci. Rep.*, 13, 3040 (2023)
4. Beibei Yao, Marian Paluch, Jaroslaw Paturej, Shannon McLaughlin, Anne McGrogan, Malgorzata Swadzba-Kwasny, Jie Shen, Beatrice Ruta, Martin Rosenthal, Jiliang Liu, Danuta Kruk and Zaneta Wojnarowska, *Self-assembled nanostructures in aprotic ionic liquids facilitate charge transport at elevated pressure*, *ACS Appl. Mater. Interfaces*, under review.

# Streszczenie

Jako jedno z najbardziej intrygujących zjawisk fizycznych, przejście fazowe ciec-ciecz (LLT) między dwoma stanami ciekłymi materiału jednoskładnikowego ma strategiczne znaczenie w dziedzinie fizyki materii skondensowanej. W ostatnim czasie cieszy się dużym zainteresowaniem ze względu na swoje potencjalne zastosowania w różnych obszarach. Niniejsza praca bada zjawisko LLT w szeregu fosfoniowych cieczy jonowych (ILs) za pomocą kalorymetrii, spektroskopii dielektrycznej i innych technik (reologia, pomiary ramanowskie, niskokątowe rozpraszanie promieniowania rentgenowskiego). Analizowany jest wpływ struktury chemicznej IL na LLT, koncentrując się zarówno na odmianach kationów, jak i anionów. Dopasowując łańcuch alkilowy kationu triheksylo-tetradecylo-fosfoniowego ( $[P_{666,14}]^+$ ), pokazano, że 14 węgli w łańcuchu jest krytyczną długością umożliwiającą generowanie niepolarnych domen lokalnych, a tym samym obserwację dwóch różnych stanów przechłodzonej cieczy w jednoskładnikowej cieczy jonowej. Choć nie zaobserwowano kalorymetrycznych dowodów na istnienie LLT w przypadku IL z kationem  $[P_{666,m}]^+$  ( $m = 2,6,8,12$ ), dynamika jonów w tych materiałach wykazuje podobne zmiany do tych obserwowanych podczas LLT.

Z drugiej strony zmiana anionów w IL przy zachowaniu kationu  $[P_{666,14}]^+$  jedynie subtelnie wpływa na zachowanie LLT. W szczególności dynamika jonów ujawnia anomalne zachowanie podczas LLT dla wszystkich badanych IL, tj. czasy relaksacji przewodnictwa  $\tau_\sigma$  są znacznie dłuższe, a ich rozkład staje się szerszy; niemniej jednak LLT występuje przy nieco innym  $\tau_\sigma$ , które jest specyficzne dla anionu. Jednakże, gdy  $[P_{666,14}]^+$  połączono z dużymi anionami (tj.  $V_{vdW} > 0.2 \text{ nm}^3$ ), przejścia LLT nie można było bezpośrednio wykryć za pomocą skaningowej kalorymetrii różnicowej i spektroskopii dielektrycznej. Ponadto dynamika jonów tych układów okazała się być tożsama z tą obserwowaną dla typowych materiałów szklotwórczych w cieczy przechłodzonej, tj. zależność temperaturowa czasu relaksacji przewodnictwa ( $\log \tau_\sigma (1000/T)$ ) jest zgodna z prawem Vogla–Fulchera–Tammanna (VFT), a kształt procesu relaksacji przewodnictwa spełnia regułę superpozycji czasowo-temperaturowej (TTS).

Co więcej, w niniejszej pracy po raz pierwszy wykryto różnicę skal czasowych między dyfuzją jonów a dynamiką strukturalną w czystych aprotonowych cieczach jonowych z powodu występowania LLT. Zasugerowano, że samoorganizacja cieczy 2 jest fizycznym źródłem tego zjawiska. Pokazano również że skala czasowa relaksacji przewodnictwa w przejściu LL jest zależna od próbki, jednakże nie zmienia się w warunkach izotermicznej kompresji oraz izobarycznego chłodzenia, tj. wykazuje charakter izochroniczny  $\tau_\sigma (T_{LL}, P_{LL}) = \text{const}$ . Wrażliwość na ciśnienie i fluktuacje

entalpii dały z kolei możliwość oszacowania zmian objętości podczas LLT. Warto wspomnieć, że w badanych IL stwierdzono również występowanie innych interesujących zjawisk fizycznych, takich jak poliamorfizm wskazujący na obecność dwóch stanów amorficznych w jednym materiale oraz punkt przegięcia w ciśnieniowej zależności relaksacji przewodnictwa. Wyniki te dają wgląd w naturę zjawiska LLT i różnorodne możliwości projektowania wysoce efektywnych elektrolitów wykorzystujących ciecze jonowe o tendencjach do samoorganizacji.

Wyniki przedstawione w rozprawie zostały przedstawione w następujących publikacjach:

1. Beibei Yao, Marian Paluch, Mateusz Dulski, Courtney Quinn, Shannon McLaughlin, Anne McGrogan, Malgorzata Swadzba-Kwasny, and Zaneta Wojnarowska, *Tailoring Phosphonium Ionic Liquids for a Liquid–Liquid Phase Transition*, J. Phys. Chem. Lett., 14, 2958-2964 (2023)
2. Zaneta Wojnarowska, Shinian Cheng, Beibei Yao, Malgorzata Swadzba-Kwasny, Shannon McLaughlin, Anne McGrogan, Yoan Delavoux, and Marian Paluch, *Pressure-induced liquid-liquid transition in a family of ionic materials*, Nat. Commun., 13,1342 (2022)
3. Beibei Yao, Marian Paluch, and Zaneta Wojnarowska, *Effect of bulky anions on the liquid-liquid phase transition in phosphonium ionic liquids: Ambient and high-pressure dielectric studies*, Sci. Rep., 13, 3040 (2023)
4. Beibei Yao, Marian Paluch, Jaroslaw Paturej, Shannon McLaughlin, Anne McGrogan, Malgorzata Swadzba-Kwasny, Jie Shen, Beatrice Ruta, Martin Rosenthal, Jiliang Liu, Danuta Kruk and Zaneta Wojnarowska, *Self-assembled nanostructures in aprotic ionic liquids facilitate charge transport at elevated pressure*, ACS Appl. Mater. Interfaces, under review.

# Contents

Acknowledgments .....	2
Abstract .....	3
Streszczenie .....	5
1 Introduction.....	10
1.1 Motivation.....	10
1.2 Reference .....	12
2 Theoretical Background.....	14
2.1 The Liquid State.....	14
2.2 Liquid-Liquid Phase Transition .....	14
2.3 Ionic Liquids as Candidates to Study the Liquid-Liquid Transition .....	15
2.4 Thermodynamics of Ionic Liquids.....	17
2.5 Dynamics of Ionic Liquids .....	19
2.6 Dynamics of Ionic Liquids at High Pressure .....	24
2.7 Reference .....	25
3 Experiment Description .....	31
3.1 Studied Materials .....	31
3.2 Differential Scanning Calorimetry (DSC) .....	34
3.3 Broadband Dielectric Spectroscopy (BDS) at Ambient and Elevated Pressure .....	35
3.4 Supplementary Measurements .....	38
3.4.1 Rheological Measurements.....	38
3.4.2 Density Measurements.....	39
3.4.3 Raman Scattering Measurements.....	39
3.4.4 X-Ray Diffraction (XRD) Measurements.....	40
3.4.5 Molecular Dynamics Simulation .....	40
3.5 Reference .....	41
4 Tailoring Phosphonium Ionic Liquids for a Liquid–Liquid Phase Transition .....	43
4.1 Abstract.....	45

4.2 Main text .....	45
4.3 Acknowledgements.....	54
4.4 Supplementary Information .....	54
4.5 Reference .....	76
5 Pressure-Induced Liquid-Liquid Transition in a Family of Ionic Materials.....	79
5.1 Abstract.....	81
5.2 Introduction.....	81
5.3 Results and Discussion .....	86
5.3.1 Calorimetric Studies of Phase Transitions.....	86
5.3.2 Changes in Ion Dynamics Accompanying LLT .....	88
5.3.3 The LLT Under High-Pressure Conditions .....	91
5.4 Methods .....	95
5.5 Acknowledgements.....	97
5.6 Supplementary information .....	97
5.7 References.....	118
6 Effect of Bulky Anions on the Liquid-Liquid Phase Transition in Phosphonium Ionic Liquids: Ambient and High-Pressure Dielectric Studies.....	121
6.1 Abstract.....	122
6.2 Introduction.....	122
6.3 Results and discussion .....	124
6.4 Conclusions.....	134
6.5 Methods .....	134
6.6 Acknowledgements.....	136
6.7 Supplementary information .....	136
6.8 References.....	138
7 Self-Assembled Nanostructures in Aprotic Ionic Liquids Facilitate Charge Transport at Elevated Pressure.....	140
7.1 Abstract.....	142
7.2 Introduction.....	142
7.3 Materials and Methods.....	144

7.4 Results & Discussion .....	146
7.4.1 Samples characterization. ....	146
7.4.2 Charge transport mechanism above and below the $T_{LL}$ .....	148
7.4.3 Compression through the liquid-liquid and liquid-glass transitions....	154
7.4.4 MD simulations of the charge transport mechanism .....	155
7.5 Conclusions.....	156
7.6 Acknowledgement .....	157
7.7 Supplementary information .....	157
7.8 Reference .....	163
8 Conclusion .....	166
8.1 Outlook .....	176
8.2 Reference .....	176
9 Appendix.....	178
Co-authored publications .....	178
Conference Contributions .....	178

# 1 Introduction

## 1.1 Motivation

As one of the fundamental states of matter, liquid plays an essential role in our lives compared to gas and solid because of its unique properties. Specifically, due to their versatility, fluidity, relatively high heat capacity, and solubility, liquids are the ideal materials for a wide range of applications in industry, pharmacy, and energy. The most famous example is water. Water is a vital component of life and is essential for many biological processes, such as hydration, digestion, and temperature regulation. Moreover, water is used as a coolant in power plants and as a solvent in chemical reactions. In agriculture, water is necessary for irrigation and growing crops.

On the other hand, the liquid is indeed complicated. One reason is that liquids are considered “condensed phases,”[1] meaning that their molecules are much closer than in a gas but not as tightly packed as in a solid, which results in the diversity of the intermolecular forces in liquids and extensive physicochemical properties. Furthermore, liquids exhibit physical phenomena (e.g., surface tension, diffusion, viscosity, and elasticity) influenced by many factors, such as temperature, pressure, and chemical composition, making them difficult to predict and understand. Despite the wealth of studies dedicated to elucidating the structure and dynamics of liquids, covering various aspects including but not limited to experimental methods, computer simulations, and theoretical frameworks, some open questions remain. For example, glass transition [2],[3] and liquid-liquid phase transition [4],[5],[6],[7] are yet to be fully understood. Therefore, as frontier challenges in condensed matter physics, both play a pivotal role in a deeper understanding of the nature of liquids and their applications.

It is well known that a liquid can be transformed into a solid state through a first-order phase transition. However, such a physical understanding of the liquid state has been upended by a controversial phenomenon known as “liquid polymorphism” [8],[9],[10]. That is, a single component material may have two or more distinct liquid states separated via a first-order liquid-liquid phase transition (LLT). Over the years, numerous examples of two liquid states with locally different local structures, densities, molecular dynamics, and thermodynamic properties have been reported. The famous systems are water [11],[12],[13],[14] and triphenyl phosphite (TPP) [15],[16],[17], two other molecular liquids: n-butanol [18] and D-mannitol [19], some atomic elements (e.g., C[20], P [21], S [22], Si [23]), oxides (such as SiO<sub>2</sub>, GeO<sub>2</sub>, B<sub>2</sub>O<sub>3</sub>, and Al<sub>2</sub>O<sub>3</sub>-Y<sub>2</sub>O<sub>3</sub> mixture [24]), water-trehalose mixtures [25], and some metallic glasses [26],[27],[28] have also been suggested for the existence of LLT. However, there is currently no consensus on the

actual presence of LLT in these systems since the occurrence of crystallization can hinder experimental access to LLT [4],[29]. Furthermore, it has been reported that the liquid-liquid transition can occur without a noticeable density change in the melt of sodium acetate trihydrate [30], which makes this physical phenomenon even more puzzling. The controversy around LLT is not limited to experiments but also involves numerical simulations [4],[31]. Additionally, due to the significant prevalence of LLT in the supercooled liquid state, it has been considered that this phenomenon exhibits a strong connection with the vitrification process. So far, all LLTs in molecular systems have been discovered by chance, and their universality has not been clarified. Therefore, an important research topic is which critical intrinsic factors and potential features can induce such an exciting and intriguing phenomenon. Moreover, we face the great challenge of how to identify LLT in a systematic fashion through experimental verification.

According to the theoretical description of the liquid-liquid phase transition proposed by Tanaka [4],[29],[32], the only necessary conditions to have LLT in a liquid are the cooperative formation of locally favored structures and the cooperativity in the ordering. Under certain temperature and pressure conditions, any liquid tends to form a locally ordered structure favorable in terms of energy or entropy.[4] Therefore, one can expect LLT to be present in every liquid. As fluids of the greatest interest for decades in all areas of physics, chemistry, biology, and materials science, ionic liquids (ILs), composed solely of ions, should definitely be considered. ILs possess multifaceted and exceptional physiochemical properties, such as high thermal and chemical stability, negligible vapor pressure, extended liquid-state temperature range, and non-flammability. But the most fascinating feature is their microstructural organization, intermolecular interactions (e.g., van der Waals, Coulomb forces, and hydrogen bonding), and transport properties can be fine-tuned over a wide range by the combination of different cations and anions, which opens up numerous possibilities for exploring the generality of LLT and understanding the mechanism of LLT. Especially the microscopic segregation of polar and nonpolar domains in many ILs paves the way for self-assembled nanostructures, which is a fundamental aspect underpinning the intricate physical and chemical properties exhibited by ILs. Thus, the possibility of forming distinct liquid structures (LLT) in ILs increased. In fact, the investigations into the presence of LLT in pure ILs were not overlooked. Angell suggested that studying a fragile ionic liquid with a phase transition similar to that of triphenyl phosphite should be considered an urgent task.[33] Very recently, Harris et al. first proved the evidence of LLT in an aprotic ionic liquid (a class of ILs without transferable protons) with tetra-alkyl-phosphonium cation [34].

In this context, the question naturally arises, *is this ionic liquid an isolated example or a member of a systematic ILs family with specific characteristics, and if so, how do cations and anions affect the presence of LLT?* One task of this work is to search for a series of ILs that exhibit LLT and to investigate their thermodynamic and ion dynamic behavior during the LLT, thereby gaining insight into the structure-property relationships governing the LLT in ILs and establishing general features that characterize LLTs within a particular systematic family of ILs. Notably, the relaxation dynamics under high pressure was also monitored to study the effect of compression on LLT and density fluctuations at the temperature of LLT. Furthermore, by controlling self-assembly in ILs, we expect to find the critical features dominating LLT in ILs.

The organization of this work is as follows: Chapter 2 starts by introducing the general characteristics of the liquid state and liquid-liquid phase transition, as well as presents the reason why ILs are potential candidates for studies of LLT. Then the specific thermodynamic and ion dynamic properties of ILs at ambient and elevated pressure are described, covering the normal liquid, supercooled liquid, and glassy states. The characterization of studied ILs and description of experimental techniques and methods used in this work are presented in Chapter 3. The following chapters (Chapters 4, 5, 6, and 7) present the thermodynamics and dielectric response at ambient and elevated pressures of studied ILs, including the impact of cation and anion on LLT, and the charge transport mechanism during LLT. In the final Chapter 8, the main findings are outlined and discussed by addressing some fundamental questions concerning the nature of the LLT phenomenon. Perspectives on the prospects for future research on LLT in ILs and for applications related to ILs are also provided.

## 1.2 Reference

- [1] D. A. Robinson and J. McK. Woollard, *Chemistry for Colleges and Schools*, (Macmillan Education UK, London, **1982**), pp. 192–215.
- [2] P. G. Debenedetti and F. H. Stillinger, *Nature* **410**, 259 (2001).
- [3] L. Berthier and G. Biroli, *Rev. Mod. Phys.* **83**, 587 (2011).
- [4] H. Tanaka, *J. Chem. Phys.* **153**, 130901 (2020).
- [5] J. C. Palmer, P. H. Poole, F. Sciortino, and P. G. Debenedetti, *Chem. Rev.* **118**, 9129 (2018).
- [6] G. G. N. Angilella, F. E. Leys, N. H. March, and R. Pucci, *Phys. Chem. Liq.* **41**, 211 (2003).
- [7] V. V. Brazhkin, S. V. Popova, and R. N. Voloshin, *Int. J. High Pressure Res.* **15**, 267 (1997).
- [8] H. E. Stanley, *Liquid Polymorphism* (Wiley Online Library, **2013**), Vol. 152.

- [9] P. H. Poole, T. Grande, C. A. Angell, and P. F. McMillan, *Science* **275**, 322 (1997).
- [10] F. Mallamace, *Proc. Natl. Acad. Sci.* **106**, 15097 (2009).
- [11] O. Mishima and H. E. Stanley, *Nature* **396**, 329 (1998).
- [12] C. A. Angell, *Science* **319**, 582 (2008).
- [13] T. E. Gartner, P. M. Piaggi, R. Car, A. Z. Panagiotopoulos, and P. G. Debenedetti, *Phys. Rev. Lett.* **129**, 255702 (2022).
- [14] L. Liu, S.-H. Chen, A. Faraone, C.-W. Yen, and C.-Y. Mou, *Phys. Rev. Lett.* **95**, 117802 (2005).
- [15] M. Kobayashi and H. Tanaka, *Nat. Commun.* **7**, 13438 (2016).
- [16] R. Kurita and H. Tanaka, *Science* **306**, 845 (2004).
- [17] H. Tanaka, R. Kurita, and H. Mataka, *Phys. Rev. Lett.* **92**, 025701 (2004).
- [18] R. Kurita and H. Tanaka, *J. Phys. Condens. Matter* **17**, L293 (2005).
- [19] M. Zhu, J.-Q. Wang, J. H. Perepezko, and L. Yu, *J. Chem. Phys.* **142**, 244504 (2015).
- [20] J. N. Glosli and F. H. Ree, *Phys. Rev. Lett.* **82**, 4659 (1999).
- [21] Y. Katayama, T. Mizutani, W. Utsumi, O. Shimomura, M. Yamakata, and K. Funakoshi, *Nature* **403**, 170 (2000).
- [22] L. Henry, M. Mezouar, G. Garbarino, D. Sifré, G. Weck, and F. Datchi, *Nature* **584**, 382 (2020).
- [23] S. Sastry and C. Austen Angell, *Nat. Mater.* **2**, 739 (2003).
- [24] S. Aasland and P. F. McMillan, *Nature* **369**, 633–636 (1994).
- [25] Y. Suzuki, *Proc. Natl. Acad. Sci.* **119**, e2113411119 (2022).
- [26] S. Wei, F. Yang, J. Bednarcik, I. Kaban, O. Shuleshova, A. Meyer, and R. Busch, *Nat. Commun.* **4**, 2083 (2013)
- [27] J. Shen, Y. H. Sun, J. Orava, H. Y. Bai, and W. H. Wang, *Acta Mater.* **225**, 117588 (2022).
- [28] H. W. Sheng, H. Z. Liu, Y. Q. Cheng, J. Wen, P. L. Lee, W. K. Luo, S. D. Shastri, and E. Ma, *Nat. Mater.* **6**, 192 (2007).
- [29] H. Tanaka, *Phys. Rev. E* **62**, 6968 (2000).
- [30] X. Liu, S. Liu, E. Chen, L. Peng, and Y. Yu, *J. Phys. Chem. Lett.* **10**, 4285 (2019).
- [31] D. T. Limmer and D. Chandler, *J. Chem. Phys.* **135**, 134503 (2011)
- [32] H. Tanaka, *J. Chem. Phys.* **111**, 3163 (1999).
- [33] A. Angell, Fragile Glass Formers: Evidence for a New Paradigm, and a New Relation to Strong Liquids, in *Structural Glasses and Supercooled Liquids Theory: Experiment, and Applications* (P. G. Wolynes, V. Lubchenko, editors. John Wiley & Sons, Inc., Hoboken, NJ, USA, **2012**), pp. 237–278.
- [34] M. A. Harris, T. Kinsey, D. V. Wagle, G. A. Baker, and J. Sangoro, *Proc. Natl. Acad. Sci.* **118**, e2020878118 (2021).

# 2 Theoretical Background

## 2.1 The Liquid State

In general, liquid has a certain volume at atmospheric pressure but can flow and change its shape. The arrangement of particles in liquids is conventionally regarded to be somewhere between the gas and solid states. For the gas state, the particles are free to move randomly, and the interactions between them can be basically ignored, while in a crystal, the particles are organized in a well-defined lattice pattern with strong intermolecular forces. Therefore, the liquid state is categorized as a condensed phase of matter in which the constituent particles have a disordered arrangement but can possess a short-range bond-orientational order. Above melting temperature, the particles in liquids have higher translational and rotational degrees of freedom, while rapid cooling below the melting point can drive the liquid to enter a metastable supercooled liquid state, in which the particles' motions become noticeably slower. Further cooling below the glass transition temperature produces a glass whose structure fundamentally resembles the liquid from which the glass was generated. However, the ability to resist flow is enhanced. In other words, the viscosity of glass is dramatically increased by more than 15 orders of magnitude compared with the normal liquid state.[1],[2],[3]. On the other hand, when the cooling rate is high enough, the material does not achieve a regular lattice pattern due to insufficient time to form crystalline nuclei. Thus, the lack of long-range order is essential in distinguishing glassy and crystalline.

## 2.2 Liquid-Liquid Phase Transition

Two or more distinct liquid phases may exist in a single-component material, which is known as liquid polymorphism, and the transition between them is called liquid-liquid phase transition (LLT).[4],[5],[6],[7] Tanaka proposed that any liquids tend to form locally ordered structures favored at energy and entropy levels, and they drew a physical picture where locally favored structures with limited lifespan can spontaneously arise and annihilate in a sea of normal liquid structures. [8],[9],[10],[11] Based on this, the LLT can be explained as a first-order phase transition between one type of local structure (i.e., normal-liquid structure) and another kind of preferred local structure with lower energy and degeneracy. The biggest obstacle to LLT is the formation of crystals. Therefore, according to the relative position of melting point,  $T_m$ , and critical point of LLT,  $T_{LL}$ , the LLT may occur in the following situations[4]: (i) for atomic systems with  $T_{LL} > T_m$ , LLT

can exist in a stable equilibrium liquid state; (ii) for  $T_{LL} < T_m$ , LLT exists in a supercooled liquid state usually observed in molecular systems.

On the other hand, it should be pointed out that the LLT is first-order nature similar to crystallization. Therefore,  $H$  or  $V_{sp}$  should discontinuously change at the liquid-liquid transition temperature. However, it does not mean that the two distinct liquid phases cannot coexist in the system during LLT. During the first-order phase transition, the coexistence regions of both phases may exist in the system, e.g., the ice and liquid water coexist when the ice melts. So far, some reported systems exhibiting LLT had been proven their first-order nature. More specifically, the researchers observed the coexistence of two distinct liquid phases, a sharp transformation between them, and no detectable intermediate state, in liquid P [12], S [13], TPP [14], and high-pressure hydrogen [15] by in-situ density, X-ray diffraction, flash differential scanning calorimetry, Raman scattering measurements, and quantum Monte Carlo method.

Actually, the LLT itself is not difficult to understand. Instead, the puzzle is in the origin and evolution of the transition between liquid 1 and liquid 2. Furthermore, it is worth going deep into this intriguing phenomenon not only because of its counterintuitive nature but also because it provides crucial information on the fundamental nature of the liquid state. For example, LLT has been considered to contribute to explaining water's anomalies.[16],[17],[18],[19] However, the homogeneous ice nucleation increases the difficulty of obtaining direct proof for LLT in real water through experiments and numerical simulations. As a result, there is no unified conclusion on the presence of LLT in real water at present. The same strait of LLT also applies to other types of systems, including molecular and atomic systems [12],[13],[20]. Thus, the LLT is still a controversial topic in the field of condensed matter physics.

## **2.3 Ionic Liquids as Candidates to Study the Liquid-Liquid Transition**

Ionic liquids (ILs) are a particular category of lower melting salts composed solely of ions with various molecular symmetry and charge delocalization. [21] In 1914, Paul Walden [22] synthesized the first IL, ethyl ammonium nitrate (EAN), which exhibited a melting point of 285 K and a rather low viscosity. Unfortunately, this work did not attract much attention from various scientific communities at that time. Forty years later, Hurley and Wier [23] synthesized organic chloroaluminates by mixing aluminum compounds with alkylpyriferinium chloride salts and recognized that this approach could decrease the melting temperature of molten salt materials. In the 1980s, ILs were proposed as solvents

for organic synthesis and were active in the field of electrochemical synthesis. In addition, the scope of research spread to chemistry, physics, biology, materials science, and environmental science. Particularly, publications on ILs have been marked by exponential growth over the last three decades. By carefully choosing the combinations of cations and anions, as well as mixing, matching, and incorporating different atoms or functional groups into ions, a variety of ILs with varying physicochemical properties can be synthesized. The diversity of ILs provides numerous possibilities for many industrial applications. Combining the advantages of high ionic conductivity, good thermal and chemical stability, negligible volatilities, and non-flammability, ILs meet the needs of electrochemistry, organic chemistry, catalysis, energy storage, engineering, and pharmacy. [23],[24],[25]

First, it is worth emphasizing that most ILs are good glass formers and can be easily supercooled to the glassy state without crystallization. As mentioned before, the foremost challenge in studying LLT processes is the occurrence of crystallization, which poses a significant obstacle to obtaining clear evidence of LLT. Therefore, ILs with excellent glass-forming ability should be prioritized as potential candidates for the LLT research. Second, it is logical to expect that a case of LLT in an IL system would emerge in the supercooled liquid state since a lot of examples of LLT in the literature occur in the supercooled regime below melting point, especially for molecular liquids (i.e., water and triphenyl phosphite). Moreover, some ILs that have been thoroughly investigated deep down to the glassy state can be temporarily ignored, as LLT is unlikely to be overlooked within them.[26] On the other hand, compared with other glass formers, the decisive Coulomb forces among the polar domains and the favorable van der Waals interaction among the non-polar domains in the constituent ions are the key drivers to constructing mesoscale aggregated structures and remarkable ion clusters in ILs.[21] A combination of polar and non-polar components and a subtle balance of intermolecular interactions result in various potential liquid morphologies and may direct the occurrence of LLT.

We can only make speculations on the morphology necessary for LLT in an IL system. As one of the most widely applied ILs families in the industry, (tetra)alkylphosphonium-based ILs exhibit superior physicochemical properties compared to nitrogen-based ILs and imidazolium-based ILs,[27] such as lower viscosity, higher thermal stability and ion conductivity. The most frequently studied ILs in the (tetra)alkylphosphonium family are those based on the trihexyl(tetradecyl)phosphonium cation ( $[P_{66,14}]^+$ ) due to its relatively low price.[28] In addition, the segregation of polar and non-polar domains in ILs and the existence of long alkyl chains providing the flexible

molecular structures of  $[P_{666,14}]$  cation facilitate the nanoscale aggregation of the non-polar alkyl domain in ILs. Therefore, (tetra)alkylphosphonium-based ILs are ideal for studying the LLT.

Recently, Harris et al. presented a report that LLT can occur in ILs [34], which opened a new perspective on the study of LLT. They found that upon rapid cooling of trihexyl(tetradecyl)phosphonium borohydride,  $[P_{666,14}][BH_4]$ , the extension and ordering of the polarity-alternation structure, which is dependent on the configuration of the alkyl chains on the  $[P_{666,14}]$  cation, can be accessed by wide-angle X-ray scattering (WAXS) and Raman spectra. Furthermore, such a structural reorganization coincides well with the calorimetric scan, indicating a first-order thermodynamic transition.

As stated above, we expect that  $[P_{666,14}][BH_4]$  is not an isolated example but belongs to a systematic family of ionic liquids that exhibit LLT, and studying these compounds will provide insight into the nature of LLT and the structure-property relationships governing LLT formation.

## 2.4 Thermodynamics of Ionic Liquids

One of the essential characteristics of ILs is the substantially wider temperature range of the liquid state compared with traditional organic solvents. Some ILs exhibit first-order liquid-crystal phase transition upon cooling with a rapid decrease in volume at crystallization temperature. However, most ILs form glasses rather than organized crystalline structures at lower temperatures. [29] When we decrease temperature rapidly, the ion motions slow down, leading to a rise in viscosity and a continuous reduction in volume. The diagram of the specific volume  $V_{sp}$  or enthalpy  $H$  on temperature for ILs has been shown in Fig. 2.1a. Due to further cooling below the glass transition temperature  $T_g$ , ILs enter a glassy state, where the ion motion almost ‘stops’ on the laboratory timescale, and the volume changes only slightly. Additionally, different cooling rates affect the properties of the induced glass. Specifically, a faster cooling rate causes a higher glass transition temperature. This unique behavior is due to the kinetic nature of the vitrification process. The slower the cooling rate, the more liquid can be supercooled before reaching the glassy state, and its molecules have more time to move around and find tighter lower-energy arrangements. Therefore, the system will be frozen at a lower temperature.

Another feature of glass transition is a continuous step-like change in the heat capacity,  $C_P \equiv \left(\frac{\partial H}{\partial T}\right)_P$ , which is depicted in Fig. 2.1b. The change in heat capacity between supercooled liquid and glassy state in the vicinity of glass transition is known as  $\Delta C_P$ . The gradual change in  $C_P(T)$  curve indicates that the glass transition is not a second-

order phase transition, in which the first derivatives of free energy are continuous but exhibit discontinuity in the second derivatives. It should be emphasized that the glass transition does not occur at a fixed temperature but rather within a temperature range. For most glass formers, the glass transition temperature  $T_g$  is usually determined as the midpoint of the transition region[30]. (see Fig. 2.1b)

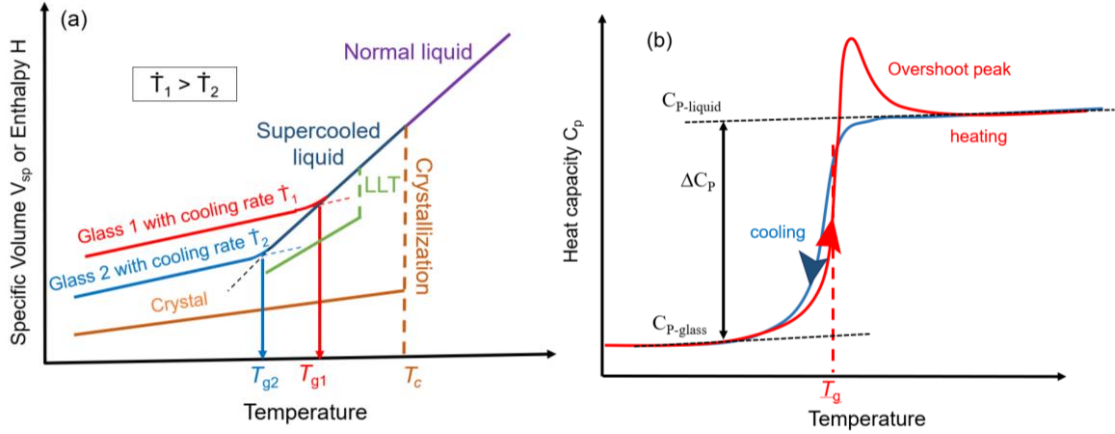


**Fig. 2.1** (a) Schematic diagram of specific volume or enthalpy as the function of temperature from the normal liquid state to crystal or glassy state. (b) Temperature dependence of heat capacity during the glass transition on the cooling and subsequent heating process.

Furthermore, the width of the glass transition provides significant information about the dynamic heterogeneity in glass-forming systems. It is well-known that molecules move very slowly near  $T_g$ . It may take hours for some molecules to reorient, while some molecules only a few nanometers away may need several days to rearrange. This dynamic heterogeneity leads to the broader glass transition region. Generally, the most intuitive and commonly used method to quantify the dynamic heterogeneity of glass formers near the glass transition temperature is to calculate the number of dynamically correlated molecules,  $N_\alpha$ , by Donth method [31], which represents the number of particles having the same molecular mobility in one average cooperatively rearranging region. Based on the fluctuation-dissipation theorem, both temperature and entropy can simultaneously fluctuate. Donth et al. suggested that the entropy fluctuations are related to the specific heat capacity in the temperature range at which glass transition occurs, and the size of temperature fluctuations can be determined by the width of the glass transition between 16% and 84% of the  $\Delta C_p$  step.[31],[32] Consequently, the value of dynamically correlated particles,  $N_\alpha^D(T_g)$ , can be estimated using only calorimetric data by the following equation:

$$N_\alpha^D(T_g) = \frac{k_B T_g^2}{M(\delta T)^2} N_A \left( \frac{1}{C_p^{glass}} - \frac{1}{C_p^{liquid}} \right) \quad (2.1)$$

where  $k_B$  is Boltzmann constant,  $M$  means molar mass,  $N_A$  is Avogadro constant,  $C_p^{liquid}$  and  $C_p^{glass}$  represent the heat capacities at the supercooled liquid state and glassy state

during the glass transition, and  $\delta T$  denotes the average temperature fluctuation related to the dynamic glass transition. Usually, polymers have a larger value of  $N_\alpha^D(T_g)$ , i.e., from 200 to 800, than van der Waals liquids and H-bonding systems ( $70 < N_\alpha^D(T_g) < 300$ ) [33]. Ionic liquids exhibit dynamic heterogeneity,  $N_\alpha^D$ , in the range of 20 – 200 [33],[34]. Moreover, it is considered that the dynamic heterogeneity of ILs is closely related to the electrostatic interactions and different types of intermolecular interactions (i.e., van der Waals, H-bonding, and Coulomb forces).

It is important to recognize that glass transition is a timescale-dependent behavior. [29] Therefore, the glassy state is not a thermodynamic equilibrium phase. As a result, the structure and properties of glass, including enthalpy, volume, and mechanical properties, evolve (but very slowly) toward their equilibrium values at isothermal annealing below  $T_g$ . This process is known as structural recovery or physical aging. [35],[36] As shown in Fig. 2.1b, a  $C_P$  overshoot peak may occur in the glass transition region during the subsequent heating after cooling, reflecting the recovery of the enthalpy lost during cooling. [35],[37],[38] The overshoot peak grows with the decrease of the preceding cooling rate and with the elongation of aging time [39],[40]. Moreover, the aging temperature will also affect the size of the overshoot. [41],[42] Therefore, separating glass transition and LLT by performing physical aging of glass-forming systems is possible.

On the other hand, when the heating process is performed after quenching to the glassy state, the cold crystallization process (an exothermic transition) is frequently observed at a temperature above  $T_g$  for many ILs. Further heating causes melting at  $T_m$ . In addition, other kinds of thermal behaviors have been reported in IL systems. For example, the polymorphism in the crystalline state (solid-solid phase transition), [43],[44],[45], the mesomorphism (liquid crystalline phases) of ionic liquid crystals, [46],[47],[48],[49], and the liquid-liquid phase separation in solutions of ILs [50],[51], [52],[53].

## 2.5 Dynamics of Ionic Liquids

A variety of experimental techniques have been established and applied to study the dynamics of ILs over a wide temperature range, including mechanical measurements [54], [55], light [56] and neutron scattering [57], nuclear magnetic resonance spectroscopy (NMR) [58],[59], and broadband dielectric spectroscopy (BDS) [60],[61],[62],[63]. Although decades of intensive research, many specific features of ILs remain poorly understood at the molecular level. The dynamics of ILs covering normal, supercooled,

and glassy states are critical in studying electrolytes from both the fundamental and application perspectives.

When ILs are in the normal-liquid state, ions can move freely with a slight flow resistance described by viscosity,  $\eta$ . As the temperature increases, the molecular kinetic energy increases and promotes the breaking of intermolecular bonds, reducing fluid viscosity. Traditionally, the temperature dependence of relaxation dynamics (viscosity  $\eta$ , relaxation time  $\tau$ , etc.) in equilibrium liquid is described in terms of Arrhenius law [64]:

$$\eta = \eta_{\infty} \exp\left(\frac{E_a}{k_B T}\right) \quad (2.2)$$

where  $\eta_{\infty}$  denotes the viscosity at very high temperatures,  $k_B$  is the Boltzmann constant, and  $E_a$  is the activation energy, which is usually temperature-independent for a given system, quantifying the energy barrier needed for molecular motion. Thus, the plot of  $\log \eta$  vs  $1/T$  should be linearly related, and the slope can be used to determine the value of  $E_a$ . In this range, the value of dynamic viscosity of ILs is about  $10^0$  to  $10^{-2}$  Pa s [65],[66], and the corresponding dielectric relaxation time  $\tau$  is on the order of nano- or pico-second, indicating that ions move relatively independently.

However, as the temperature drops rapidly, the IL enters the supercooled state, charge transport slows down, and the liquid becomes denser with the cooperative motion of ions. The most prominent feature of supercooled ILs is a dramatic decrease in the direct current (dc) conductivity,  $\sigma_{dc}$ , spanning more than 12 decades from the normal liquid state (near  $T_m$ ) to the glass transition.[67] In particular,  $\sigma_{dc}$  fails to obey the simple Arrhenius behavior and becomes more sensitive to temperature variation. Among the variety of models proposed to describe such non-Arrhenius dependence, the modified form [68] of the empirical Vogel-Fulcher-Tammann (VFT) equation [69][70][71] is the most prevalent one for ILs:

$$\sigma_{dc}(T) = \sigma_0 \exp\left(-\frac{DT_0}{T-T_0}\right) \quad (2.3)$$

where  $\sigma_0$  is the pre-exponential factor,  $D$  denotes the strength parameter quantifying the discrepancy from Arrhenius behavior, and  $T_0$  is known as the ‘ideal’ glass transition temperature corresponding to the structural relaxation time at which the molecular mobility would approach zero. Considering the kinetic nature of the vitrification process, glass transition temperature  $T_g$  is usually defined at constant viscosity  $\eta(T_g) = 10^{12}$  Pa·s, structural relaxation time  $\tau_{\alpha}(T_g) = 1000$  s [72],[73], or when the value of  $\sigma_{dc}$  is achieving around  $10^{-15}$  S cm<sup>-1</sup> for many ionic conductors.[74] This definition agrees well with the value of  $T_g$  measured by the calorimetric scan for most ionic glass-forming materials.

From the perspective of the degree of deviation from the Arrhenius-type temperature dependence, the glass-forming system can be classified as “fragile”, “moderately fragile”, or “strong”.[ 75 ] For strong liquids, the temperature dependence of any quantity describing the glassy dynamics (i.e., viscosity, relaxation time, and conductivity) closely obeys an Arrhenius behavior near  $T_g$ , while fragile liquids significantly depart from the Arrhenius type dependence. The Angell plot [68] ( $\log_{10} \eta$  vs.  $T_g/T$  or  $\log_{10} \tau_a$  vs.  $T_g/T$ ) (see Fig. 2.2) is commonly used to illustrate the fragility of different glass-forming materials. Correspondingly, the fragility index (also called as isobaric steepness index),  $m_P$  is defined as the slope of viscosity or relaxation time on  $T_g$  scale at  $T_g$  [76]:

$$m_P = \left( \frac{\partial \log_{10} \tau}{\partial (T_g/T)} \right)_P \Big|_{T=T_g} \quad (2.4)$$

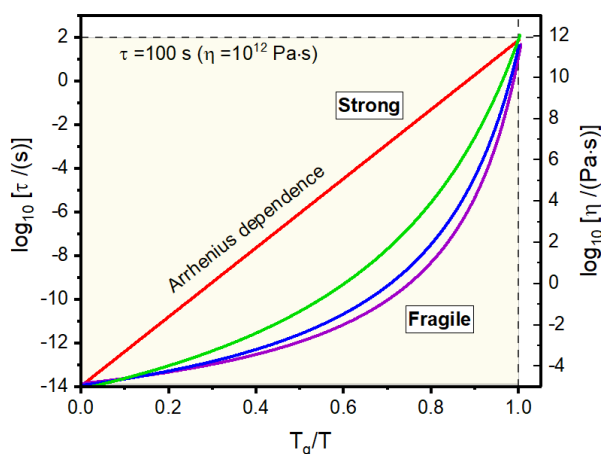


**Fig. 2.2** The Angell plot of relaxation time  $\tau$  or viscosity  $\eta$  as a function of  $T_g/T$

Normally, the value of  $m_P$  is less than 30 for strong glass-forming liquids and more than 100 for fragile liquids, such as polymers. In particular, numerous aprotic ionic liquids have  $m_P$  values in the range of 40 -140 [72],[77]. In addition to the fragility index, the strength parameter  $D$  obtained from the VFT equation is another index that characterizes the fragility of materials, and its value is related to  $m_P$  by  $m_P = 16 + 590/D$  [76]. Notably, the more fragile the material, the smaller the  $D$  value ( $D < 10$ ), denoting the significant deviation of relaxation time from Arrhenius behavior.

There is no doubt that the VFT equation plays a key role in describing the molecular dynamics of supercooled liquids. For most ILs, one VFT is sufficient to represent the ionic conductivity over a wide temperature range, except for several cases [34],[78]. However, many low-molecular glass-forming liquids need two VFT equations to represent the structural relaxation time. In these cases, the crossover temperature  $T_b$  has been defined at the kink of relaxation dynamics from one VFT to another at around  $1.2T_g$  or even higher [79]. Within a set of exceptional phenomena, the molecular dynamics

move from “simple” to “complex” at  $T_b$  upon cooling, such as (i) the dispersion of the primary relaxation process is narrow above  $T_b$  but becomes broader below  $T_b$  [80], (ii) the secondary relaxation process appears and splits off from the primary relaxation [81], [82], (iii) the relaxation times at the crossover closely match the so-called "magic" relaxation times, i.e.,  $\tau(T_b) \approx 10^{-7}$ s [83],[84]. Interestingly, this "magic" relaxation time satisfies for also several ILs exhibiting the crossover temperature  $T_b$ . [78] To determine the value of  $T_b$ , Stickel [85] and co-workers [86] proposed a derivative analysis of temperature dependence of relaxation time or viscosity by the following function:

$$\Phi = \left[ \frac{d(\log \tau)}{d(1000/T)} \right]^{-1/2} \quad (2.5)$$

As presented in Fig. 2.3, the Stickel operator performs a linear temperature dependence within one VFT equation. The existence of crossover temperature  $T_b$  illustrates the enhancement of intermolecular cooperative interactions. In this context, it is worth exploring whether the LLT occurring in ILs will also cause a similar feature.

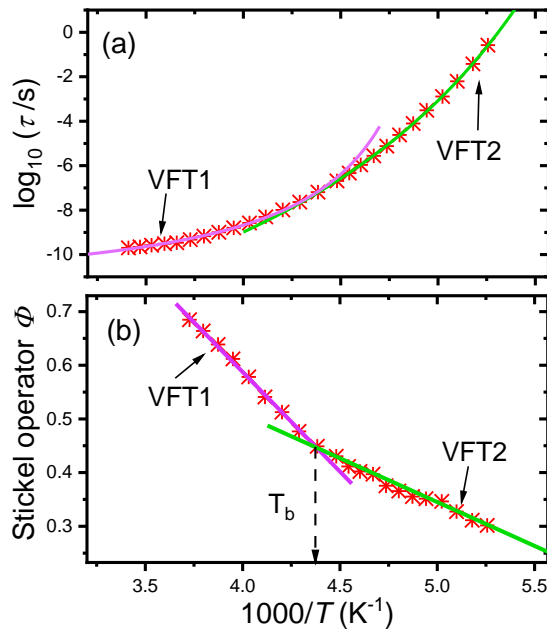


**Fig. 2.3 (a)** Temperature dependence of structural relaxation time for a glass-forming system, solid lines indicate different fits to the VFT equation. **(b)** Stickel analysis of data from panel a as the function of  $1000/T$ , solid lines represent linear fits, and dashed arrow denotes the position of  $T_b$ .

All ILs are assumed to have some level of ion conductivity. However, not all of the ions present appear to be available to engage in conduction activities. According to the fractional Walden rule[87],[88], the ionic conductivity of most aprotic ILs is inversely related to viscosity. That is, the product of molar conductivity  $\Lambda$  and fluidity ( $1/\text{viscosity}$ ,  $1/\eta$ ) is constant:

$$\Lambda \eta^{-k} = \sigma_{dc} M \rho^{-1} \eta^{-k} = \text{constant} \quad (2.6)$$

where  $k$  is the temperature-dependent constant,  $M$  is molar mass, and  $\rho$  means density. The Walden plot ( $\log \Lambda$  vs  $\log \eta^{-1}$ ) is often used to quantify and understand the ionicity of ILs.[89] If the ion diffusion is coupled to the viscosity of ILs, namely, the charge transport mechanism is fully controlled by the viscosity, then the Walden diagram should be close to the reference Walden line, which denotes dilute aqueous KCl solution with a slope equal to 1. Whereas most ILs fall more or less below the line depending on their structures.[87],[89]

As pure electrolytes composed solely of cations and anions, ILs possess remarkable ionic conductivity, which arises from the free movement of charge carriers (i.e., cations and anions). Consequently, the charge transport usually depends on the viscosity of ILs over a wide temperature range. That is, the conductivity relaxation time, contributing to the translational motion of ions, is coupled with structural relaxation time. However, this behavior may not universally apply to all ionic liquids at all temperatures. As the temperature is decreased toward  $T_g$  and into the glassy state, numerous experiments of protic ionic liquids show that the proton transfer is faster than molecular diffusion, showing a decoupling between charge transport and structural dynamics. [90],[91]. The decoupling in protic ILs is believed to be due to the proton hopping within the hydrogen bonding network formed by charge carriers. [92],[93] Moreover, strong decoupling between ionic conductivity and structural relaxation has also been found in polymerized ionic liquids, which is proposed to originate from the different contributions of the cations and the anions in regulating the two processes near  $T_g$ . [94] The structural dynamics is dominated by cations covalently attached to the polymer chains, whereas the anions control ionic conductivity due to their small size and free, fast motions. On the contrary, most aprotic ILs reveal coupling between structural and conductivity relaxation times. It means that charge transfer and ion motion are coupled.[95]

When the IL is cooled far enough in the deep glassy state, the relaxation time of the system exceeds the range measurable in the laboratory, so secondary relaxation processes representing fast localized motions dominate in the monitored frequency range. [96], [97] Generally, the secondary relaxation process is less sensitive to thermodynamic variables than structural relaxation. Correspondingly, the secondary relaxation behavior obeys the Arrhenius law (Eq. 2.2).[97],[98] Many ILs have one or more well-resolved secondary relaxation processes, while some ILs do not appear to have any secondary relaxation, at least within the examined temperature and pressure range.[96]

## 2.6 Dynamics of Ionic Liquids at High Pressure

It is common knowledge that temperature is an important thermodynamic variable for studying supercooled liquids and glasses, but cooling is not the only path to induce the glassy state. Isothermal compression can also lead to an intensive increase in structural relaxation time and viscosity. In other words,  $T$  and  $P$  similarly affect molecular dynamics [99]. Nevertheless, temperature affects the rotation and translation motions of molecules mainly by varying their thermal energy, while pressure affects the distance between molecules. Therefore, from this point of view, applying pressure and temperature as independent but complementary variables provides an excellent opportunity to provide a complete physical description of the dynamics of ILs.

The pressure counterpart of the Arrhenius law[67] is commonly used to parameterize the effect of pressure on the ion dynamics of most electrolytes in the normal liquid state.

$$\log \sigma_{dc} = \log \sigma_0 + \frac{\log(e)P\Delta V}{RT} \quad (2.7)$$

where  $\sigma_0$  denotes the value of dc-conductivity at  $P = 0.1$  MPa and can be taken from ambient pressure measurement,  $R$  is the gas constant,  $\Delta V$  is the activation volume denoting the volume difference between activated to nonactivated state.

Herein, it is worth mentioning that the activation volume is constant only when the logarithm of dc-conductivity is linearly related to the pressure. However, for most ionic conductors, the non-linear relationship of  $\log_{10} \sigma_{dc}(P)$  has been observed experimentally, especially near  $T_g$ . [100],[101] Among many non-linear models, the pressure counterpart of the VFT equation is most commonly used [67],[102]:

$$\sigma_{dc} = \sigma_0 \exp\left(\frac{D_P P}{P_0 - P}\right) \quad (2.8)$$

where  $D_P$  and  $P_0$  are fitting parameters. Thus, the value of  $\Delta V$  reflects the magnitude of local ion motion, and directly it can be determined from the derivative of  $\log_{10} \sigma_{dc}(P)$  dependence at constant temperature:

$$\Delta V = RT \ln(10) \left( \frac{\partial \log_{10} \sigma_{dc}}{\partial P} \right)_T \quad (2.9)$$

Similar to the  $T_g$ , the glass transition pressure  $P_g$  can be defined when the ionic conductivity reaches  $10^{-15}$  S cm<sup>-1</sup>. As a result, one can get the  $P_g$  by extrapolating  $\log_{10} \sigma_{dc}(P) = -15$  at different temperatures and then plot  $T_g(P_g)$  dependence. Due to the increase in molecular packing induced by compression,  $T_g$  does not increase linearly with increasing  $P$ . [99] The relationship of  $T_g(P_g)$  is usually described by means of the Andersson-Andersson empirical equation[103]:

$$T_g = k_1 \left(1 + \frac{k_2}{k_3} P\right)^{\frac{1}{k_2}} \quad (2.10)$$

where  $k_1$ ,  $k_2$ ,  $k_3$  are fitting parameters. Therefore the sensitivity of glass transition temperature on pressure, i.e.,  $dT_g/dP$  coefficient, can be calculated directly from the mathematical fitting analysis:

$$dT_g/dP|_{P=0.1MPa} = \frac{k_1}{k_3} \quad (2.11)$$

One striking phenomenon that occurs only in pressure dependence of molecular dynamics is the existence of an inflection point. In 1925, Bridgman first reported the concave-convex character in the viscosity behavior of several materials under high pressure.[104] The presence of the inflection point indicates that  $\log_{10} \eta(P)$  dependence changes from a slower than exponential growth, i.e., negative curvature at low pressures, to faster than exponential growth at high pressures (positive curvature). Consequently, the pressure dependence of activation volume reveals a clear minimum at a constant temperature in the low-pressure regime. Herbst et al.[105] proposed that the inflection point can be attributed to a non-linearity change of volume with increasing pressure. In comparison, Casalini and Bair [106] recommended that it is related to the pressure dependence of the compressibility and the apparent activation energy at constant volume. Furthermore, Bair [107] proposed a hybrid model that well parameterizes the  $\eta(P)$  dependence over the entire pressure range by combining the pressure counterpart of the VFT equation with the McEwen equation:

$$\eta(P) = \eta_0 \left(1 + \frac{\alpha_0}{q} P\right)^q \exp\left(\frac{D_P P}{P_0 - P}\right) \quad (2.12)$$

where  $\alpha_0$  and  $q$  are the McEwen parameters. Recently, Thoms et al. [108] reported the first IL ( $C_8HIM NTF_2$ ) exhibiting the same behavior in conductivity, and Eq. 2.12 was successfully applied to fit the measured conductivity data. So far, the inflection point only has been observed in several ILs. [109]

## 2.7 Reference

- [1] C. A. Angell, *J. Phys. Chem. Solids*. **49**, 863 (1988).
- [2] M. D. Ediger, C. A. Angell, and S. R. Nagel, *J. Phys. Chem.* **100**, 13200 (1996).
- [3] M. I. Ojovan, *Molecules* **25**, 4029 (2020).
- [4] H. Tanaka, *J. Chem. Phys.* **153**, 130901 (2020).
- [5] H. Tanaka, *Eur. Phys. J. E* **35**, 113 (2012).
- [6] H. Tanaka, *J. Phys.: Condens. Matter* **11**, L159 (1999).
- [7] H. Tanaka, *J. Non-Cryst. Solids* **351**, 3371 (2005).

- [8] F. C. Frank and N. F. Mott, *Pro. R. Soc. London. Ser. A.* **215**, 43 (1997).
- [9] J. Michalski, A. C. Mitus, and A. Z. Patashinskii, *Phys. Lett. A* **123**, 293 (1987).
- [10] A. Z. Patashinski, A. C. Mitus, and M. A. Ratner, *Phys. Rep.* **288**, 409 (1997).
- [11] K. F. Kelton, G. W. Lee, A. K. Gangopadhyay, R. W. Hyers, T. J. Rathz, J. R. Rogers, M. B. Robinson, and D. S. Robinson, *Phys. Rev. Lett.* **90**, 195504 (2003).
- [12] Y. Katayama, T. Mizutani, W. Utsumi, O. Shimomura, M. Yamakata, and K. Funakoshi, *Nature* **403**, 170 (2000).
- [13] L. Henry, M. Mezouar, G. Garbarino, D. Sifré, G. Weck, and F. Datchi, *Nature* **584**, 382 (2020).
- [14] M. Kobayashi and H. Tanaka, *Nat. Commun.* **7**, 13438 (2016).
- [15] M. A. Morales, C. Pierleoni, E. Schwegler, and D. M. Ceperley, *Proc. Natl. Acad. Sci.* **107**, 12799 (2010).
- [16] O. Mishima and H. E. Stanley, *Nature* **396**, 329 (1998).
- [17] P. Gallo, K. Amann-Winkel, C. A. Angell, M. A. Anisimov, F. Caupin, C. Chakravarty, E. Lascaris, T. Loerting, A. Z. Panagiotopoulos, J. Russo, J. A. Sellberg, H. E. Stanley, H. Tanaka, C. Vega, L. Xu, and L. G. M. Pettersson, *Chem. Rev.* **116**, 7463 (2016).
- [18] O. Mishima, L. D. Calvert, and E. Whalley, *Nature* **310**, 393 (1984).
- [19] F. Sciortino, *Proc. Natl. Acad. Sci.* **114**, 8141 (2017).
- [20] H. Tanaka, R. Kurita, and H. Mataka, *Phys. Rev. Lett.* **92**, 025701 (2004).
- [21] Y. L. Wang, B. Li, S. Sarman, F. Mocci, Z.-Y. Lu, J. Yuan, A. Laaksonen, and M. D. Fayer, *Chem. Rev.* **120**, 5798 (2020).
- [22] F. H. Hurley and T. P. Wier, *J. Electrochem. Soc.* **98**, 207 (1951).
- [23] D. R. MacFarlane, M. Forsyth, P. C. Howlett, M. Kar, S. Passerini, J. M. Pringle, H. Ohno, M. Watanabe, F. Yan, W. Zheng, S. Zhang, and J. Zhang, *Nat. Rev. Mater.* **1**, 1 (2016).
- [24] Z. Tshemese, S. C. Masikane, S. M. and N. Revaprasadu, Z. Tshemese, S. C. Masikane, and S. M. and N. Revaprasadu, *Progress in Green Solvents for the Stabilisation of Nanomaterials: Imidazolium Based Ionic Liquids* (IntechOpen, **2018**).
- [25] R. Patel, M. Kumari, and A. B. Khan, *Appl. Biochem. Biotechnol.* **172**, 3701 (2014).
- [26] Harris, Matthew Albert, *Liquid-Liquid Transition in Ionic Liquids*. PhD diss., University of Tennessee, **2022**.
- [27] D. H. Zaitsau, N. Plechkova, and S. P. Verevkin, *J. Chem. Thermodyn.* **130**, 204 (2019).
- [28] M. G. Freire, P. J. Carvalho, R. L. Gardas, L. M. N. B. F. Santos, I. M. Marrucho, and J. A. P. Coutinho, *J. Chem. Eng. Data* **53**, 2378 (2008).

- [29] R. M. Douglas, K. Mega, and M.P. Jennifer, *Fundamentals of Ionic Liquids* (Wiley-VCH Verlag GmbH & Co. KGaA, Weinheim, Germany, **2017**), pp. 103–147.
- [30] Q. Zheng, Y. Zhang, M. Montazerian, O. Gulbiten, J. C. Mauro, E. D. Zanotto, and Y. Yue, *Chem. Rev.* **119**, 7848 (2019).
- [31] E. Donth, *J. Non-Cryst. Solids* **53**, 325 (1982).
- [32] E. Hempel, G. Hempel, A. Hensel, C. Schick, and E. Donth, *J. Phys. Chem. B* **104**, 2460 (2000).
- [33] K. Grzybowska, A. Grzybowski, Z. Wojnarowska, J. Knapik, and M. Paluch, *Sci. Rep.* **5**, 16876 (2015).
- [34] M. Musiał, S. Cheng, Z. Wojnarowska, and M. Paluch, *J. Phys. Chem. B* **125**, 4141 (2021).
- [35] Y. P. Koh and S. L. Simon, *Macromolecules* **46**, 5815 (2013).
- [36] L. C. E. Struik, *Polym. Eng. & Sci.* **17**, 165 (1977).
- [37] X. Guo, M. Potuzak, J. C. Mauro, D. C. Allan, T. J. Kiczanski, and Y. Yue, *J. Non-Cryst. Solids* **357**, 3230 (2011).
- [38] I. M. Hodge, *J. Non-Cryst. Solids* **169**, 211 (1994).
- [39] L. Boehm, M. D. Ingram, and C. A. Angell, *J. Non-Cryst. Solids* **44**, 305 (1981).
- [40] X. Monnier, S. Marina, X. Lopez de Pariza, H. Sardón, J. Martin, and D. Cangialosi, *Polymers (Basel)* **13**, 954 (2021).
- [41] G. P. Johari, *Thermochim. Acta* **693**, 178715 (2020).
- [42] X. Monnier, A. Saiter, and E. Dargent, *Thermochim. Acta* **648**, 13 (2017).
- [43] A. Triolo, A. Mandanici, O. Russina, V. Rodriguez-Mora, M. Cutroni, C. Hardacre, M. Nieuwenhuyzen, H.-J. Bleif, L. Keller, and M. A. Ramos, *J. Phys. Chem. B* **110**, 21357 (2006).
- [44] S. Hayashi, R. Ozawa, and H. Hamaguchi, *Chem. Lett.* **32**, 498 (2003).
- [45] F. Qu, Q. Q. Zhu, and C. L. Liu, *Cryst. Growth Des.* **14**, 6421 (2014).
- [46] K. Lava, K. Binnemans, and T. Cardinaels, *J. Phys. Chem. B* **113**, 9506 (2009).
- [47] K. Stappert, D. Ünal, B. Mallick, and A.-V. Mudring, *J. Mater. Chem. C* **2**, 7976 (2014).
- [48] N. Kapernaum, A. Lange, M. Ebert, M. A. Grunwald, C. Haege, S. Marino, A. Zens, A. Taubert, F. Giesselmann, and S. Laschat, *ChemPlusChem* **87**, e202100397 (2022).
- [49] K. Goossens, K. Lava, C. W. Bielawski, and K. Binnemans, *Chem. Rev.* **116**, 4643 (2016).
- [50] A. Butka, V. R. Vale, D. Saracsan, C. Rybarsch, V. C. Weiss, and W. Schröer, *Pure Appl. Chem.* **80**, 1613 (2008).
- [51] M. Wagner, O. Stanga, and W. Schröer, *Phys. Chem. Chem. Phys.* **6**, 1750 (2004).
- [52] W. Schröer, *Contrib. to Plasma Phys.* **52**, 78 (2012).

- [53] S. Woutersen, B. Ensing, M. Hilbers, Z. Zhao, and C. A. Angell, *Science* **359**, 1127 (2018).
- [54] O. Palumbo, A. Paolone, D. Rauber, C. W. M. Kay, F. Philippi, and T. Welton, *J. Alloys Compd.* **919**, 165860 (2022).
- [55] T. Cosby, Z. Vicars, Y. Wang, and J. Sangoro, *J. Phys. Chem. Lett.* **8**, 3544 (2017).
- [56] S. Das, D. Radhakrishnan, V. S. Bhadram, C. Narayana, and A. J. Bhattacharyya, *Solid State Ion.* **363**, 115603 (2021).
- [57] C. P. Cabry, L. D'Andrea, N. S. Elstone, S. Kirchhecker, A. Riccobono, I. Khazal, P. Li, S. E. Rogers, D. W. Bruce, and J. M. Slattery, *Phys. Chem. Chem. Phys.* **24**, 15811 (2022).
- [58] D. Kruk, M. Wojciechowski, M. Florek-Wojciechowska, and R. K. Singh, *Mat.* **13**, 4351 (2020).
- [59] S. K. Davidowski, F. Thompson, W. Huang, M. Hasani, S. A. Amin, C. A. Angell, and J. L. Yarger, *J. Phys. Chem. B* **120**, 4279 (2016).
- [60] J. R. Sangoro and F. Kremer, *Acc. Chem. Res.* **45**, 525 (2012).
- [61] S. Kriptomou, G. Tsonos, A. Mezzetta, A. Mero, L. Guazzelli, K. Moutzouris, I. Stavrakas, and C. Tsonos, *Int. J. Mol. Sci.* **23**, 5642 (2022).
- [62] E. Thoms, P. Sippel, D. Reuter, M. Weiß, A. Loidl, and S. Krohns, *Sci. Rep.* **7**, 7463 (2017).
- [63] C. J. Jafta, C. Bridges, L. Haupt, C. Do, P. Sippel, M. J. Cochran, S. Krohns, M. Ohl, A. Loidl, E. Mamontov, P. Lunkenheimer, S. Dai, and X.-G. Sun, *ChemSusChem* **11**, 3512 (2018).
- [64] S. Glasstone, K. J. Laidler, and H. Eyring, *The Theory of Rate Processes* (McGraw-Hill, New York, **1941**).
- [65] S. Jiang, Y. Hu, Y. Wang, and X. Wang, *J. Phys. Chem. Ref. Data.* **48**, 033101 (2019).
- [66] F. Kremer and A. Schönhal, *Broadband Dielectric Spectroscopy* (Springer Berlin Heidelberg, Berlin, Heidelberg, **2003**).
- [67] M. Paluch, editor, *Dielectric Properties of Ionic Liquids* (Springer International Publishing, Cham, 2016).
- [68] C. A. Angell, Strong and fragile liquids. In *Relaxations in complex systems*, eds. K. L. Ngai, & G. B. Wright (NRL, Washington, DC, **1985**).
- [69] H. Vogel, *Phys. Z* **22**, 645 (1921).
- [70] G. S. Fulcher, *J. Am. Ceram. Soc.* **8**, 339 (1923).
- [71] G. Tammann, W. Hesse, *Z. Anorg. Allg. Chem.* **156**, 245 (1926).
- [72] P. Sippel, P. Lunkenheimer, S. Krohns, E. Thoms, and A. Loidl, *Sci. Rep.* **5**, 13922 (2015).

- [73] Z. Wojnarowska, C. M. Roland, A. Swiety-Pospiech, K. Grzybowska, and M. Paluch, *Phys. Rev. Lett.* **108**, 015701 (2012).
- [74] F. Mizuno, J.-P. Belieres, N. Kuwata, A. Pradel, M. Ribes, and C. A. Angell, *J. Non-Cryst. Solids* **352**, 5147 (2006).
- [75] C.A. Angell, *J. Non-Cryst. Solids* **131**, 13-31 (1991).
- [76] R. Böhmer, K. L. Ngai, C. A. Angell, and D. J. Plazek, *J. Chem. Phys.* **99**, 4201 (1993).
- [77] R. Tao, E. Gurung, M. M. Cetin, M. F. Mayer, E. L. Quitevis, and S. L. Simon, *Thermochim. Acta* **654**, 121 (2017).
- [78] Z. Wojnarowska, M. Musiał, M. Dzida, and M. Paluch, *Phys. Rev. Lett.* **123**, 125702 (2019).
- [79] E.-J. Donth, *The Glass Transition: Relaxation Dynamics in Liquids and Disordered Materials*, Vol. 48 (Springer Berlin Heidelberg, Berlin, Heidelberg, **2001**).
- [80] J. C. Martinez-Garcia, J. Martinez-Garcia, S. J. Rzoska, and J. Hulliger, *J. Chem. Phys.* **137**, 064501 (2012).
- [81] R. Casalini, M. Paluch, and C. M. Roland, *J. Chem. Phys.* **118**, 5701 (2003).
- [82] T. Fujima, H. Frusawa, and K. Ito, *Phys. Rev. E* **66**, 031503 (2002).
- [83] R. Casalini and C. M. Roland, *Phys. Rev. Lett.* **92**, 245702 (2004).
- [84] V. N. Novikov and A. P. Sokolov, *Phys. Rev. E* **67**, 031507 (2003).
- [85] F. Stickel, E. W. Fischer, and R. Richert, *J. Chem. Phys.* **102**, 6251 (1995).
- [86] C. Hansen, F. Stickel, R. Richert, and E. W. Fischer, *J. Chem. Phys.* **108**, 6408 (1998).
- [87] A. Pinkert, K. L. Ang, K. N. Marsh, and S. Pang, *Phys. Chem. Chem. Phys.* **13**, 5136 (2011).
- [88] A. N. Campbell and E. T. van der Kouwe, *Can. J. Chem.* **46**, 1294–1298 (1968)
- [89] D. R. MacFarlane, M. Forsyth, E. I. Izgorodina, A. P. Abbott, G. Annat, and K. Fraser, *Phys. Chem. Chem. Phys.* **11**, 4962 (2009).
- [90] Z. Wojnarowska, K. Kołodziejczyk, K. J. Paluch, L. Tajber, K. Grzybowska, K. L. Ngai, and M. Paluch, *Phys. Chem. Chem. Phys.* **15**, 9205 (2013).
- [91] Z. Wojnarowska and M. Paluch, *J. Phys.: Condens. Matter* **27**, 073202 (2015).
- [92] Z. Wojnarowska, E. Thoms, B. Blanchard, S. N. Tripathy, P. Goodrich, J. Jacquemin, J. Knapik-Kowalczyk, and M. Paluch, *Phys. Chem. Chem. Phys.* **19**, 14141 (2017).
- [93] Z. Wojnarowska, Y. Wang, K. J. Paluch, A. P. Sokolov, and M. Paluch, *Phys. Chem. Chem. Phys.* **16**, 9123 (2014).
- [94] J. R. Sangoro, C. Iacob, A. L. Agapov, Y. Wang, S. Berdzinski, H. Rexhausen, V. Strehmel, C. Friedrich, A. P. Sokolov, and F. Kremer, *Soft Matter* **10**, 3536 (2014).
- [95] Z. Wojnarowska, A. Lange, A. Taubert, and M. Paluch, *ACS Appl. Mater. Interfaces* **13**, 30614 (2021).

- [96] A. Rivera and E. A. Rössler, *Phys. Rev. B* **73**, 212201 (2006).
- [97] P. J. Griffin, A. P. Holt, K. Tsunashima, J. R. Sangoro, F. Kremer, and A. P. Sokolov, *J. Chem. Phys.* **142**, 084501 (2015).
- [98] C. Krause, J. R. Sangoro, C. Iacob, and F. Kremer, *J. Phys. Chem. B* **114**, 382 (2010).
- [99] G. Floudas, M. Paluch, A. Grzybowski, and K. Ngai, *Molecular Dynamics of Glass-Forming Systems*, Vol. 1 (Springer Berlin Heidelberg, Berlin, Heidelberg, **2011**).
- [100] M. Paluch, S. J. Rzoska, P. Habdas, and J. Ziolo, *J. Phys.: Condens. Matter* **10**, 4131 (1998).
- [101] M. Paluch, J. Ziolo, S. J. Rzoska, and P. Habdas, *Phys. Rev. E* **54**, 4008 (1996).
- [102] M. Paluch, S. J. Rzoska, P. Habdas, and J. Ziolo, *J. Phys.: Condens. Matter* **8**, 10885 (1996).
- [103] S. P. Andersson and O. Andersson, *Macromolecules* **31**, 2999 (1998).
- [104] P. W. Bridgman, *Proc. Natl. Acad. Sci.* **11**, 603 (1925).
- [105] C. A. Herbst, R. L. Cook, and H. E. King Jr, *Nature* **361**, 518 (1993).
- [106] R. Casalini and S. Bair, *J. Chem. Phys.* **128**, 084511 (2008).
- [107] S. Bair, *Tribol. Int.* **97**, 272 (2016).
- [108] E. Thoms, Z. Wojnarowska, P. Goodrich, J. Jacquemin, and M. Paluch, *J. Chem. Phys.* **146**, 181102 (2017).
- [109] M. Musiał, S. Bair, S. Cheng, Z. Wojnarowska, and M. Paluch, *J. Mol. Liq.* **331**, 115772 (2021).

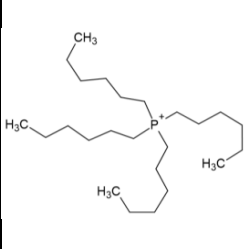
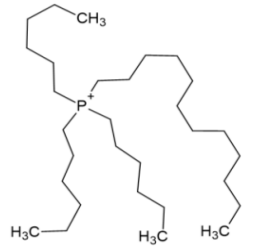
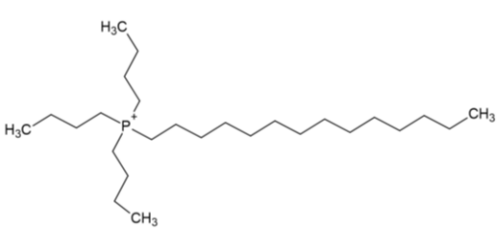
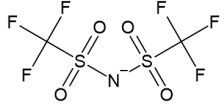
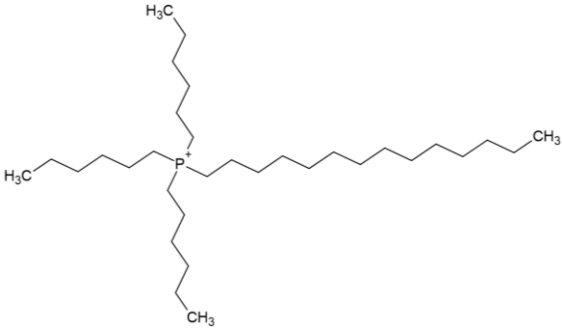
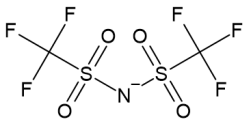
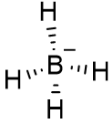
# 3 Experiment Description

## 3.1 Studied Materials

In this dissertation, I selected twenty (tetra)alkylphosphonium-based ILs with different cations and anions. The chemical structures and basic physical properties of them are presented in Tab. 3.1. The cation difference is controlled by alkyl chain length. Based on the structure of trihexyl(tetradecyl)phosphonium cation ( $[P_{666,14}]^+$ ), first, we kept the longest  $C_{14}$ -alkyl chain and shortened the other three alkyl chains, specifically from 6 to 4. Second, maintain the length of three shorter ( $C_6$ -) alkyl chains and reduce the single long aliphatic chain (from 14 to 2). The most commonly used anions bis(trifluoromethanesulfon)imide ( $[TFSI]^-$ ) and chloride were used in combination with the above-mentioned cations. Finally, we kept the  $[P_{666,14}]^+$  cation and selected anions reflecting different sizes, spatial arrangement, flexibility, and coordination aptitude.

**Tab. 3.1** The basic physicochemical properties and structures of the studied ILs

Acronym	$[P_{666,2}][TFSI]$	$[P_{666,6}][TFSI]$	$[P_{666,8}][TFSI]$	$[P_{666,12}][TFSI]$
Name	Ethyltriethylphosphonium bis(trifluoromethylsulfon)imide	Tetrahexylphosphonium bis(trifluoromethylsulfon)imide	Octyltriethylphosphonium bis(trifluoromethylsulfon)imide	Dodecyltriethylphosphonium bis(trifluoromethylsulfon)imide
M/g mol <sup>-1</sup>	564.71	620.81	648.87	704.97
$\rho/g\text{ cm}^{-3}$	-	-	1.10	-
wt/ppm	200	600	120	680
Purity	> 98%	> 98%	> 98%	> 98%
Supplier	QUILL	QUILL	QUILL	QUILL
Cation				
Anion				

Acronym	[P <sub>666,6</sub> ][Cl]	[P <sub>666,12</sub> ][Cl]	[P <sub>444,14</sub> ][Cl]	[P <sub>444,14</sub> ][TFSI]
Name	Tetrahexylphosphonium chloride	Dodecyltriethylphosphonium chloride	Tributyl(tetradecyl)phosphonium chloride	Tributyl(tetradecyl)phosphonium bis(trifluoromethylsulfonyl)imide
M/g mol <sup>-1</sup>	376.12	460.28	404.17	648.87
ρ/g cm <sup>-3</sup>	-	-	0.95	1.10
wt/ppm	1553	2096	1238	80
Purity	> 98%	> 98%	> 98%	> 98%
Supplier	QUILL	QUILL	QUILL	QUILL
Cation				
Anion	$\text{Cl}^-$			
Acronym	[P <sub>666,14</sub> ][Cl]	[P <sub>666,14</sub> ][TFSI]	[P <sub>666,14</sub> ][BH <sub>4</sub> ]	[P <sub>666,14</sub> ][BF <sub>4</sub> ]
Name	Trihexyl(tetradecyl)phosphonium chloride	Trihexyl(tetradecyl)phosphonium bis(trifluoromethylsulfonyl)imide	Trihexyl(tetradecyl)phosphonium borohydride	Trihexyl(tetradecyl)phosphonium tetrafluoroborate
M/g mol <sup>-1</sup>	519.31	763.24	498.70	570.66
ρ/g cm <sup>-3</sup>	0.88	1.07	0.84	0.93
wt/ppm	899	683	25517	637
Purity	> 98%	> 98%	> 95%	> 98%
Supplier	QUILL	QUILL	QUILL	QUILL
Cation				
Anion	$\text{Cl}^-$			

Acronym	[P <sub>666,14</sub> ][Dec]	[P <sub>666,14</sub> ][SCN]	[P <sub>666,14</sub> ][TCM]	[P <sub>666,14</sub> ][DCA]
Name	Trihexyl(tetradecyl)phosphonium decanoate	Trihexyl(tetradecyl)phosphonium thiocyanate	Trihexyl(tetradecyl)phosphonium tricyanomethanide	Trihexyl(tetradecyl)phosphonium dicyanamide
M/g mol <sup>-1</sup>	655.11	541.94	669.97	549.89
ρ/g cm <sup>-3</sup>	0.88	0.90	0.90	0.90
wt/ppm	2587	404	344	336
Purity	> 95%	> 98%	> 98%	> 95%
Supplier	IoLiTec	QUILL	QUILL	IoLiTec
Cation				
Anion				
Acronym	[P <sub>666,14</sub> ][TAU]	[P <sub>666,14</sub> ][BOB]	[P <sub>666,14</sub> ][BTMPP]	[P <sub>666,14</sub> ][BEHP]
Name	Trihexyl(tetradecyl)phosphonium taurine	Trihexyl(tetradecyl)phosphonium bis(oxalate)borate	Trihexyl(tetradecyl)phosphonium bis(2,4,4-trimethylpentyl)phosphinate	Trihexyl(tetradecyl)phosphonium bis(2-ethylhexyl) phosphate
M/g mol <sup>-1</sup>	607.99	670.70	773.27	805.27
ρ/g cm <sup>-3</sup>	0.94	0.99	0.89	0.91
wt/ppm	650	2100	847	517
Purity	> 98%	> 95%	> 90%	> 98%
Supplier	QUILL	QUILL	IoLiTec	IoLiTec
Cation				
Anion				
Density measured at 298.15 K; wt: water content				
QUILL: Queen's University Ionic Liquid Laboratories				

## 3.2 Differential Scanning Calorimetry (DSC)

Calorimetry is a powerful analytical tool for measuring the thermal transfer of a system caused by some physical processes and chemical reactions. Among others, differential scanning calorimetry (DSC) is one of the most commonly used analytical techniques, stemming from its ability to provide rapid and accurate measurements of heat flow and heat capacity changes associated with physical and chemical processes, such as vitrification, melting, crystallization, mixing, vaporization, etc. The fundamental principle of DSC is to detect the amount of heat absorbed or emitted by the tested sample and the reference in order to maintain the same temperature as the system is cooled, heated, or held under isothermal conditions. The measured heat flow or heat capacity can be expressed as a function of temperature or time. Consequently, the DSC measurements provide valuable information on the thermal events in the tested sample. For example, it can be used to identify the phase transitions and estimate their temperatures and enthalpy, and it also allows the determination of glass transition temperature and the characterization of the thermal stability of supercooled materials. The most notable advantage of DSC is that only a tiny amount of sample is required.

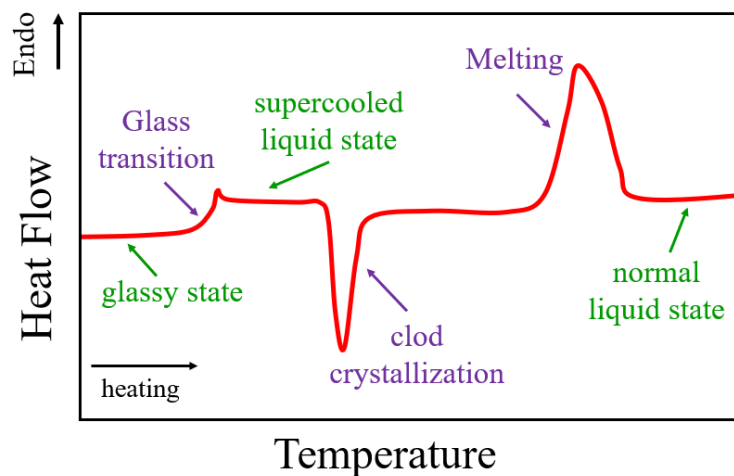


**Fig. 3.1** The DSC diagram of ILs upon heating containing typical thermal events, i.e., glass transition, cold crystallization, and melting process.

As illustrated in Fig. 3.1, the glass transition is presented as a step-like change in heat flow, and the middle point of this region is defined as  $T_g$ . The heating rate influences the value of  $T_g$ . Usually,  $T_g$  is determined on heating with a rate of 10 K/min. Except for the glass transition behavior, the cold crystallization process (metastable supercooled liquid state transform to ordered crystal phase) commonly occurs above  $T_g$  during heating, and the subsequent melting process (the solid crystalline convert to normal liquid state) occurs at  $T_m$ . (see Fig. 3.1) [1] Additionally, the LLT, a polymorphic transition between two distinct liquid states, would show up as a reversible enthalpic peak in the DSC signal,

similar to the peaks for the liquid-solid and solid-solid transitions. According to the literature, analogous to the molecular liquids with LLT, the feature of LLT for an IL system would appear in the supercooled liquid state between  $T_g$  and  $T_m$  with a high probability.

The DSC measurements performed in this work were done by a Mettler Toledo DSC1STAR System equipped with an HSS8 ceramic sensor (having 120 thermocouples) and a liquid nitrogen cooling accessory. Indium and zinc standards were used to calibrate the system for the high-temperature range, as well as CCl<sub>4</sub> and n-heptane (182.15 K, 140.5 J/g) for the low-temperature range with different scanning rates (0.7, 1, 5, 10 K/min). In order to ensure reproducibility and high accuracy, each sample was measured at least three times, and each time a new sample (around 10-20 mg) was sealed in an aluminum crucible (40  $\mu$ L) with a pierced lid. Throughout the experiment, The nitrogen flow was kept at 60 mL/min. The measurable temperature range of this DSC system can cover from 133 K to 523K.

### 3.3 Broadband Dielectric Spectroscopy (BDS) at Ambient and Elevated Pressure

Broadband dielectric spectroscopy (BDS) is a powerful experimental tool for addressing the molecular dynamics of supercooled liquid and glass since its distinctive ability to probe the translational diffusion of charge carriers and dipolar relaxation over a wide frequency, temperature, and pressure range. BDS is widely used to study the charge transport and the dynamic glass transition of ILs as well as localized molecular fluctuations (secondary relaxations), [2],[3],[4],[5],[6],[7] providing valuable insights into the optimal utilization of ILs in a variety of scientific and technological applications. The basic principle of BDS involves applying an external, alternating electric field  $E^*(f)$  to the sample under investigation. This is typically done by placing the tested material between two stainless steel electrodes with a fixed distance to form a capacitor in the sample cell. When the electric field is applied, the dielectric material induces the polarization response, aligning its electric dipoles with the field. This polarization describes dielectric displacement within the material. Consequently, the dielectric permittivity function  $\varepsilon^*(f)$  can be derived by measuring the complex impedance of the sample  $Z_s^*(f)$  covering the frequency range from  $10^{-2}$  to  $10^7$  Hz. [4]

$$\varepsilon^*(f) = \varepsilon'(f) + i\varepsilon''(f) = \frac{1}{i2\pi f C_0 Z_s^*(f)} \quad (3.1)$$

where  $\varepsilon'(f)$  and  $\varepsilon''(f)$  are the real and imaginary parts of the complex dielectric permittivity  $\varepsilon^*(f)$ , and  $C_0$  represents the vacuum capacitance. Correspondingly, the complex electric

conductivity  $\sigma^*(f)$  and complex electric modulus  $M^*(f)$  can be calculated using the following relations:

$$\varepsilon^*(f) = 1 / M^*(f) = \sigma^*(f) / i2\pi f \varepsilon_0 \quad (3.2)$$

In the case of ionic systems, the dielectric data are conventionally analyzed in the complex electric modulus formalism,  $M^*(f) = \varepsilon^*(f)^{-1}$ . This is because ionic conductivity dominates the dielectric loss function,  $\varepsilon^*(f)$ , at low frequencies, which entirely masks the structural relaxation process. [4],[8]. On the other hand, conductivity formalism,  $\sigma^*(f)$ , is commonly adopted to express the charge transport properties of conducting materials. [2],[9] The typical dielectric spectra of ionic liquid are presented in Fig. 3.2. The real part of the complex conductivity  $\sigma'$  is characterized by three different regions: (1) a plateau in the middle-frequency range (the value denotes dc-conductivity  $\sigma_{dc}$ ), which is related to the number of moving ions, (2) a typical power law increase on the high-frequency side for most disordered ionic conductors (ac-conductivity region), and (3) a decrease of  $\sigma'$  from  $\sigma_{dc}$  at lower frequencies, due to the slowing down of charge carriers at electrodes (so-called electrode polarization). On the other hand, the imaginary part of complex modulus  $M''$  reveal a well-resolved conductivity relaxation peak attributed to ion motion. The conductivity relaxation time corresponds to the frequency at which  $M''$  achieves a maximum, i.e.,  $\tau_\sigma = 1/2\pi f_{max}$ . It should be noted that the  $M''$  peak usually occurs near the connection region in  $\sigma'$  between the dc-conductivity and ac-conductivity parts. (see Fig. 3.2) The conductivity relaxation time and dc-conductivity satisfy the following relationship:

$$\tau_\sigma = \varepsilon_0 \varepsilon_s / \sigma_{dc} \quad (3.3)$$

where  $\varepsilon_s$  is the dielectric constant. Eq. 3.3 can also be used to determine the conductivity relaxation time for ionic systems.

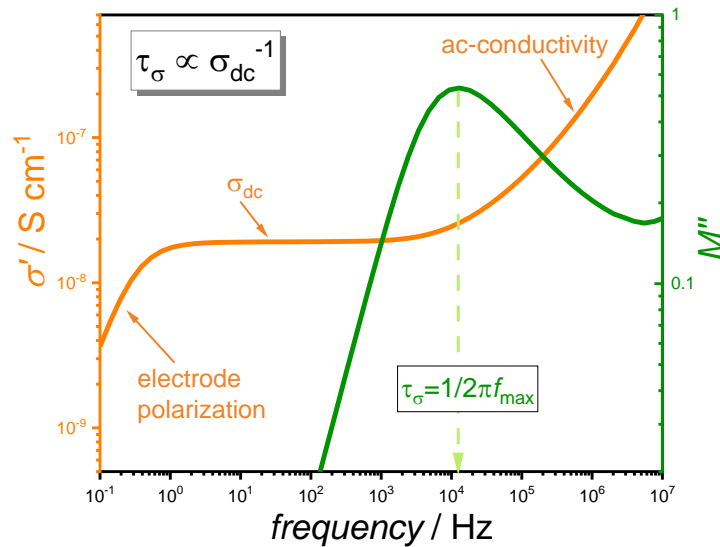


**Fig. 3.2** The dielectric spectrum of an IL presented in  $\sigma'$  and  $M''$  as a function of frequency at the same temperature. The conductivity relaxation time is inversely proportional to the dc-conductivity.

At room temperature, the conductivity relaxation time  $\tau_\sigma$  is usually around  $10^{-8}$  s for many ILs.[10],[11],[12] With decreasing temperature,  $\tau_\sigma$  increases strongly and can be approximated by the empirical Vogel-Fulcher-Tammann (VFT) equation:

$$\tau_\sigma(T) = \tau_0 \exp\left(\frac{DT_0}{T-T_0}\right) \quad (3.4)$$

where  $\tau_0$ ,  $D$  and  $T_0$  are fitting parameters. At  $T_g$ , the conductivity relaxation time  $\tau_\sigma$  generally reaches 100 s for most ILs. [13]

In addition, wide-ranging dielectric experiments show that the dielectric relaxation function of multiple ionic conductors is broader and asymmetric. The stretched-exponential function, Kohlrausch-Williams-Watts (KWW) function [14], is widely used to describe time-dependent relaxation responses:

$$\phi(t) \approx \exp[-(t/\tau_\sigma)^{\beta_{KWW}}] \quad (3.5)$$

where the exponent  $\beta_{KWW}$  is the stretching parameter. As is well known, the structural relaxation of supercooled liquids subjected to various thermal, mechanical, and electrical perturbations may not proceed in a simple exponential fashion toward equilibrium.[15], [16] As a result, this non-exponential feature of the relaxation function, which is one of the important characteristics of the dynamics of glass-forming liquids, can be well expressed by the KWW function. This rule holds for the conductivity relaxation process as well. The stretching parameter  $\beta_{KWW}$  varying from 0 to 1 represents the distribution of relaxation times. Specifically, the smaller the value of  $\beta_{KWW}$ , the broader and more asymmetric the relaxation process, as well as the higher the dynamic heterogeneity.

In the present work, a Novo-Control GMBH Alpha dielectric spectrometer has been used to perform the dielectric measurements in a wide frequency range of  $10^{-2}$  to  $10^7$  Hz. The sample was prepared on 15 mm stainless steel electrodes for temperature dependence measurements at ambient pressure, and a quartz ring was used to maintain a fixed distance (0.1 mm). A Quatro system with a nitrogen gas cryostat was used to control the temperature with an accuracy of 0.1 K during the measurements. The dielectric measurements at elevated pressure were performed using UNIPRESS high-pressure system with a specially designed capacitor with flat parallel plates electrically separated by Teflon. The Teflon capsule, which was previously filled with the studied ionic liquid, seals the capacitor with the help of a metal clamp and screw. As a result, the sample acts as its own pressure-transmitting fluid in this system. The Unipress setup provided a pressure monitor with a resolution of 1 MPa, and stabilized the temperature to within 0.1 K using a Weiss Fridge. When linked to the proper impedance analyzer, the high-pressure configurations described above allow us to monitor the migration of charge carriers in the presence of an electrical field at varied  $T$ - $P$  thermodynamic conditions.

## 3.4 Supplementary Measurements

### 3.4.1 Rheological Measurements

Rheological measurements have been widely used to obtain the mechanical properties of materials, such as viscosity and dynamic shear modulus. Furthermore, by combining rheological characterization with other techniques, one can provide valuable insights into the structural dynamics and physical properties of complex fluids and gels.[17] As an ideal experimental tool for studying ILs, rheological measurements have been extensively employed to investigate the relaxation dynamics and structure-property relationships in ILs.[18] Specifically, viscosity analysis under different temperatures and shear rates can reveal necessary information about the ionic interactions in ILs.[19] Moreover, many rheological measurements have concentrated on investigating the relaxation dynamics of ILs in the vicinity of glass transition.[20]

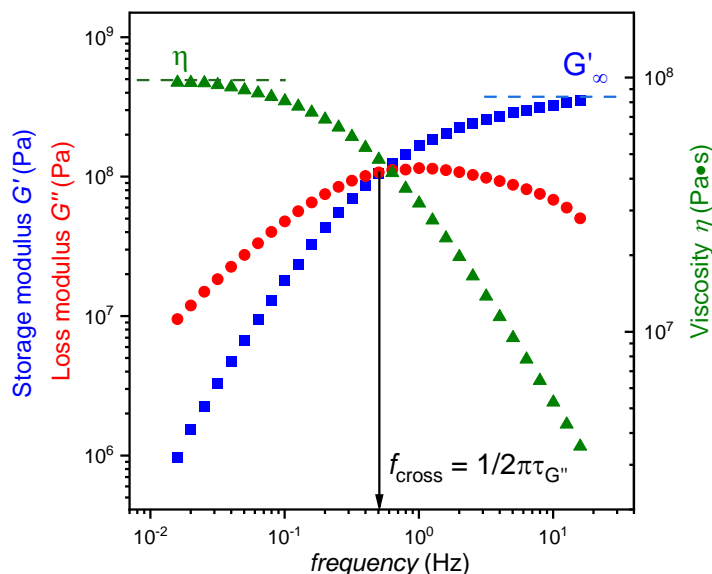


**Fig. 3.3** The representative frequency dependence of shear modulus (storage and loss) and viscosity of an IL near the glass transition temperature.

Fig. 3.3 shows the real and imaginary parts of the shear modulus and complex viscosity as a function of frequency for a typical ionic liquid around the glass transition. Similar to the response of simple glass-forming materials, ILs show liquid-like behavior at low-frequency parts and solid-like behavior at high-frequency parts.[21] The crossover of storage modulus  $G'$  and loss modulus  $G''$  is commonly used to calculate the shear relaxation time  $\tau_{G''} = 1/2\pi f_{\text{cross}}$ , indicating the transition between the viscous-dominated and the elastic-dominated behaviors.[22],[23] At low-frequency parts,  $f < f_{\text{cross}}$ , the  $G''(f)$  decreases toward lower frequencies and is clearly higher than  $G'(f)$ , which falls off even faster. Moreover, the complex viscosity  $\eta$  reaches a plateau in this frequency regime,

characterizing the nature of the viscous flow. In contrast, the solid-like behavior governs the higher frequency regions with  $G'(f) > G''(f)$ . The high-frequency plateau of  $G'(f)$  is called  $G'_\infty$ . It connects  $\tau_\alpha$  with viscosity according to the Maxwell relation:  $\tau_\alpha = \eta/G'_\infty$ . [24]

The viscosity and shear modulus of studied ILs in the present work were obtained by means of an ARES G2 Rheometer. Aluminum parallel plates with a diameter of 4 mm were used near the glass transition, while the steeliness stell geometry of diameter 25 mm was used to measure the viscosity in the equilibrium liquid state. Moreover, the strain should also be adjusted according to the structural state. In general, in the frequency range from 0.1 to 100  $\text{rad}\cdot\text{s}^{-1}$  with 10 points per decade, strain equals 0.01% in the vicinity of the liquid glass transition and increases by one order of magnitude per 10 K. The relative uncertainty of the reported viscosity measurements  $u_r(\eta)$  from calibration, temperature and pressure control, as well as sample purities, did not exceed 7%.

### 3.4.2 Density Measurements

Density measurements of studied ILs were performed by means of a vibrating tube densimeter DMA 4500 M (Anton Paar, Austria) in the temperature range from 263.15 K to 363.15 K. Dry air and bi-distilled water was used for calibration before measurements. The DMA 4500 M densimeter works based on harmonic oscillation. The sample is introduced into a forced-oscillation U-tube whose oscillation period depends on the density of the sample. The accuracy of the densimeter is  $5\times 10^{-5} \text{ g/cm}^3$ , and repeatability of  $\pm 0.00002 \text{ g/cm}^3$ . The density-measuring cell is thermostated with temperature stability of 0.01 K.

### 3.4.3 Raman Scattering Measurements

Raman spectroscopy [25],[26] is a powerful experimental tool together with other techniques, such as Fourier transform infrared (FTIR) spectroscopy [27],[28], and nuclear magnetic resonance (NMR) spectroscopy [29],[30], for characterizing the conformational changes in alkyl chains. The most significant advantage of Raman spectroscopy over the other two is determining molecular changes in conformational order.[31],[32]. Such direct information about conformational order provides a unique opportunity to gain insight into intermolecular interactions in the region occupied by alkyl chains. Specifically,  $\nu(\text{C-H})$ ,  $\nu(\text{C-C})$ , and  $\delta(\text{C-H})$  modes appearing in the different regions of the Raman spectrum associated with the conformational order information, including the degree of coupling between alkyl chains, intramolecular motion, and chain bending.[31]

A WITec confocal Raman microscope (CRM) alpha 300R with a solid-state laser ( $\lambda = 532 \text{ nm}$ ) has been used for collecting the Raman spectra in this work. The excitation laser coupled into the microscope via a 50  $\mu\text{m}$  diameter polarization-maintaining single-mode fiber. Laser radiation is focused onto the sample by a long-distance Olympus

MPLAN (50x/0.76NA) objective lens, and the scattered light is passed through a multi-mode fiber (50  $\mu\text{m}$  diameter). The sample is placed on coverslips as a tiny droplet, which is then mounted on a THMS600 Linkam stage. The liquid nitrogen was used to control the temperature during the measurements.

#### **3.4.4 X-Ray Diffraction (XRD) Measurements**

X-Ray diffraction is a technique for examining the atomic or molecular structure of materials, and it has been already proven an effective tool for studying crystal structure. However, from this century, researchers have begun exploring its application in non-crystalline materials, i.e., liquids, gases, polymers, amorphous solids, and complex materials.[33] In 1916, Debye and Scherrer [34] first reported the observed diffraction rings with broad and diffuse features in liquid. A key challenge in studying liquids with X-ray diffraction is the amorphous nature of liquids. Due to the disordered arrangement of molecules in liquids, X-ray diffraction patterns typically exhibit continuous diffuse rings instead of discrete diffraction peaks. Nevertheless, significant progress has been made in obtaining structural information from liquids through advanced data analysis techniques and simulation methods. [35] Generally, X-ray diffraction can be employed to investigate local ordering and molecular arrangement, as well as phase transitions and structural dynamics of ionic liquids[35], which are significant for understanding the microscopic structures, interactions, and phase transition mechanisms in ILs.

The X-ray diffraction (XRD) measurements with an energy of 12 keV were performed in this work to investigate the microscopic structural changes during LLT in ILs on a larger scale. We utilized both small-angle X-ray scattering (SAXS) and wide-angle X-ray scattering (WAXS) measurements to capture a comprehensive picture. For the SAXS measurements, we explored the scattering behavior within the  $q$  range of 0.13 to 0.8  $\text{\AA}^{-1}$ . Conversely, for the WAXS measurements, we focused on a broader  $q$  range of 0.6 to 4.9  $\text{\AA}^{-1}$ . The Linkam system was employed to maintain precise temperature control with a cooling rate of 10 K/min.

#### **3.4.5 Molecular Dynamics Simulation**

With the advancement of computational power and the maturation of advanced modeling techniques and force fields, atomistic molecular dynamics (MD) simulations have evolved into an essential tool for providing molecular-scale insight into structure-property relationships.[36] Ionic liquids have attracted the attention of modeling and simulation due to their potential applications in energy storage, chemistry, and biology. In this work, MD simulations have been performed using a bead-spring model at a coarse-grained resolution to verify the charge transport mechanism for studied amphiphile-containing ILs. We adopted the numerical model that was used in the previous study of

conductivity in dry ionic liquids. [37] This model consisted of an amphiphilic molecule comprising a positively charged head attached to a rigid and uncharged tail, along with a negatively charged free counterion. The investigation encompassed the examination of morphologies under different conditions, including high and low reduced temperatures and varied pressures. Additionally, two distinct anion-to-cation size ratios were taken into account during the analysis.

### 3.5 Reference

- [1] R. M. Douglas, K. Mega, and M.P. Jennifer, *Fundamentals of Ionic Liquids* (Wiley-VCH Verlag GmbH & Co. KGaA, Weinheim, Germany, **2017**), pp. 103–147.
- [2] J. R. Sangoro and F. Kremer, *Acc. Chem. Res.* **45**, 525 (2012).
- [3] S. Kripotou, G. Tsonos, A. Mezzetta, A. Mero, L. Guazzelli, K. Moutzouris, I. Stavrakas, and C. Tsonos, *Int. J. Mol. Sci.* **23**, 5642 (2022).
- [4] F. Kremer and A. Schönhals, *Broadband Dielectric Spectroscopy* (Springer Berlin Heidelberg, Berlin, Heidelberg, **2003**).
- [5] M. Paluch, editor, *Dielectric Properties of Ionic Liquids* (Springer International Publishing, Cham, **2016**).
- [6] C. Krause, J. R. Sangoro, C. Iacob, and F. Kremer, *J. Phys. Chem. B* **114**, 382 (2010).
- [7] A. Rivera and E. A. Rössler, *Phys. Rev. B* **73**, 212201 (2006).
- [8] I. M. Hodge, K. L. Ngai, and C. T. Moynihan, *J. Non-Cryst. Solids* **351**, 104(2005).
- [9] Z. Wojnarowska, J. Knapik, M. Díaz, A. Ortiz, I. Ortiz, and M. Paluch, *Macromolecules* **47**, 4056 (2014).
- [10] Z. Wojnarowska, A. Lange, A. Taubert, and M. Paluch, *ACS Appl. Mater. Interfaces* **13**, 30614 (2021).
- [11] D. M. Correia, C. M. Costa, R. Sabater i Serra, J. A. Gómez Tejedor, L. Teruel Biosca, V. de Zea Bermudez, J. M. S. S. Esperança, P. M. Reis, A. Andrio Balado, J. M. Meseguer-Dueñas, S. Lanceros-Méndez, and J. L. Gomez Ribelles, *Polymer* **171**, 58 (2019).
- [12] M. Musiał, Z. Wojnarowska, S. Cheng, K. L. Ngai, and M. Paluch, *J. Phys. Chem. C* **123**, 22089 (2019).
- [13] P. Sippel, P. Lunkenheimer, S. Krohns, E. Thoms, and A. Loidl, *Sci. Rep.* **5**, 13922 (2015).
- [14] G. Williams and D. C. Watts, *Trans. Faraday Soc.* **66**, 80 (1970).
- [15] T. Fujima, H. Frusawa, and K. Ito, *Phys. Rev. E* **66**, 031503 (2002).
- [16] A. Menelle, R. Bellissent, and A. M. Flank, *EPL* **4**, 705 (1987).
- [17] J. Lefebvre, and J. L. Doublier. "Rheological Behavior of Polysaccharides Aqueous Systems, (in *Polysaccharides: Structural Diversity and Functional Versatility* 2nd Edition, S. Dumitriu, Ed.)" New York: Marcel Dekker, **2005**, pp 357-394.

- [18] N. V. Pogodina, M. Nowak, J. Lauger, C. O. Klein, M. Wilhelm, and Ch. Friedrich, *J. Rheol.* **55**, 241 (2011).
- [19] A. Shakeel, H. Mahmood, U. Farooq, Z. Ullah, S. Yasin, T. Iqbal, C. Chassagne, and M. Moniruzzaman, *ACS Sustainable Chem. Eng.* **7**, 13586 (2019).
- [20] A. Balogun, D. Lazarenko, F. Khabaz, and R. Khare, *Soft Matter* **17**, 7210 (2021).
- [21] R. Tao and S. L. Simon, *J. Phys. Chem. B* **119**, 11953 (2015).
- [22] H. M. Wyss, in *Fluids, Colloids and Soft Materials: An Introduction to Soft Matter Physics*, edited by A. Fernandez-Nieves and A. M. Puertas (John Wiley & Sons, Inc, Hoboken, NJ, USA, **2016**), pp. 149–164.
- [23] H. Ramli, N. F. A. Zainal, M. Hess, and C. H. Chan, *Chem. Teacher Int.* **4**, 307 (2022).
- [24] J. C. Maxwell, *The Scientific Papers of James Clerk Maxwell*, edited by W. D. Niven (Dover, New York, **1965**), Vol. 2, p. 26.
- [25] M. Ho and J. E. Pemberton, *Anal. Chem.* **70**, 4915 (1998).
- [26] S. L. Wunder, *Macromolecules* **14**, 1024 (1981).
- [27] R. G. Snyder, M. Maroncelli, S. P. Qi, and H. L. Strauss, *Science* **214**, 188 (1981).
- [28] H. L. Casal, P. W. Yang, and H. H. Mantsch, *Can. J. Chem.* **64**, 1544 (1986).
- [29] M. Porsch, R. Brindle, A. Ellwanger, L. C. Sander, C. M. Bell, H. Handel, and K. Albert, *Solid State Nucl. Magn. Reson.* **9**, 191 (1997).
- [30] R. Markiewicz, A. Klimaszuk, M. Jarek, M. Taube, P. Florczak, M. Kempka, Z. Fojud, and S. Jurga, *Int. J. Mol. Sci.* **22**, 5935 (2021).
- [31] C. J. Orendorff, M. W. Jr. Ducey, and J. E. Pemberton, *J. Phys. Chem. A* **106**, 6991 (2002).
- [32] M. Harrand, *J. Chem. Phys.* **79**, 5639 (1983).
- [33] S. Bates. in *International Tables for Crystallography (2019)*. Vol. H, ch. 5.6, pp. 617-648.
- [34] P. Debye, P. Scherrer, *Nachr. Gesell. Wiss, Gottingen.* **16**, (1916)
- [35] L. Gontrani, P. Ballirano, F. Leonelli, and R. Caminiti, in *The Structure of Ionic Liquids*, edited by R. Caminiti and L. Gontrani (Springer International Publishing, Cham, **2014**), pp. 1–37.
- [36] D. Bedrov, J.-P. Piquemal, O. Borodin, A. D. Jr. MacKerell, B. Roux, and C. Schroder, *Chem. Rev.* **119**, 7940 (2019).
- [37] A. Erbař and M. O. de la Cruz, *Phys. Chem. Chem. Phys.* **18**, 6441 (2016).

# 4 Tailoring Phosphonium Ionic Liquids for a Liquid–Liquid Phase Transition

THE JOURNAL OF  
PHYSICAL CHEMISTRY  
LETTERS  
A JOURNAL OF THE AMERICAN CHEMICAL SOCIETY



pubs.acs.org/JPCLETT

Letter

## Tailoring Phosphonium Ionic Liquids for a Liquid–Liquid Phase Transition

Beibei Yao, Marian Paluch, Mateusz Dulski, Courtney Quinn, Shannon McLaughlin, Anne McGrogan, Malgorzata Swadzba-Kwasny, and Zaneta Wojnarowska\*

Cite This: *J. Phys. Chem. Lett.* 2023, 14, 2958–2964

Read Online

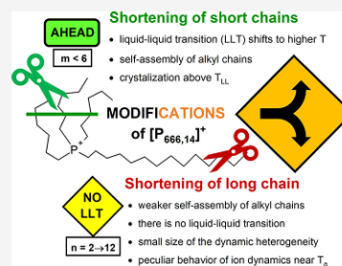
ACCESS |

Metrics & More

Article Recommendations

Supporting Information

**ABSTRACT:** The existence of more than one liquid state in a single-component system remains the most intriguing physical phenomenon. Herein, we explore the effect of cation self-assembly on ion dynamics in the vicinity of liquid–liquid and liquid–glass transition of tetraalkyl phosphonium ( $[P_{mmmm,n}]^+$ ,  $m = 4, 6$ ;  $n = 2–14$ ) ionic liquids. We found that nonpolar local domains formed by 14-carbon alkyl chains are crucial in obtaining two supercooled states of different dynamics within a single ionic liquid. Although the nano-ordering, confirmed by Raman spectroscopy, still occurs for shorter alkyl chains ( $m = 6$ ,  $n < 14$ ), it does not bring calorimetric evidence of LLT. Instead, it results in peculiar behavior of ion dynamics near the liquid–glass transition and 20-times smaller size of the dynamic heterogeneity compared to imidazolium ionic liquids. These results represent a crucial step toward understanding the nature of the LLT phenomenon and offer insight into the design of efficient electrolytes based on ionic liquids revealing self-assembly behavior.



Reprinted with permission from *J. Phys. Chem. Lett.* 2023, 14, 12, 2958–2964

<https://doi.org/10.1021/acs.jpcllett.3c00099> Copyright © 2023 The Authors. Published by American Chemical Society

## Author Declaration:

*"Tailoring Phosphonium Ionic Liquids for a Liquid–Liquid Phase Transition," J. Phys. Chem. Lett., 14, 2958-2964 (2023)*

B. Yao planned and carried out the experimental work, analyzed the data, prepared figures, and co-wrote the manuscript.

Signature: 

M. Dulski carried out the Raman measurements and analyzed the data.

Signature: 

S. McLaughlin characterized and synthesized the ionic liquids.

Signature: 

A. McGrogan characterized and synthesized the ionic liquids.

Signature: 

C. Quinn characterized and synthesized the ionic liquids.

Signature: 

M. Swadzba-Kwasny supervised the characterization and synthesis of ionic liquids.

Signature: 

Z. Wojnarowska conceived and supervised the project.

Signature: 

M. Paluch co-wrote the manuscript.

Signature: 

## 4.1 Abstract

The existence of more than one liquid state in a single-component system remains the most intriguing physical phenomenon. Herein, we explore the effect of cation self-assembly on ion dynamics in the vicinity of liquid-liquid and liquid-glass transition of tetra(alkyl)phosphonium ( $[P_{mmm,n}]^+$ ,  $m = 4, 6$ ;  $n = 2-14$ ) ionic liquids. We found that non-polar local domains formed by 14-carbon alkyl chains are crucial in obtaining two supercooled states of different dynamics within a single ionic liquid. Although the nano-ordering, confirmed by Raman spectroscopy, still occurs for shorter alkyl chains ( $m = 6$ ,  $n < 14$ ), it does not bring calorimetric evidence of LLT. Instead, it results in peculiar behavior of ion dynamics near the liquid-glass transition and 20-times smaller size of the dynamic heterogeneity compared to imidazolium ionic liquids. These results represent a crucial step toward understanding the nature of the LLT phenomenon and offer insight into the design of efficient electrolytes based on ionic liquids revealing self-assembly behavior.

## 4.2 Main text

Within 100 years since the discovery of ethylammonium nitrate by Paul Walden, [1] ionic liquids (ILs) have emerged as an exceptional class of molten salts with unique physical, chemical, and biological properties.[2],[3] The numerous possibilities for mixing, matching and incorporating different atoms or functional groups into ILs provide a unique opportunity to fine-tune their physicochemical properties for many industrial applications. Among others, ILs meet the needs of electrochemistry, energy storage, catalysis, engineering, and pharmacy. [4],[5],[6]

A key advantage of ILs over molecular fluids is their excellent ability to exhibit vitrification. Under cooling, low-viscosity liquid becomes a supercooled equilibrium fluid that transforms to a nonequilibrium amorphous solid at the glass transition temperature  $T_g$ . [7] Among the factors controlling the glass-forming ability of ILs, one can mention the symmetry of ionic species, charge delocalization, size of ions, and competing for interionic interactions (van der Waals vs. Coulomb forces and H-bonding). [8],[9] For example, incorporating a small chloride anion into the IL structure increases  $T_g$ . [10],[11] The same is achieved by introducing strong H-bonding interactions or elongating the alkyl chain in the cation. [12],[13],[14] However, the latter can also lead to various short-range ordering structures, e.g., clusters or mesoscopic agglomerates, [15],[16],[17] which might dramatically influence the properties of ILs. [18],[19],[20] Therefore, understanding the molecular-level interactions within ILs is crucial for their industrial applications.

Recently, the self-organization of ions in quaternary phosphonium-based ILs has been considered an origin of the first-order liquid–liquid phase transition (LLT). [21],[22] Specifically, on cooling,  $[P_{666,14}][BH_4]$  was transformed from one supercooled liquid state to another with different local structures, static dielectric permittivity, and thermodynamic properties. Compared to nonionic systems, including water, [23],[24] atomic elements (Si, Ge), [25],[26] triphenyl phosphite (TPP), [27],[28] water–trehalose mixtures, [29] or metallic glasses, [30] the LLT in  $[P_{666,14}][BH_4]$  can be classified as a genuine transition where both supercooled liquids can flow. It has also been shown that the exchange of borohydride anion to  $[TFSI]^-$ ,  $[TCM]^-$ ,  $[SCN]^-$ , or taurine keeps both liquid phases and does not affect the temperature of LLT substantially. Furthermore, independently on anion, LLT was observed at a similar time scale of ionic motions (from 0.3 to 13 ms). [22] All these facts suggest that the tendency of amphiphilic phosphonium cations to form local structures is responsible for LLT. In this context, the question naturally arises, *what is the critical length of alkyl chains to create nonpolar local domains and consequently to observe two different supercooled states within a single-component system?* In general, longer alkyl chains favor nano-organization. However, it has been reported that increasing the volume fraction of alkyl groups in the phosphonium ILs does not necessarily promote mesoscale aggregation. [31] A detailed analysis of  $[P_{222,12}][TFSI]$  and  $[P_{444,12}][TFSI]$  has shown disruption of the mesoscale aggregates with increasing lengths of the shorter alkyl chains. At the same time, the LLT has not been observed in these materials. Therefore, a thorough understanding of the formation of heterogeneous microstructures by phosphonium ILs characterized by different combinations of alkyl chain lengths seems essential for the precise control of LLT.

To address this issue, we have synthesized two different sets of phosphonium ILs (see Supporting Information for details). The former contains ILs with trialkyl(tetradecyl) phosphonium cation  $[P_{nnn,14}]^+$ , specifically  $[TFSI]^-$  and chloride salts of  $[P_{444,14}]$  and  $[P_{666,14}]$ , while the ILs from the second group are characterized by trihexyl alkyl-phosphonium cations,  $[P_{666,n}]^+$  ( $n = 2, 6, 8, 12$ ), combined again with  $[Cl]^-$  and  $[TFSI]^-$  anions. The chemical structures of investigated ILs are shown in Fig. 4.1, parts a and b. To verify whether the chosen systems undergo LLT, differential scanning calorimetry (DSC) is employed. Later on, the effect of cation self-assembly on the ion dynamics is examined by means of dielectric spectroscopy. Using the Raman measurements, we investigate a local organization of ILs over a broad temperature range.

The DSC technique has been used to provide thermal characteristics of  $[P_{nnn,14}]^+$  and  $[P_{666,n}]^+$ -based ILs. The thermograms obtained on heating with the standard rate of 10 K/min are presented in Fig. 4.1, parts a and b.

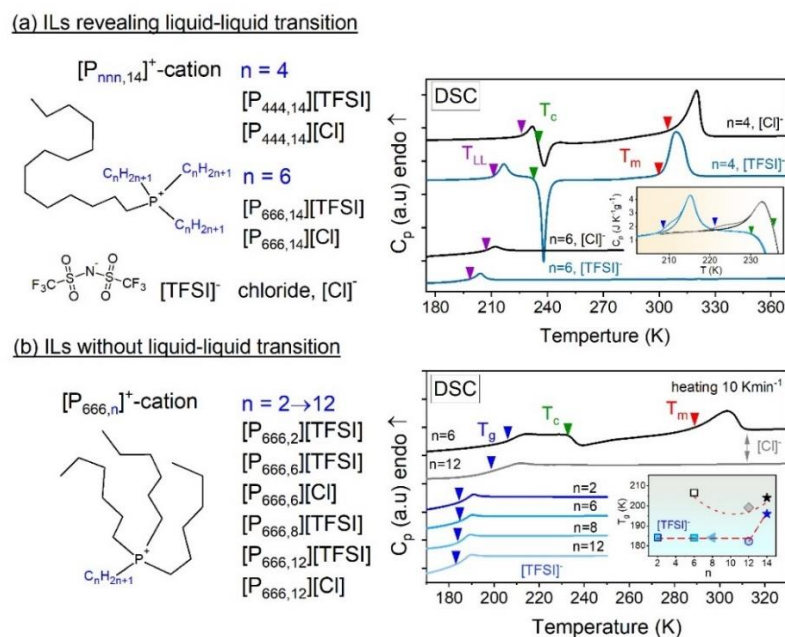


**Fig. 4.1** Chemical structures and DSC thermograms of ILs with (a) and without (b) LLT. The inset in DSC panel (a) is the comparison between DSC traces obtained during standard heating and after the aging process at 203.15 and 193.15 K for  $[P_{444,14}][Cl]$  (gray) and  $[P_{444,14}][TFSI]$  (light blue), respectively. The arrows indicate the characteristic temperatures of studied ILs: onset of LLT (violet arrows); onset of crystallization (green arrows); onset of melting (red arrows); glass transition temperature (blue arrows). The bottom inset presents the glass transition temperature as a function of alkyl chain length for examined  $[P_{666,n}]^+$ -based ILs.

Calorimetric experiments show that all studied ILs could be vitrified on cooling; however, they reveal different behaviors during the heating process. In particular, tributyl- and trihexyl tetradecyl phosphonium ILs show well-resolved endothermic peaks identified with the liquid–liquid phase transition. At the same time, the DSC traces of studied  $[P_{666,n}]^+$ -based ILs ( $n = 2–12$ ) exhibit a clear signature of liquid–glass transition and no signs of the LLT, even if  $n = 12$ . Hence, the 14-carbon chain seems necessary to induce a transition between two supercooled states. At the same time, modification of three other substituents while keeping the  $–[CH_2]_{13}–CH_3$  structure of the fourth one brings substantial differences in temperature and enthalpy of LLT, as well as affects the crystallization tendency of ILs. In particular, the shortening of three cation side chains from hexyl to butyl increases the enthalpy of LLT (especially for IL with  $[TFSI]^-$  anion  $\Delta H$  increases twice) and shifts its onset to higher temperatures.  $T_{LL}$  rises by 11 K for ILs with  $[TFSI]^-$  anion and 20 K for chloride salts. The values of  $T_{LL}$  and  $\Delta H$  are listed in Table S4.1. High enthalpy of LLT found for  $[P_{444,14}]$ -ILs indicates that the alkyl chains self-assembly causing LLT is better constituted compared to  $[P_{666,14}]$ -ILs, and therefore, they crystallize above  $T_{LL}$ . This is visible as a sharp exotherm followed by an endotherm, revealing a subsequent melting process on DSC thermograms. Due to the sterical

hindrance provided by the [TFSI]<sup>-</sup> anion, liquid 1 of [P<sub>444,14</sub>][TFSI] shows a slightly weaker tendency to crystallize than it does for [P<sub>444,14</sub>]Cl.

As mentioned above, the shortening of a single alkyl chain in [P<sub>666,14</sub>]<sup>+</sup> cation by the CH<sub>2</sub>-CH<sub>2</sub>- group, i.e., from 14 to 12 carbons, inhibits the ability of IL to undergo LLT and markedly decreases the temperature of the liquid-glass transition. Note that the  $T_g$  of ILs with LLT was identified on DSC scans by the time-dependent annealing (aging) experiments performed at  $T < T_g$ . Then the liquid-glass transition becomes visible as a step-like change of heat capacity at  $T < T_{LL}$  (see the inset to Fig. 4.1a and Table S4.1 for  $T_g$  values). Interestingly, a further shortening of alkyl chain length in [P<sub>666,n</sub>][TFSI] systems from  $n = 12$  to  $n = 2$  does not change the thermal properties. Namely,  $T_g$  remains constant, and none of them shows a crystallization tendency. That is at odds with the behavior of imidazolium-based ILs, where  $T_g$  was found to decrease for material with a shorter alkyl substituent. [12],[13] At the same time, in the case of [P<sub>666,n</sub>]Cl,  $T_g$  plotted as a function of alkyl chain length reveals a nonmonotonic behavior; i.e., it decreases with the elongation of the alkyl chain from 6 to 12 carbons and gets higher for C<sub>14</sub>. Furthermore, among all studied [P<sub>666,n</sub>]<sup>+</sup>-systems, only [P<sub>666,6</sub>]Cl reveals the crystallization tendency above  $T_g$ .

A closer inspection of thermograms obtained for [P<sub>666,n</sub>]<sup>+</sup>-containing ILs ( $n = 2-12$ ) reveals a substantial broadening of the glass transition step compared to classical ILs. Such a result is commonly identified with a broad distribution of structural relaxation times (larger dynamic heterogeneities) within the material and characterizes rather polymerized ionic liquids and multicomponent systems than simple low-molecular ILs. [32],[33],[34] Therefore, one might expect the formation of some heterogeneous microstructures in [P<sub>666,n</sub>]<sup>+</sup>-based IL, although there is no evidence of LLT. To explore this issue thoroughly, the Donth [35],[36] approach defining the number of dynamically correlated particles,  $N_\alpha^D$ , in the  $T_g$  region has been employed for [P<sub>666,n</sub>]<sup>+</sup>-ILs, (see Supporting Information for details). Interestingly, the obtained values of  $N_\alpha^D(T_g)$  are exceptionally low (less than ten) for all examined here [P<sub>666,n</sub>]<sup>+</sup>-ILs (see Table S4.1). It means that only several particles move cooperatively close to the glassy state. This indicates the existence of some aggregates with strong van der Waals interactions and short intermolecular distances between the alkyl chains of [P<sub>666,n</sub>]<sup>+</sup>-ILs. Such a conclusion is supported by recent reports where  $N_\alpha^D(T_g)$  was strongly correlated with the length of alkyl chain attached to the cation (more -CH<sub>2</sub>- groups, lower  $N_\alpha^D$ ). [11] However, so far, the lowest reported value of  $N_\alpha^D(T_g)$  was equal to 20, and interestingly, it was found for IL with the phosphate anion, i.e., [C<sub>1</sub>C<sub>2</sub>Im][DBP]. Further dielectric studies were performed to verify whether such exceptionally small regions of dynamic heterogeneity

affect the ion dynamics in  $[P_{666,n}]^+$ -ILs and how much their relaxation behavior is different from  $[P_{nnn,14}]^+$ -ILs that reveal a clear LLT.

To avoid cold crystallization and maintain the same thermal history, all examined herein ILs were initially quenched to the glass state, and the dielectric data were recorded during the heating scan. Parts a and b of Fig. 4.2 show the dielectric modulus spectra  $M''(f)$  of representative ILs with and without LLT on DSC thermograms, that is, for  $[P_{444,14}][TFSI]$  and  $[P_{666,6}][TFSI]$ .

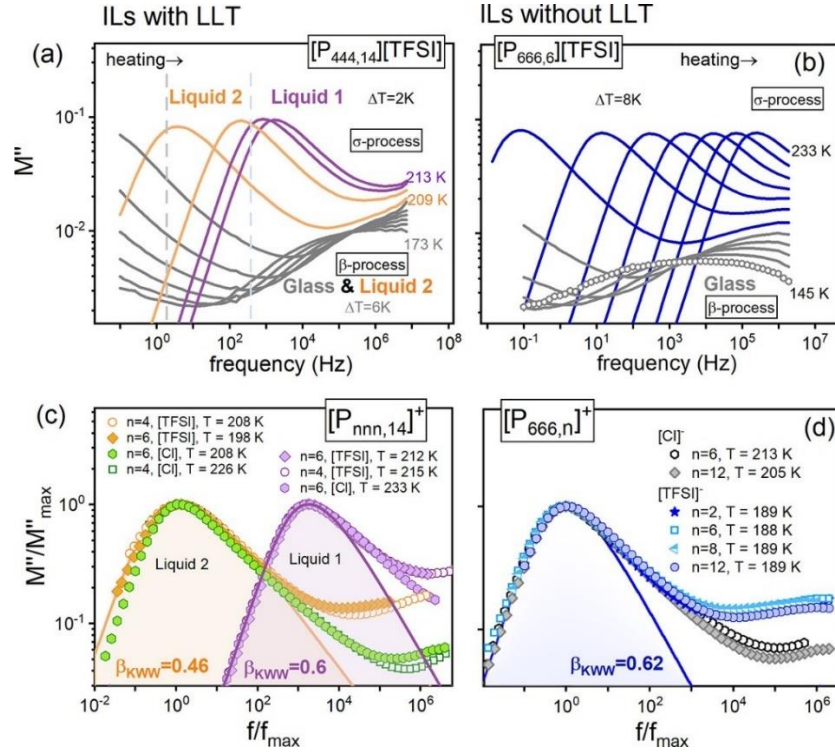


**Fig. 4.2** Representative electric loss modulus spectra of ILs with and without LLT, *i.e.*,  $[P_{444,14}][TFSI]$  (a) and  $[P_{666,6}][TFSI]$  (b), recorded at various temperatures in the liquid and glassy states. The dashed lines in panel (a) separate the glass from liquid 2, and liquid 1. Panels (c) and (d) show the normalized  $M''$  spectra recorded for various ILs and various temperatures, however, with a similar frequency of the modulus peak maximum. The solid lines denote the fits of the Kohlrausch function,  $\phi(t) = \exp[-(t/\tau_\alpha)^{\beta_{KWW}}]$ .

A single secondary relaxation (labeled as  $\beta$ -process) is visible in the glassy state of all studied ILs. The only difference is in the secondary process's amplitude, which is more pronounced in ILs with  $[TFSI]^-$  anion. As the temperature increases, another relaxation mode, the so-called conductivity relaxation process ( $\sigma$ -process), related to the translational mobility of ions, becomes the main feature in the dielectric spectra. Similarly to other ionic glass formers, the  $M''$ -peak of each  $[P_{666,n}]^+$  and  $[P_{nnn,14}]^+$ -based ILs shifts toward higher frequencies on heating. However, in the latter cases, the temperature sensitivity of  $\sigma$ -mode changes substantially from liquid 2 to liquid 1. Furthermore, from the data normalization presented in panels c and d of Fig. 4.2, it is evident that the  $M''(f)$

spectra are getting narrower when the temperature increases above  $T_{LL}^{DSC}$ . Meanwhile, the  $M''(f)$  peak of  $[P_{666,n}]^+$ -ILs keeps the same shape at various  $T$  values over the supercooled state and for different lengths of the fourth alkyl chain ( $n = 2-12$ ) (see Fig. 4.2, parts c and d, and Table S4.1).

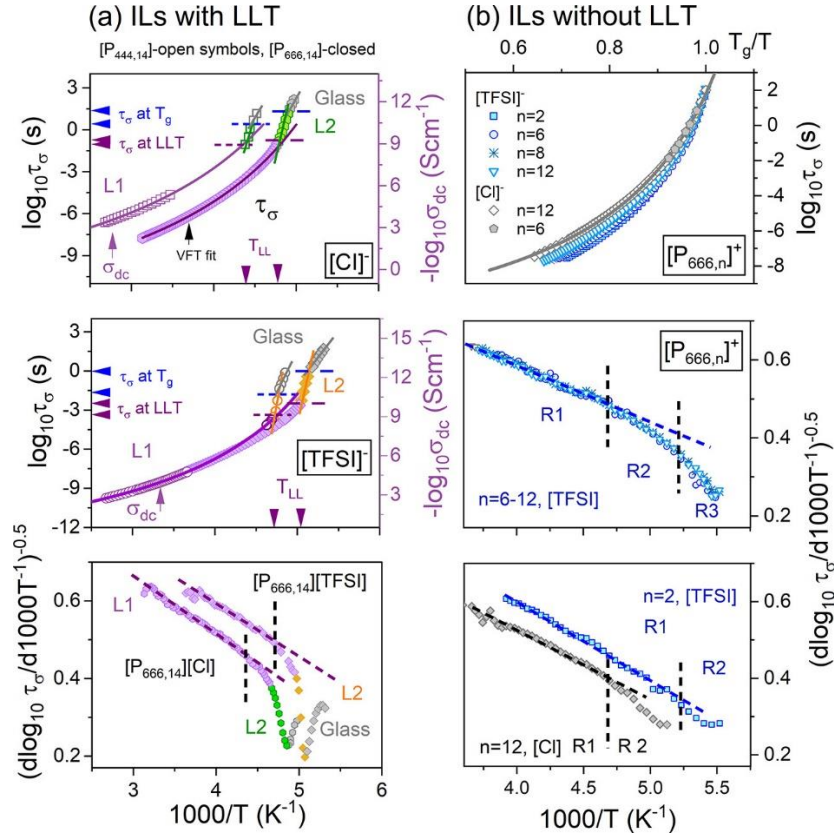


**Fig. 4.3** Temperature dependence of  $\tau_\sigma$  and dc-conductivity  $\sigma_{dc}$  for chloride and TFSI salts of  $[P_{444,14}]^+$  and  $[P_{666,14}]^+$  (a) and  $[P_{666,n}]^+$ -based ILs (b). Solid lines indicate the fits of the VFT function to dc-conductivity data recorded in liquid 1 state. Violet arrows denote the  $\tau_\sigma$  and  $T_{LL}$  at LLT, while blue arrows denote the  $\tau_\sigma$  at  $T_g$ . Temperature evolution of  $\tau_\sigma$  of  $[P_{666,n}][TFSI]$  and  $[P_{666,n}]Cl$  is presented in the  $T_g/T$  scale. The bottom panels present the Stickel plots. The dashed lines denote the intersection of distinct linear regions (R).

In the next step, we have constructed the relaxation maps to highlight the effect of IL morphology on ion dynamics above and below  $T_g$ . The characteristic of local dynamics ( $\beta$ -processes) is presented in Figure S4.2 in the Supporting Information. One can note that the glassy dynamics of  $[P_{666,n}]^+$ -ILs and  $[P_{nnn,14}]^+$ -ILs are very similar. Namely, there is a single  $\beta$ -process with the activation energy oscillating around  $35 \pm 2$  kJ/mol for ILs with  $[TFSI]^-$  anion and  $E_a = 28 \pm 3$  kJ/mol for chloride salts of tetraalkyl phosphonium liquids. However, when we consider a given  $T < T_g$ , the dependence between the alkyl chain length and the time scale of  $\beta$ -relaxation occurs. In particular, the local dynamics slows down with the elongation of alkyl substituent from 2 to 14 carbons; however, at the same time, it is insensitive to structural changes arising from LLT. Considering the relatively

low energy consumption of  $\beta$ -relaxation, some intramolecular motions within phosphate cation are expected for the occurrence of this mode in the  $M''(f)$  spectra.

Fig. 4.3a shows the temperature evolution of conductivity relaxation times ( $\tau_\sigma = 1/2\pi f_{max}$ ) determined for ILs containing  $[P_{444,14}]^+$  and  $[P_{666,14}]^+$  cations. As can be seen, the dynamics of both examined  $[P_{666,14}]^+$ -systems follows the Vogel–Fulcher–Tammann (VFT) in liquid 1 state and markedly changes the behavior at  $T_{LL}^{DSC}$ . At the same time, the  $\tau_\sigma(T)$  data of  $[P_{444,14}]^+$ -ILs are unavailable above their  $T_{LL}$  due to the strong crystallization tendency. Therefore, the temperature dependence of dc-conductivity  $\log \sigma_{dc} (T^{-1})$  determined in the vicinity of  $T_m$  has been employed to characterize their ion dynamics in the liquid 1 state. As can be seen, around calorimetric LLT, the VFT fit, representing the behavior of  $\tau_\sigma$  in liquid 1, meets the experimentally determined  $\tau_\sigma(T^{-1})$  in liquid 2 state. This procedure enables us to estimate the time scale of conductivity relaxation at  $T_{LL}$  for  $[P_{444,14}][TFSI]$  and  $[P_{444,14}]Cl$ . From a direct comparison of  $\tau_\sigma(T^{-1})$  dependences for both examined  $Cl^-$  salts, one can note that  $\tau_\sigma(T_{LL})$  is almost the same ( $\sim 0.1$  s). However, an exchange of  $Cl^-$  anion to  $[TFSI]^-$  shifts  $\tau_\sigma(T_{LL})$  almost three decades toward shorter relaxation times ( $[P_{444,14}][TFSI]$ , 0.8 ms;  $[P_{666,14}][TFSI]$ , 5 ms). Interestingly, the time scale of charge transport at  $T_g$  also differs for  $[P_{nnn,14}]^+$ -based ILs, and it is much shorter than 100 s ( $\log \tau_\sigma(T_g) = 2$ ) commonly identified with the freezing of ions mobility at  $T_g$ . Specifically,  $\log \tau_\sigma(T_g) = 0.5$  and  $-1.5$  for  $[P_{444,14}]Cl$  and  $[P_{444,14}][TFSI]$ , respectively. It means that the charge transport still occurs when the structural dynamics become arrested. Such a decoupling between charge transport and structural relaxation in aprotic ionic liquids needs further examination. An exchange to  $[P_{666,14}]$  makes the ILs more coupled ( $\log \tau_\sigma(T_g) = 1.5$  and  $0$  for  $[P_{666,14}]Cl$  and  $[P_{666,14}][TFSI]$ ) compared to  $[P_{444,14}]^+$ -ILs. The liquid-liquid and liquid-glass transitions are also clearly detectable when the Stickel analysis  $[d(\log_{10}\tau_\sigma)/d(1000/T)]^{-0.5}$  is performed. For conventional ILs with single VFT behavior, the Stickel operator transforms the VFT function into a linear dependence. On the other hand, when two VFT equations are required to parametrize the experimental data, two linear regions intersect at certain temperatures, usually called  $T_b$ . In the latter case, the Stickel plot indicates a fragility change when passing the crossover temperature. As seen in the bottom panel of Fig. 4.3a, the data deviate from the linear behavior around  $T_{LL}$  and reveal a minimum at  $T_g$ . Note that at  $T_{LL}$ , the slope of  $[d(\log_{10}\tau_\sigma)/d(1000/T)]^{-0.5}$  dependence is getting larger, which is in contrast to the Stickel graph of any other glass-forming liquid, [37] and therefore, it can be treated as a dynamic signature of LLT.

At first sight, the temperature dependence of conductivity relaxation times determined for  $[P_{666,n=2-12}]^+$ -ILs resembles classical ILs with the single VFT-type temperature dependence of  $\tau_\sigma$  and  $T_g = T$  ( $\tau_\sigma = 100$  s). However, a derivative analysis

reveals again a unique curvature of the Stickel plot, similar to that found for  $[P_{666,14}]^+$ -ILs undergoing LLT. Namely, at a specific temperature  $[d(\log_{10}\tau_\sigma)/d(1000/T)]^{-0.5}$  data of  $[P_{666,n}]^+$ -ILs ( $n = 2-12$ ) depart from the high-temperature linear regime (R1) with a deviation degree being to some extent dependent on anion and alkyl-chain length. Precisely, the slope change of Stickel plot is almost negligible for  $[P_{666,2}][TFSI]$  and  $[P_{666,12}][Cl]$ , while three regions of different grades can be detected for  $[P_{666,n}][TFSI]$ ,  $n = 6-12$  (see Fig. 4.3b). Raman spectroscopy has been employed to reveal the molecular origin behind this observation.

As a structurally sensitive technique, Raman measurements have been performed for  $[P_{666,12}][TFSI]$ ,  $[P_{666,2}][TFSI]$ ,  $[P_{666,14}][TFSI]$ , and  $[P_{444,14}][TFSI]$ , the latter two as representative ILs with LLT. The obtained results are depicted in Fig. 4.4. The attention has been focused on the analysis of vibrational modes of the alkyl chains, including (i) stretching mode within the chain ( $1025-1125\text{ cm}^{-1}$ ) and (ii) deformational modes of  $CH_x$  ( $x = 2,3$ ) ( $1275-1525\text{ cm}^{-1}$ ) as well as (iii) the stretching vibration of  $CH_x$  ( $2800-3050\text{ cm}^{-1}$ ). [38] The first region is sensitive to the conformational order, the second corresponds to the degree of coupling, and the latter provides information about the ordering of alkyl chains. As can be seen in Fig. 4.4d, cooling of  $[P_{444,14}][TFSI]$  from liquid 1 to liquid 2 brings a slight upshift ( $\sim 3\text{ cm}^{-1}$ ) of  $\nu(C-C)$ -related bands (at  $1053$  and  $1098\text{ cm}^{-1}$ , and  $\tau(CH_2)$ -modes at  $1306\text{ cm}^{-1}$ ) and downshifting of  $CH_x$ -bands ( $\sim 3\text{ cm}^{-1}$ ) within the  $2800-3050\text{ cm}^{-1}$  range. All these spectral changes point to a molecular reorganization, which in analogy to data described recently for  $[P_{666,14}][BH_4]$ , confirmed chain coupling and a more ordered arrangement of alkyl tails in liquid 2 of  $[P_{444,14}][TFSI]$ . Note that the Raman spectra recorded for supercooled 1 and 2 states markedly differ from that of crystalline  $[P_{444,14}][TFSI]$  (see a gray line in Fig. 4.4d). Specifically, crystallization was observed as increased intensity and narrowing of bands corresponding to  $SO_2$  vibrations in  $[TFSI]^-$  anion and  $\nu(C-C)$ ,  $\tau(CH_2)$ , and  $\delta(CH_3)$  in the  $[P_{444,14}]^+$  cation. Furthermore, the stretching-related modes, including  $\nu_s(CH_2)$  and  $\nu_{as}(CH_2)$  are shifted to  $2853$  and  $2883\text{ cm}^{-1}$ , respectively. Such changes result from an increase in molecular packing related to crystal-like ordering. [39],[40]

Parts a and b of Fig. 4.4 show the Raman data recorded for  $[P_{666,12}][TFSI]$  and  $[P_{666,2}][TFSI]$ . In analogy to  $[P_{666,14}][TFSI]$ , cooling brings higher intensity and downshift ( $\sim 2-3\text{ cm}^{-1}$ ) of  $\nu(C-C)$  (from  $1071\text{ cm}^{-1}$ ) and  $\tau(C-C)$  (at  $1310\text{ cm}^{-1}$ ) bands. At the same time, these related to the stretching of  $\nu(CH_2)$  and  $\nu(CH_3)$  are oppositely shifted (to  $2858$  and  $2941\text{ cm}^{-1}$ , respectively). Additionally, a slight shift of the  $\delta(CH_2)$  up to  $1447\text{ cm}^{-1}$  suggests a slowing down alkyl chains' local motions. All these facts are clear evidence of aliphatic chain coupling due to their mutual ordering, which is similar to that accompanying LLT (see Fig. 4.4c for comparison). Interestingly, decreasing temperature

from 200 to 186 K brings only an intensity increase of the LLT-sensitive bands without their shift, evidencing further molecular nano-segregation of [P<sub>666,12</sub>][TFSI] and [P<sub>666,2</sub>][TFSI]. These changes are more pronounced for IL with a 12-carbon long aliphatic chain than for [P<sub>666,2</sub>]<sup>+</sup>, suggesting weaker nano-ordering of the latter.

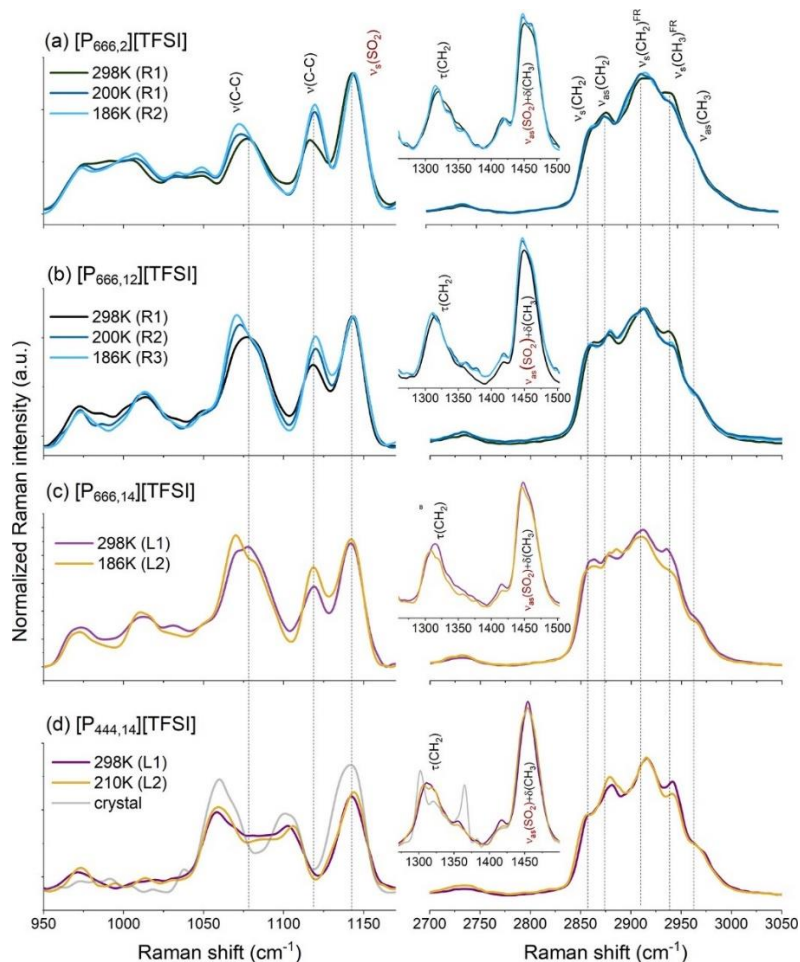


**Fig. 4.4** Raman measurements of selected ILs recorded at three different temperatures corresponding to liquid 1 (L1) and liquid 2 (L2) states of [P<sub>444,14</sub>][TFSI] and [P<sub>666,14</sub>][TFSI] as well as different regions (R1, R2, R3) marked on the Stickel plot for [P<sub>666,12</sub>][TFSI] and [P<sub>666,2</sub>][TFSI]. The comparison between the spectral lines recorded at room temperature of [P<sub>444,14</sub>][TFSI], [P<sub>666,12</sub>][TFSI], and [P<sub>666,2</sub>][TFSI] is presented in the Supporting Information.

In summary, our experimental Raman studies revealed the local arrangements of alkyl chains in all examined herein tetraalkyl phosphonium ILs; however, only [P<sub>444,14</sub>]<sup>+</sup>- and [P<sub>666,14</sub>]<sup>+</sup>-based systems undergo a liquid–liquid phase transition. The LLT has been disclosed by an endotherm peak on the DSC heating scan and the substantial departure of ion dynamics ( $\tau_\sigma$ ,  $\sigma_{dc}$ ) from VFT behavior. High enthalpy of LLT found for [P<sub>444,14</sub>]<sup>+</sup>-ILs compared to [P<sub>666,14</sub>]<sup>+</sup>-ILs indicates that the alkyl chains self-assembly is better constituted in the former case, and therefore brings spontaneous crystallization just above  $T_{LL}$ . On the other hand, for [P<sub>666,n</sub>]<sup>+</sup>-based ILs, there is no sign of LLT shown in thermodynamic and dynamic properties. However, an analysis of dielectric data in terms

of the Stickel operator gave the results to some extent similar to that observed for ILs with LLT; that is, negative deviation from the high-temperature linear regime. Thus, shortening the aliphatic chain reduces the possibility of LLT but keeps the potential of ILs for partial nanorganization. In turn, the latter brings peculiar ion dynamics behavior near  $T_g$  and exceptionally small regions of dynamic heterogeneity  $N_\alpha(T_g)$  (below 10) determined from Donth analysis of calorimetric measurements.

### 4.3 Acknowledgements

This research was funded in whole by National Science Centre, Poland [Opus 21, 2021/41/B/ST5/00840]. For the purpose of Open Access, the author has applied a CC-BY public copyright license to any Author Accepted Manuscript (AAM) version arising from this submission. The studies were implemented as part of strategy of the University of Silesia -Inicjatywa Doskonałości (POB 1) - Priorytetowy Obszar Badawczy 1: Harmonijny rozwój człowieka - troska o ochronę zdrowia i jakość życia. The authors kindly thank Ionic Technologies for providing [P<sub>66614</sub>]Cl free of charge. AMcG and CQ acknowledge EPSRC and SMcL acknowledges DfE for PhD studentship funding.

### 4.4 Supplementary Information

#### Experimental Methods

##### Differential Scanning Calorimetry (DSC)

Calorimetric experiments of studied ILs were carried out by a Mettler Toledo DSC1STAR System equipped with a liquid nitrogen cooling accessory and an HSS8 ceramic sensor (a heat flux sensor with 120 thermocouples). The gas nitrogen keeps flowing at 60 mL min<sup>-1</sup> during the whole experiment. The DSC device was calibrated for enthalpy and temperature using indium and zinc standards, as well as n-heptane (182.15 K, 140.5 Jg<sup>-1</sup>) at different scanning rates (0.7, 1, 5, and 10 Kmin<sup>-1</sup>) for low-temperature verification. The DSC curves were exported by a dedicated software Mettler Toledo DSC1STAR, allowing various calculations (heat capacity, onset, normalized enthalpy, etc.) for the original heat flow curves. The baseline was constructed as a straight line from the onset to the endpoint. All DSC measurements were performed from 373 K cooling to 123 K and then heating to 373 K with a rate of 10 K min<sup>-1</sup>. The 6-hour aging experiments were performed at 203.15 K and 193.15 K for [P<sub>444,14</sub>][Cl] and [P<sub>444,14</sub>][TFSI], respectively. The liquid-liquid transition temperature and melting point were obtained at the onset of the peak, while the glass transition temperature was determined as the midpoint of the heat capacity increment. Based on the fluctuation-dissipation theorem, Donth proposed that the volume of one average cooperatively rearranging region (CRR) at  $T_g$  can be calculated by the following equation:

$$V_{\alpha}(T_g) = \frac{k_B T_g^2 \left( \frac{1}{c_p^{glass}} - \frac{1}{c_p^{liquid}} \right)}{\rho \delta T^2} \Bigg|_{T_g} \quad (\text{S4.1})$$

where  $k_B = 1.38 \times 10^{-23} \text{ J K}^{-1}$  is Boltzmann constant,  $\rho$  is the density of the bulk material.  $c_p^{liquid}$  and  $c_p^{glass}$  represent the isobaric heat capacities of liquid and glass at  $T_g$ .  $\delta T$  denotes the average temperature fluctuation of a CRR related to the dynamic glass transition ( $\delta T = \Delta T/2.5$  is the average temperature fluctuation calculated as the temperature interval  $\Delta T$  where the heat capacity changes from 16% to 84% of the total heat capacity step  $\Delta c_p$  at  $T_g$  upon heating (see Figure S4.1).  $N_{\alpha}$  is the number of the particles in one average CRR with volume  $V_{\alpha}$ . Thus  $N_{\alpha}$  can be calculated by:

$$N_{\alpha}(T_g) = \frac{V_{\alpha}(T_g) \rho N_A}{M} = \frac{k_B T_g^2}{M (\delta T)^2} N_A \left( \frac{1}{c_p^{glass}} - \frac{1}{c_p^{liquid}} \right) \quad (\text{S4.2})$$

where  $M$  is the molar mass,  $N_A = 6.02 \times 10^{23} \text{ mol}^{-1}$  is the Avogadro constant.

The scheme for the determination of the  $N_{\alpha}^D(T_g)$  is presented in Figure S4.1, taking [P<sub>666,8</sub>][TFSI] as the reference. Other quantities are collected in Table S4.1.

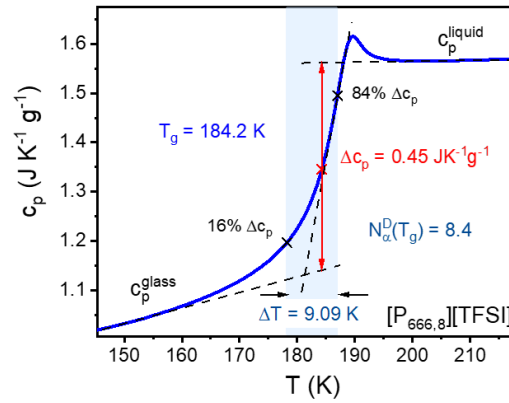


**Figure S4.1** The scheme for the determination of the  $N_{\alpha}^D(T_g)$  using Donth method (eq S4.2) for [P<sub>666,8</sub>][TFSI].

### Broadband Dielectric Spectroscopy (BDS).

Dielectric measurements were performed by means of a Novo-Control GMBH Alpha impedance analyzer over a frequency range from  $10^{-2}$  Hz to  $10^7$  Hz at different temperatures corresponding to the supercooled liquid state of studied ILs. During the measurements, the sample was placed between two stainless steel electrodes (diameter = 15 mm) with a fixed distance (0.1 mm) provided by the quartz ring, and the temperature was controlled by a Quatro system using a nitrogen gas cryostat with an accuracy of 0.1 K. Additionally, [P<sub>444,14</sub>]Cl and [P<sub>666,6</sub>]Cl were heated up above melting temperature with the capacitor plate before measurements.

When the studied ILs supercooled from liquid to glassy state, the localized motions have been found in modulus spectra. These local motions are known as secondary ( $\beta$ -) relaxation processes. In order to analyze and interpret the thermal behavior of  $\beta$ -relaxation,

we performed a numerical fitting analysis of  $M''(f)$  data below  $T_g$ , in terms of the Cole-Cole function,

$$M^*(\omega) = 1/\varepsilon^*(\omega) = \left( \varepsilon_\infty + \frac{\Delta\varepsilon}{[1+(i\omega\tau_{CC})^{\alpha_{CC}}]^1} \right)^{-1} \quad (\text{S4.3})$$

where  $\Delta\varepsilon$  is the dielectric strength,  $\varepsilon_\infty$  is the high-frequency limit permittivity,  $\tau_{CC}$  defines the characteristic relaxation time and  $\alpha_{CC}$  is shape parameter. The characteristic relaxation times of  $\beta$ -process can be calculated according to the fitting parameters:

$$\tau_\beta = \tau_{CC} \left[ \sin\left(\frac{\alpha_{CC}\pi}{2+2}\right) \right]^{-1/\alpha_{CC}} \left[ \sin\left(\frac{\alpha_{CC}\cdot 1\cdot\pi}{2+2}\right) \right]^{1/\alpha_{CC}} \quad (\text{S4.4})$$

The obtained  $\log_{10} \tau_\beta$  as function of  $1000/T$  have been plotted in Figure S4.2. As can be seen, all the secondary processes obey the Arrhenius law:

$$\tau_\beta = \tau_\infty \exp\left(\frac{E_a}{RT}\right) \quad (\text{S4.5})$$

where  $\tau_\infty$  is the pre-exponential factor,  $R$  is the gas constant, and  $E_a$  denotes the energy barrier. The values of  $E_a$  are listed in Table S4.1 for all studied ILs.

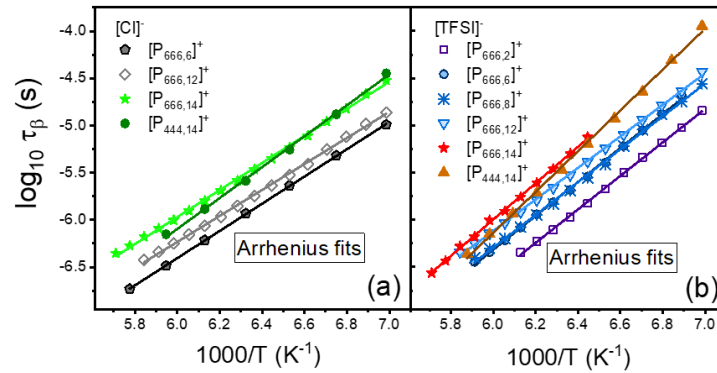


**Figure S4.2** Relaxation map of secondary relaxations of all studied ILs with anion  $\text{Cl}^-$  (a), and  $[\text{TFSI}]^-$  (b). Solid lines are fits of the Arrhenius law to experimental data.

### Raman measurements

Raman measurements were performed using a WITec confocal Raman microscope (CRM) alpha 300R with a solid-state laser ( $\lambda = 532$  nm) coupled into the microscope through a polarization-maintaining single-mode optical fiber with a 50  $\mu\text{m}$  diameter. The laser radiation was focused onto the sample via a long-distance Olympus MPLAN (50x/0.76NA) objective, while then the scattered light passed through a multi-mode fiber (50  $\mu\text{m}$  diameter). The spectrometer monochromator working with a 600 line/mm grating has been checked before the measurements using a silicon plate ( $520.7$   $\text{cm}^{-1}$ ). The sample, put on the cover glass as a tiny droplet, was next mounted on the THMS600 Linkam stage. Raman spectra of TFSI salts of  $[\text{P}_{666,12}]^+$ ,  $[\text{P}_{666,2}]^+$  and  $[\text{P}_{444,14}]^+$  at room temperature were gathered at 20 mW on the sample using ten scans, an integration time of 20 s, and a resolution of 3  $\text{cm}^{-1}$ . Then, individual samples were cooled down to 200 K, 186 K ( $[\text{P}_{666,12}][\text{TFSI}]$ ,  $[\text{P}_{666,2}][\text{TFSI}]$ ), and 210 K ( $[\text{P}_{444,14}][\text{TFSI}]$ ) at 100 K/min cooling rate with

0.1 K stabilization temperature to avoid crystallization. At each interested temperature, Raman spectra were accumulated using ten scans, an integration time of 20 s, and a resolution of  $3 \text{ cm}^{-1}$ . All collected spectra were subjected to a post-processing analysis, including cosmic ray removal and baseline correction, using WITec Project Five Plus software. Finally, Raman spectra were normalized to the most intense band ( e.g.,  $745 \text{ cm}^{-1}$ ), which high-intensity results from a large polarizability change due to the expansion and contraction of the whole  $[\text{TFSI}]^-$  anion [41]. A proposed normalization stems from the comparable amount of the TFSI<sup>-</sup> anion in all samples and their insensitivity to conformational changes due to temperature [41]

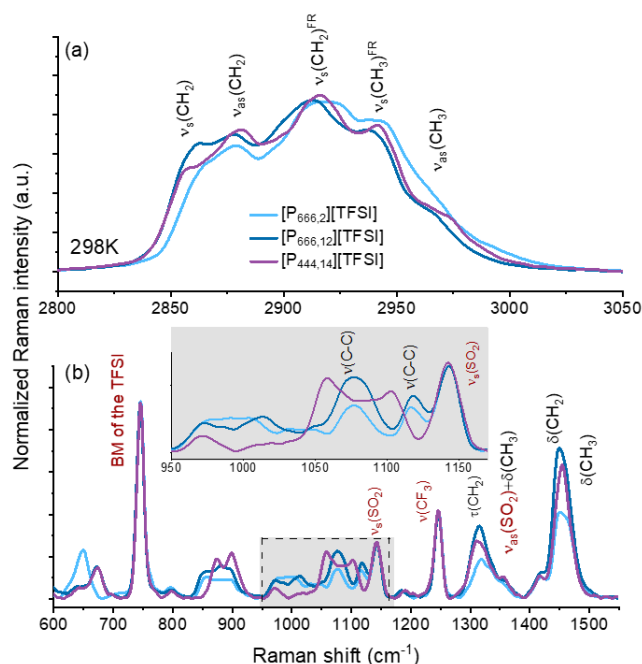


**Figure S4.3** Raman measurements of examined ILs at RT.

As the first, spectra of  $[\text{P}_{666,12}][\text{TFSI}]$ ,  $[\text{P}_{666,2}][\text{TFSI}]$  and  $[\text{P}_{444,14}][\text{TFSI}]$  obtained at room temperature showed a similar number of the bands insensitively to the changeable  $\text{CH}_2$  content but with lower intensity depending on the aliphatic length. Differences in the bands' intensity depending on the ILs are observed comparing individual spectra in the  $\text{CH}_x$ -related ranges (Fig. S4.3 panel a). In turn, the varied proportion between short and long chains correlates only with the shift of aliphatic-related bands without altering the position of the  $\text{CH}_x$ -related bands (Fig. S4.3 panel a). Thus, the most crucial, from the analytical point of view, aliphatic  $\nu(\text{C-C})$ -related bands are around  $1056/1076 \text{ cm}^{-1}$  and  $1101/1117 \text{ cm}^{-1}$  ( $[\text{P}_{444,14}][\text{TFSI}]/[\text{P}_{666,12}][\text{TFSI}]$ ,  $[\text{P}_{666,2}][\text{TFSI}]$ ), twisting  $\tau(\text{CH}_2)$ -modes appear at  $1310/1315/1318 \text{ cm}^{-1}$  ( $[\text{P}_{444,14}][\text{TFSI}]/[\text{P}_{666,12}][\text{TFSI}]/[\text{P}_{666,2}][\text{TFSI}]$ ) and stretching  $\nu(\text{CH}_x, x=2,3)$ -related bands occur at  $2856/2880/2941 \text{ cm}^{-1}$  ( $\nu_s\text{CH}_2/\nu_{as}\text{CH}_2/\nu_s\text{CH}_3$  for  $[\text{P}_{444,14}][\text{TFSI}]$ ),  $2860/2877/2938 \text{ cm}^{-1}$  ( $\nu_s\text{CH}_2/\nu_{as}\text{CH}_2/\nu_s\text{CH}_3$  for  $[\text{P}_{666,12}][\text{TFSI}]$ ),  $2865/2878/2943 \text{ cm}^{-1}$  ( $\nu_s\text{CH}_2/\nu_{as}\text{CH}_2/\nu_s\text{CH}_3$  for  $[\text{P}_{666,2}][\text{TFSI}]$ ). Importantly, their position turned out to be slightly shifted concerning other literature-available data (Fig. S4.3 panel

b) due to the type of chains and the mutual interaction between cation and TFSI<sup>-</sup> anion. Other  $\delta(\text{CH}_x, x=2,3)$ -related bands with maxima around 1455/1447 $\text{cm}^{-1}$  ([P<sub>444,14</sub>][TFSI]/ [P<sub>666,12</sub>][TFSI], [P<sub>666,2</sub>][TFSI]) turned out less sensitive to the structural reorganization associated with the LLT.

**Table S4.1** Thermodynamic and dynamic properties of studied ILs. Molar masses,  $M$ ; glass transition temperature,  $T_g$ ; liquid-liquid transition temperature,  $T_{LL}$ ; crystallization temperature,  $T_c$ ; and melting temperature,  $T_m$ .  $\Delta H_{LL}$  denotes enthalpy of liquid-liquid transition;  $\Delta H_c$  enthalpy of crystallization; and  $\Delta H_m$  enthalpy of melting, all determined during the heating scan. The isobaric heat capacities at  $T_g$  for liquid,  $c_p^{liquid}$ , and glass,  $c_p^{glass}$ . Temperature interval  $\Delta T$  determined from the  $c_p(T)$  curve between 16% and 84% of the  $\Delta c_p$  step. Number of dynamically correlated molecules,  $N_\alpha^D(T_g)$ .  $wt$  water content.  $\beta_{KWW}$  stretching parameter.  $m_p$  dynamic fragility.  $E_d$  activation energy of secondary dynamics.

ILs	[P <sub>666,14</sub> ] Cl	[P <sub>666,14</sub> ] [TFSI]	[P <sub>444,14</sub> ] Cl	[P <sub>444,14</sub> ] [TFSI]	[P <sub>666,6</sub> ] Cl	[P <sub>666,12</sub> ] Cl	[P <sub>666,2</sub> ] [TFSI]	[P <sub>666,6</sub> ] [TFSI]	[P <sub>666,8</sub> ] [TFSI]	[P <sub>666,12</sub> ] [TFSI]
$M$ (g/mol)	519.31	763.24	404.17	648.87	376.12	460.28	564.71	620.81	648.87	704.97
$T_g$ (K)	197.9* 201**	195.9* 194.2**	221.2* 223**	208.5* 209**	206.6* 201.3**	199.1* 195.2**	184.2* 181.3**	184.1* 181.5**	184.2* 180.6**	182.3* 181.2**
$T_{LL}$ (K)	205.9* 210**	200.1* 201.2**	227.1* 228**	211.5* 212**	-	-	-	-	-	-
$\Delta H_{LL}$ (J/g)	5.23	6.6	5.73	11.14	-	-	-	-	-	-
$T_c$ (K)	-	-	233.8	236.1	232.6	-	-	-	-	-
$-\Delta H_c$ (J/g)	-	-	63.52	66.97	8.45	-	-	-	-	-
$T_m$ (K)	-	-	309.8	301.7	288.9	-	-	-	-	-
$\Delta H_m$ (J/g)	-	-	62.78	65.26	8.65	-	-	-	-	-
$c_p^{liquid}$ (J/K g)	-	-	-	-	1.95	1.31	1.42	1.35	1.57	1.54
$c_p^{glass}$ (J/K g)	-	-	-	-	1.55	0.81	0.98	0.94	1.12	0.87
$\Delta T$ (K)	-	-	-	-	9.8	17.2	11.1	10.8	9.1	14
$N_\alpha^D(T_g)$	-	-	-	-	8.2	7.1	8.1	7.9	8.4	6.5
$wt$ (ppm)	899	683	1238	80	1553	2096	200	600	120	680
$\beta_{KWW}$	0.6 <sup>L1</sup> 0.58 <sup>L2</sup>	0.6 <sup>L1</sup> 0.52 <sup>L2</sup>	0.6 <sup>L1</sup> 0.48 <sup>L2</sup>	0.6 <sup>L1</sup> 0.46 <sup>L2</sup>	0.62	0.62	0.62	0.62	0.62	0.62
$m_p(T_g)$	-	-	-	-	68	73	80	101	90	89
$E_d^\beta$ (kJ/mol)	27.4	36.9	31.3	41.4	27.6	26.4	34	34.4	33.4	32

\*The glass transition temperature and LLT temperature were determined from DSC measurements.

\*\*The glass transition temperature and LLT temperature were determined from BDS.

## Samples synthesis and characterization

Lithium bis(trifluoromethanesulfonyl) imide was bought from 3M and used as received. Trihexylphosphine was kindly provided by Solvay (Cytex). All other chemicals were sourced from Sigma-Aldrich and used as received, unless otherwise stated.

XRF analysis was performed on a Rigaku NEX QC+ QuantEZ High-Resolution Energy Dispersive X-ray Fluorescence (EDXRF) Spectrometer. NMR spectra were recorded on a Bruker Avance III 400 MHz spectrometer in acetonitrile- $d_3$ . CHNS analysis was conducted on a Perkin Elmer 2400 Series II in a quartz combustion tube using acetanilide and cysteine as standards. TOF Mass spectrometry was performed using a Waters Xevo G2-XS Q-ToF. All samples were dissolved in acetonitrile for CHNS and TOF-MS analysis.

**[P<sub>666,14</sub>]Cl. Trihexyl(tetradecyl)phosphonium chloride**, was provided by Ionic Technologies and was used as received.

**[P<sub>666,14</sub>][TFSI].** Trihexyl(tetradecyl)phosphonium chloride, [P<sub>666,14</sub>]Cl (0.010 mol eq.) and lithium bis(trifluoromethanesulfonyl)imide Li[TFSI] (0.013 mol eq.) were separately dissolved in 25 cm<sup>3</sup> deionised water (18.2 M $\Omega$ .cm) (total 50 cm<sup>3</sup>) and then combined in a round-bottomed flask (250 cm<sup>3</sup>), resulting in the formation of a biphasic liquid system; the mixture was left to react (1 h, room temperature, 600 rpm). The aqueous layer was separated, and the organic layer was collected and washed, firstly with deionized water (18.2 M $\Omega$ .cm) (10 cm<sup>3</sup>) and then dichloromethane, DCM (10 cm<sup>3</sup>). Subsequent washes were performed with solution of Li[TFSI] in deionised water (18.2 M $\Omega$ .cm). Final three washes were performed with deionised water (18.2 M $\Omega$ .cm) until no chloride could be detected with silver nitrate solution. Subsequently, DCM was removed *via* rotary evaporation (30 min, 308.15 K) and the ionic liquid was dried under high vacuum (12h, 343.15 K, 10<sup>-2</sup> mbar). XRF analysis confirmed chloride content was below the detectable limit. <sup>1</sup>H, <sup>13</sup>C, <sup>19</sup>F and <sup>31</sup>P NMR spectra of the IL were recorded in *d*<sub>6</sub>-DMSO.

<sup>1</sup>H NMR (400.13 MHz, *d*<sub>6</sub>-DMSO)  $\delta$ : 0.83-0.92 (m, 12H), 1.21-1.27 (m, 18H), 1.28-1.35 (m, 14H), 1.35-1.43 (m, 8H), 1.43-1.55 (m, 8H), 2.11-2.23 (m, 8H).

<sup>13</sup>C{<sup>1</sup>H} NMR (100.61 MHz, *d*<sub>6</sub>-DMSO)  $\delta$ : 13.53 (s, P-(CH<sub>2</sub>)<sub>5</sub>-CH<sub>3</sub>), 13.64 (s, P-(CH<sub>2</sub>)<sub>13</sub>-CH<sub>3</sub>), 17.45 (d, <sup>1</sup>J<sub>CP</sub> = 188 Hz, P-CH<sub>2</sub>-(CH<sub>2</sub>)<sub>4</sub>-CH<sub>3</sub>), 17.52 (d, <sup>1</sup>J<sub>CP</sub> = 192 Hz, P-CH<sub>2</sub>-(CH<sub>2</sub>)<sub>12</sub>-CH<sub>3</sub>), 20.46 (s, ), 20.50 (s, ), 20.54 (s, ), 21.75 (s, ), 22.07 (s, ), 28.81 (d, 2J<sub>CP</sub> = 116 Hz, P-CH<sub>2</sub>-CH<sub>2</sub>-(CH<sub>2</sub>)<sub>3</sub>-CH<sub>3</sub>), 28.90 (d, <sup>2</sup>J<sub>CP</sub> = 128 Hz, P-CH<sub>2</sub>-CH<sub>2</sub>-(CH<sub>2</sub>)<sub>11</sub>-CH<sub>3</sub>), 29.04 (s, P-(CH<sub>2</sub>)<sub>4</sub>-CH<sub>2</sub>-CH<sub>3</sub>), 29.09 (s, ), 29.70 (d, 3J<sub>CP</sub> = 60 Hz, P-(CH<sub>2</sub>)<sub>2</sub>-CH<sub>2</sub>-(CH<sub>2</sub>)<sub>10</sub>-CH<sub>3</sub>), 29.95 (d, <sup>3</sup>J<sub>CP</sub> = 60 Hz, P-(CH<sub>2</sub>)<sub>2</sub>-CH<sub>2</sub>-(CH<sub>2</sub>)<sub>2</sub>-CH<sub>3</sub>), 30.34 (s, P-(CH<sub>2</sub>)<sub>3</sub>-CH<sub>2</sub>-(CH<sub>2</sub>)<sub>9</sub>-CH<sub>3</sub>), 31.32 (s, P-(CH<sub>2</sub>)<sub>3</sub>-CH<sub>2</sub>-CH<sub>2</sub>-CH<sub>3</sub>), 119.50 (q, 1J<sub>CF</sub> = 1280 Hz CF<sub>3</sub>).

<sup>19</sup>F NMR (376.50 MHz, *d*<sub>6</sub>-DMSO)  $\delta$ : -79.00.

<sup>31</sup>P{<sup>1</sup>H} NMR (161.98 MHz, *d*<sub>6</sub>-DMSO)  $\delta$ : 33.55.

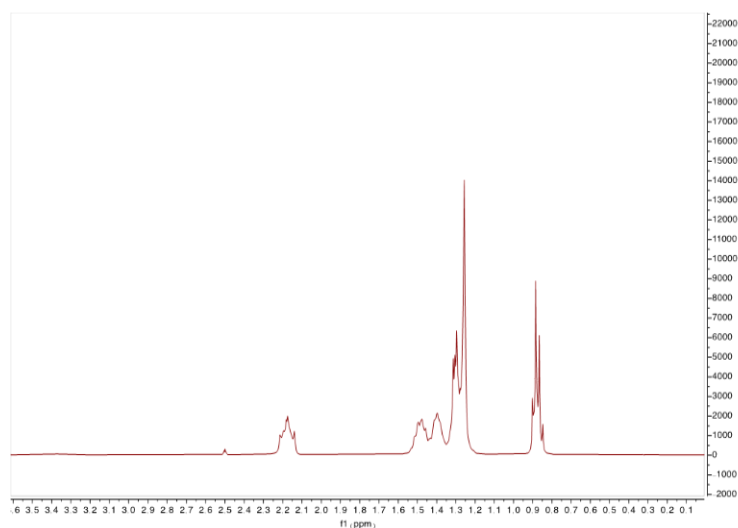


**Figure S4.4.**  $^1\text{H}$  NMR spectrum ( $d_6$ -DMSO, 400.13 MHz, 298.15 K) of  $[\text{P}_{666,14}][\text{TFSI}]$ .

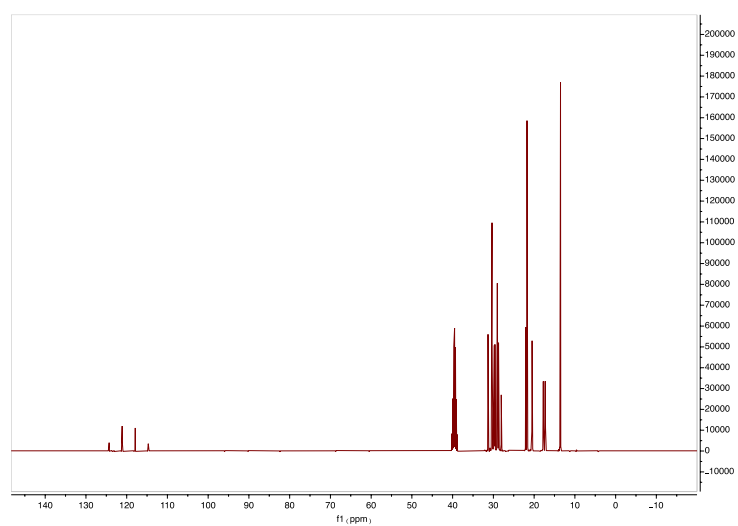


**Figure S4.5.**  $^{13}\text{C}$  NMR spectrum ( $d_6$ -DMSO, 100.61 MHz, 298.15 K) of  $[\text{P}_{666,14}][\text{TFSI}]$ .

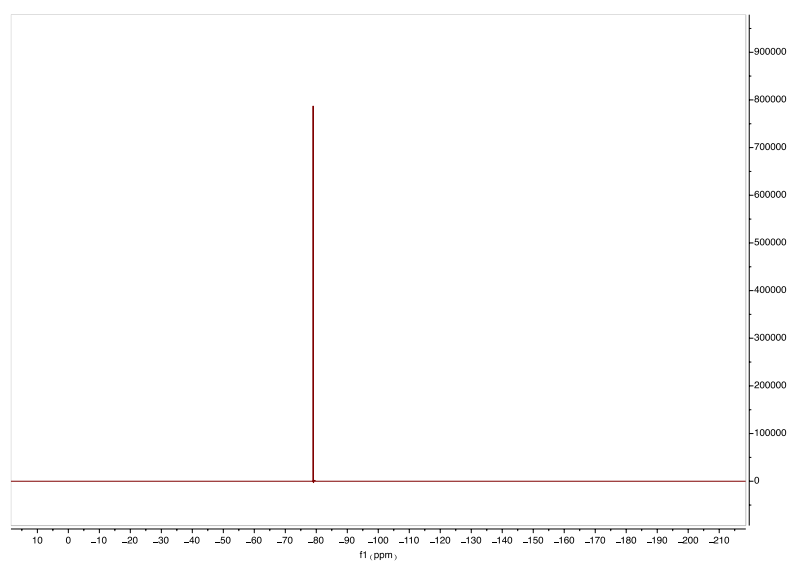


**Figure S4.6.**  $^{19}\text{F}$  NMR spectrum ( $d_6$ -DMSO, 376.50 MHz, 298.15 K) of  $[\text{P}_{666,14}][\text{TFSI}]$ .

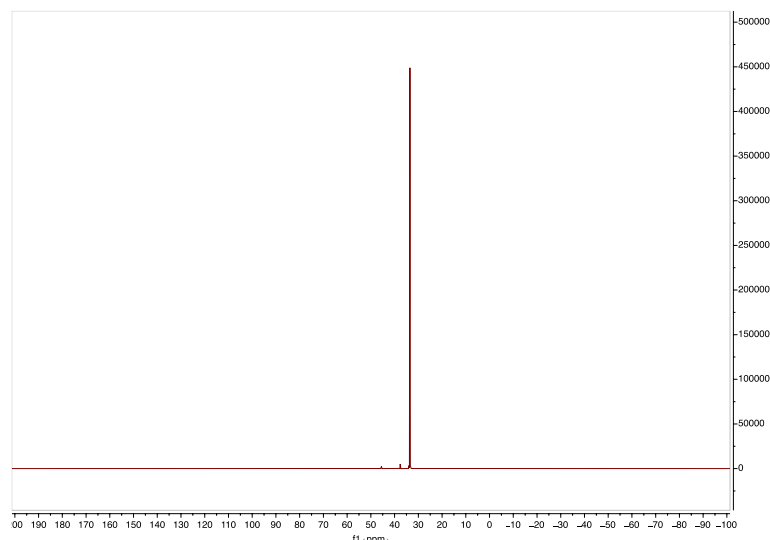


**Figure S4.7.**  $^{31}\text{P}$  NMR spectrum of ( $d_6$ -DMSO, 161.98 MHz, 298.15 K)  $[\text{P}_{666,14}][\text{TFSI}]$ .

**$[\text{P}_{444,14}]\text{Cl}$ .** Tributyl(tetradecyl)phosphonium chloride was provided by Solvay.

$^1\text{H}$  NMR:  $\delta$ : 0.85 (t, 3H), 0.92 (t, 9H), 1.25 (m, 20H), 1.45 (m, 16H), 2.07 (m, 8H).

$^{13}\text{C}$  NMR:  $\delta$ : 13.60 (P-( $\text{CH}_2$ ) $_3$ - $\text{CH}_3$ ), 14.41 (P-( $\text{CH}_2$ ) $_{13}$ - $\text{CH}_3$ ), 18.98 (d,  $^1J_{\text{C-P}} = 47.26$  Hz) (P- $\text{CH}_2$ - $(\text{CH}_2)_2$ - $\text{CH}_3$ ), 19.16 (d,  $^1J_{\text{C-P}} = 47.26$  Hz) (P- $\text{CH}_2$ - $(\text{CH}_2)_{12}$ - $\text{CH}_3$ ), 21.87 (d,  $^2J_{\text{C-P}} = 5.03$  Hz) (P- $\text{CH}_2$ - $\text{CH}_2$ - $\text{CH}_2$ - $\text{CH}_3$ ), 23.37 (P-( $\text{CH}_2$ ) $_{12}$ - $\text{CH}_2$ - $\text{CH}_3$ ), 23.93 (d,  $^2J_{\text{C-P}} = 5.03$  Hz) (P- $\text{CH}_2$ - $\text{CH}_2$ - $(\text{CH}_2)_{11}$ - $\text{CH}_3$ ), 24.49 (d,  $^3J_{\text{C-P}} = 15.08$  Hz) (P-( $\text{CH}_2$ ) $_2$ - $\text{CH}_2$ - $(\text{CH}_2)_{10}$ - $\text{CH}_3$ ), 29.38 (P-( $\text{CH}_2$ ) $_3$ - $\text{CH}_2$ - $(\text{CH}_2)_9$ - $\text{CH}_3$ ), 29.91 (P-( $\text{CH}_2$ ) $_4$ - $\text{CH}_2$ - $(\text{CH}_2)_8$ - $\text{CH}_3$ ), 30.03 (P-( $\text{CH}_2$ ) $_5$ - $\text{CH}_2$ - $(\text{CH}_2)_7$ - $\text{CH}_3$ ), 30.22 (P-( $\text{CH}_2$ ) $_6$ - $\text{CH}_2$ - $(\text{CH}_2)_6$ - $\text{CH}_3$ ), 30.31 (P-( $\text{CH}_2$ ) $_7$ - $\text{CH}_2$ - $(\text{CH}_2)_5$ - $\text{CH}_3$ ), 30.33 (P-( $\text{CH}_2$ ) $_8$ - $\text{CH}_2$ - $(\text{CH}_2)_4$ - $\text{CH}_3$  and P-( $\text{CH}_2$ ) $_9$ - $\text{CH}_2$ - $(\text{CH}_2)_3$ - $\text{CH}_3$ ), 30.37 (P-( $\text{CH}_2$ ) $_{10}$ - $\text{CH}_2$ - $(\text{CH}_2)_2$ - $\text{CH}_3$  and P-( $\text{CH}_2$ ) $_{11}$ - $\text{CH}_2$ - $\text{CH}_2$ - $\text{CH}_3$ ), 31.20 (d,  $^3J_{\text{C-P}} = 15.08$  Hz) (P-( $\text{CH}_2$ ) $_2$ - $\text{CH}_2$ - $\text{CH}_3$ ), 32.62 (P-( $\text{CH}_2$ ) $_{12}$ - $\text{CH}_2$ - $\text{CH}_3$ ).

$^{31}\text{P}\{^1\text{H}\}$  NMR:  $\delta$ : 33.56

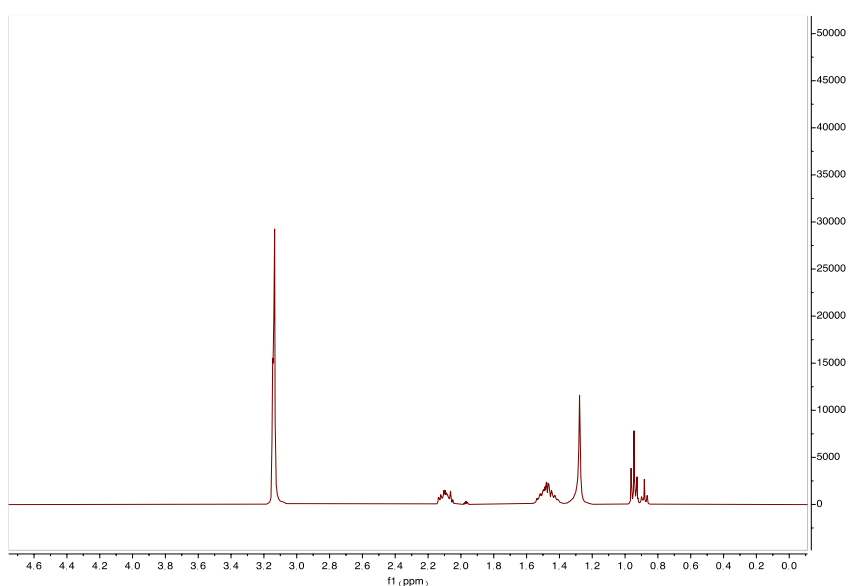


**Figure S4.8.**  $^1\text{H}$  NMR spectrum (acetonitrile- $d_3$ , 399.91 MHz, 300 K) of  $[\text{P}_{444,14}]\text{Cl}$ .

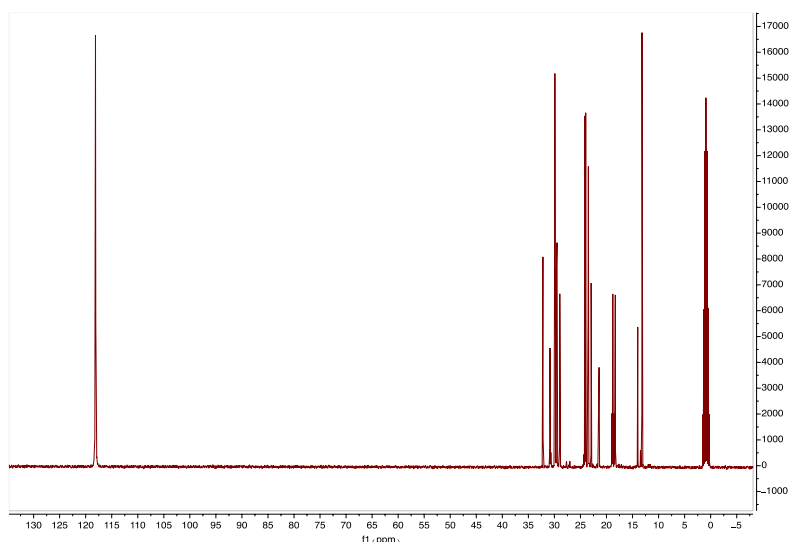


**Figure S4.9.**  $^{13}\text{C}$  NMR spectrum (acetonitrile- $d_3$ , 100.56 MHz, 301.4 K) of  $[\text{P}_{444,14}]\text{Cl}$ .

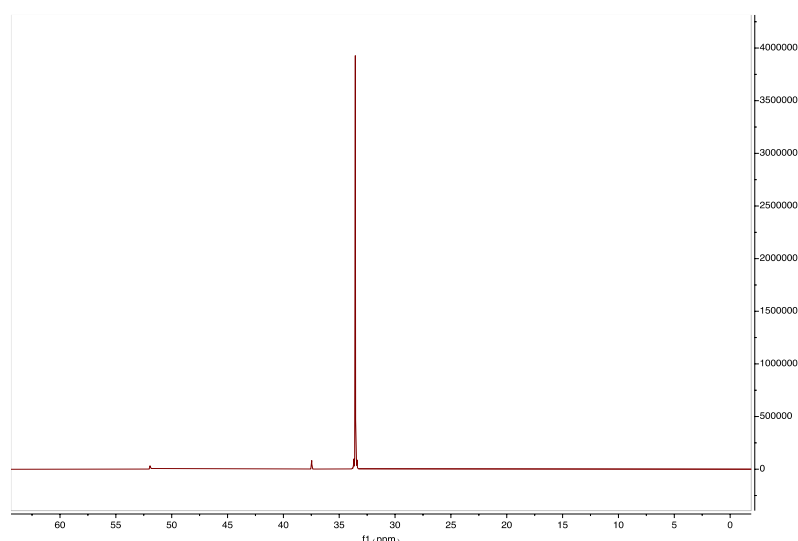


**Figure S4.10.**  $^{31}\text{P}$  NMR spectrum (acetonitrile- $d_3$ , 161.89 MHz, 300.1 K) of  $[\text{P}_{444,14}]\text{Cl}$ .

**$[\text{P}_{444,14}][\text{TFSI}]$ .** Tributyl(tetradecyl)phosphonium chloride,  $[\text{P}_{444,14}]\text{Cl}$  (0.088 mol eq.) and lithium bis(trifluoromethanesulfon)imide  $\text{Li}[\text{TFSI}]$  (0.115 mol eq.) were separately dissolved in  $200\text{ cm}^3$  deionised water ( $18.2\text{ M}\Omega\cdot\text{cm}$ ) (total  $400\text{ cm}^3$ ) and then combined in a round-bottomed flask ( $500\text{ cm}^3$ ), resulting in the formation of a biphasic liquid system; the mixture was left to react (1 h, room temperature, 600 rpm). The aqueous layer was separated, and the organic layer was collected and washed, firstly with deionized water ( $18.2\text{ M}\Omega\cdot\text{cm}$ ) ( $100\text{ cm}^3$ ) and then dichloromethane, DCM ( $100\text{ cm}^3$ ). Subsequent washes were performed with solution of  $\text{Li}[\text{TFSI}]$  in deionised water ( $18.2\text{ M}\Omega\cdot\text{cm}$ ). Final three washes were performed with deionised water ( $18.2\text{ M}\Omega\cdot\text{cm}$ ). The organic layer was washed 12 times in total. Subsequently, DCM was removed *via* rotary evaporation (30 min, 303.15 K) and the ionic liquid was dried under high vacuum (12h, 343.15 K,  $10^{-2}$  mbar). XRF analysis confirmed chloride content was below the detectable limit.  $^1\text{H}$ ,  $^{13}\text{C}$ ,  $^{19}\text{F}$  and  $^{31}\text{P}$  NMR spectra of the IL were recorded in acetonitrile- $d_3$ .

$^1\text{H}$  NMR:  $\delta$ : 0.89 (t, 3H), 0.95 (t, 9H), 1.28 (m, 20H), 1.47 (m, 16H), 2.06 (m, 8H).

$^{13}\text{C}$  NMR:  $\delta$ : (TFSI peaks 125.81, 122.62, 119.43, 116.24 (q,  $^1J_{\text{C-F}} = 320.82$  Hz)), 13.58 (P-(CH<sub>2</sub>)<sub>3</sub>-CH<sub>3</sub>), 14.47 (P-(CH<sub>2</sub>)<sub>13</sub>-CH<sub>3</sub>), 19.01 (d,  $^1J_{\text{C-P}} = 48.27$  Hz) (P-CH<sub>2</sub>-(CH<sub>2</sub>)<sub>2</sub>-CH<sub>3</sub>), 19.21 (d,  $^1J_{\text{C-P}} = 48.27$  Hz) (P-CH<sub>2</sub>-(CH<sub>2</sub>)<sub>12</sub>-CH<sub>3</sub>), 21.91 (d,  $^2J_{\text{C-P}} = 4.02$  Hz) (P-CH<sub>2</sub>-CH<sub>2</sub>-CH<sub>2</sub>-CH<sub>3</sub>), 23.46 (P-(CH<sub>2</sub>)<sub>12</sub>-CH<sub>2</sub>-CH<sub>3</sub>), 23.95 (d,  $^2J_{\text{C-P}} = 4.02$  Hz) (P-CH<sub>2</sub>-CH<sub>2</sub>-(CH<sub>2</sub>)<sub>11</sub>-CH<sub>3</sub>), 24.54 (3d,  $J_{\text{C-P}} = 15.09$  Hz) (P-(CH<sub>2</sub>)<sub>2</sub>-CH<sub>2</sub>-(CH<sub>2</sub>)<sub>10</sub>-CH<sub>3</sub>), 29.45 (P-(CH<sub>2</sub>)<sub>3</sub>-CH<sub>2</sub>-(CH<sub>2</sub>)<sub>9</sub>-CH<sub>3</sub>), 30.00 (P-(CH<sub>2</sub>)<sub>4</sub>-CH<sub>2</sub>-(CH<sub>2</sub>)<sub>8</sub>-CH<sub>3</sub>), 30.14 (P-(CH<sub>2</sub>)<sub>5</sub>-CH<sub>2</sub>-(CH<sub>2</sub>)<sub>7</sub>-CH<sub>3</sub>), 30.30 (P-(CH<sub>2</sub>)<sub>6</sub>-CH<sub>2</sub>-(CH<sub>2</sub>)<sub>6</sub>-CH<sub>3</sub>), 30.40 (P-(CH<sub>2</sub>)<sub>7</sub>-CH<sub>2</sub>-(CH<sub>2</sub>)<sub>5</sub>-CH<sub>3</sub>), 30.43 (P-(CH<sub>2</sub>)<sub>8</sub>-CH<sub>2</sub>-(CH<sub>2</sub>)<sub>4</sub>-CH<sub>3</sub> and P-(CH<sub>2</sub>)<sub>9</sub>-CH<sub>2</sub>-(CH<sub>2</sub>)<sub>3</sub>-CH<sub>3</sub>), 30.47 (P-(CH<sub>2</sub>)<sub>10</sub>-CH<sub>2</sub>-(CH<sub>2</sub>)<sub>2</sub>-CH<sub>3</sub> and P-(CH<sub>2</sub>)<sub>11</sub>-CH<sub>2</sub>-CH<sub>2</sub>-CH<sub>3</sub>), 31.27 (d,  $^3J_{\text{C-P}} = 15.09$  Hz) (P-(CH<sub>2</sub>)<sub>2</sub>-CH<sub>2</sub>-CH<sub>3</sub>), 32.72 (P-(CH<sub>2</sub>)<sub>12</sub>-CH<sub>2</sub>-CH<sub>3</sub>).

$^{19}\text{F}$  NMR:  $\delta$ : -80.01

$^{31}\text{P}\{^1\text{H}\}$  NMR:  $\delta$ : 33.64

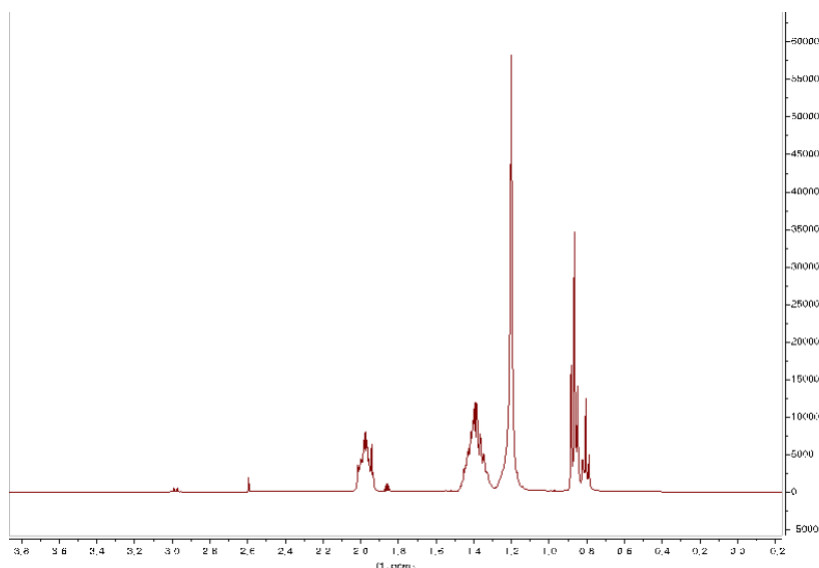


**Figure S4.11.**  $^1\text{H}$  NMR spectrum (acetonitrile- $d_3$ , 399.91 MHz, 299.9 K) of [P<sub>444,14</sub>][TFSI].

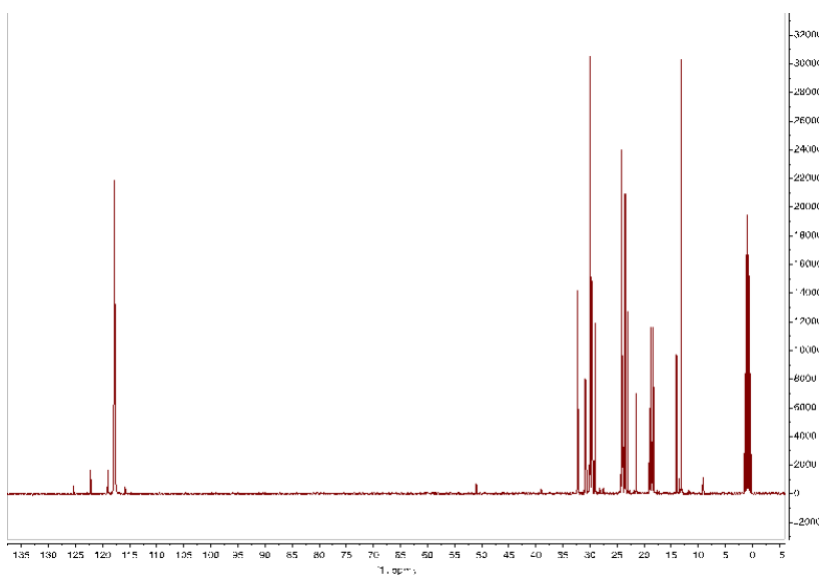


**Figure S4.12.**  $^{13}\text{C}$  NMR spectrum (acetonitrile- $d_3$ , 100.57 MHz, 299.9 K) of [P<sub>444,14</sub>][TFSI].

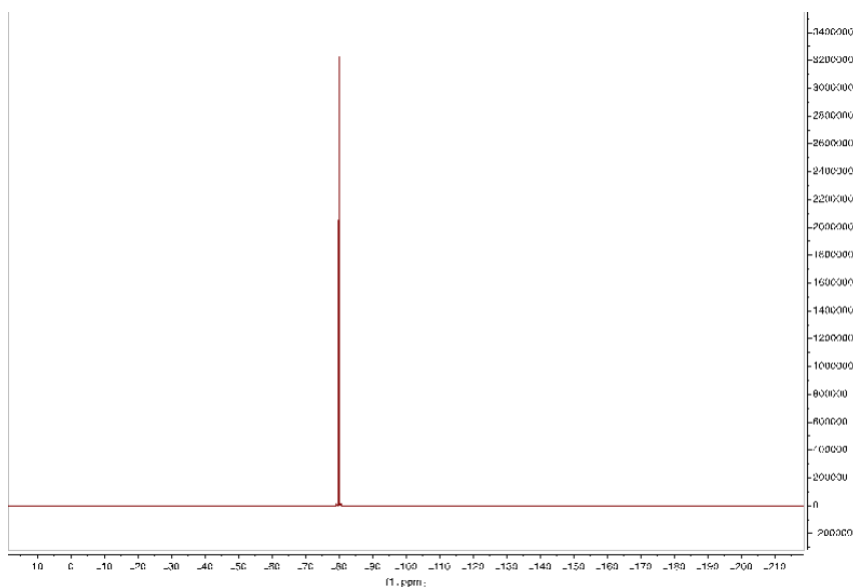


**Figure S4.13.**  $^{19}\text{F}$  NMR spectrum (acetonitrile- $d_3$ , 376.29 MHz, 299.2 K) of  $[\text{P}_{444,14}][\text{TFSI}]$ .

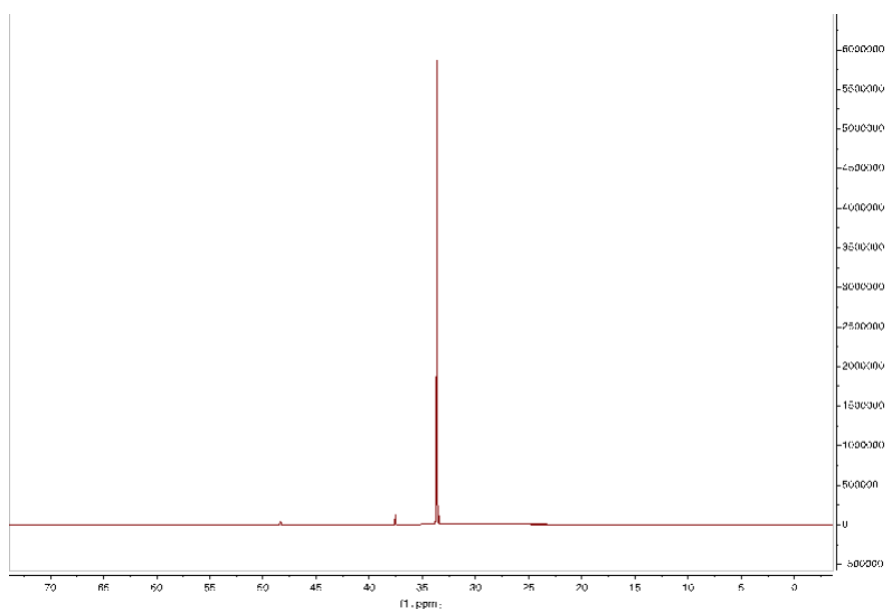


**Figure S4.14.**  $^{31}\text{P}$  NMR spectrum (acetonitrile- $d_3$ , 161.86 MHz, 300 K) of  $[\text{P}_{444,14}][\text{TFSI}]$ .

$[\text{P}_{666,2}][\text{TFSI}]$ . Trihexylphosphine (60g) was charged to an autoclave glass reactor under a dinitrogen atmosphere and placed into the stainless-steel cage holder, and quickly attached to the cover plate. A gas cylinder containing chloroethane was connected to the autoclave through the gas inlet tube. The gas and inlet valves were opened after the set up was leak tested and the gas flow was maintained at approximately  $2 \text{ cm}^3 \text{ min}^{-1}$ . The reaction mixture was slowly heated over several hours in an oil bath until the temperature inside of the reactor reached 418.15 K. The pressure in the reactor was built up by an excess of chloroalkane and did not exceed 4 bar with increasing temperature. The gas inlet was closed after approximately one hour and the reaction was maintained (4h, 418.15 K). After the reaction was cooled down to room temperature the pressure was released.

The content of the reactor was transferred to a round-bottomed flask (100 cm<sup>3</sup>) and dried *in vacuo* (48h, 338.15 K). The synthesised trihexyl(ethyl)phosphonium chloride, [P<sub>666,2</sub>]Cl (1.000 mol eq.) was dissolved in dichloromethane, DCM (100 cm<sup>3</sup>) while stirring mildly in an Erlenmeyer flask (250 cm<sup>3</sup>). Lithium bis(trifluoromethanesulfonyl)imide Li[TFSI] (1.020 mol eq.) was separately dissolved in 20 cm<sup>3</sup> deionised water (18.2 MΩ.cm) and then combined resulting in the formation of a biphasic liquid system; the mixture was left to react (1.5 h, room temperature). The aqueous layer was separated, and the organic layer was collected and washed, firstly with dichloromethane, DCM (3 x 30 cm<sup>3</sup>). The combined washes were then washed with deionized water (18.2 MΩ.cm) (15 x 30 cm<sup>3</sup>). The dichloromethane, DCM solution was dried by addition of anhydrous sodium sulfate (*ca.* 10 g), then isolated *via* vacuum filtration of the Na<sub>2</sub>SO<sub>4</sub> (P3 glass sintered funnel with Celite). The filtrate was transferred to a round bottom flask, and dichloromethane, DCM was removed *in vacuo* by rotary evaporation at (303.15 K) and further under high vacuum (48h, 343.15 K, 10<sup>-2</sup> mbar), leaving clear liquid product. XRF analysis confirmed chloride content was below the detectable limit. <sup>1</sup>H, <sup>13</sup>C, <sup>19</sup>F and <sup>31</sup>P NMR spectra of the IL were recorded in acetonitrile-*d*<sub>3</sub>.

<sup>1</sup>H NMR: δ: 0.91 (t, 9H), 1.15 (m, 3H), 1.32 (m, 12H), 1.44 (m, 12H), 2.06 (m, 8H).

<sup>13</sup>C NMR: (TFSI peaks 125.84, 122.65, 119.45, 116.27 (q, <sup>1</sup>J<sub>C-F</sub> = 320.82 Hz)), 5.91 (d, <sup>2</sup>J<sub>C-P</sub> = 6.03 Hz) (P-CH<sub>2</sub>-CH<sub>3</sub>), 13.02 (d, <sup>1</sup>J<sub>C-P</sub> = 50.28 Hz) (P-CH<sub>2</sub>-CH<sub>3</sub>), 14.30 (P-(CH<sub>2</sub>)<sub>5</sub>-CH<sub>3</sub>), 18.87 (d, <sup>1</sup>J<sub>C-P</sub> = 47.26 Hz) (P-CH<sub>2</sub>-(CH<sub>2</sub>)<sub>4</sub>-CH<sub>3</sub>), 21.91 (d, <sup>2</sup>J<sub>C-P</sub> = 5.03 Hz) (P-CH<sub>2</sub>-CH<sub>2</sub>-(CH<sub>2</sub>)<sub>3</sub>-CH<sub>3</sub>), 23.07 (P-(CH<sub>2</sub>)<sub>4</sub>-CH<sub>2</sub>-CH<sub>3</sub>), 30.99 (d, <sup>3</sup>J<sub>C-P</sub> = 15.08 Hz) (P-(CH<sub>2</sub>)<sub>2</sub>-CH<sub>2</sub>-(CH<sub>2</sub>)<sub>2</sub>-CH<sub>3</sub>), 31.68 (P-(CH<sub>2</sub>)<sub>3</sub>-CH<sub>2</sub>-CH<sub>2</sub>-CH<sub>3</sub>).

<sup>19</sup>F NMR: δ: -80.01

<sup>31</sup>P{<sup>1</sup>H} NMR: δ: 35.30

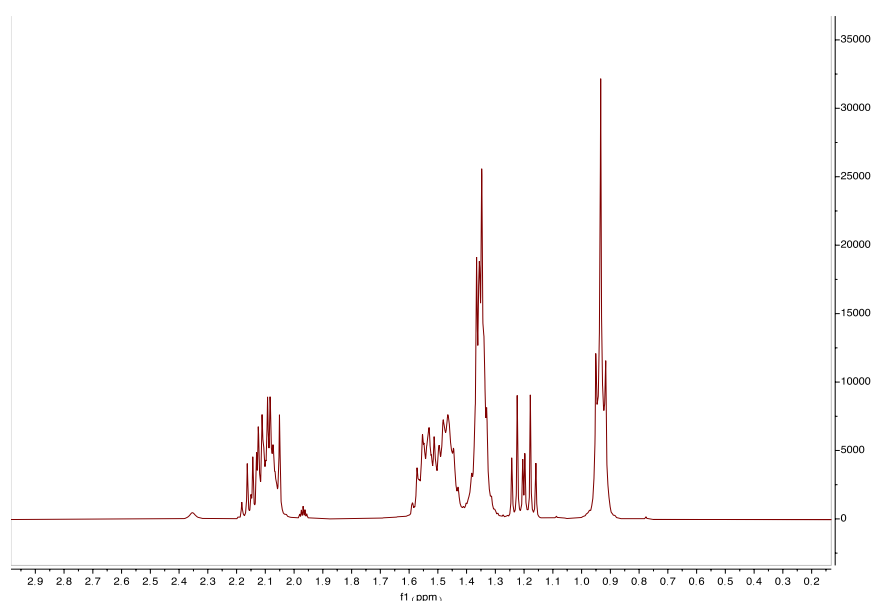


**Figure S4.15.** <sup>1</sup>H NMR spectrum (acetonitrile-*d*<sub>3</sub>, 399.1 MHz, 300.5 K) of [P<sub>666,2</sub>][TFSI].

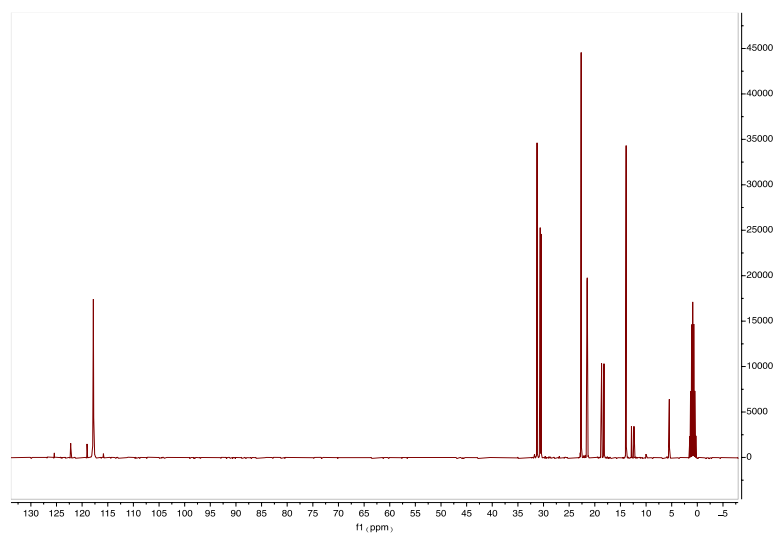


**Figure S4.16.** <sup>13</sup>C NMR spectrum (acetonitrile-*d*<sub>3</sub>, 100.56 MHz, 301.1 K) of [P<sub>666,2</sub>][TFSI].

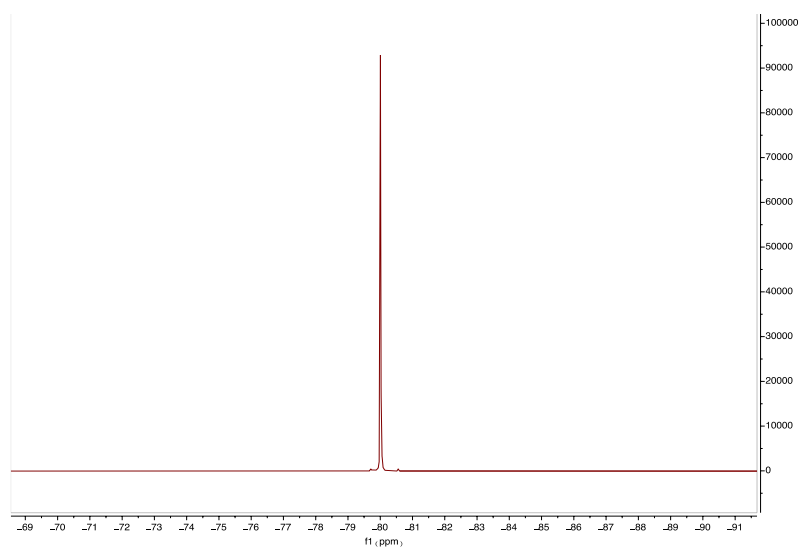


**Figure S4.17.** <sup>19</sup>F NMR spectrum (acetonitrile-*d*<sub>3</sub>, 376.29 MHz, 300.2 K) of [P<sub>666,2</sub>][TFSI].

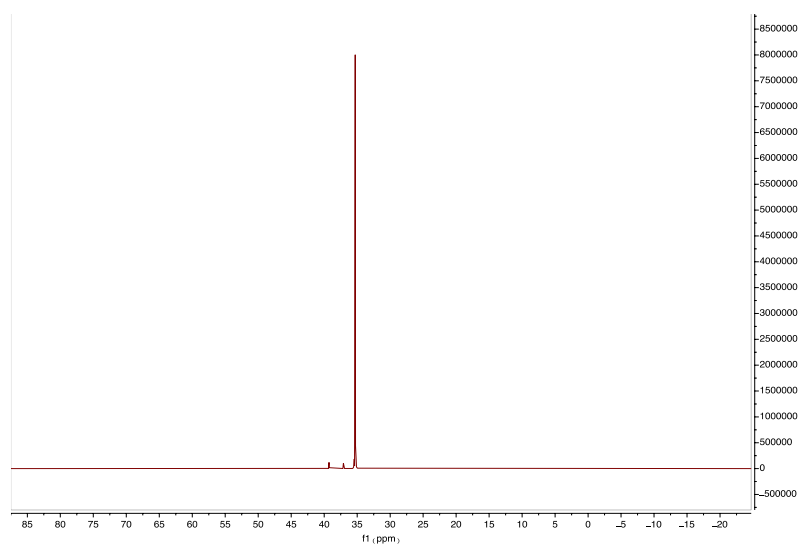


**Figure S4.18.** <sup>31</sup>P NMR spectrum (acetonitrile-*d*<sub>3</sub>, 161.88 MHz, 300 K) of [P<sub>666,2</sub>][TFSI].

**[P<sub>666,6</sub>]Cl**. Trihexylphosphine (1.000 mol eq.) and 1-chlorohexane (C<sub>6</sub>H<sub>13</sub>Cl) (1.100 mol eq.) were placed in a round-bottomed flask (50 cm<sup>3</sup>). The mixture was stirred and heated under a reflux condenser connected to a Schlenk line flushed with dinitrogen (12h, 418.15 K). In order to remove the excess of starting C<sub>6</sub>H<sub>13</sub>Cl, the purification step involved dissolution of the product in hexane, followed by extraction with water. The product was dried at *in vacuo* (48 h, 338.15 K). <sup>1</sup>H, <sup>13</sup>C, and <sup>31</sup>P NMR spectra of the IL were recorded in acetonitrile-*d*<sub>3</sub>.

<sup>1</sup>H NMR: δ: 0.75 (t, 12H), 1.17 (m, 16H), 1.29 (m, 8H), 1.41 (m, 8H), 2.34 (m, 8H).

<sup>13</sup>C NMR: δ: 14.01 (P-(CH<sub>2</sub>)<sub>5</sub>-CH<sub>3</sub>), 19.05 (d, <sup>1</sup>J<sub>C-P</sub> = 47.26 Hz) (P-CH<sub>2</sub>-(CH<sub>2</sub>)<sub>4</sub>-CH<sub>3</sub>), 21.76 (d, <sup>2</sup>J<sub>C-P</sub> = 4.02 Hz) (P-CH<sub>2</sub>-CH<sub>2</sub>-(CH<sub>2</sub>)<sub>3</sub>-CH<sub>3</sub>), 22.59 (P-(CH<sub>2</sub>)<sub>4</sub>-CH<sub>2</sub>-CH<sub>3</sub>), 30.67 (d, <sup>3</sup>J<sub>C-P</sub> = 15.08 Hz) (P-(CH<sub>2</sub>)<sub>2</sub>-CH<sub>2</sub>-(CH<sub>2</sub>)<sub>2</sub>-CH<sub>3</sub>), 31.27 (P-(CH<sub>2</sub>)<sub>3</sub>-CH<sub>2</sub>-CH<sub>2</sub>-CH<sub>3</sub>).

<sup>31</sup>P{<sup>1</sup>H} NMR: δ: 33.04

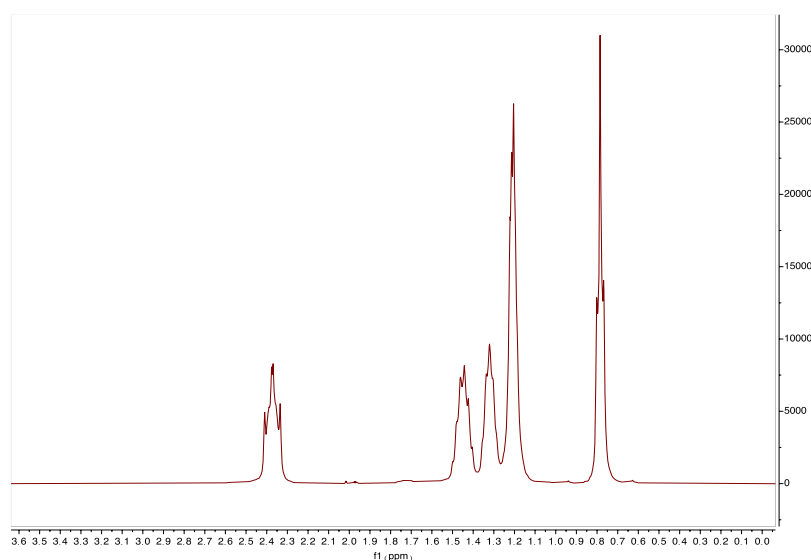


**Figure S4.19.** <sup>1</sup>H NMR spectrum (acetonitrile-*d*<sub>3</sub>, 399.90 MHz, 300.2 K) of [P<sub>666,6</sub>]Cl.

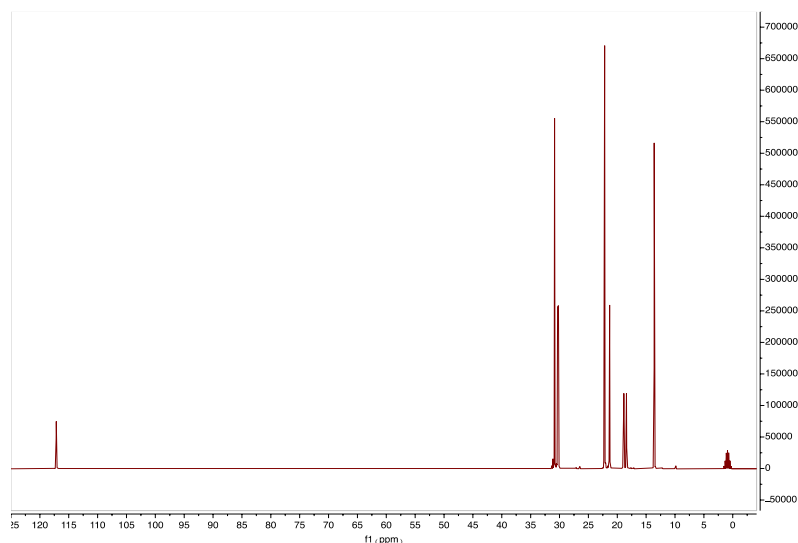


**Figure S4.20.** <sup>13</sup>C NMR spectrum (acetonitrile-*d*<sub>3</sub>, 100.55 MHz, 301.1 K) of [P<sub>666,6</sub>]Cl.

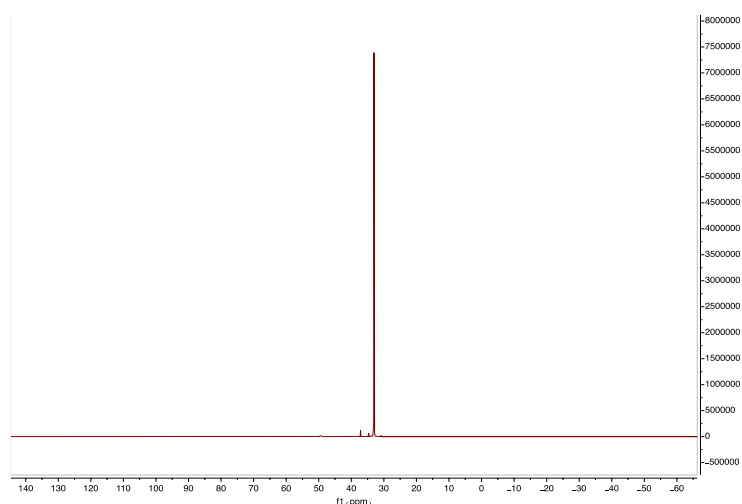


**Figure S4.21.**  $^{31}\text{P}$  NMR spectrum (acetonitrile- $d_3$ , 161.89 MHz, 300 K) of  $[\text{P}_{666,6}]\text{Cl}$ .

**$[\text{P}_{666,6}][\text{TFSI}]$ .** Tetrahexylphosphonium chloride,  $[\text{P}_{666,6}]\text{Cl}$  (0.009 mol eq.) and lithium bis(trifluoromethanesulfon)imide  $\text{Li}[\text{TFSI}]$  (0.012 mol eq.) were separately dissolved in  $25\text{ cm}^3$  deionised water ( $18.2\text{ M}\Omega\cdot\text{cm}$ ) (total  $50\text{ cm}^3$ ) and then combined in a round-bottomed flask ( $250\text{ cm}^3$ ), resulting in the formation of a biphasic liquid system; the mixture was left to react (1 h, room temperature, 600 rpm). The aqueous layer was separated, and the organic layer was collected and washed, firstly with deionized water ( $18.2\text{ M}\Omega\cdot\text{cm}$ ) ( $10\text{ cm}^3$ ) and then dichloromethane, DCM ( $10\text{ cm}^3$ ). Subsequent washes were performed with solution of  $\text{Li}[\text{TFSI}]$  in deionised water ( $18.2\text{ M}\Omega\cdot\text{cm}$ ). Final three washes were performed with deionised water ( $18.2\text{ M}\Omega\cdot\text{cm}$ ). The organic layer was washed 10 times in total. Subsequently, DCM was removed *via* rotary evaporation (30 min, 308.15 K) and the ionic liquid was dried under high vacuum (12h, 343.15 K,  $10^{-2}$  mbar). XRF analysis confirmed chloride content was below the detectable limit.  $^1\text{H}$ ,  $^{13}\text{C}$ ,  $^{19}\text{F}$  and  $^{31}\text{P}$  NMR spectra of the IL were recorded in acetonitrile- $d_3$ .

$^1\text{H}$  NMR:  $\delta$ : 0.91 (t, 12H), 1.32 (m, 16H), 1.43 (m, 16H), 2.05 (m, 8H).

$^{13}\text{C}$  NMR:  $\delta$ : (TFSI peaks 125.83, 122.64, 119.45, 116.26 (q,  $^1\text{J}_{\text{C-F}} = 320.82\text{ Hz}$ ), 14.31 (P-( $\text{CH}_2$ ) $_5$ -**CH** $_3$ ), 19.24 (d,  $^1\text{J}_{\text{C-P}} = 47.27\text{ Hz}$ ) (P-**CH** $_2$ -( $\text{CH}_2$ ) $_4$ - $\text{CH}_3$ ), 21.95 (d,  $^2\text{J}_{\text{C-P}} = 5.03\text{ Hz}$ ) (P- $\text{CH}_2$ -**CH** $_2$ -( $\text{CH}_2$ ) $_3$ - $\text{CH}_3$ ), 23.07 (P-( $\text{CH}_2$ ) $_4$ -**CH** $_2$ - $\text{CH}_3$ ), 30.98 (d,  $^3\text{J}_{\text{C-P}} = 15.09\text{ Hz}$ ) (P-( $\text{CH}_2$ ) $_2$ -**CH** $_2$ -( $\text{CH}_2$ ) $_2$ - $\text{CH}_3$ ), 31.67 (P-( $\text{CH}_2$ ) $_3$ -**CH** $_2$ - $\text{CH}_2$ - $\text{CH}_3$ ).

$^{19}\text{F}$  NMR:  $\delta$ : -79.97

$^{31}\text{P}\{^1\text{H}\}$  NMR:  $\delta$ : 33.50

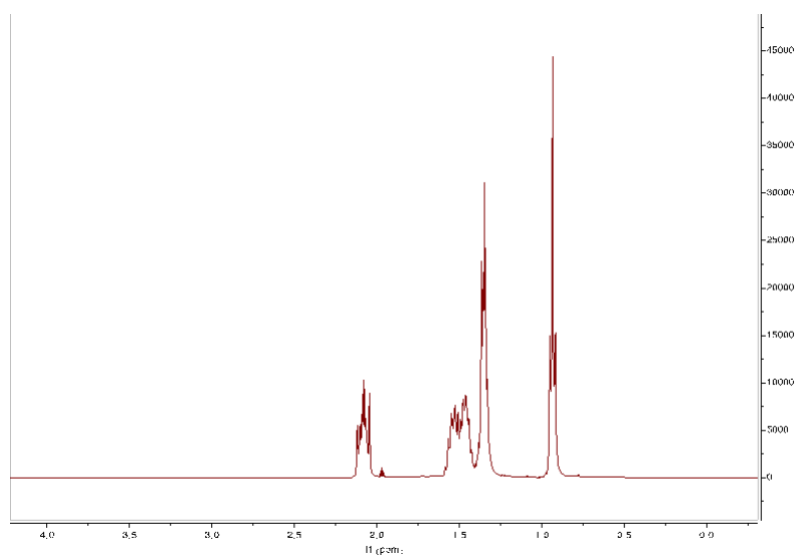


**Figure S4.22.**  $^1\text{H}$  NMR spectrum (acetonitrile- $d_3$ , 399.91 MHz, 300.9 K) of  $[\text{P}_{666,6}][\text{TFSI}]$ .

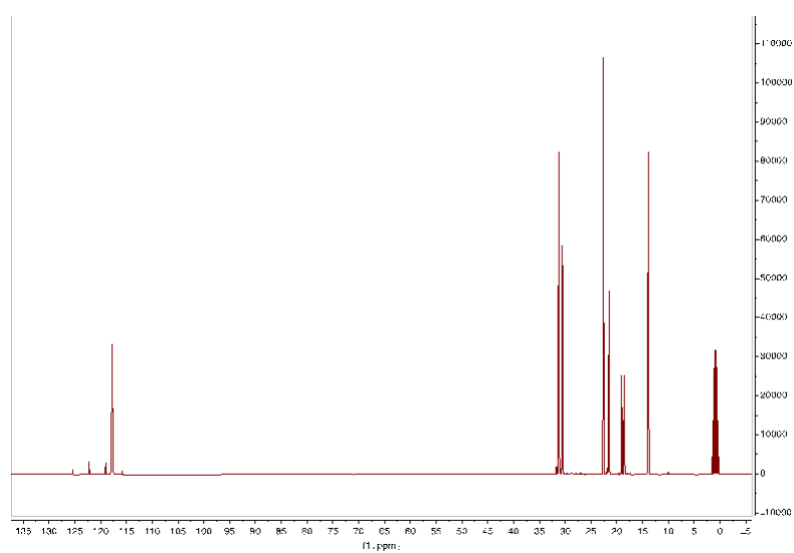


**Figure S4.23.**  $^{13}\text{C}$  NMR spectrum (acetonitrile- $d_3$ , 100.57 MHz, 300.5 K) of  $[\text{P}_{666,6}][\text{TFSI}]$ .

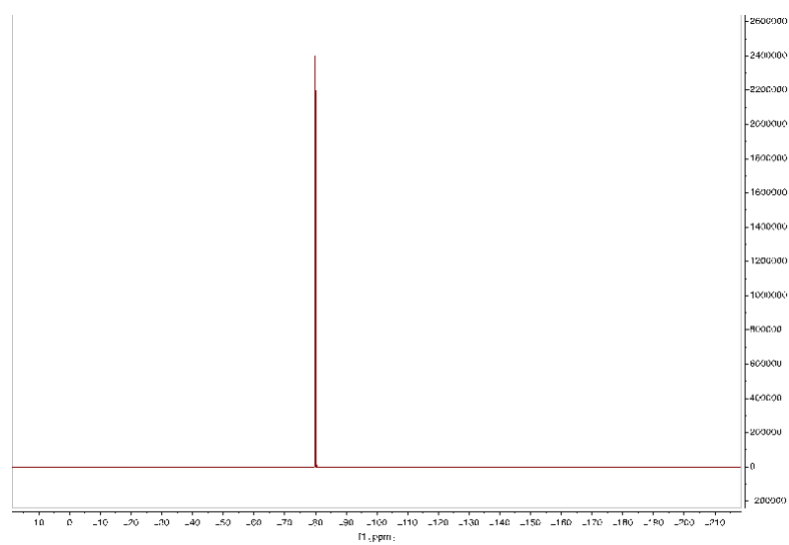


**Figure S4.24.**  $^{19}\text{F}$  NMR spectrum (acetonitrile- $d_3$ , 376.29 MHz, 299.7 K) of  $[\text{P}_{666,6}][\text{TFSI}]$ .

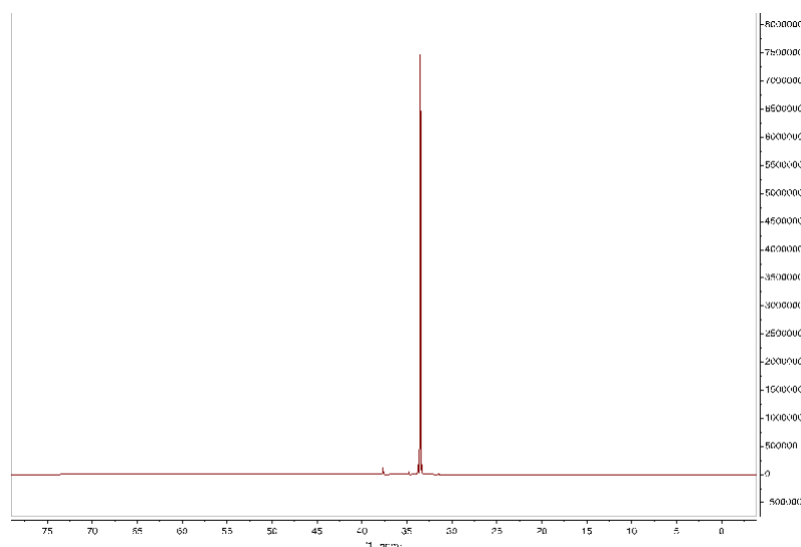


**Figure S4.25.**  $^{31}\text{P}$  NMR spectrum (acetonitrile- $d_3$ , 161.89 MHz, 300.2 K) of  $[\text{P}_{666,6}][\text{TFSI}]$ .

$[\text{P}_{666,8}][\text{TFSI}]$ . Trihexylphosphine (1.000 mol eq.) and 1-chlorooctane ( $\text{C}_8\text{H}_{17}\text{Cl}$ ) (1.100 mol eq.) were placed in a round-bottomed flask ( $50\text{ cm}^3$ ). The mixture was stirred and heated under a reflux condenser connected to a Schlenk line flushed with dinitrogen (14h, 418.15 K). In order to remove the excess of starting  $\text{C}_8\text{H}_{17}\text{Cl}$ , the purification step involved dissolution of the product in hexane, followed by extraction with water. The synthesised trihexyl(octyl)phosphonium chloride,  $[\text{P}_{6668}]\text{Cl}$  (1.000 mol eq.) was dissolved in dichloromethane, DCM ( $100\text{ cm}^3$ ) while stirring mildly in an Erlenmeyer flask ( $250\text{ cm}^3$ ). Lithium bis(trifluoromethanesulfon)imide  $\text{Li}[\text{TFSI}]$  (1.020 mol eq.) was separately dissolved in  $20\text{ cm}^3$  deionised water ( $18.2\text{ M}\Omega\cdot\text{cm}$ ) and then combined resulting in the formation of a biphasic liquid system; the mixture was left to react (1.5 h, room temperature). The aqueous layer was separated, and the organic layer was collected and washed, firstly with dichloromethane, DCM ( $3 \times 30\text{ cm}^3$ ). The combined washes were then washed with deionized water ( $18.2\text{ M}\Omega\cdot\text{cm}$ ) ( $15 \times 30\text{ cm}^3$ ). The dichloromethane, DCM solution was dried by addition of anhydrous sodium sulfate (*ca.* 10 g), then isolated *via* vacuum filtration of the  $\text{Na}_2\text{SO}_4$  (P3 glass sintered funnel with Celite). The filtrate was transferred to a round bottom flask, and dichloromethane, DCM was removed *in vacuo* by rotary evaporation at (303.15 K) and further under high vacuum (48h, 343.15 K,  $10^{-2}$  mbar), leaving clear liquid product. XRF analysis confirmed chloride content was below the detectable limit.  $^1\text{H}$ ,  $^{13}\text{C}$ ,  $^{19}\text{F}$  and  $^{31}\text{P}$  NMR spectra of the IL were recorded in acetonitrile- $d_3$ .

$^1\text{H}$  NMR:  $\delta$ : 0.91 (m, 12H), 1.32 (m, 20H), 1.44 (m, 16H), 2.06 (m, 8H).

$^{13}\text{C}$  NMR: (TFSI peaks 125.87, 122.67, 119.48, 116.29 (q,  $^1J_{\text{C-F}} = 321.79\text{ Hz}$ )), 14.36 (P-( $\text{CH}_2$ ) $_5$ - $\text{CH}_3$ ), 14.50 (P-( $\text{CH}_2$ ) $_7$ - $\text{CH}_3$ ), 19.27 (d,  $^1J_{\text{C-P}} = 48.27\text{ Hz}$ ) (P- $\text{CH}_2$ -( $\text{CH}_2$ ) $_4$ - $\text{CH}_3$  and P- $\text{CH}_2$ -( $\text{CH}_2$ ) $_6$ - $\text{CH}_3$ ), 21.99 (d,  $^2J_{\text{C-P}} = 5.03\text{ Hz}$ ) (P- $\text{CH}_2$ - $\text{CH}_2$ -( $\text{CH}_2$ ) $_3$ - $\text{CH}_3$  and P- $\text{CH}_2$ - $\text{CH}_2$ -( $\text{CH}_2$ ) $_5$ - $\text{CH}_3$ ), 23.10 (P-( $\text{CH}_2$ ) $_4$ - $\text{CH}_2$ - $\text{CH}_3$ ), 23.43 (P-( $\text{CH}_2$ ) $_6$ - $\text{CH}_2$ - $\text{CH}_3$ ), 29.43 (P-( $\text{CH}_2$ ) $_3$ - $\text{CH}_2$ -( $\text{CH}_2$ ) $_3$ - $\text{CH}_3$ ), 29.71 (P-

$(\text{CH}_2)_4\text{-CH}_2\text{-(CH}_2)_2\text{-CH}_3$ , 31.00 (d,  $3J_{\text{C-P}} = 15.08$  Hz) (P-(CH<sub>2</sub>)<sub>2</sub>-CH<sub>2</sub>-(CH<sub>2</sub>)<sub>2</sub>-CH<sub>3</sub>), 31.29 (d,  $^3J_{\text{C-P}} = 15.08$  Hz) (P-(CH<sub>2</sub>)<sub>2</sub>-CH<sub>2</sub>-(CH<sub>2</sub>)<sub>4</sub>-CH<sub>3</sub>), 31.70 (P-(CH<sub>2</sub>)<sub>3</sub>-CH<sub>2</sub>-CH<sub>2</sub>-CH<sub>3</sub>), 32.57 (P-(CH<sub>2</sub>)<sub>5</sub>-CH<sub>2</sub>-CH<sub>2</sub>-CH<sub>3</sub>).

$^{19}\text{F}$  NMR:  $\delta$ : -79.84

$^{31}\text{P}\{^1\text{H}\}$  NMR:  $\delta$ : 33.46

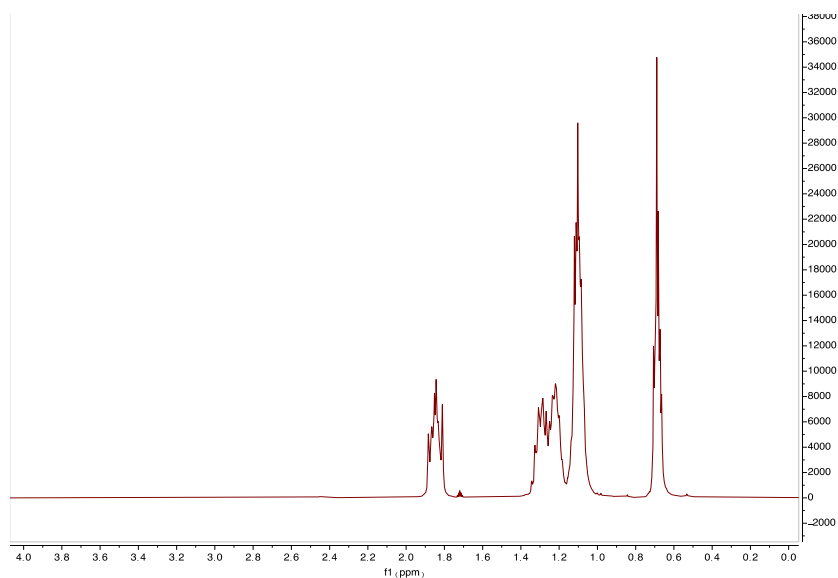


**Figure S4.26.**  $^1\text{H}$  NMR spectrum (acetonitrile- $d_3$ , 399.91 MHz, 300 K) of [P<sub>666,8</sub>][TFSI].

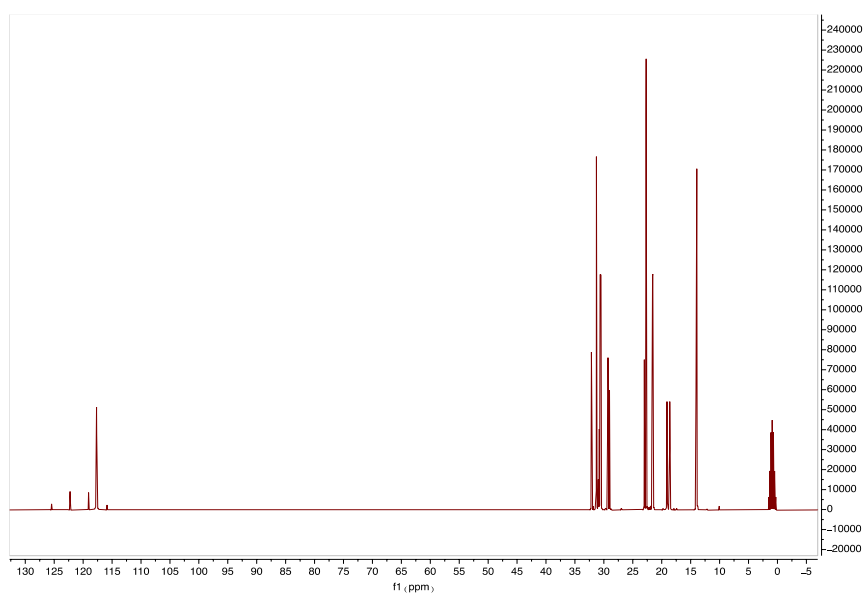


**Figure S4.27.**  $^{13}\text{C}$  NMR spectrum (acetonitrile- $d_3$ , 100.56 MHz, 301.1 K) of [P<sub>666,8</sub>][TFSI].

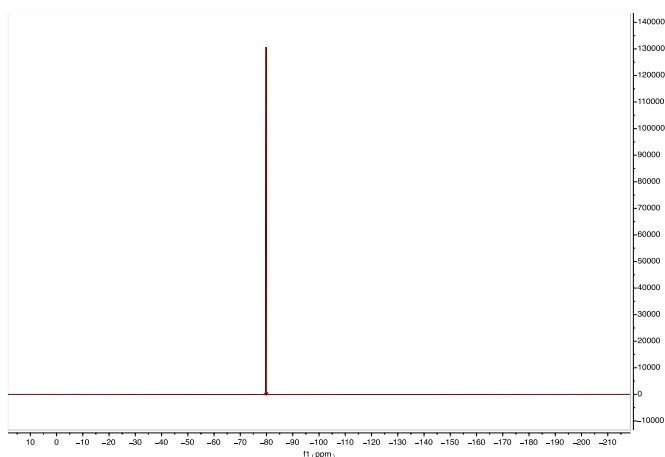


**Figure S4.28.**  $^{19}\text{F}$  NMR spectrum (acetonitrile- $d_3$ , 376.29 MHz, 300.2 K) of  $[\text{P}_{666,8}][\text{TFSI}]$ .

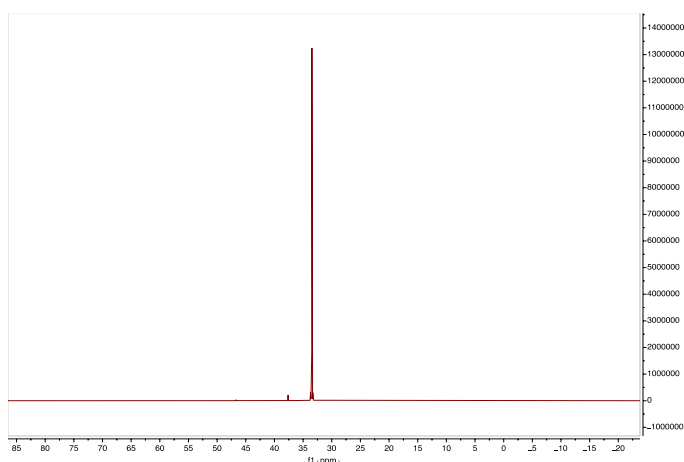


**Figure S4.29**  $^{31}\text{P}$  NMR spectrum (acetonitrile- $d_3$ , 161.89 MHz, 300 K) of  $[\text{P}_{666,8}][\text{TFSI}]$ .

**$[\text{P}_{666,12}]\text{Cl}$ .** Trihexylphosphine (1.000 mol eq.) and 1-chlorododecane ( $\text{C}_{12}\text{H}_{25}\text{Cl}$ ) (1.100 mol eq.) were placed in a round-bottomed flask ( $50\text{ cm}^3$ ). The mixture was stirred and heated under a reflux condenser connected to a Schlenk line flushed with dinitrogen (16h, 418.15 K). In order to remove the excess of starting  $\text{C}_{12}\text{H}_{25}\text{Cl}$ , the purification step involved dissolution of the product in hexane, followed by extraction with water. The product was dried at *in vacuo* (48 h, 338.15 K).  $^1\text{H}$ ,  $^{13}\text{C}$ , and  $^{31}\text{P}$  NMR spectra of the IL were recorded in acetonitrile- $d_3$ .

$^1\text{H}$  NMR:  $\delta$ : 0.86 (m, 12H), 1.24 (m, 28H), 1.38 (m, 8H), 1.58 (m, 8H), 2.27 (m, 8H).

$^{13}\text{C}$  NMR:  $\delta$ : 14.25 (P-( $\text{CH}_2$ ) $_5$ - $\text{CH}_3$ ), 14.36 (P-( $\text{CH}_2$ ) $_{11}$ - $\text{CH}_3$ ), 19.34 (d,  $^1\text{J}_{\text{C-P}} = 47.26\text{ Hz}$ ) (P- $\text{CH}_2$ -( $\text{CH}_2$ ) $_4$ - $\text{CH}_3$  and P- $\text{CH}_2$ -( $\text{CH}_2$ ) $_{10}$ - $\text{CH}_3$ ), 22.01 (d,  $^2\text{J}_{\text{C-P}} = 5.03\text{ Hz}$ ) (P- $\text{CH}_2$ - $\text{CH}_2$ -( $\text{CH}_2$ ) $_3$ - $\text{CH}_3$  and P- $\text{CH}_2$ - $\text{CH}_2$ -( $\text{CH}_2$ ) $_9$ - $\text{CH}_3$ ), 22.95 (P-( $\text{CH}_2$ ) $_4$ - $\text{CH}_2$ - $\text{CH}_3$ ), 23.28 (P-( $\text{CH}_2$ ) $_{10}$ - $\text{CH}_2$ - $\text{CH}_3$ ), 29.40 (P-( $\text{CH}_2$ ) $_9$ - $\text{CH}_2$ - $\text{CH}_2$ - $\text{CH}_3$ ), 29.90 (P-( $\text{CH}_2$ ) $_8$ - $\text{CH}_2$ -( $\text{CH}_2$ ) $_2$ - $\text{CH}_3$ ), 29.97 (P-( $\text{CH}_2$ ) $_7$ - $\text{CH}_2$ -( $\text{CH}_2$ ) $_3$ - $\text{CH}_3$ ), 30.18 (P-( $\text{CH}_2$ ) $_6$ - $\text{CH}_2$ -( $\text{CH}_2$ ) $_4$ - $\text{CH}_3$ ), 30.24 (P-( $\text{CH}_2$ ) $_5$ - $\text{CH}_2$ -( $\text{CH}_2$ ) $_5$ - $\text{CH}_3$ ), 30.27 (P-( $\text{CH}_2$ ) $_4$ - $\text{CH}_2$ -( $\text{CH}_2$ ) $_6$ - $\text{CH}_3$ ), 30.98 (d,  $^3\text{J}_{\text{C-P}} = 15.08\text{ Hz}$ ) (P-( $\text{CH}_2$ ) $_2$ - $\text{CH}_2$ -( $\text{CH}_2$ ) $_8$ - $\text{CH}_3$ ), 31.26 (d,  $^3\text{J}_{\text{C-P}} = 15.08\text{ Hz}$ ) (P-( $\text{CH}_2$ ) $_2$ - $\text{CH}_2$ -( $\text{CH}_2$ ) $_2$ - $\text{CH}_3$ ), 31.61 (P-( $\text{CH}_2$ ) $_3$ - $\text{CH}_2$ - $\text{CH}_2$ - $\text{CH}_3$ ), 32.53 (P-( $\text{CH}_2$ ) $_3$ - $\text{CH}_2$ -( $\text{CH}_2$ ) $_7$ - $\text{CH}_3$ ).

$^3\text{P}\{^1\text{H}\}$  NMR:  $\delta$ : 33.29

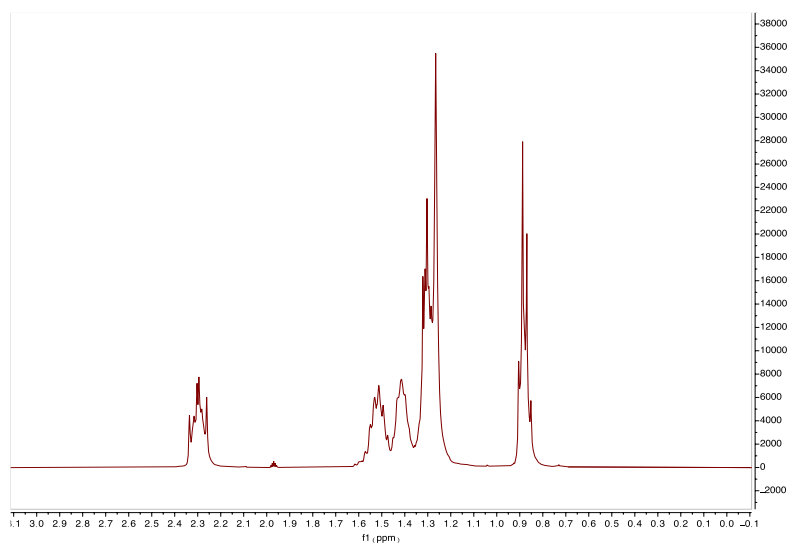


**Figure S4.30.**  $^1\text{H}$  NMR spectrum (acetonitrile- $d_3$ , 399.91 MHz, 299.9 K) of  $[\text{P}_{666,12}]\text{Cl}$ .

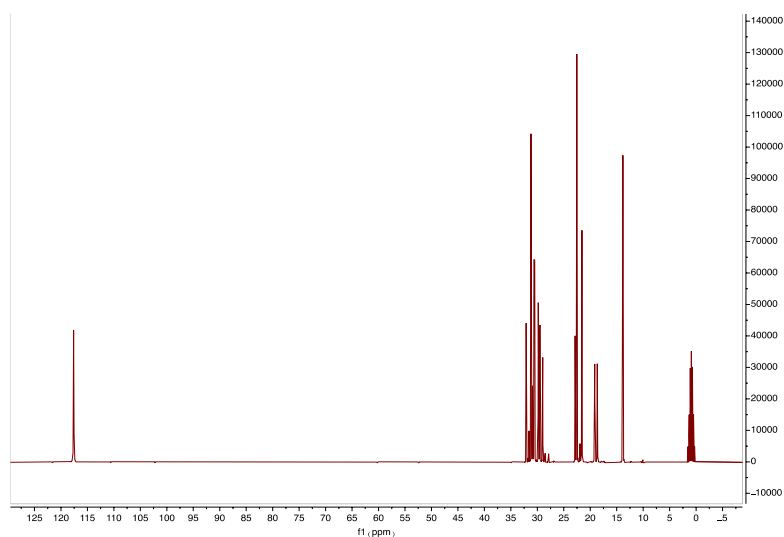


**Figure S4.31.**  $^{13}\text{C}$  NMR spectrum (acetonitrile- $d_3$ , 100.55 MHz, 301.2 K) of  $[\text{P}_{666,12}]\text{Cl}$ .

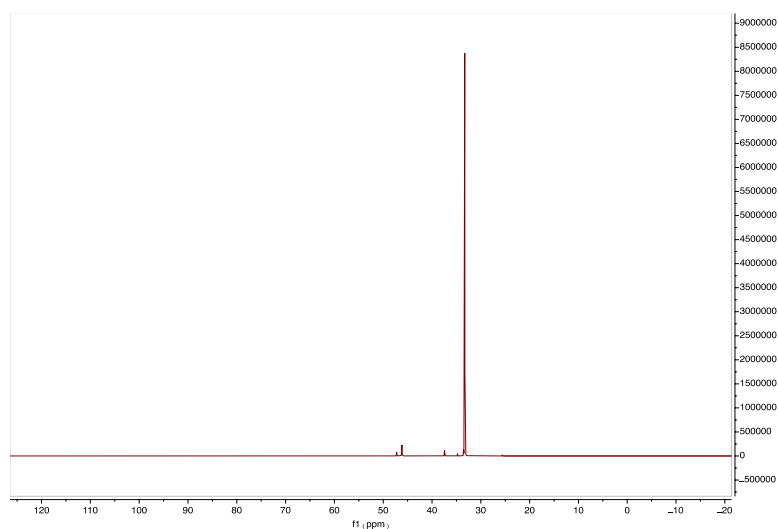


**Figure S4.32.**  $^{31}\text{P}$  NMR spectrum (acetonitrile- $d_3$ , 161.89 MHz, 300 K) of  $[\text{P}_{666,12}]\text{Cl}$ .

**[P<sub>666,12</sub>][TFSI]**. Trihexyl(dodecyl)phosphonium chloride, [P<sub>666,12</sub>]Cl (0.008 mol eq.) and lithium bis(trifluoromethanesulfonyl)imide Li[TFSI] (0.011 mol eq.) were separately dissolved in 25 cm<sup>3</sup> deionised water (18.2 MΩ.cm) (total 50 cm<sup>3</sup>) and then combined in a round-bottomed flask (250 cm<sup>3</sup>), resulting in the formation of a biphasic liquid system; the mixture was left to react (1 h, room temperature, 600 rpm). The aqueous layer was separated, and the organic layer was collected and washed, firstly with deionized water (18.2 MΩ.cm) (10 cm<sup>3</sup>) and then dichloromethane, DCM (10 cm<sup>3</sup>). Subsequent washes were performed with solution of Li[TFSI] in deionised water (18.2 MΩ.cm). Final three washes were performed with deionised water (18.2 MΩ.cm). The organic layer was washed 10 times in total. Subsequently, DCM was removed *via* rotary evaporation (30 min, 308.15 K) and the ionic liquid was dried under high vacuum (12h, 343.15 K, 10<sup>-2</sup> mbar). XRF analysis confirmed chloride content was below the detectable limit. <sup>1</sup>H, <sup>13</sup>C, <sup>19</sup>F and <sup>31</sup>P NMR spectra of the IL were recorded in acetonitrile-*d*<sub>3</sub>.

<sup>1</sup>H NMR: δ: 0.91 (m, 12H), 1.29 (m, 28H), 1.43 (m, 16H), 2.05 (m, 8H).

<sup>13</sup>C NMR: δ: (TFSI peaks 125.82, 122.63, 119.43, 116.24 (q, <sup>1</sup>J<sub>C-F</sub> = 320.79 Hz), 14.31 (P-(CH<sub>2</sub>)<sub>5</sub>-CH<sub>3</sub>), 14.48 (P-(CH<sub>2</sub>)<sub>11</sub>-CH<sub>3</sub>), 19.23 (d, <sup>1</sup>J<sub>C-P</sub> = 48.27 Hz) (P-CH<sub>2</sub>-(CH<sub>2</sub>)<sub>4</sub>-CH<sub>3</sub> and P-CH<sub>2</sub>-(CH<sub>2</sub>)<sub>10</sub>-CH<sub>3</sub>), 21.94 (d, <sup>2</sup>J<sub>C-P</sub> = 4.02 Hz) (P-CH<sub>2</sub>-CH<sub>2</sub>-(CH<sub>2</sub>)<sub>3</sub>-CH<sub>3</sub> and P-CH<sub>2</sub>-CH<sub>2</sub>-(CH<sub>2</sub>)<sub>9</sub>-CH<sub>3</sub>), 23.07 (P-(CH<sub>2</sub>)<sub>4</sub>-CH<sub>2</sub>-CH<sub>3</sub>), 23.25 (P-(CH<sub>2</sub>)<sub>10</sub>-CH<sub>2</sub>-CH<sub>3</sub>), 23.46 (P-(CH<sub>2</sub>)<sub>9</sub>-CH<sub>2</sub>-CH<sub>2</sub>-CH<sub>3</sub>), 29.43 (P-(CH<sub>2</sub>)<sub>8</sub>-CH<sub>2</sub>-(CH<sub>2</sub>)<sub>2</sub>-CH<sub>3</sub>), 29.98 (P-(CH<sub>2</sub>)<sub>7</sub>-CH<sub>2</sub>-(CH<sub>2</sub>)<sub>3</sub>-CH<sub>3</sub>), 30.15 (P-(CH<sub>2</sub>)<sub>6</sub>-CH<sub>2</sub>-(CH<sub>2</sub>)<sub>4</sub>-CH<sub>3</sub>), 30.30 (P-(CH<sub>2</sub>)<sub>5</sub>-CH<sub>2</sub>-(CH<sub>2</sub>)<sub>5</sub>-CH<sub>3</sub>), 30.41 (P-(CH<sub>2</sub>)<sub>4</sub>-CH<sub>2</sub>-(CH<sub>2</sub>)<sub>6</sub>-CH<sub>3</sub>), 30.98 (d, <sup>3</sup>J<sub>C-P</sub> = 15.08 Hz) (P-(CH<sub>2</sub>)<sub>2</sub>-CH<sub>2</sub>-(CH<sub>2</sub>)<sub>8</sub>-CH<sub>3</sub>), 31.23 (d, <sup>3</sup>J<sub>C-P</sub> = 15.08 Hz) (P-(CH<sub>2</sub>)<sub>2</sub>-CH<sub>2</sub>-(CH<sub>2</sub>)<sub>2</sub>-CH<sub>3</sub>), 31.68 (P-(CH<sub>2</sub>)<sub>3</sub>-CH<sub>2</sub>-CH<sub>2</sub>-CH<sub>3</sub>), 32.72 (P-(CH<sub>2</sub>)<sub>3</sub>-CH<sub>2</sub>-(CH<sub>2</sub>)<sub>7</sub>-CH<sub>3</sub>).

<sup>19</sup>F NMR: δ: -79.98

<sup>31</sup>P{<sup>1</sup>H} NMR: δ: 33.52

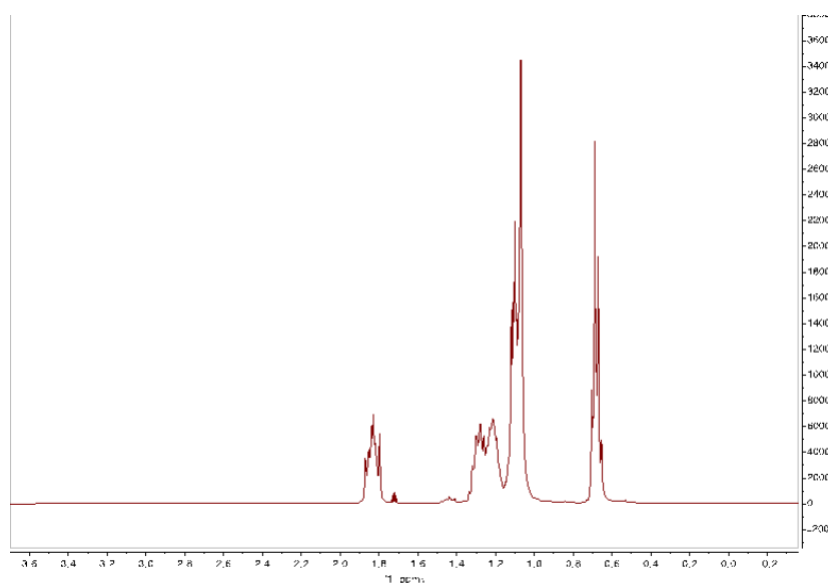


**Figure S4.33.** <sup>1</sup>H NMR spectrum (acetonitrile-*d*<sub>3</sub>, 399.91 MHz, 300 K) of [P<sub>666,12</sub>][TFSI].

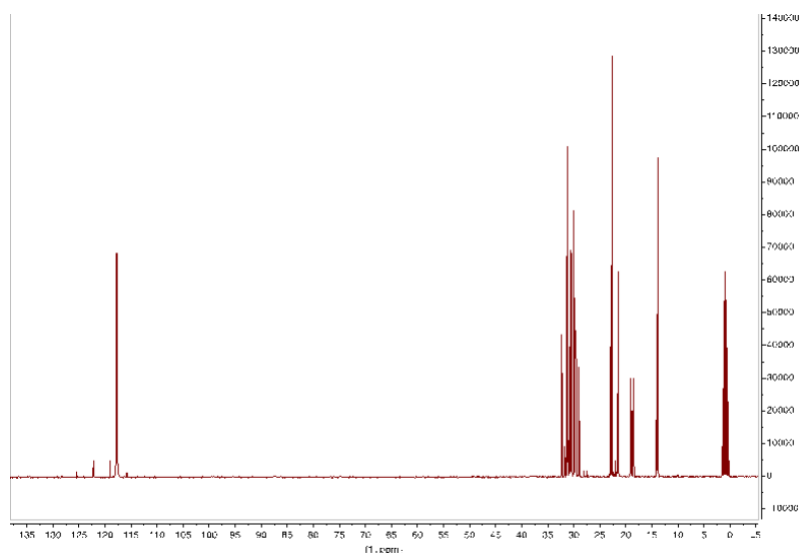


**Figure S4.34.**  $^{13}\text{C}$  NMR spectrum (acetonitrile- $d_3$ , 100.56 MHz, 300.4 K) of  $[\text{P}_{666,12}][\text{TFSI}]$ .

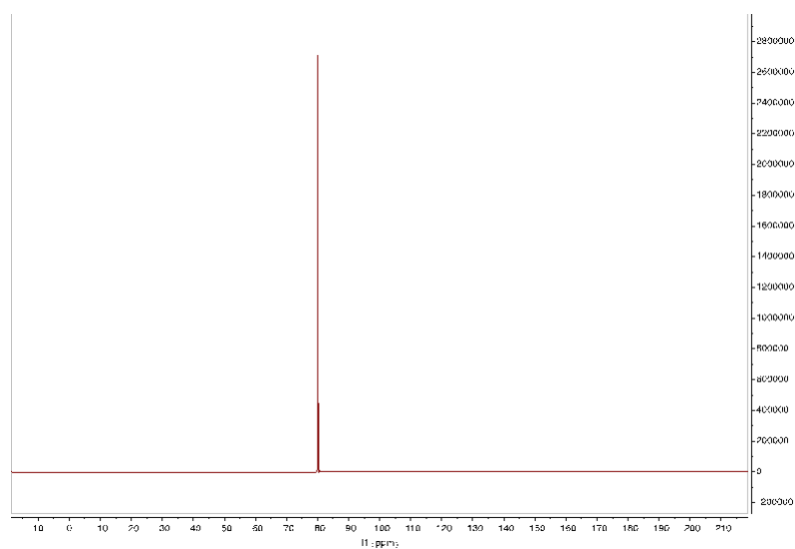


**Figure S4.35.**  $^{19}\text{F}$  NMR spectrum (acetonitrile- $d_3$ , 376.29 MHz, 299.7 K) of  $[\text{P}_{666,12}][\text{TFSI}]$ .

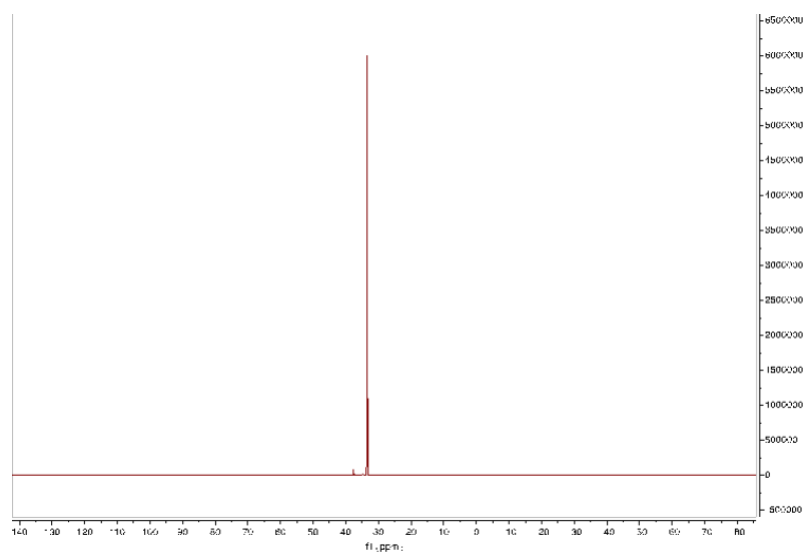


**Figure S4.36.**  $^{31}\text{P}$  NMR spectrum (acetonitrile- $d_3$ , 161.89 MHz, 302.4 K) of  $[\text{P}_{666,12}][\text{TFSI}]$ .

**Table S4.2.** CHNS analysis of synthesized ionic liquids

	C / %		H / %		N / %		S / %	
	calc.	exp.	calc.	exp.	calc.	exp.	calc.	exp.
[P <sub>444,14</sub> ]Cl	71.76	68.00	12.97	13.63	-	-	-	-
[P <sub>444,14</sub> ][TFSI]	49.47	51.36	8.30	9.25	2.06	1.82	9.43	9.94
[P <sub>666,2</sub> ][TFSI]	44.36	44.76	7.45	7.32	2.35	2.21	10.76	10.98
[P <sub>666,6</sub> ]Cl	70.81	68.50	12.88	13.36	-	-	-	-
[P <sub>666,6</sub> ][TFSI]	47.91	48.66	8.04	8.89	2.19	1.89	9.84	10.09
[P <sub>666,8</sub> ][TFSI]	49.47	50.00	8.30	8.70	2.06	1.83	9.43	9.61
[P <sub>666,12</sub> ]Cl	73.35	71.66	13.13	11.68	-	-	-	-
[P <sub>666,12</sub> ][TFSI]	52.22	52.91	8.76	9.80	1.90	1.53	8.71	8.64

**Table S4.3.** Identification of anions and cations by electrospray ionization mass spectrometry in both positive and negative modes.

	ES <sup>+</sup> <sub>t</sub>	ES <sup>+</sup> <sub>exp</sub>	ES <sup>-</sup> <sub>t</sub>	ES <sup>-</sup> <sub>exp</sub>
[P <sub>444,14</sub> ]Cl	399.4115	399.3885	-	
[P <sub>444,14</sub> ][TFSI]	399.4115	400.3982	279.9178	279.9012
[P <sub>666,2</sub> ][TFSI]	315.3176	316.2943	279.9178	279.9164
[P <sub>666,6</sub> ]Cl	371.3802	372.8089	-	-
[P <sub>666,6</sub> ][TFSI]	371.3802	371.3311	279.9178	279.9160
[P <sub>666,8</sub> ][TFSI]	399.4115	400.3738	279.9178	281.9225
[P <sub>666,12</sub> ]Cl	455.4741	456.4358	-	-
[P <sub>666,12</sub> ][TFSI]	455.4741	456.4536	279.9178	281.9193

## 4.5 Reference

- [1] P. Walden, *Bull. Acad. Imper. Sci. (St. Petersburg)* **1800**, 405-422 (1914).
- [2] M. Armand, F. Endres, D. R. MacFarlane, H. Ohno, and B. Scrosati, *Nat. Mater* **8**, 621 (2009).
- [3] C. A. Angell, W. Xu, M. Yoshizawa-Fujita, A. Hayashi, J.-P. Belieres, P. Lucas., M. Videa, Z.-F. Zhao, K. Ueno, Y. Ansari, J. Thomson, and D. Gervasio, in *Electrochemical Aspects of Ionic Liquids* (John Wiley & Sons, Ltd, **2011**), pp. 5–31.
- [4] P. Simon and Y. Gogotsi, *Nat. Mater* **7**, 845 (2008).
- [5] D. R. MacFarlane, M. Forsyth, P. C. Howlett, M. Kar, S. Passerini, J. M. Pringle, H. Ohno, M. Watanabe, F. Yan, W. Zheng, S. Zhang, and J. Zhang, *Nat. Rev. Mater* **1**, 1 (2016).

- [6] R. Patel, M. Kumari, and A. B. Khan, *Appl. Biochem. Biotechnol.* **172**, 3701 (2014).
- [7] C. A. Angell, *Science* **267**, 1924 (1995).
- [8] M. Y. Ivanov, N. V. Surovtsev, and M. V. Fedin, *Russ. Chem. Rev.* **91**, RCR5031 (2022).
- [9] C. Calahoo and L. Wondraczek, *J. Non. Cryst. Solids*, X **8**, 100054 (2020).
- [10] M. Musiał, S. Cheng, Z. Wojnarowska, and M. Paluch, *J. Phys. Chem. B* **125**, 4141 (2021).
- [11] T. Erdmenger, J. Vitz, F. Wiesbrock, and U. S. Schubert, *J. Mat. Chem.* **18**, 5267 (2008).
- [12] I. Abdurrokhman, K. Elamin, O. Danyliv, M. Hasani, J. Swenson, and A. Martinelli, *J. Phys. Chem. B* **123**, 4044 (2019).
- [13] H. Tokuda, K. Hayamizu, K. Ishii, Md. A. B. H. Susan, and M. Watanabe, *J. Phys. Chem. B* **109**, 6103 (2005).
- [14] M. Musiał, S. Cheng, Z. Wojnarowska, B. Yao, K. Jurkiewicz, and M. Paluch, *Soft Matter* **16**, 9479 (2020).
- [15] O. Russina, F. Lo Celso, N. Plechkova, C. J. Jafta, G. B. Appetecchi, and A. Triolo, *Top. Curr. Chem. (Z)* **375**, 58 (2017).
- [16] Y. Ke, W. Jin, Q. Yang, X. Suo, Y. Yang, Q. Ren, and H. Xing, *ACS Sustainable Chem. Eng.* **6**, 8983 (2018).
- [17] J. Qian, X. Liu, R. Yan, C. Li, X. Zhang, and S. Zhang, *Ind. Eng. Chem. Res.* **57**, 7633 (2018).
- [18] J. C. Araque, J. J. Hettige, and C. J. Margulis, *J. Phys. Chem. B* **119**, 12727 (2015).
- [19] Y.-L. Wang, B. Li, S. Sarman, F. Mocci, Z.-Y. Lu, J. Yuan, A. Laaksonen, and M. D. Fayer, *Chem. Rev.* **120**, 5798 (2020).
- [20] R. Hayes, G. G. Warr, and R. Atkin, *Chem. Rev.* **115**, 6357 (2015).
- [21] M. A. Harris, T. Kinsey, D. V. Wagle, G. A. Baker, and J. Sangoro, *Proc. Natl. Acad. Sci.* **118**, e2020878118 (2021).
- [22] Z. Wojnarowska, S. Cheng, B. Yao, M. Swadzba-Kwasny, S. McLaughlin, A. McGrogan, Y. Delavoux, and M. Paluch, *Nat. Commun.* **13**, 1342 (2022).
- [23] C. A. Angell, *Science* **319**, 582 (2008).
- [24] K. Ito, C. T. Moynihan, and C. A. Angell, *Nature* **398**, 492 (1999).
- [25] H. Tanaka, *Phys. Rev. E* **62**, 6968 (2000).
- [26] S. Sastry and C. Austen Angell, *Nat. Mater* **2**, 739 (2003).
- [27] H. Tanaka, R. Kurita, and H. Mataka, *Phys. Rev. Lett.* **92**, 025701 (2004).
- [28] M. Kobayashi and H. Tanaka, *Nat. Commun.* **7**, 13438 (2016).
- [29] Y. Suzuki, *Proc. Natl. Acad. Sci.* **119**, e2113411119 (2022).
- [30] S. Wei, F. Yang, J. Bednarcik, I. Kaban, O. Shuleshova, A. Meyer, and R. Busch, *Nat. Commun.* **4**, 2083 (2013).

- [31] T. Cosby, Z. Vicars, M. Heres, K. Tsunashima, and J. Sangoro, *J. Chem. Phys.* **148**, 193815 (2018).
- [32] V. Bocharova, N. Jayakody, J. Yang, R. L. Sacci, W. Yang, S. Cheng, B. Doughty, S. Greenbaum, S. P. Jeong, I. Popov, S. Zhao, C. Gainaru, and Z. Wojnarowska, *ACS Appl. Mater. Interfaces* **12**, 31842 (2020).
- [33] Z. Wojnarowska, H. Feng, M. Diaz, A. Ortiz, I. Ortiz, J. Knapik-Kowalczyk, M. Vilas, P. Verdía, E. Tojo, T. Saito, E. W. Stacy, N.-G. Kang, J. W. Mays, D. Kruk, P. Wlodarczyk, A. P. Sokolov, V. Bocharova, and M. Paluch, *Chem. Mater.* **29**, 8082 (2017).
- [34] S. Cheng, Z. Wojnarowska, J. Sangoro, and M. Paluch, *Phys. Rev. E* **105**, 054502 (2022).
- [35] E. Donth, *J. Non. Cryst. Solids* **53**, 325 (1982).
- [36] E.-J. Donth, *The Glass Transition: Relaxation Dynamics in Liquids and Disordered Materials*, Vol. 48 (Springer Berlin Heidelberg, Berlin, Heidelberg, **2001**).
- [37] G. Floudas, M. Paluch, A. Grzybowski, and K. Ngai, *Molecular Dynamics of Glass-Forming Systems*, Vol. 1 (Springer Berlin Heidelberg, Berlin, Heidelberg, **2011**).
- [38] S. Li, G. K. Rothsopf, B. R. Sohnlein, and D.-S. Yang, *J. Phys. Chem. A* **106**, 6941 (2002).
- [39] S. Corsetti, T. Rabl, D. McGloin, and J. Kiefer, *Phys. Chem. Chem. Phys.* **19**, 13941 (2017).
- [40] C. J. Orendorff, M. W. Jr. Ducey, and J. E. Pemberton, *J. Phys. Chem. A* **106**, 6991 (2002).
- [41] M. Herstedt, M. Smirnov, P. Johansson, M. Chami, J. Grondin, L. Servant, and J. C. Lassègues, *J. Raman Spectrosc.* **36**, 762 (2005).

# 5 Pressure-Induced Liquid-Liquid Transition in a Family of Ionic Materials



ARTICLE



<https://doi.org/10.1038/s41467-022-29021-0>

OPEN

## Pressure-induced liquid-liquid transition in a family of ionic materials

Zaneta Wojnarowska <sup>1✉</sup>, Shinian Cheng <sup>1,2</sup>, Beibei Yao <sup>1</sup>, Malgorzata Swadzba-Kwasny <sup>3</sup>, Shannon McLaughlin <sup>3</sup>, Anne McGrogan <sup>3</sup>, Yoan Delavoux <sup>3</sup> & Marian Paluch <sup>1</sup>

Liquid–liquid transition (LLT) between two disordered phases of single-component material remains one of the most intriguing physical phenomena. Here, we report a first-order LLT in a series of ionic liquids containing trihexyl(tetradecyl)phosphonium cation  $[P_{666,14}]^+$  and anions of different sizes and shapes, providing an insight into the structure-property relationships governing LLT. In addition to calorimetric proof of LLT, we report that ion dynamics exhibit anomalous behavior during the LLT, i.e., the conductivity relaxation times ( $\tau_\sigma$ ) are dramatically elongated, and their distribution becomes broader. This peculiar behavior is induced by isobaric cooling and isothermal compression, with the  $\tau_\sigma(T_{LL}, P_{LL})$  constant for a given system. The latter observation proves that LLT, in analogy to liquid-glass transition, has an isochronal character. Finally, the magnitude of discontinuity in a specific volume at LLT was estimated using the Clausius-Clapeyron equation.

---

Reprinted with permission from Nature Communications volume 13, Article number: 1342 (2022)

<https://doi.org/10.1038/s41467-022-29021-0> Copyright © 2022, The Author(s). Published by Nature Communications

## Author Declaration:

“Pressure-induced liquid-liquid transition in a family of ionic materials,” *Nat. Commun.*, 13,1342 (2022)

B. Yao planned and carried out the experimental work, analyzed the data, prepared figures, and co-wrote the manuscript.

Signature: 

S. Cheng planned and carried out the experimental work, analyzed the dielectric data, and prepared the figures.

Signature: 

S. McLaughlin characterized and synthesized the ionic liquids.

Signature: 

A. McGrogan characterized and synthesized the ionic liquids.

Signature: 

Y. Delavoux characterized and synthesized the ionic liquids.

Signature: 

M. Swadzba-Kwasny supervised the characterization and synthesis of ionic liquids.

Signature: 

Z. Wojnarowska conceived the project, prepared figures, and co-wrote the manuscript.

Signature: 

M. Paluch supervised the project.

Signature: 

## 5.1 Abstract

Liquid–liquid transition (LLT) between two disordered phases of single-component material remains one of the most intriguing physical phenomena. Here, we report a first-order LLT in a series of ionic liquids containing trihexyl(tetradecyl)phosphonium cation  $[P_{666,14}]^+$  and anions of different sizes and shapes, providing an insight into the structure-property relationships governing LLT. In addition to calorimetric proof of LLT, we report that ion dynamics exhibit anomalous behavior during the LLT, i.e., the conductivity relaxation times ( $\tau_\sigma$ ) are dramatically elongated, and their distribution becomes broader. This peculiar behavior is induced by isobaric cooling and isothermal compression, with the  $\tau_\sigma(T_{LL}, P_{LL})$  constant for a given system. The latter observation proves that LLT, in analogy to liquid-glass transition, has an isochronal character. Finally, the magnitude of discontinuity in a specific volume at LLT was estimated using the Clausius-Clapeyron equation.

## 5.2 Introduction

When isotropic liquid is cooled below the melting point, it either solidifies into a crystal or enters into a metastable supercooled state, which then enters a non-equilibrium amorphous phase at the glass transition temperature  $T_g$  [1]. The characteristic feature of the latter transformation is a continuous increase of density, accompanied by a slowing down of molecular dynamics and enormous elongation of structural relaxation times: from the time scale of picoseconds at  $T_m$  up to hundreds of seconds in the vicinity of  $T_g$  [2]. If cooled rapidly enough, nearly all materials can be transformed into an amorphous form. Thus, the glass-forming ability can be considered as a universal property of condensed matter.

Over the years, such a well-established physical picture of the liquid state has been upended by numerous examples of two distinct liquid phases in single-component materials. The first-order liquid-liquid transition (LLT), separating fluids of different local structures, density, magnetic susceptibility and thermodynamic properties, has been reported for various systems, including atomic elements (sulfur, phosphorus [3], silicon [4],[5], carbon [6] and strongly interacting liquids [7], such as molten oxides [8],[9], e.g.,  $Al_2O_3$ - $Y_2O_3$  [10]. Only four molecular liquids (water [11],[12], triphenyl phosphite (TPP) [13],[14],[15], n-butanol [16], and D-mannitol [17] have been found with compelling evidence for LLT. Nevertheless, the LLT in these systems remains controversial since it occurs in the supercooled state capable of cold crystallization [18]. The theoretical and experimental observations show that a first-order LLT can occur without a noticeable density change, making this phenomenon even more puzzling [19]. Furthermore,

magnetic fields can affect the local structure and lead to another liquid phase [20]. It was reported that an aligned liquid state of Co alloys can be transformed into another liquid phase under magnetic fields [21],[22]. At the same time, except for a few cases [6],[7],[23],[24] not much is known about the effect of molecular packing on LLT. Consequently, it has not been clarified how universal the LLT is and what is the critical factor inducing such a transition. Since it has been difficult to identify other examples of LLT in a systematic fashion, the experimental verification of these problems poses a great challenge.

Aprotic ionic liquids (AILs)—a class of glass-formers composed solely of ions [25], give a unique opportunity to investigate the universality of LLT. The most interesting feature of AILs is that their structural and transport properties can be finely tuned within a wide range by the combination of different positively and negatively charged ions [26]. Thereby, a vast structural diversity of ionic species and various types of competing intermolecular interactions (van der Waals, H-bonding and Coulomb forces), make AILs excellent materials to probe the mechanism underpinning LLT. Furthermore, several previous studies show unique ordering behavior of ionic liquid, namely formation of nanoscale domains of polar and nonpolar groups [27],[28],[29], that potentially can lead to LLT. However, over the years there was no proof of LLT in ILs capable for domains formation. The first report on LLT in ionic liquid has been provided very recently by Harris et al. for an AIL with a tetra(alkyl)phosphonium cation [30]. At a specific temperature, trihexyl(tetradecyl)phosphonium borohydride, noted as [P<sub>666,14</sub>][BH<sub>4</sub>], was found to undergo enhanced ordering of the alkyl chains in the nonpolar domains. Such a structural reorganization coincides well with the first-order thermodynamic transition, visible in calorimetric, XRD and IR spectroscopy data.

Motivated by this work, we embarked on a quest to identify not an isolated example but a systematically studied family of compounds that would exhibit LLTs, thereby gaining an insight into the structure-property relationships governing the LLT formation. Furthermore, by monitoring the relaxation dynamics of selected AILs under high-pressure conditions, we addressed the long-standing questions regarding the effect of compression on LLT and density fluctuations at  $T_{LL}$ .

We designed six AILs based on the [P<sub>666,14</sub>]<sup>+</sup> cation, combined with six different anions (chemical structures shown in Fig. 5.1). The [P<sub>666,14</sub>][BH<sub>4</sub>] was also examined as a reference. The commonly used phosphonium cation imparted the AILs a relatively high thermal and electrochemical stability, as well as decent ionic conductivity and apolar/polar solvation ability [31]. Anions have been selected to reflect differences in size, geometry, conformational flexibility and coordinating ability (i.e., Lewis basicity). The linear thiocyanate, [SCN]<sup>-</sup>, trigonal planar tricyanomethanide, [TCM]<sup>-</sup> and tetrahedral

tetrafluoroborate  $[\text{BF}_4]^-$  are all rigid due to their small size. The larger anions include a bulky and rigid bis(oxalate)borate  $[\text{BOB}]^-$ , with distorted tetrahedral symmetry around the central boron atom, the bis(trifluoro-methanesulfon)imide,  $[\text{TFSI}]^-$  that is known to assume cis and trans conformations, and taurine,  $[\text{TAU}]^-$ , featuring a flexible alkyl chain allowing for multiple conformations. The basicity of an anion that is—its ability to donate an electron pair can be quantified by Gutmann Donor Number (DN) [32]. On this scale,  $[\text{TFSI}]^-$  is a very weak donor,  $[\text{TCM}]^-$  is slightly stronger, whereas  $[\text{SCN}]^-$  is a moderately strong donor (Table 5.1). DN for  $[\text{BOB}]^-$  and  $[\text{TAU}]^-$  have not been measured, but  $[\text{BOB}]^-$  is reported to be a very weak donor, and  $[\text{TAU}]^-$  has an amine functionality, which by definition imparts its high propensity to share an electron pair (high DN).

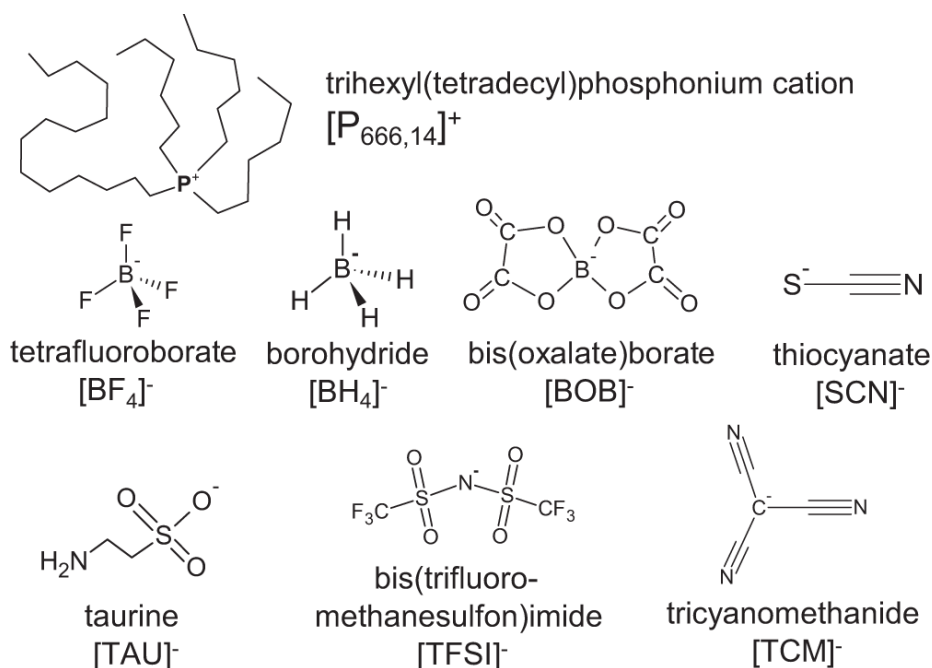


**Fig. 5.1** Chemical structures of studied ILs. Seven ionic liquids have been used in this study, containing the trihexyl(tetradecyl)phosphonium cation  $[\text{P}_{666,14}]^+$  and anions: tetrafluoroborate  $[\text{BF}_4]^-$ , borohydride  $[\text{BH}_4]^-$ , bis(oxalate)borate  $[\text{BOB}]^-$ , thiocyanate  $[\text{SCN}]^-$ , taurine  $[\text{TAU}]^-$ , bis(trifluoromethanesulfon)imide  $[\text{TFSI}]^-$ , tricyanomethanide  $[\text{TCM}]^-$ .

**Table 5.1** The thermodynamic characterization of studied systems.

Anion	$T_{LL}^c$ K	$-\Delta H_{LL}^c$ Jg <sup>-1</sup>	$T_{LL}^h$ K	$\Delta H_{LL}^h$ Jg <sup>-1</sup>	$T_g$ K	$T_{LL}^{BDS}$ K	$T_c$ K	$-\Delta H_c$ Jg <sup>-1</sup>	$T_m$ K	$\Delta H_m$ Jg <sup>-1</sup>	$\nu$ nm <sup>3</sup>	DN kcal mol <sup>-1</sup>
[SCN] <sup>-</sup>	212.1 <sup>*</sup>	16.6 <sup>*</sup>	207.4 <sup>*</sup>	16.6 <sup>*</sup>			231.4 <sup>*</sup>	38.0 <sup>*</sup>	270.8 <sup>*</sup>	58.2 <sup>*</sup>		
	211.6 <sup>**</sup>	14.9	206.2	15.1	197.7 <sup>a</sup>		234.2	39.2	267.4	57.0	0.0405	45.9
	213.0 <sup>***</sup>	12.9	207.5	13.2	199.1 <sup>b</sup>	210.3	251.9	9.51	273.0	18.1	0.048 <sup>c</sup>	
	213.3	11.4	207.1	11.6			254.3	1.9	272.3	5.0		
	213.8 <sup>*</sup>	8.5 <sup>*</sup>	206.0 <sup>*</sup>	8.3 <sup>*</sup>			222.5 <sup>*</sup>	51.1 <sup>*</sup>	270.7 <sup>*</sup>	82.5 <sup>*</sup>		
[BH4] <sup>-</sup>	214.6 <sup>**</sup>	6.4 <sup>**</sup>	206.8 <sup>**</sup>	6.7 <sup>**</sup>	198.5 <sup>a</sup>		232.7 <sup>**</sup>	59.6 <sup>**</sup>	271.1 <sup>**</sup>	77.4 <sup>**</sup>	0.03	
	214.7 <sup>***</sup>	5.6 <sup>***</sup>	207.3 <sup>***</sup>	6.0 <sup>***</sup>	201.3 <sup>b</sup>	210.9	242.3 <sup>***</sup>	62.8 <sup>***</sup>	270.4 <sup>***</sup>	73.8 <sup>***</sup>	0.046 <sup>c</sup>	
	216.1	4.6	207.6	5.0			250.9	34.5	271.9	34.6		
[BF4] <sup>-</sup>	-	-	-	-	-	-	270.0 <sup>*</sup>	49.3 <sup>*</sup>	295 <sup>*</sup>	61.4 <sup>*</sup>	0.079	7.3
	206.7 <sup>*</sup>	13.1 <sup>*</sup>	203.7 <sup>*</sup>	13.1 <sup>*</sup>			229.0	21.9	295	61.7	0.07 <sup>c</sup>	
[TCM] <sup>-</sup>	206.8 <sup>**</sup>	12.3 <sup>**</sup>	204.4 <sup>**</sup>	12.0 <sup>**</sup>	197.7 <sup>a</sup>		-	-	-	-	0.121	26.1
	207.1 <sup>***</sup>	9.9 <sup>***</sup>	204.6 <sup>***</sup>	10.2 <sup>***</sup>	196.3 <sup>b</sup>	203.6	-	-	-	-	0.093 <sup>c</sup>	
	207.4	8.1	204.8	8.6			-	-	-	-		
	214.9 <sup>*</sup>	6.0 <sup>*</sup>	201.6 <sup>*</sup>	6.1 <sup>*</sup>			-	-	-	-		
[TAU] <sup>-</sup>	214.8 <sup>**</sup>	4.8 <sup>**</sup>	202.1 <sup>**</sup>	4.7 <sup>**</sup>	197.5 <sup>a</sup>		-	-	-	-		
	215.8 <sup>***</sup>	4.4 <sup>***</sup>	203.3 <sup>***</sup>	4.1 <sup>***</sup>	199.5 <sup>b</sup>	206.5	-	-	-	-	0.098 <sup>c</sup>	
	216.1	3.8	203.9	3.9			-	-	-	-		

	213.4 <sup>*</sup>	0.64 <sup>*</sup>	202.2 <sup>*</sup>	1.3 <sup>*</sup>				
[BOB] <sup>-</sup>	213.5 <sup>**</sup>	0.51 <sup>**</sup>	202.8 <sup>**</sup>	1.2 <sup>**</sup>	202.1 <sup>a</sup>			0.174
	214.5 <sup>***</sup>	0.42 <sup>***</sup>	203.7 <sup>***</sup>	1.1 <sup>***</sup>	198.4 <sup>b</sup>	-	-	0.164 <sup>c</sup>
	216.1	0.38	204.8	0.8				
	203.5 <sup>*</sup>	8.6 <sup>*</sup>	200.5 <sup>*</sup>	9.7 <sup>*</sup>				
	204.3 <sup>**</sup>	7.3 <sup>**</sup>	200.4 <sup>**</sup>	8.2 <sup>**</sup>	195.9 <sup>a</sup>			0.161
[TFSI] <sup>-</sup>	204.8 <sup>***</sup>	6.5 <sup>***</sup>	199.8 <sup>***</sup>	7.1 <sup>***</sup>	194.2 <sup>b</sup>	201.2	-	0.163 <sup>c</sup>
	205.6	5.9	200.1	6.6				11.2

$T_{LL}$  and  $\Delta H$  denote respectively the temperature and enthalpy of liquid-liquid transition determined during the cooling (c) and heating (h) scan.

An increase of  $\Delta H_{LL}$  with a decreased scanning rate indicates that phase 1 needs a certain amount of time to transfer to phase 2.

$T_g$  glass transition temperature,  $T_c$  crystallization temperature,  $T_m$  melting temperature,  $\Delta H_m$  enthalpy of melting,  $\Delta H_c$  enthalpy of crystallization,  $v$  molecular volume of anions.

<sup>a</sup>The glass transition temperature was determined from DSC measurements after 6 h aging at 183.15 K with the heating rate 10 K/min.

<sup>b</sup>The glass-transition temperature determined from BDS measurements according to definition  $T_g = T(\sigma_{dc} = 10^{-14} \text{ S/cm})$ .

<sup>\*</sup>1 K/min; <sup>\*\*</sup>2 K/min; <sup>\*\*\*</sup>5 K/min; Others: 10 K/min.

<sup>c</sup>The van der Waals volume was calculated by using the Bondi method.

## 5.3 Results and Discussion

### 5.3.1 Calorimetric Studies of Phase Transitions

To firmly establish the LLT scenario, it is desirable to show its reversibility without crystallization. For this purpose, we first analyzed the conventional differential scanning calorimetry (DSC) thermograms obtained on cooling and subsequent heating of tested materials (Fig. 5.2a). Decreasing temperature with a standard rate of  $10 \text{ K min}^{-1}$  resulted in a step-like transition for  $[\text{P}_{666,14}][\text{BOB}]$  and  $[\text{P}_{666,14}][\text{TAU}]$ , a sharp exothermic peak at 226 K for  $[\text{P}_{666,14}][\text{BF}_4]$ , and a broader exotherm of much lower enthalpy observed at 205–216 K for the other four AILs. On heating, the thermal curve for  $[\text{P}_{666,14}][\text{BOB}]$ ,  $[\text{P}_{666,14}][\text{TAU}]$ ,  $[\text{P}_{666,14}][\text{TFSI}]$ ,  $[\text{P}_{666,14}][\text{TCM}]$ ,  $[\text{P}_{666,14}][\text{SCN}]$ , and  $[\text{P}_{666,14}][\text{BH}_4]$  featured an endotherm, quite symmetrical with respect to the cooling cycles. Note that this peak is the most pronounced for  $[\text{TCM}]^-$ -based IL and the weakest for  $[\text{BOB}]^-$ -IL. Upon further heating,  $[\text{P}_{666,14}][\text{SCN}]$  and  $[\text{P}_{666,14}][\text{BH}_4]$  undergo cold crystallization and melting. An endotherm indicating the melting process of  $[\text{P}_{666,14}][\text{SCN}]$  and  $[\text{P}_{666,14}][\text{BH}_4]$  was recorded at 272 K, while  $[\text{P}_{666,14}][\text{BF}_4]$  reveals  $T_m$  at 295 K. Herein, it should be stressed that the cold crystallization of  $[\text{P}_{666,14}][\text{BH}_4]$  was not reported in ref. [30]. This indicates higher purity of material examined herein.

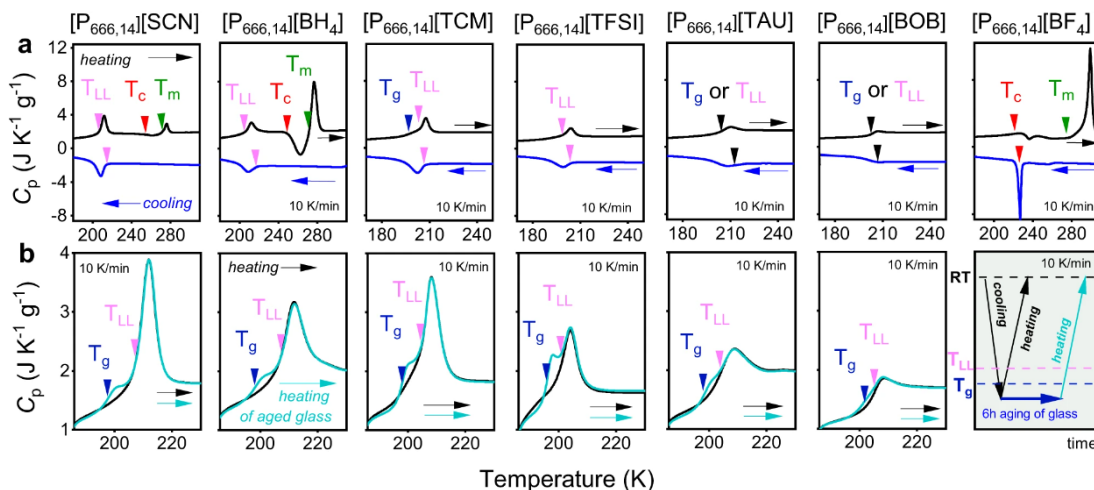


**Fig. 5.2: Differential scanning calorimetry (DSC) traces of  $[\text{P}_{666,14}]^+$ -based ILs.** **a** The DSC data collected on cooling (blue curve) and subsequent heating (black curve) with the rate of  $10 \text{ K min}^{-1}$  of  $[\text{P}_{666,14}][\text{SCN}]$ ,  $[\text{P}_{666,14}][\text{BH}_4]$ ,  $[\text{P}_{666,14}][\text{TCM}]$ ,  $[\text{P}_{666,14}][\text{TFSI}]$ ,  $[\text{P}_{666,14}][\text{TAU}]$ ,  $[\text{P}_{666,14}][\text{BOB}]$  and  $[\text{P}_{666,14}][\text{BF}_4]$  from left to right respectively. Arrows indicate the onset of: LLT (pink one), melting point (green one), cold crystallization (red one) and  $T_g$  (blue one). The values of liquid–liquid transition temperature ( $T_{LL}$ ), onset of cold crystallization ( $T_c$ ), melting temperature ( $T_m$ ) and enthalpy of these processes  $\Delta H$  are collected in Table 5.1. **b** Comparison between DSC traces obtained during the standard heating with rate  $10 \text{ K min}^{-1}$  (black curved) and after the aging process performed in the glassy state, i.e., at 183 K (turquoise curve) of  $[\text{P}_{666,14}][\text{SCN}]$ ,  $[\text{P}_{666,14}][\text{BH}_4]$ ,  $[\text{P}_{666,14}][\text{TCM}]$ ,  $[\text{P}_{666,14}][\text{TFSI}]$ ,  $[\text{P}_{666,14}][\text{TAU}]$  and  $[\text{P}_{666,14}][\text{BOB}]$  from left to right respectively. Pink arrows indicate

the onset of LLT. The jump in the specific heat capacity during the liquid–glass transition is presented as blue arrows. On the last right panel the procedure of the DSC experiment is presented.

To examine the physical nature of phase transition observed in  $[P_{666,14}]^+$ -based AILs, DSC experiments with various scanning rates have been performed. As visible in Supplementary Note 1, a slower heating rate slightly moves the step-like increase of  $C_p$  towards lower temperatures for  $[P_{666,14}][BOB]$  and  $[P_{666,14}][TAU]$ . This, together with the very small enthalpy of this process, suggests its kinetic nature and thus simple vitrification (i.e., liquid-glass transition) of mentioned ILs. On the other side of the spectrum is  $[P_{666,14}][BF_4]$ , where decreasing the scanning rate from 10 to 1 K min<sup>-1</sup> shifted the exothermic peak from 229 to 270 K, whereas the endotherm occurred at around 295 K in both cases. Thus,  $[P_{666,14}][BF_4]$  crystallizes on cooling, and  $T_c$  increases with a decrease of cooling rate, which is typical behavior. Interestingly, a slight change of anion from  $[BF_4]^-$  to  $[BH_4]^-$  provides an IL with the supercooling ability and cold crystallization observed on a subsequent heating scan. In turn, independently of the applied heating rate, a broad endotherm observed for ILs with  $[BH_4]^-$ ,  $[SCN]^-$ ,  $[TCM]^-$ , and  $[TFSI]^-$  anions appears at the same temperature for given IL ( $T \pm 1$  K), with the only difference in  $\Delta H$ , i.e., the lower the ramp rate, the higher the  $\Delta H$  value (see Table 5.1). However, even the highest obtained  $\Delta H$  is still around five times lower than the enthalpy of melting process  $\Delta H_m$  obtained, e.g., for  $[P_{666,14}][BF_4]$ . Note that phase 2 observed below the endotherm is an optically transparent homogenous disordered phase, as confirmed by microscopic observations. These findings lead to conclusion that the prominent peak observed in DSC thermograms of  $[P_{666,14}][TFSI]$ ,  $[P_{666,14}][TCM]$ , and at lower temperature ranges for  $[P_{666,14}][SCN]$ , and  $[P_{666,14}][BH_4]$  indicates the liquid–liquid phase transition (LLT). Herein, it should be mentioned that in addition to LLT, the liquid–glass transition of  $[P_{666,14}][TCM]$  is also detectable at  $T < T_{LL}$ . (see Fig. 5.2a and Supplementary Fig. S5.30). However,  $T_g$  does not appear on the thermogram of any other examined IL. Since an amorphous phase has a non-equilibrium nature, its thermodynamic and dynamic properties (e.g., the specific volume, enthalpy or relaxation dynamics) evolve over time [33]. This phenomenon, known as physical aging, is accompanied by an increase of heat capacity in the glass transition region (so-called overshoot peak) and therefore can be useful to reveal  $T_g$  of  $[P_{666,14}]^+$ -based ILs. Therefore, in the further step, aging experiments have been performed on all  $[P_{666,14}]^+$  ILs, excluding that of  $[BF_4]^-$  anion, to confirm that cooling transforms liquid 2 to the glassy state. The experimental protocol of aging involves: (i) decreasing temperature to 183 K (the  $T$  expected to fall below  $T_g$ ), (ii) time-dependent isothermal step at this  $T$ , and (iii) subsequent heating. The thermograms corresponding to the final heating scans are compared with data obtained in standard DSC measurement in Fig. 5.2b. As a result of the aging experiments, the liquid–glass transition

emerged at  $T < T_{LL}$  for 4 samples, i.e., ILs with  $[\text{BH}_4]^-$ ,  $[\text{SCN}]^-$ ,  $[\text{TCM}]^-$ , and  $[\text{TFSI}]^-$  anions. However, at the same time, for  $[\text{P}_{666,14}][\text{TAU}]$  and  $[\text{P}_{666,14}][\text{BOB}]$  there are no overshoot peaks that would confirm typical liquid–glass transition in these ILs (see Supplementary Fig. S5.31 for comparison). Instead, a slight increase of  $C_p$  is visible on the low-temperature side of the endotherm, while the  $C_p^{max}$  remains unchanged. This indicates that both  $T_g$  and  $T_{LL}$  co-exist in the close vicinity for  $[\text{P}_{666,14}][\text{TAU}]$  and  $[\text{P}_{666,14}][\text{BOB}]$ . The values of  $T_g$  determined from the heating scan of aged glass with the rate of  $10 \text{ K min}^{-1}$  and the onset points of LLT are collected in Table 5.1.

A closer inspection of the DSC results indicates that the temperature of liquid–glass transition remains constant for studied ILs while TLL decreases in the following order:  $[\text{BH}_4]^- < [\text{SCN}]^- < [\text{TCM}]^- < [\text{TAU}]^- < [\text{TFSI}]^- < [\text{BOB}]^-$  that corresponds well with decreasing basicity and increasing van der Waals volume of the anion. Noteworthy, the sign of LLT is the weakest for IL with large, rigid and non-coordinating anion  $[\text{BOB}]^-$ . Interestingly, more flexible, lower symmetry  $[\text{TFSI}]^-$  of similar size induced the well-detectable LLT. Furthermore, the small, symmetrical and non-coordinating  $[\text{BF}_4]^-$  induced crystallization, whereas for  $[\text{BH}_4]^-$  both liquid–glass and LLTs are also observed. On the other hand,  $[\text{SCN}]^-$  which is small but has lower symmetry and higher basicity than  $[\text{BF}_4]^-$ , also featured LLT and crystallization/melting behavior. Consequently, it appears that LLT is relatively easy to induce in  $[\text{P}_{666,14}]^+$ -based ILs, but certain conditions concerning size, symmetry, conformational flexibility and possibly Lewis basicity of the anions must be met. One can deduce that the  $V_{vdW} < 0.1 \text{ nm}^3$  for rigid structure and  $V_{vdW} < 0.2 \text{ nm}^3$  for flexible one is the limiting value to observe clear LLT in  $[\text{P}_{666,14}]^+$ -based ILs. Too large anions most likely complicate the ordering of the alkyl chains in the nonpolar domains and consequently prevent the LLT.

### 5.3.2 Changes in Ion Dynamics Accompanying LLT

To further advance the knowledge on LLT in  $[\text{P}_{666,14}]$ -based ILs, dielectric spectroscopy has been employed. First, the single-frequency experiments, analogous to DSC scans, have been performed for all AILs. The evolution of dielectric constant ( $\epsilon'$ ) at 1 MHz, accompanying cooling and subsequent heating of  $[\text{P}_{666,14}][\text{TFSI}]$ ,  $[\text{P}_{666,14}][\text{TCM}]$ ,  $[\text{P}_{666,14}][\text{BOB}]$ ,  $[\text{P}_{666,14}][\text{TAU}]$ ,  $[\text{P}_{666,14}][\text{SCN}]$ , and  $[\text{P}_{666,14}][\text{BF}_4]$  at  $1 \text{ K min}^{-1}$ , is illustrated in Supplementary Fig.S5.32. The  $\epsilon'(T)$  curves obtained for the  $[\text{TAU}]^-$ ,  $[\text{TFSI}]^-$  and  $[\text{TCM}]^-$  samples reveal reversible character with a step-like signature of LLT. In turn, the behavior of  $\epsilon'$  for  $[\text{P}_{666,14}][\text{BOB}]$  and  $[\text{P}_{666,14}][\text{BF}_4]$  resembles the characteristics of the liquid–glass transition and crystallization, respectively, which corresponds to calorimetric data. At the same time,  $[\text{P}_{666,14}][\text{SCN}]$  shows LLT, crystallization, and melting processes during the heating scan, which agrees with DSC results.

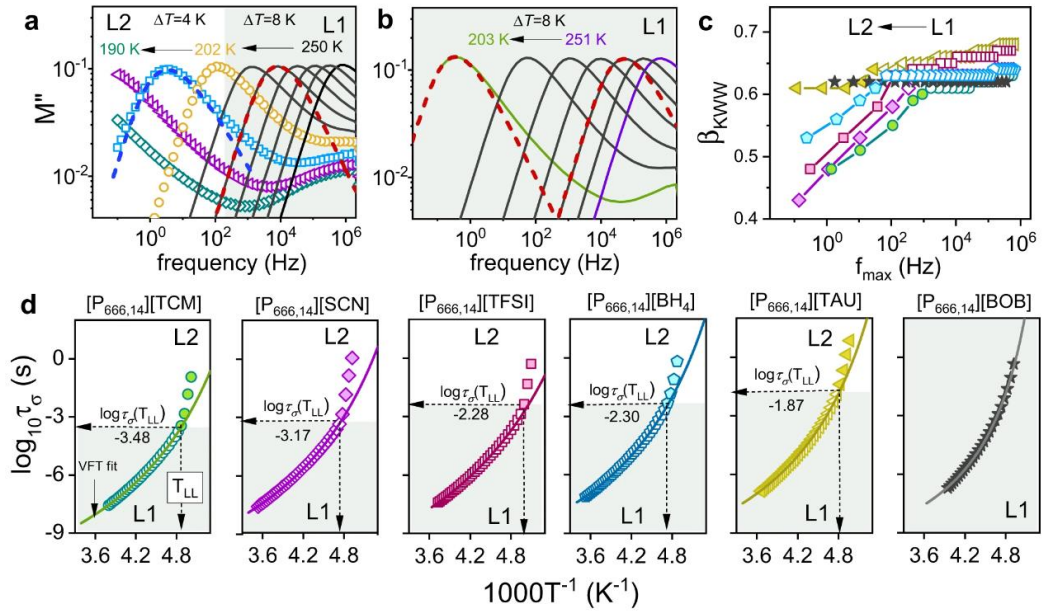


**Fig. 5.3: Dielectric response of studied ILs measured at ambient pressure conditions.** **a** The representative dielectric data of  $[P_{666,14}][TFSI]$  in liquid 1 (solid lines) and liquid 2 (scatters) phases recorded on cooling and presented in electric modulus representation. Dashed lines denote fits of KWW function to experimental data with  $\beta_{KWW} = 0.65$  (red dashed line) and 0.53 (blue dashed line), in liquid 1 and liquid 2, respectively. **b** The representative dielectric data of  $[P_{666,14}][BOB]$  measured in the supercooled liquid 1 state. Dashed lines denote fits of the KWW function with the exponent equal to 0.62. Note that the same value of  $\beta_{KWW}$  was used in the close vicinity of  $T_g$  and far from liquid–glass transition. **c** The  $\beta_{KWW}$  exponent is plotted as a function of the frequency of modulus peak maximum for all studied ILs. **d** Temperature dependence of conductivity relaxation time for  $[P_{666,14}][TCM]$ ,  $[P_{666,14}][SCN]$ ,  $[P_{666,14}][TFSI]$ ,  $[P_{666,14}][BH_4]$ ,  $[P_{666,14}][TAU]$ , and  $[P_{666,14}][BOB]$  (from left to right respectively). Scatters-experimental data, solid lines denote the fit of VFT function  $\tau_\sigma = \tau_\infty \exp(DT_0/(T-T_0))$  to experimental data. Dashed lines indicate  $T_{LL}$  and  $\tau_\sigma$  at LLT. The type and color of data points in **c**, **d** are specific for a given IL. The color area on **a**, **b** and **d** denotes the liquid 1 phase. L1 denotes liquid 1 while L2 liquid 2.

To verify whether the LLT manifests itself in molecular dynamics behavior, the dielectric measurements over a wide frequency ( $10^{-2}$ – $10^7$  Hz) and temperature range were performed. For ionic systems, the translational displacement of charge carriers (dc-conductivity) dominates the dielectric loss  $\varepsilon''(f)$  function, conventionally employed for data analysis [34]. Therefore, complex electric conductivity  $\sigma^*(f) = \varepsilon_0(Z^*(f)C_0)^{-1}$  and complex electric modulus  $M^*(f) = \varepsilon^*(f)^{-1}$ , are usually adopted to express their dielectric properties [35]. The latter formalism allows for the determination of three relevant quantities describing the ion dynamics in AILs: dc-conductivity  $\sigma_{dc} = 2\pi f \varepsilon_0 (M'')^{-1}$  calculated from a low-frequency region of  $M''(f)$ ; conductivity relaxation times  $\tau_\sigma = (2\pi f_{max})^{-1}$  determined directly from  $M''$  maximum; and distribution of relaxation times reflected in the width of  $M''(f)$  peak. Therefore, this representation was selected to evaluate the data recorded in this work.  $[P_{666,14}][BF_4]$  has been excluded from these studies due to the high tendency to crystallization. Figure 5.3a shows the representative

electric modulus spectra of [P<sub>666,14</sub>][TFSI] collected at 0.1 MPa and various temperatures. This graph shows that the  $M''(f)$  peak (denoted as  $\sigma$ -process or conductivity relaxation peak), describing the time scale of translational motions of ions, shifts to lower frequencies upon cooling. This gradual change is in keeping with cooling effects seen in other ionic systems and reflects ions' suppressed mobility [36]. However, starting from a certain temperature, coinciding well with the calorimetric LLT, the temperature sensitivity of the  $\sigma$ -process becomes markedly stronger while the  $M''$  peak is broadening significantly. These effects, visualized for [P<sub>666,14</sub>][TFSI], are characteristic of all studied herein AILs (see Supplementary Note 2 for all  $M''$  spectra collected for studied herein IL) except for [P<sub>666,14</sub>][BOB]. For the latter ILs, the temperature decrease brings a usual slowing down of ion dynamics, i.e. the  $M''(f)$  peak is keeping the same shape over a broad  $T$  range (see Fig. 5.3b).

To quantify changes in the shape of conductivity relaxation peak across the LLT, the Kohlrausch function,  $\Phi(t)=\exp[-(t/\tau_\alpha)^{\beta_{KWW}}]$  [37], has been used (exemplary fitting curves are presented in Fig. 5.3a, b). The  $\beta_{KWW}$  parameters obtained from fitting of  $M''$  peaks are plotted as a function of the frequency of  $M''$  peak maximum ( $f_{max}$ ) in Fig. 5.3c. It is well-known that the broader and more asymmetric the peak is, the lower is the value of  $\beta_{KWW}$ . As shown in Fig. 5.3c, for a given IL, the exponent characterizing the liquid 1 stays approximately constant and falls in the range  $0.62 < \beta_{KWW} < 0.67$ , which is in the middle of the range reported for various ionic glass-formers [38]. On the other hand, a transition to liquid 2 brings a substantial decrease of  $\beta_{KWW}$ . The most significant drop is denoted for AIL with [SCN]<sup>-</sup> anion. On the second place [TCM]<sup>-</sup> is located, then [TFSI]<sup>-</sup>, [BH<sub>4</sub>]<sup>-</sup> and the weakest drop occurs for IL with the [TAU]<sup>-</sup>. Interestingly, this order corresponds well with the decrease of enthalpy accompanying LLT. The obtained results indicate that the distribution of the relaxation times becomes broader during the transformation from liquid 1 to liquid 2. In other words, in liquid 1 the species are more dynamically correlated (i.e., components relax with similar  $\tau_\sigma$ ), whereas in phase 2 there is higher heterogeneity (i.e., some components are more mobile and some are less mobile). This result is in agreement with dielectric data measured across LLT for TPP [39].

At the same time, the LLT of [P<sub>666,14</sub>][BOB] is not detectable on  $\beta_{KWW}(f_{max})$  graph mainly because the transition to liquid 2 overlaps with the liquid–glass transition, where the conductivity relaxation is too long to be directly measured ( $f_{max}(T_g) = 1.6 \cdot 10^{-3}$  Hz). Consequently, the dielectric response of liquid 1 is recorded over the entire available frequency range, i.e., from  $10^6$  to  $10^{-2}$  Hz. In this context, it is not surprising that the shape of  $M''(f)$  function collected for [P<sub>666,14</sub>][BOB] is invariant, i.e., satisfy the time-temperature superposition (TTS) rule being a typical behavior of glass-forming systems in a supercooled state.

The temperature dependence of conductivity relaxation times  $\tau_\sigma(T^{-1})$ , calculated directly from the modulus peak maxima, also exhibits a peculiar behavior near the calorimetric LLT (Fig. 5.3d). In particular,  $\tau_\sigma$  collected in liquid 1 reveals a typical non-Arrhenius behavior, and a substantial departure from the Vogel–Fulcher–Tammann (VFT) law occurs at the onset of phase transition; that is, an abrupt increase is observed in apparent activation energy. A closer inspection of Fig. 5.3d reveals that the values of  $\tau_\sigma(T_{LL})$  are in the range 0.3 – 15 ms for most of the studied AILs that is far from the time scale commonly identified with the liquid–glass transition ( $\tau_\sigma = 100$  s). The LLT is also clearly detectable when the Stickel operator,  $[\text{dlog}\tau_\sigma/\text{d}(1000/T)]^{-0.5}$ , is applied; such procedure gives two linear regions that intersect at  $T_{LL}$  (Supplementary Fig. S5.34). Notably, the sign of LLT is also detectable in dc-conductivity ( $\sigma_{dc}$ ) behavior. As shown in Supplementary Fig. S5.35, further cooling of ILs below LLT brings a change of  $\sigma_{dc}(T^{-1})$  from VFT to Arrhenius behavior observed at  $\sigma_{dc} = 10^{-14}$  S cm<sup>-1</sup>, which is commonly accepted as the value characterizing  $T_g$ . Note that  $T_g$  values determined as a crossover point of  $\sigma_{dc}(T^{-1})$  dependencies are in good agreement with the calorimetric  $T_g$  of aged glass (see Table 5.1).

As could be expected from raw dielectric spectra, the  $\log\tau_\sigma(T^{-1})$  and  $\sigma_{dc}(T^{-1})$  data obtained for [P<sub>666,14</sub>][BOB] do not reveal any peculiar behavior. Namely, the experimental points follow a single VFT equation in almost the whole examined temperature range. The only deviation from VFT to Arrhenius dependence occurs at  $\sigma_{dc} = 10^{-14}$  S/cm and indicates the liquid–glass transition (see Fig. 5.3d and Supplementary Fig. S5.35).

### 5.3.3 The LLT Under High-Pressure Conditions

Although rapid cooling is probably the most straightforward method for inducing a first-order phase transition, it is not the only route. The LLT of phosphorus [40] or nitrogen [41] can also be realized by isothermal compression. However, according to experimental results reported in the literature, to induce LLT in these systems, extreme temperature and pressure conditions have to be applied, for example, 50 GPa and 1920 K for nitrogen. In this context, one may question the possibility of achieving LLT in [P<sub>666,14</sub>]<sup>+</sup> ILs through the isothermal compression.

Four ILs have been chosen for high-pressure tests: [P<sub>666,14</sub>][TCM] and [P<sub>666,14</sub>][TFSI]—as revealing the most spectacular changes in relaxation dynamics across the LLT at 0.1 MPa, as well as [P<sub>666,14</sub>][BOB] and [P<sub>666,14</sub>][TAU]—as counterexamples. The representative high-pressure spectra collected at 223 K for [P<sub>666,14</sub>][TCM] are shown in Fig. 5.4a (see Supplementary Note 2 for all collected high-pressure data). The observed pattern of behavior upon compression is analogous to the isobaric cooling experiment:

despite maintaining the same pressure step, after reaching certain pressure the shifts in  $f_{max}$  are markedly faster. Also, the shape of the  $M''(f)$  peak behaves similarly to the ambient pressure experiment—during the isothermal compression, past certain pressure, the peaks broaden significantly. A direct comparison of the spectra collected at given  $f_{max}$  under various  $T$ - $P$  conditions shows that the shape of the  $\sigma$ -relaxation is independent of thermodynamic variables if phase 1 is considered (Fig. 5.4b and Supplementary Fig. S5.38). Such a phenomenon, called the temperature-pressure superposition principle, is a typical feature of glass-forming materials [42]. However, for superimposed spectra of liquid 2, the shape of  $M''(f)$  function at a given value of  $\tau\sigma$  becomes narrower with increasing  $T$  and  $P$ . In other words, compression at higher temperatures reduces the distribution of relaxation times in phase 2, making it more homogenous in terms of molecular dynamics. The same pattern has been detected for  $[P_{666,14}][TFSI]$ ; however, the dielectric spectra of  $[P_{666,14}][TAU]$  are getting slightly broader under pressure. In contrast, the  $\sigma$ -dispersion in  $[P_{666,14}][BOB]$  has been constant at any chosen  $\tau\sigma$  (see Fig. 5.4c and Supplementary Fig. S5.38). Consequently, the changes of  $M''(f)$  peak with pressure cannot be treated as a feature unique to  $[P_{666,14}]^+$  ILs, but rather as a unique characteristic of the liquid–liquid transformation. This peculiar behavior is, to some extent, similar to the effect of pressure on polymerization reactions when the material of a narrower distribution of molecular weight is obtained under higher pressure [43].

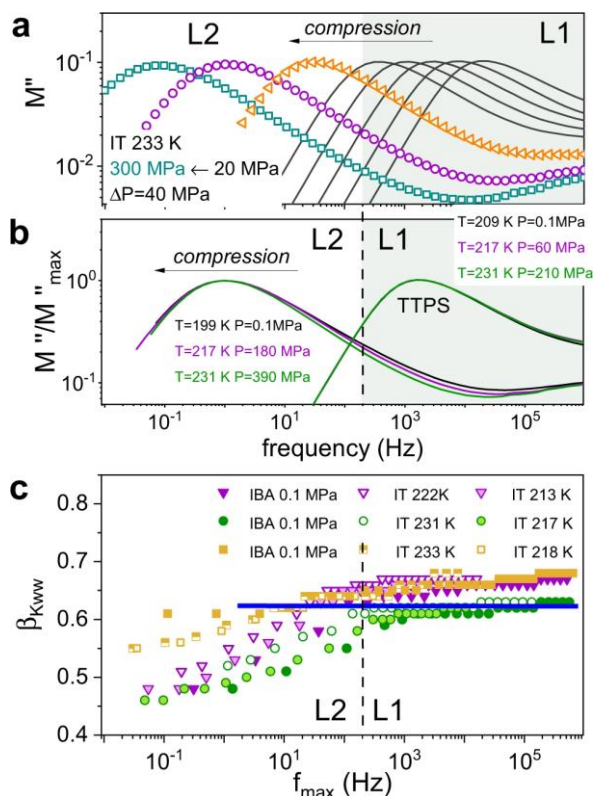


**Fig. 5.4: Dielectric response of studied ILs measured at high-pressure conditions.** **a** The representative dielectric data recorded for  $[P_{666,14}][TCM]$  in liquid 1 (solid lines) and liquid 2 (scatters)

phases, recorded during compression at isothermal (IT) conditions of 233 K and presented in electric modulus representation. **b** The representative  $M''(f)$  spectra of [P<sub>666,14</sub>][TCM] recorded at various  $T$ - $P$  conditions however at the same  $\tau_\sigma$  superimposed to each other in liquid 1 and liquid 2, respectively. Note that time temperature pressure superposition (TTPS) rule is valid. **c** The  $\beta_{KWW}$  exponent is plotted as a function of the frequency of modulus peak maximum at various thermodynamic conditions. IBA denotes 0.1 MPa and various temperatures, while IT denotes isotherm and various pressure. Triangles-[P<sub>666,14</sub>][TFSI], circles-[P<sub>666,14</sub>][TCM], squares-[P<sub>666,14</sub>][TAU]. The horizontal line indicates  $\beta_{KWW}$  for [P<sub>666,14</sub>][BOB] being constant at various  $T$ - $P$  conditions. The color area on **a**, **b** denotes the liquid 1 phase. L1 denotes liquid 1 while L2 liquid 2.

The analysis of isothermal  $\tau_\sigma$ - $P$  dependences determined for the studied ILs reveals another intriguing feature of the LLT. As illustrated in Fig. 5.5a, isothermal compression has fundamentally the same effect on the ion dynamics as isobaric cooling, i.e. the conductivity relaxation times  $\tau_\sigma$  are getting longer with squeezing. The  $\tau_\sigma(P)$  data of [P<sub>666,14</sub>][BOB] follow the  $p$ VFT behavior over the entire examined pressure range, while the experimental points recorded for [P<sub>666,14</sub>][TCM], [P<sub>666,14</sub>][TAU] and [P<sub>666,14</sub>][TFSI] markedly rise in slope at certain  $P$  bringing an almost four-fold increase in apparent activation volume  $V^\# = 2.303RT(d\log\tau_\sigma/dP)_T$ . (Fig. 5.5b). However, what is interesting, the kink of the  $\tau_\sigma$ - $P$  curve, being a manifestation of LLT, is independent of  $T$ - $P$  conditions and appears at constant conductivity relaxation times for a given system; specifically, at  $\tau_\sigma$  of milliseconds. This result shows that in analogy to liquid–glass transition, the L-L transformation is isochronal in nature. Nevertheless, the time scale of ion dynamics at LLT,  $\tau_\sigma(T_{LL}, P_{LL})$  is not universal but depends on intermolecular interactions.

Defining  $P_{LL}$  as the pressure at which the activation volume starts to increase, we obtain the pressure dependence of  $T_{LL}$  plotted in Fig. 5.5c. As presented,  $T_{LL}$  increases with pressure in a linear fashion, with the slope equal to 81 K GPa<sup>-1</sup> for [P<sub>666,14</sub>][TFSI], 87 K GPa<sup>-1</sup> for [P<sub>666,14</sub>][TCM] and 82.4 K GPa<sup>-1</sup> for [P<sub>666,14</sub>][TAU]. It means that the pressure in the order of 1.2 GPa is required to observe the LLT at room temperature conditions. Interestingly, when the isothermal  $\tau_\sigma(P)$  data are extrapolated to  $\tau_\sigma = 100$  s (that is a standard definition of  $T_g$ , i.e.  $T_g = T(\tau_\sigma = 100 \text{ s})$  or  $\sigma_{dc} = 10^{-14} \text{ S cm}^{-1}$ , non-linear  $T_g(P)$  dependences with the  $dT_g/dP$  coefficient of  $125 \pm 5 \text{ K GPa}^{-1}$  is obtained for [P<sub>666,14</sub>][TFSI], [P<sub>666,14</sub>][TCM] and [P<sub>666,14</sub>][BOB]. This indicates that dynamics of phase 2 of [P<sub>666,14</sub>][TCM] and [P<sub>666,14</sub>][TFSI] freezes (transform to glass) with the same characteristic as supercooled liquid 1 of [P<sub>666,14</sub>][BOB]. The  $dT_g/dP$  for [P<sub>666,14</sub>][TAU] was slightly lower (106 K GPa<sup>-1</sup>), but still much higher than  $dT_{LL}/dP$ .

The determined values of  $dT_{LL}/dP$  offer a unique possibility to estimate the variations in volume accompanying the LLT ( $\Delta V_{LL}$ ) using a simple Clausius-Clapeyron equation,  $dP/dT = \Delta S_{LL}(\Delta V_{LL})^{-1}$ . The  $\Delta S_{LL}$  denotes the entropy changes during the LLT and can be obtained as  $\Delta S_{LL} = \Delta H_{LL}(T_{LL})^{-1}$ , where  $\Delta H_{LL}$  is the enthalpy of first-order transition. The

calculated values of  $\Delta V_{LL}$  are equal to  $0.0056 \text{ cm}^3 \text{ g}^{-1}$ ,  $0.0039 \text{ cm}^3 \text{ g}^{-1}$  and  $0.0025 \text{ cm}^3 \text{ g}^{-1}$  for  $[\text{P}_{666,14}][\text{TCM}]$ ,  $[\text{P}_{666,14}][\text{TFSI}]$  and  $[\text{P}_{666,14}][\text{TAU}]$  respectively. To put these numbers into perspective, we measured the density of these ILs as a function of temperature and extrapolated the obtained dependence to  $T_{LL}$  (see Supplementary Fig. S5.39). Such procedure gives  $V_{LL} = 0.8759 \text{ cm}^3 \text{ g}^{-1}$  for  $[\text{P}_{666,14}][\text{TFSI}]$ ,  $0.9944 \text{ cm}^3 \text{ g}^{-1}$  for  $[\text{P}_{666,14}][\text{TAU}]$  and  $1.0452 \text{ cm}^3 \text{ g}^{-1}$  for  $[\text{P}_{666,14}][\text{TCM}]$ , indicating that changes of around 0.5% occur at LLT, that is within the error in dilatometric measurements. These small variations in the specific volume can be easily overlooked in direct  $V(T,P)$  measurements and reveal that density is not the dominant order parameter governing the LLT in ILs. This is in agreement with the experimental data recorded for sodium acetate trihydrate ( $\text{CH}_3\text{COONa} \cdot 3\text{H}_2\text{O}$ ) where a first-order LLT without density discontinuity was identified [19]. Moreover, LLTs without density change were suggested to take place in several metallic glass-formers [44].

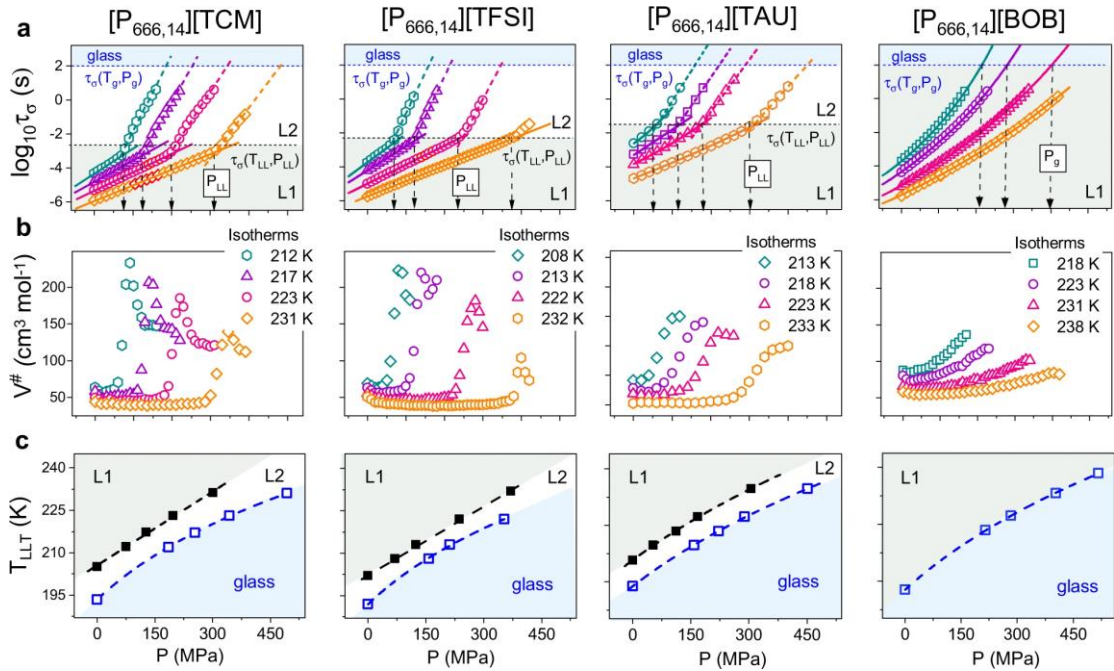


**Fig. 5.5: High-pressure data of  $[\text{P}_{666,14}][\text{TCM}]$ ,  $[\text{P}_{666,14}][\text{TFSI}]$ ,  $[\text{P}_{666,14}][\text{TAU}]$ , and  $[\text{P}_{666,14}][\text{BOB}]$  (from left to right respectively). **a** Presents the pressure dependence of conductivity relaxation time measured at various  $T$ . Solid lines denote the pVFT fit  $\tau_{\sigma} = \tau_0 \exp(BP/(P_0 - P))$  to experimental data. Dashed lines indicate liquid-liquid transition pressure ( $P_{LL}$ ) and  $\tau_{\sigma}$  at LLT.  $P_g$  denotes liquid-glass transition pressure. **b** Presents pressure dependence of apparent activation volume,  $V^{\#}$ . The four-time increase in  $V^{\#}$  at LLT indicates a formation of nonpolar domains of large scale in liquid 2. **c**  $T_{LL}$  and  $T_g$  as a function of  $P$  is presented. The color area on a and c denotes the liquid 1 phase (gray) and glass region (blue). L1 denotes liquid 1 while L2 liquid 2.**

In summary, our findings provide experimental support for the hypothesis that the LLT occurs in ion-containing systems. Our studies of a series of  $[\text{P}_{666,14}]^+$ -based AILs and seven different anions demonstrate that the LLT takes place in AILs with  $[\text{TCM}]^-$ ,

[TFSI]<sup>-</sup>, [TAU]<sup>-</sup>, [BH<sub>4</sub>]<sup>-</sup> and [SCN]<sup>-</sup> anions, but not with [BF<sub>4</sub>]<sup>-</sup> that shows crystallization. On the other hand, for [P<sub>666,14</sub>][BOB], the LLT overlaps with the liquid–glass transition. Interestingly,  $T_g$  is approximately the same for all studied AILs, while  $T_{LL}$  is decreasing with an increase of anion van der Waals volume. This demonstrates that IILs can be fine-tuned to display  $T_{LL}$ , which is dependent on several parameters, such as anion size, geometry, conformational flexibility, Lewis basicity and the strength of interionic interactions. In this context, the question about the differences between liquid structures formed by [P<sub>666,14</sub>]<sup>+</sup>-based AILs appears and should be addressed in the future e.g. by using SAXS or neutron scattering.

Our study also provides an important approach to the LLT-correlated properties. We found that the parameters characterizing the ion dynamics ( $\tau_\sigma$ ,  $\sigma_{dc}$ ) and distribution of relaxation times ( $\beta_{KWW}$ ) monitored on isobaric cooling and isothermal compression reveal peculiar behavior at the LLT. Furthermore, independently of  $T$ - $P$  conditions, the sign of LLT is observed at  $\tau_\sigma = \text{const.}$  within a given system, i.e., it occurs at a certain time scale of ionic motions dependent on interionic interactions. Further studies of this issue e.g., by using dynamic light scattering (DLS) under high-pressure conditions are desired. Upon transition liquid 1→liquid 2 (induced by cooling or high-pressure), the AILs become more heterogeneous in terms of ion mobility. Additionally, the  $dT_{LL}/dP$  coefficient determined for [TCM]<sup>-</sup>, [TAU]<sup>-</sup> and [TFSI]<sup>-</sup>-based IILs in a high-pressure experiment, together with  $\Delta H_{LL}$  and  $T_{LL}$  let us estimate the volume changes accompanying LLT by using the Clausius-Clapeyron equation. We found that  $\Delta V_{LL}$  is very small and can be undetectable in conventional dilatometry measurement. Such an LLT may offer a unique opportunity for investigating the subtle structural and dynamic changes of liquid.

## 5.4 Methods

### Synthesis

[P<sub>666,14</sub>][TFSI]: Trihexyl(tetradecyl)phosphonium chloride [P<sub>666,14</sub>]<sup>+</sup>Cl<sup>-</sup> (0.010 mol eq.) and Li[TFSI] were separately dissolved in deionised water, combined in a round-bottomed flask, and left to react (1 h, RT, 600 rpm). The organic layer was separated and washed with deionized water and then dichloromethane. Subsequent washes were performed with solution of Li[TFSI] in deionised water, and then with deionised water, until no chloride could be detected with silver nitrate solution. DCM was removed via rotary evaporation (30 min, 35 °C) and the ionic liquid was dried under high vacuum (12 h, 70 °C, 10<sup>-2</sup> mbar). The product was analysed by <sup>1</sup>H, <sup>13</sup>C, <sup>19</sup>F and <sup>31</sup>P NMR spectroscopy (d<sub>6</sub>-DMSO) and by XRF for chloride content. [P<sub>666,14</sub>][SCN], [P<sub>666,14</sub>][TCM] and [P<sub>666,14</sub>][BF<sub>4</sub>] were prepared following analogous procedures, from their respective salts.

[P<sub>666,14</sub>][TAU]: [P<sub>666,14</sub>]Cl was converted to [P<sub>666,14</sub>][OH] (solution in methanol). Taurine (0.012 mol eq.) was dissolved in deionised water, to which methanol solution of [P<sub>666,14</sub>][OH] (0.015 mol eq.) was added and left to react (2 h, RT, 600 rpm). Solvents were then removed via rotary evaporation (3 h, 30–80 °C), and the crude product was dissolved in dry acetonitrile and stored in the fridge (5 °C, 12 h) until the excess taurine crystallised and was filtered off. Acetonitrile was removed via rotary evaporation (30 min, 60 °C) and the ionic liquid was dried under high vacuum (overnight, 70 °C, 10<sup>-2</sup> mbar). The product was analysed <sup>1</sup>H, <sup>13</sup>C and <sup>31</sup>P NMR spectroscopy (d<sub>6</sub>-DMSO) and by XRF for chloride content.

[P<sub>666,14</sub>][BH<sub>4</sub>]: [P<sub>666,14</sub>]Cl (0.10 mol eq.) and Na[BH<sub>4</sub>] (0.13 mol eq.) were separately dissolved in deionised water, combined in a round-bottomed flask, and left to react (48 h, RT, 600 rpm). Chloroform was added to dissolve the ionic liquid layer, and the aqueous layer was separated. The organic layer was washed ten times with Na[BH<sub>4</sub>] solution, then chloroform was removed via rotary evaporation (30 min, 35 °C) and the solution was dried overnight under high vacuum (12 h, 70 °C, 10<sup>-2</sup> mbar). Chloride removal was carried out in three subsequent polishing steps (multiple sodium borohydride washes) until chloride content was below 2000 ppm by XRF analysis.

[P<sub>666,14</sub>][BOB]: Was synthesized in a two-step synthesis. Firstly, oxalic acid (0.03 mol eq.) and boric acid (0.01 mol eq.) were separately dissolved in water and then combined under vigorous stirring. Na<sub>2</sub>CO<sub>3</sub> (0.5 mol eq.) was slowly added and the turbid solution was heated in an oil bath at 120 °C. Water was distilled off until a dry white powder was obtained, which then was dispersed in hot acetonitrile (60 °C, 1 h), filtered, washed with cold ethanol and finally dried overnight under high vacuum (12 h, 60 °C, 10<sup>-2</sup> mbar). Subsequently, [P<sub>666,14</sub>][Cl] (0.01 mol eq.) and Na[BOB] (0.01 mol eq.) were stirred in dichloromethane (overnight, RT, 600 rpm) and then water was added, inducing phase separation. The organic layer was separated and washed with solution of Na[BOB] in deionized water, then with deionised water, until no chloride could be detected with silver nitrate solution. Subsequently, DCM was removed via rotary evaporation (30 min, 35 °C) and the ionic liquid was dried overnight under high vacuum (12 h, 60 °C, 10<sup>-2</sup> mbar). For more details see Supplementary Information part.

### **Differential scanning calorimetry (DSC)**

Calorimetric experiments of studied ILs were performed by means of a Mettler Toledo DSC1STAR System equipped with a liquid nitrogen cooling accessory and an HSS8 ceramic sensor (a heat flux sensor with 120 thermocouples). Each sample with a mass of around 10–20 mg was measured in aluminum crucibles with a 40 µL volume. During the experiments, the flow of nitrogen was kept at 60 mL min<sup>-1</sup>. Enthalpy and temperature calibrations were performed using indium and zinc standards. Low-

temperature verification was made using  $\text{CCl}_4$  and n-heptane (182.15 K,  $140.5 \text{ J g}^{-1}$ ) at different scanning rates (0.7, 1, 5, and  $10 \text{ K min}^{-1}$ ). The baseline was constructed as a straight line from the onset to the endpoint. A dedicated software Mettler Toledo DSC1STAR allows various calculations (onset, heat, peak temperature, etc.) from the original recorded DSC curves. Prior to the measurement, the samples were annealed 30 min at 373 K. Temperature ramps involved cooling to 143 K and then heating to 373 K with a rate of 10 K per min. Samples were cycled at least 3 times to ensure reproducibility and high accuracy. The 6-h aging experiment was performed at 183 K after cooling with the rate of  $10 \text{ K min}^{-1}$ .

### **Dielectric measurements**

The dielectric measurements at ambient pressure for studied ILs were carried out over a frequency range from  $10^{-1} \text{ Hz}$  to  $10^7 \text{ Hz}$  by means of Novo-Control GMBH Alpha dielectric spectrometer. The Novocool system controlled the temperature with an accuracy of 0.1 K. During this measurement the sample was placed between two stainless steel electrodes (diameter = 15 mm). The distance of 0.08 mm was provided by the quartz ring. For the pressure-dependent dielectric measurements, we used the capacitor filled with the studied sample, which was next placed in the high-pressure chamber and compressed using silicone oil. Note that during the measurement, the sample was only in contact with stainless steel. The pressure was measured by the Unipress setup with a resolution of 1 MPa. The temperature was controlled within 0.1 K by means of a Weiss fridge.

## **5.5 Acknowledgements**

Authors acknowledge M. Musiał for the density measurements of  $[\text{P}_{666,14}][\text{TCM}]$ . The authors Z.W., S.C. and M.P. are deeply grateful for the financial support by the National Science Centre within the framework of the Opus15 project (grant nr DEC-2018/29/B/ST3/00889 M.P.). Solvay is acknowledged for kindly providing trihexyl(tetradecyl)phosphonium chloride.

## **5.6 Supplementary information**

### **Synthesis of examined systems**

Trihexyl(tetradecyl)phosphonium chloride,  $[\text{P}_{666,14}]\text{Cl}$ , was kindly provided by Solvay. Sodium tricyanomethanide was bought from TCI Chemicals. All other chemicals were purchased from Sigma-Aldrich and used as received. XRF analysis was performed on a Rigaku NEX QC+ QuantEZ High-Resolution Energy Dispersive X-ray Fluorescence (EDXRF) Spectrometer. NMR spectra were recorded on either a Bruker Avance III 400 MHz spectrometer or a Bruker Avance II DPX 600 MHz spectrometer.

**[P<sub>666,14</sub>][TFSI]**. Trihexyl(tetradecyl)phosphonium chloride, [P<sub>666,14</sub>]Cl (0.010 mol eq.) and lithium bis(trifluoromethanesulfon)imide Li[TFSI] (0.013 mol eq.) were separately dissolved in 25 cm<sup>3</sup> deionised water (18.2 MΩ.cm) (total 50 cm<sup>3</sup>) and then combined in a round-bottomed flask (250 cm<sup>3</sup>), resulting in the formation of a biphasic liquid system; the mixture was left to react (1 h, room temperature, 600 rpm). The aqueous layer was separated, and the organic layer was collected and washed, firstly with deionized water (18.2 MΩ.cm) (10 cm<sup>3</sup>) and then dichloromethane, DCM (10 cm<sup>3</sup>). Subsequent washes were performed with solution of Li[TFSI] in deionised water (18.2 MΩ.cm). Final three washes were performed with deionised water (18.2 MΩ.cm) until no chloride could be detected with silver nitrate solution. Subsequently, DCM was removed *via* rotary evaporation (30 min, 308.15 K) and the ionic liquid was dried under high vacuum (12h, 343.15 K, 10<sup>-2</sup> mbar). XRF analysis confirmed chloride content was below the detectable limit. <sup>1</sup>H, <sup>13</sup>C, <sup>19</sup>F and <sup>31</sup>P NMR spectra of the IL were recorded in *d*<sub>6</sub>-DMSO.

<sup>1</sup>H NMR (400.13 MHz, *d*<sub>6</sub>-DMSO) δ: 0.83-0.92 (m, 12H), 1.21-1.27 (m, 18H), 1.28-1.35 (m, 14H), 1.35-1.43 (m, 8H), 1.43-1.55 (m, 8H), 2.11-2.23 (m, 8H).

<sup>13</sup>C{<sup>1</sup>H} NMR (100.61 MHz, *d*<sub>6</sub>-DMSO) δ: 13.53 (s, P-(CH<sub>2</sub>)<sub>5</sub>-CH<sub>3</sub>), 13.64 (s, P-(CH<sub>2</sub>)<sub>13</sub>-CH<sub>3</sub>), 17.45 (d, <sup>1</sup>J<sub>C/P</sub> = 188 Hz, P-CH<sub>2</sub>-(CH<sub>2</sub>)<sub>4</sub>-CH<sub>3</sub>), 17.52 (d, <sup>1</sup>J<sub>C/P</sub> = 192 Hz, P-CH<sub>2</sub>-(CH<sub>2</sub>)<sub>12</sub>-CH<sub>3</sub>), 20.46 (s, ), 20.50 (s, ), 20.54 (s, ), 21.75 (s, ), 22.07 (s, ), 28.81 (d, 2J<sub>C/P</sub> = 116 Hz, P-CH<sub>2</sub>-CH<sub>2</sub>-(CH<sub>2</sub>)<sub>3</sub>-CH<sub>3</sub>), 28.90 (d, <sup>2</sup>J<sub>C/P</sub> = 128 Hz, P-CH<sub>2</sub>-CH<sub>2</sub>-(CH<sub>2</sub>)<sub>11</sub>-CH<sub>3</sub>), 29.04 (s, P-(CH<sub>2</sub>)<sub>4</sub>-CH<sub>2</sub>-CH<sub>3</sub>), 29.09 (s, ), 29.70 (d, <sup>3</sup>J<sub>C/P</sub> = 60 Hz, P-(CH<sub>2</sub>)<sub>2</sub>-CH<sub>2</sub>-(CH<sub>2</sub>)<sub>10</sub>-CH<sub>3</sub>), 29.95 (d, <sup>3</sup>J<sub>C/P</sub> = 60 Hz, P-(CH<sub>2</sub>)<sub>2</sub>-CH<sub>2</sub>-(CH<sub>2</sub>)<sub>2</sub>-CH<sub>3</sub>), 30.34 (s, P-(CH<sub>2</sub>)<sub>3</sub>-CH<sub>2</sub>-(CH<sub>2</sub>)<sub>9</sub>-CH<sub>3</sub>), 31.32 (s, P-(CH<sub>2</sub>)<sub>3</sub>-CH<sub>2</sub>-CH<sub>2</sub>-CH<sub>3</sub>), 119.50 (q, <sup>1</sup>J<sub>C/F</sub> = 1280 Hz CF<sub>3</sub>).

<sup>19</sup>F NMR (376.50 MHz, *d*<sub>6</sub>-DMSO) δ: -79.00.

<sup>31</sup>P{<sup>1</sup>H} NMR (161.98 MHz, *d*<sub>6</sub>-DMSO) δ: 33.55.

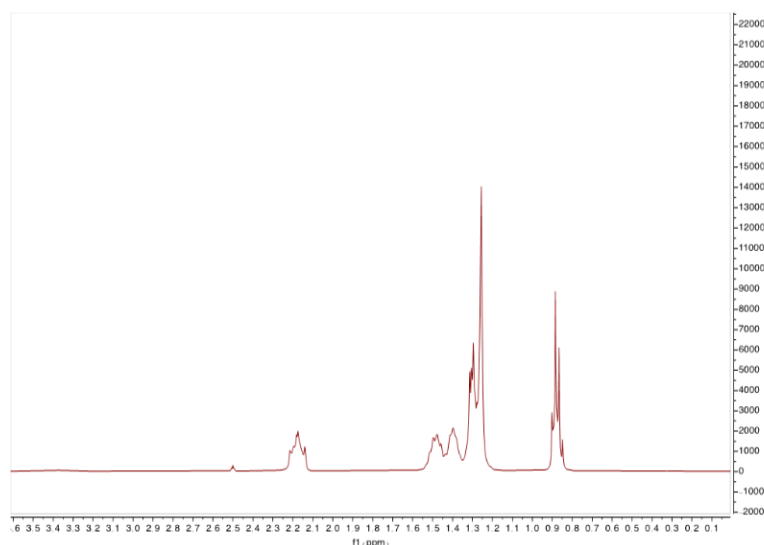


**Figure S5.1.** <sup>1</sup>H NMR spectrum (*d*<sub>6</sub>-DMSO, 400.13 MHz, 298.15 K) of [P<sub>666,14</sub>][TFSI].

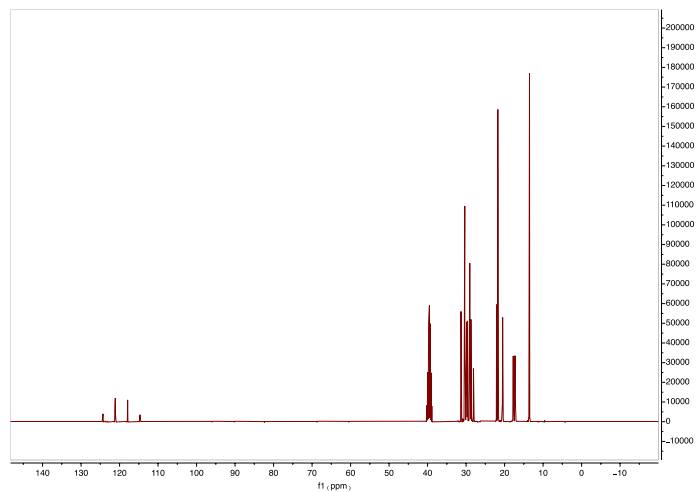


**Figure S5.2.** <sup>13</sup>C NMR spectrum (*d*<sub>6</sub>-DMSO, 100.61 MHz, 298.15 K) of [P<sub>666,14</sub>][TFSI].

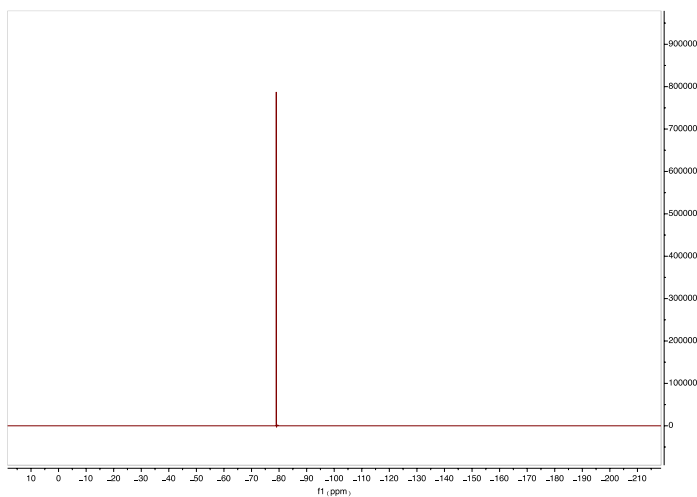


**Figure S5.3.** <sup>19</sup>F NMR spectrum (*d*<sub>6</sub>-DMSO, 376.50 MHz, 298.15 K) of [P<sub>666,14</sub>][TFSI].

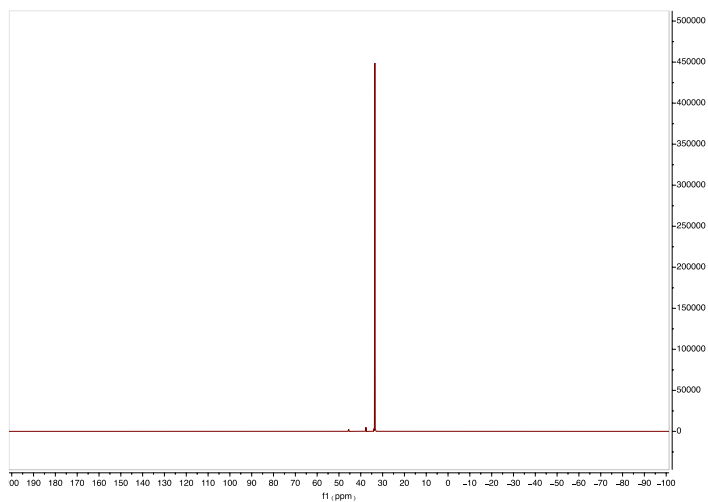


**Figure S5.4.** <sup>31</sup>P NMR spectrum of (*d*<sub>6</sub>-DMSO, 161.98 MHz, 298.15 K) [P<sub>666,14</sub>][TFSI].

**[P<sub>666,14</sub>][SCN]**. Trihexyl(tetradcyl)phosphonium chloride [P<sub>666,14</sub>]Cl (0.010 mol eq.) and K[SCN] (0.013 mol eq.) were separately added to 25 cm<sup>3</sup> deionised water (18.2 MΩ.cm) deionised water (total 50 cm<sup>3</sup>) and then combined in a round-bottomed flask (250 cm<sup>3</sup>), resulting in the formation of a biphasic liquid system; the mixture was left to react (1 h, room temperature, 600 rpm). The aqueous layer was separated, and the organic layer was collected and washed, firstly with deionised water (10 cm<sup>3</sup>) and then dichloromethane, DCM (10 cm<sup>3</sup>). Subsequent washes were performed with solution of K[SCN] in deionised water (18.2 MΩ.cm) deionised water. Final three washes were performed with deionised water (18.2 MΩ.cm) deionised water until no chloride could be detected with silver nitrate solution. Subsequently, DCM was removed *via* rotary evaporation (30 min, 35 °C) and the ionic liquid was dried under high vacuum (12h, 70 °C, 10<sup>-2</sup> mbar). XRF analysis of [P<sub>666,14</sub>][SCN] confirmed chloride content was below the detectable limit. <sup>1</sup>H, <sup>13</sup>C and <sup>31</sup>P NMR spectra of the ionic liquid were recorded in *d*<sub>6</sub>-DMSO.

<sup>1</sup>H NMR (600 MHz, *d*<sub>6</sub>-DMSO) δ: 0.86-0.94 (m, 12H), 1.23-1.30 (m, 18H), 1.31-1.36 (m, 14H), 1.37-1.44 (m, 8H), 1.45-1.55 (m, 8H), 2.16-2.24 (m, 8H).

<sup>13</sup>C{<sup>1</sup>H}NMR (150.90 MHz, *d*<sub>6</sub>-DMSO) δ: 13.58 (s, P-(CH<sub>2</sub>)<sub>5</sub>-**CH<sub>3</sub>**), 13.60 (s, P-(CH<sub>2</sub>)<sub>13</sub>-**CH<sub>3</sub>**), 18.63 (d, <sup>1</sup>J<sub>C/P</sub> = 186 Hz, P-**CH<sub>2</sub>**-(CH<sub>2</sub>)<sub>4</sub>-CH<sub>3</sub>), 21.35 (s, ), 22.01 (s, ), 22.14 (s, ), 22.27 (s, ), 27.86 (d, <sup>2</sup>J<sub>C/P</sub> = 198 Hz, P-CH<sub>2</sub>-**CH<sub>2</sub>**-(CH<sub>2</sub>)<sub>3</sub>-CH<sub>3</sub>), 28.83 (d, <sup>2</sup>J<sub>C/P</sub> = 198 Hz, P-CH<sub>2</sub>-**CH<sub>2</sub>**-(CH<sub>2</sub>)<sub>11</sub>-CH<sub>3</sub>), 28.97 (s, ), 29.28 (s, P-(CH<sub>2</sub>)<sub>4</sub>-**CH<sub>2</sub>**-CH<sub>3</sub>), 29.36 (s, ), 30.08 (d, <sup>3</sup>J<sub>C/P</sub> = 60 Hz, P-(CH<sub>2</sub>)<sub>2</sub>-**CH<sub>2</sub>**-(CH<sub>2</sub>)<sub>10</sub>-CH<sub>3</sub>), 30.43 (d, <sup>3</sup>J<sub>C/P</sub> = 60 Hz, P-(CH<sub>2</sub>)<sub>2</sub>-**CH<sub>2</sub>**-(CH<sub>2</sub>)<sub>2</sub>-CH<sub>3</sub>), 30.70 (s, P-(CH<sub>2</sub>)<sub>3</sub>-**CH<sub>2</sub>**-(CH<sub>2</sub>)<sub>9</sub>-CH<sub>3</sub>), 31.31.09 (s, P-(CH<sub>2</sub>)<sub>3</sub>-**CH<sub>2</sub>**-CH<sub>2</sub>-CH<sub>3</sub>), 31.54 (s, ), 130.67 (s, S-CN).

<sup>31</sup>P{<sup>1</sup>H}NMR (242.94 MHz, *d*<sub>6</sub>-DMSO) δ: 32.58.

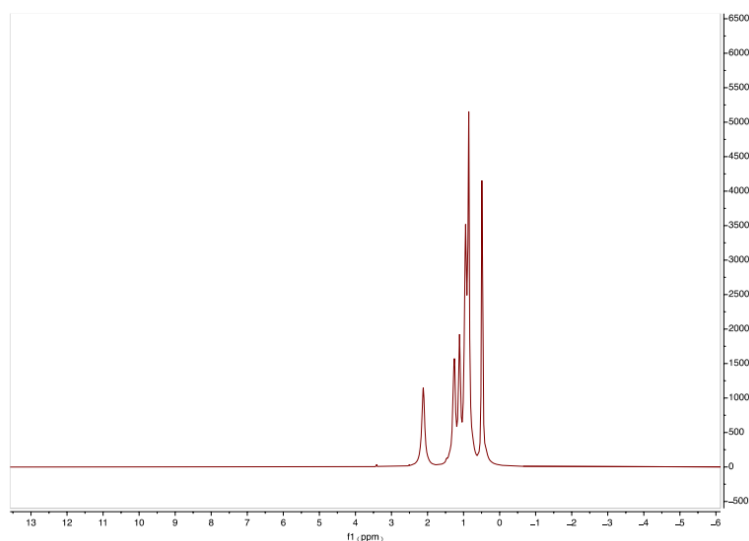


**Figure S5.5.** <sup>1</sup>H NMR spectrum (*d*<sub>6</sub>-DMSO, 600.13 MHz, 25 °C) of [P<sub>666,14</sub>][SCN].

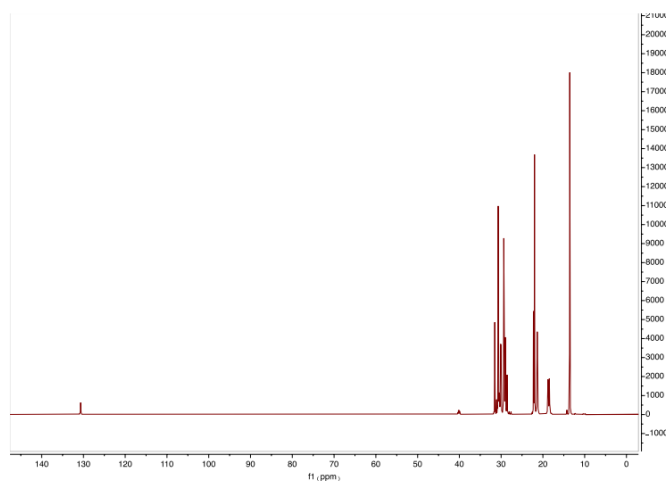


**Figure S5.6.**  $^{13}\text{C}$  NMR spectrum ( $d_6$ -DMSO, 150.90 MHz, 25 °C) of  $[\text{P}_{666,14}][\text{SCN}]$ .

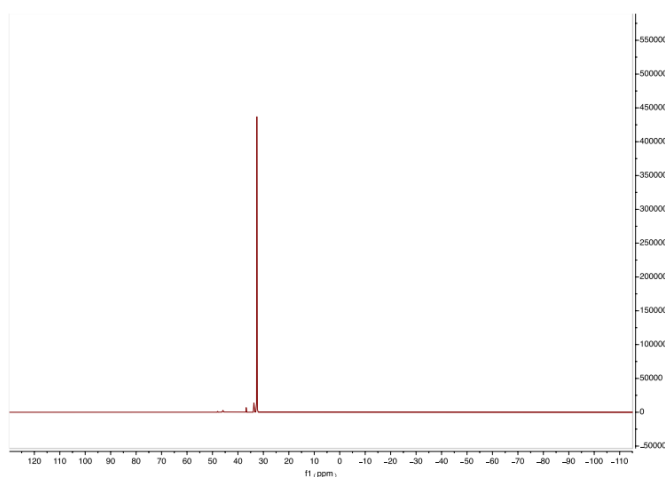


**Figure S5.7.**  $^{31}\text{P}$  NMR spectrum ( $d_6$ -DMSO, 242.94 MHz, 25 °C) of  $[\text{P}_{666,14}][\text{SCN}]$ .

**$[\text{P}_{666,14}][\text{TCM}]$ .** Trihexyl(tetradecyl)phosphonium chloride  $[\text{P}_{666,14}]\text{Cl}$  (0.010 mol eq.) and sodium tricyanomethanide,  $\text{Na}[\text{TCM}]$  (0.013 mol eq.) were separately added to 25 cm<sup>3</sup> deionised water (18.2 M $\Omega$ .cm) (total 50 cm<sup>3</sup>) and then combined in a round-bottomed flask (250 cm<sup>3</sup>), resulting in the formation of a biphasic liquid system; the mixture was left to react (1 h, room temperature, 600 rpm). The aqueous layer was separated, and the organic layer was collected and washed, firstly with deionised water (18.2 M $\Omega$ .cm) (10 cm<sup>3</sup>) and then dichloromethane, DCM (10 cm<sup>3</sup>). Six subsequent washes were performed with solution of  $\text{Na}[\text{TCM}]$  in deionised water (18.2 M $\Omega$ .cm). Final three washes were performed with deionised water (18.2 M $\Omega$ .cm) until no chloride could be detected with silver nitrate solution. Subsequently, DCM was removed via rotary evaporation (30 min, 35 °C) and the ionic liquid was dried under high vacuum (12h, 70 °C, 10<sup>-2</sup> mbar). XRF analysis of  $[\text{P}_{666,14}][\text{TCM}]$  recorded a chloride content of 89.3 ppm with a lower detection limit (LLD) of 2.80 ppm.  $^1\text{H}$ ,  $^{13}\text{C}$  and  $^{31}\text{P}$  NMR spectra of the ionic liquid were recorded in  $d_6$ -DMSO.

$^1\text{H}$  NMR (600.13 MHz,  $d_6$ -DMSO)  $\delta$ : 0.84-0.93 (m, 12H), 1.21-1.28 (m, 18H), 1.30-1.35 (m, 14H), 1.35-1.42 (m, 8H), 1.43-1.54 (m, 8H), 2.14-2.23 (m, 8H).

$^{13}\text{C}\{^1\text{H}\}$  NMR (150.90 MHz,  $d_6$ -DMSO)  $\delta$ : 4.87 (s,  $\text{C}(\text{CN})_3$ ), 13.54 (s,  $\text{P}(\text{CH}_2)_5\text{-CH}_3$ ), 13.68 (s,  $\text{P}(\text{CH}_2)_{13}\text{-CH}_3$ ), 18.28 (d,  $^1J_{\text{C/P}} = 186$  Hz,  $\text{P-CH}_2\text{-(CH}_2)_4\text{-CH}_3$ ), 20.92 (s, ), 20.95 (s, ), 21.96 (s, ), 22.34 (s, ), 28.07 (s, ), 28.63 (d,  $^2J_{\text{C/P}} = 196$  Hz,  $\text{P-CH}_2\text{-CH}_2\text{-(CH}_2)_3\text{-CH}_3$ ), 29.12 (d,  $^2J_{\text{C/P}} = 114$  Hz,  $\text{P-CH}_2\text{-CH}_2\text{-(CH}_2)_{11}\text{-CH}_3$ ), 29.33 (s, ), 29.36 (s,  $\text{P}(\text{CH}_2)_4\text{-CH}_2\text{-CH}_3$ ), 29.38 (s, ), 29.92 (d,  $^3J_{\text{C/P}} = 60$  Hz,  $\text{P}(\text{CH}_2)_2\text{-CH}_2\text{-(CH}_2)_{10}\text{-CH}_3$ ), 30.25 (d,  $^3J_{\text{C/P}} = 54$  Hz,  $\text{P}(\text{CH}_2)_2\text{-CH}_2\text{-(CH}_2)_2\text{-CH}_3$ ), 30.49 (s, ), 31.06 (s,  $\text{P}(\text{CH}_2)_3\text{-CH}_2\text{-(CH}_2)_9\text{-CH}_3$ ), 31.59 (s,  $\text{P}(\text{CH}_2)_3\text{-CH}_2\text{-CH}_2\text{-CH}_3$ ), 120.83 (s,  $\text{C}(\text{CN})_3$ ).

$^{31}\text{P}\{^1\text{H}\}$  NMR (242.94 MHz,  $d_6$ -DMSO)  $\delta$ : 32.96.

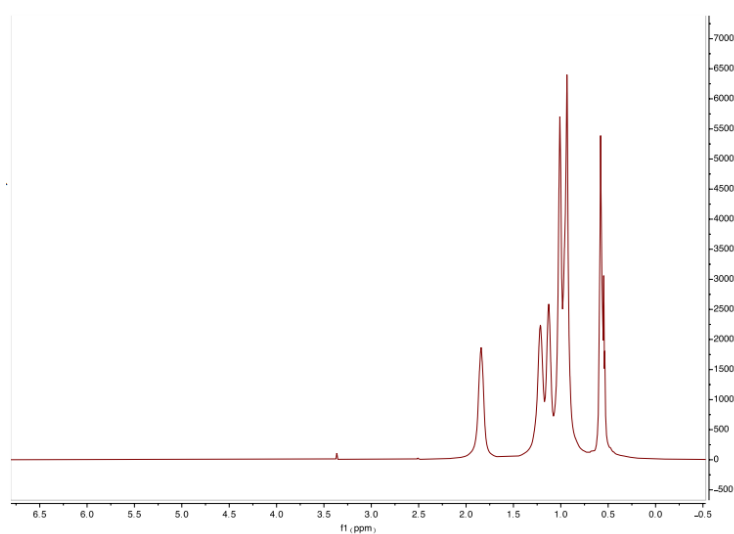


**Figure S5.8.**  $^1\text{H}$  NMR spectrum ( $d_6$ -DMSO, 600.13 MHz, 25 °C) of  $[\text{P}_{666,14}][\text{TCM}]$ .

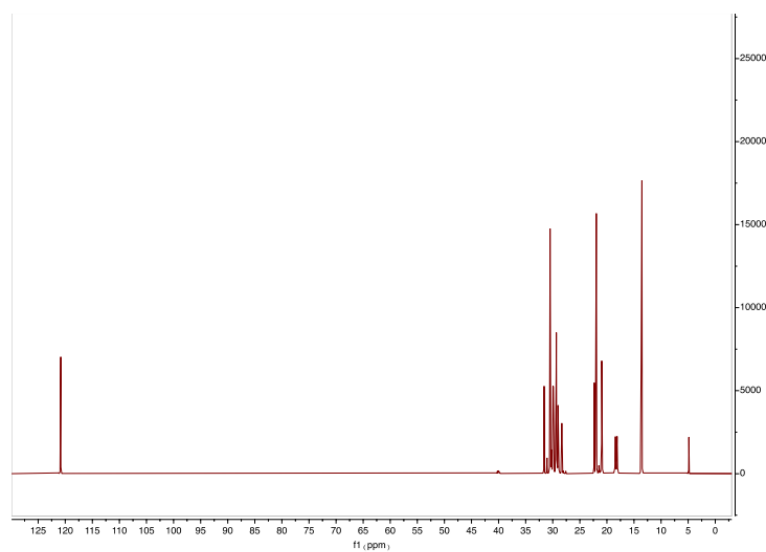


**Figure S5.9.**  $^{13}\text{C}$  NMR spectrum ( $d_6$ -DMSO, 150.90 MHz, 25 °C) of  $[\text{P}_{666,14}][\text{TCM}]$ .

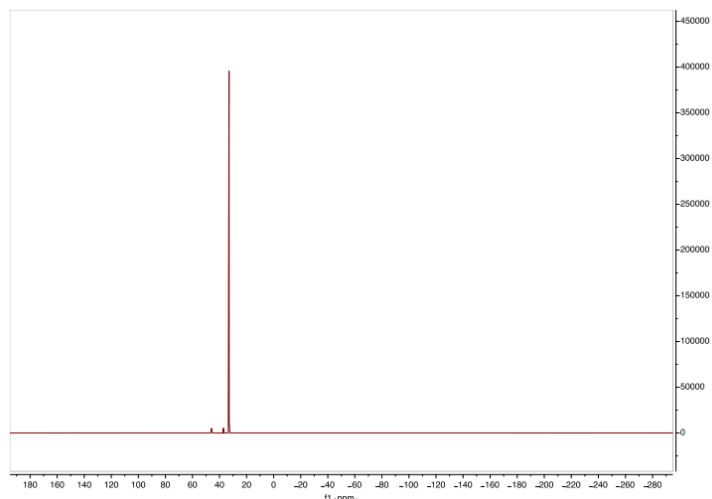


**Figure S5.10.**  $^{31}\text{P}$  NMR spectrum ( $d_6$ -DMSO, 242.94 MHz, 25 °C) of  $[\text{P}_{666,14}][\text{TCM}]$ .

**$[\text{P}_{666,14}][\text{BF}_4]$ .** Trihexyl(tetradecyl)phosphonium chloride  $[\text{P}_{666,14}]\text{Cl}$  (0.010 mol eq.) and sodium tetrafluoroborate,  $\text{Na}[\text{BF}_4]$  (0.013 mol eq.) were separately added to 25  $\text{cm}^3$  deionised water (18.2  $\text{M}\Omega\cdot\text{cm}$ ) (total 50  $\text{cm}^3$ ) and then combined in a round-bottomed flask (250  $\text{cm}^3$ ), resulting in the formation of a biphasic liquid system; the mixture was left to react (1 h, room temperature, 600 rpm). The aqueous layer was separated, and the organic layer was collected and washed, firstly with deionised water (18.2  $\text{M}\Omega\cdot\text{cm}$ ) (10  $\text{cm}^3$ ) and then dichloromethane, DCM (10  $\text{cm}^3$ ). Subsequent washes were performed with solution of  $\text{Na}[\text{BF}_4]$  in deionised water (18.2  $\text{M}\Omega\cdot\text{cm}$ ). Final three washes were performed with deionised water (18.2  $\text{M}\Omega\cdot\text{cm}$ ) until no chloride could be detected with silver nitrate solution. Subsequently, DCM was removed via rotary evaporation (30 min, 35 °C) and the ionic liquid was dried under high vacuum (12h, 70 °C,  $10^{-2}$  mbar). XRF analysis of  $[\text{P}_{666,14}][\text{BF}_4]$  recorded a chloride content of 69.0 ppm with a lower detection limit (LLD) of 2.35 ppm.  $^1\text{H}$ ,  $^{13}\text{C}$ ,  $^{11}\text{B}$  and  $^{31}\text{P}$  NMR spectra of the ionic liquid were recorded in  $d_6$ -DMSO.

$^1\text{H}$  NMR (600.13 MHz,  $d_6$ -DMSO)  $\delta$ : 0.89-0.96 (m, 12H), 1.25-1.32 (m, 18H), 1.32-1.38 (m, 14H), 1.39-1.47 (m, 8H), 1.47-1.56 (m, 8H), 2.17-2.26 (m, 8H).

$^{13}\text{C}\{^1\text{H}\}$  NMR (150.90 MHz,  $d_6$ -DMSO)  $\delta$ : 13.75 (s,  $\text{P}-(\text{CH}_2)_5\text{-CH}_3$ ), 13.83 (s,  $\text{P}-(\text{CH}_2)_{13}\text{-CH}_3$ ), 17.36 (d,  $^1\text{J}_{\text{C/P}} = 192$  Hz,  $\text{P-CH}_2\text{-(CH}_2)_4\text{-CH}_3$ ), 17.46 (d,  $^1\text{J}_{\text{C/P}} = 186$  Hz,  $\text{P-CH}_2\text{-(CH}_2)_{12}\text{-CH}_3$ ), 20.47 (s, ), 20.50 (s, ), 21.77 (s, ), 22.06 (s, ), 28.07 (s, ), 28.79 (d,  $^2\text{J}_{\text{C/P}} = 186$  Hz,  $\text{P-CH}_2\text{-CH}_2\text{-(CH}_2)_3\text{-CH}_3$ ), 28.86 (d,  $^2\text{J}_{\text{C/P}} = 186$  Hz,  $\text{P-CH}_2\text{-CH}_2\text{-(CH}_2)_{11}\text{-CH}_3$ ), 28.99 (s, ), 29.03 (s,  $\text{P}-(\text{CH}_2)_4\text{-CH}_2\text{-CH}_3$ ), 29.05 (s, ), 29.70 (d,  $^3\text{J}_{\text{C/P}} = 60$  Hz,  $\text{P}-(\text{CH}_2)_2\text{-CH}_2\text{-(CH}_2)_{10}\text{-CH}_3$ ), 29.93 (d,  $^3\text{J}_{\text{C/P}} = 60$  Hz,  $\text{P}-(\text{CH}_2)_2\text{-CH}_2\text{-(CH}_2)_2\text{-CH}_3$ ), 30.36 (s,  $\text{P}-(\text{CH}_2)_3\text{-CH}_2\text{-(CH}_2)_9\text{-CH}_3$ ), 31.28 (s,  $\text{P}-(\text{CH}_2)_3\text{-CH}_2\text{-CH}_2\text{-CH}_3$ ).

$^{11}\text{B}$  NMR (64.48 MHz,  $d_6$ -DMSO)  $\delta$ : -1.26.

$^{19}\text{F}$  NMR (564.69 MHz,  $d_6$ -DMSO)  $\delta$ : -148.42.

$^{31}\text{P}\{^1\text{H}\}$ NMR (242.94 MHz,  $d_6$ -DMSO)  $\delta$ : 33.70.

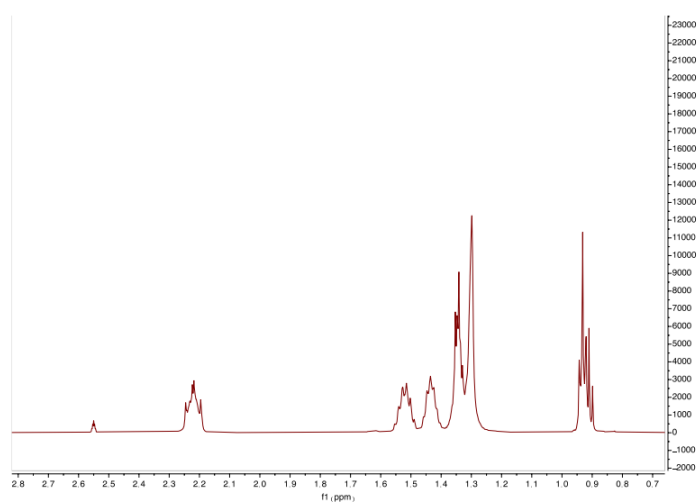


**Figure S5.11.**  $^1\text{H}$  NMR spectrum ( $d_6$ -DMSO, 600.13 MHz, 25 °C) of  $[\text{P}_{666,14}][\text{BF}_4]$ .

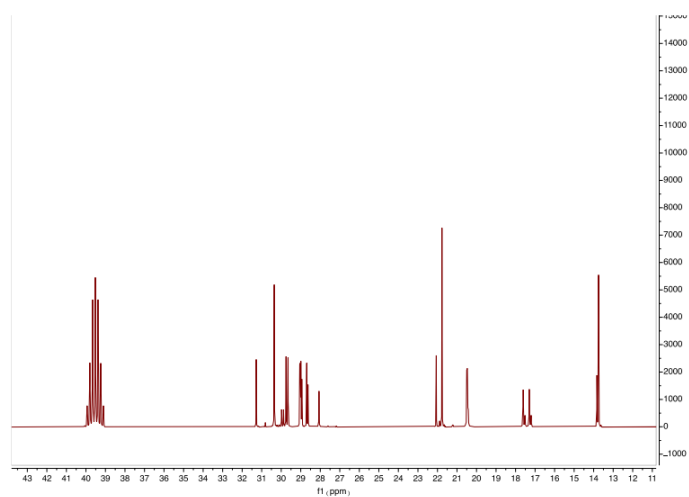


**Figure S5.12.**  $^{13}\text{C}$  NMR spectrum ( $d_6$ -DMSO, 150.90 MHz, 25 °C) of  $[\text{P}_{666,14}][\text{BF}_4]$ .

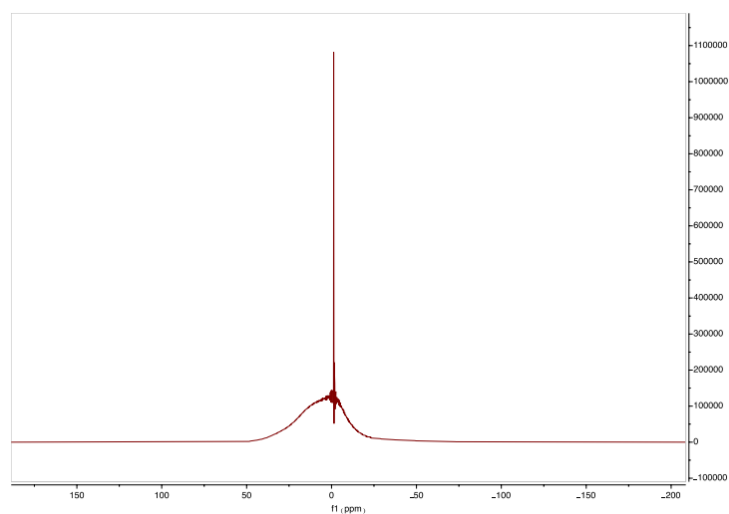


**Figure S5.13.**  $^{11}\text{B}$  NMR spectrum ( $d_6$ -DMSO, 64.48 MHz, 25 °C) of  $[\text{P}_{666,14}][\text{BF}_4]$ .

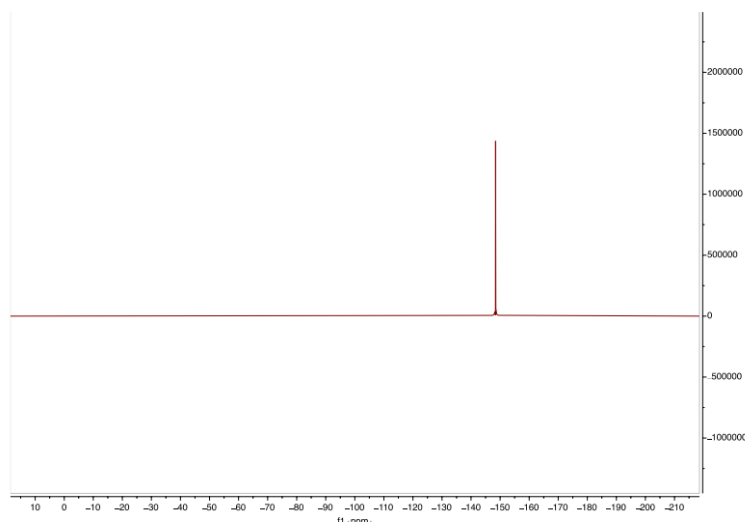


**Figure S5.14.**  $^{19}\text{F}$  NMR spectrum ( $d_6$ -DMSO, 564.69 MHz, 25 °C) of  $[\text{P}_{666,14}][\text{BF}_4]$ .

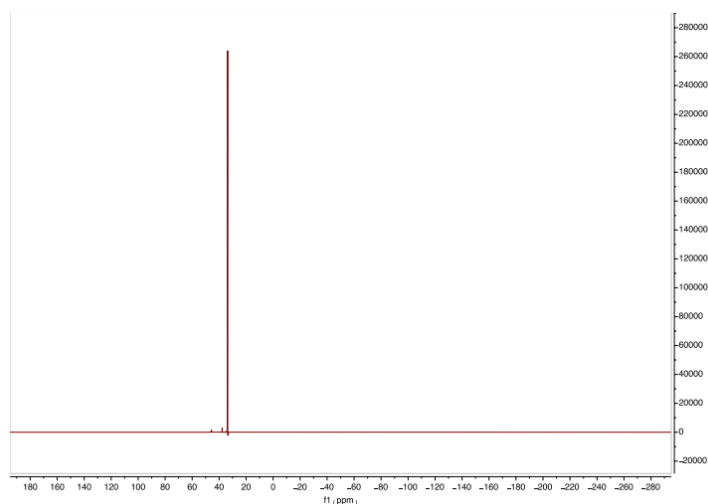


**Figure S5.15.**  $^{31}\text{P}$  NMR spectrum ( $d_6$ -DMSO, 242.94 MHz, 25 °C) of  $[\text{P}_{666,14}][\text{BF}_4]$ .

**$[\text{P}_{666,14}][\text{TAU}]$ .** Trihexyl(tetradecyl)phosphonium chloride  $[\text{P}_{666,14}]\text{Cl}$  was converted to  $[\text{P}_{666,14}][\text{OH}]$  (solution in methanol) following a literature procedure. [45]  $[\text{P}_{666,14}][\text{TAU}]$  was synthesised following a modified literature procedure.[46] Taurine (0.012 mol eq.) was dissolved in 35 cm<sup>3</sup> of deionised water (18.2 M $\Omega$ .cm) and  $[\text{P}_{666,14}][\text{OH}]$  (0.015 mol eq., solution in methanol) was added. The solution was stirred for 2 h at ambient temperature and the water-methanol mixture was removed via rotary evaporation (3 h, 30-80 °C). Crude product was dissolved in 50 ml of dry acetonitrile and stored in the fridge (5 °C) for 12h. The excess taurine crystallised and was filtered off. Acetonitrile was removed via rotary evaporation (30 min, 60 °C) and the ionic liquid was dried under high vacuum (overnight, 70 °C,  $10^{-2}$  mbar). XRF analysis of  $[\text{P}_{666,14}][\text{TAU}]$  confirmed chloride content was below the detectable limit.  $^1\text{H}$ ,  $^{13}\text{C}$ , and  $^{31}\text{P}$  NMR spectra of the ionic liquid were recorded in  $d_6$ -DMSO.

$^1\text{H}$  NMR (600.13 MHz,  $d_6$ -DMSO)  $\delta$ : 0.83-0.92 (m, 12H) 1.19-1.28 (m, 18H), 1.28-1.35 (m, 14H), 1.35-1.44 (m, 8H), 1.44-1.54 (m, 8H), 2.20-2.30 (m, 8H), 2.47-2.53 (t, 2H), 2.77-2.83 (t, 2H).

$^{13}\text{C}\{^1\text{H}\}$  NMR (150.90 MHz,  $d_6$ -DMSO)  $\delta$ : 13.61 (s, P-(CH<sub>2</sub>)<sub>5</sub>-CH<sub>3</sub>), 13.66 (s, P-(CH<sub>2</sub>)<sub>13</sub>-CH<sub>3</sub>), 17.39 (d,  $^1J_{\text{C/P}} = 186$  Hz, P-CH<sub>2</sub>-(CH<sub>2</sub>)<sub>4</sub>-CH<sub>3</sub>), 17.47 (d,  $^1J_{\text{C/P}} = 192$  Hz, P-CH<sub>2</sub>-(CH<sub>2</sub>)<sub>12</sub>-CH<sub>3</sub>), 20.56 (s, ), 20.58 (s, ), 21.75 (s, ), 22.03 (s, ), 28.13 (s, ), 28.85 (d,  $^2J_{\text{C/P}} = 204$  Hz, P-CH<sub>2</sub>-CH<sub>2</sub>-(CH<sub>2</sub>)<sub>3</sub>-CH<sub>3</sub>), 28.96 (s, ), 29.01 (d,  $^2J_{\text{C/P}} = 36$  Hz, P-CH<sub>2</sub>-CH<sub>2</sub>-(CH<sub>2</sub>)<sub>11</sub>-CH<sub>3</sub>), (s, P-(CH<sub>2</sub>)<sub>4</sub>-CH<sub>2</sub>-CH<sub>3</sub>), (s, ), 29.71 (d,  $^3J_{\text{C/P}} = 60$  Hz, P-(CH<sub>2</sub>)<sub>2</sub>-CH<sub>2</sub>-(CH<sub>2</sub>)<sub>10</sub>-CH<sub>3</sub>), 29.97 (d,  $^3J_{\text{C/P}} = 60$  Hz, P-(CH<sub>2</sub>)<sub>2</sub>-CH<sub>2</sub>-(CH<sub>2</sub>)<sub>2</sub>-CH<sub>3</sub>), 30.37 (s, P-(CH<sub>2</sub>)<sub>3</sub>-CH<sub>2</sub>-(CH<sub>2</sub>)<sub>9</sub>-CH<sub>3</sub>), 31.26 (s, P-(CH<sub>2</sub>)<sub>3</sub>-CH<sub>2</sub>-CH<sub>2</sub>-CH<sub>3</sub>) 38.52 (s, SO<sub>3</sub>-CH<sub>2</sub>-CH<sub>2</sub>-NH<sub>2</sub>), 54.76 (s, SO<sub>3</sub>-CH<sub>2</sub>-CH<sub>2</sub>-NH<sub>2</sub>).

$^{31}\text{P}\{^1\text{H}\}$  NMR (242.94 MHz,  $d_6$ -DMSO)  $\delta$ : 33.53.

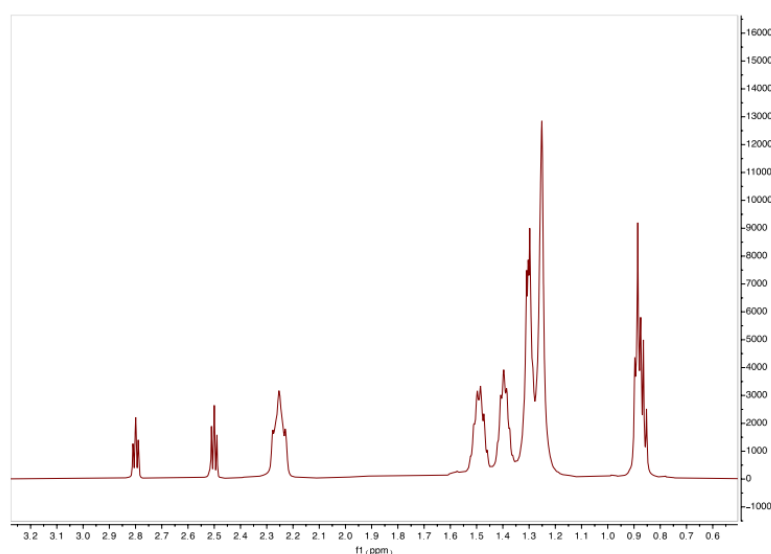


**Figure S5.16.**  $^1\text{H}$  NMR spectrum ( $d_6$ -DMSO, 600.13 MHz, 25 °C) of [P<sub>666,14</sub>][TAU].

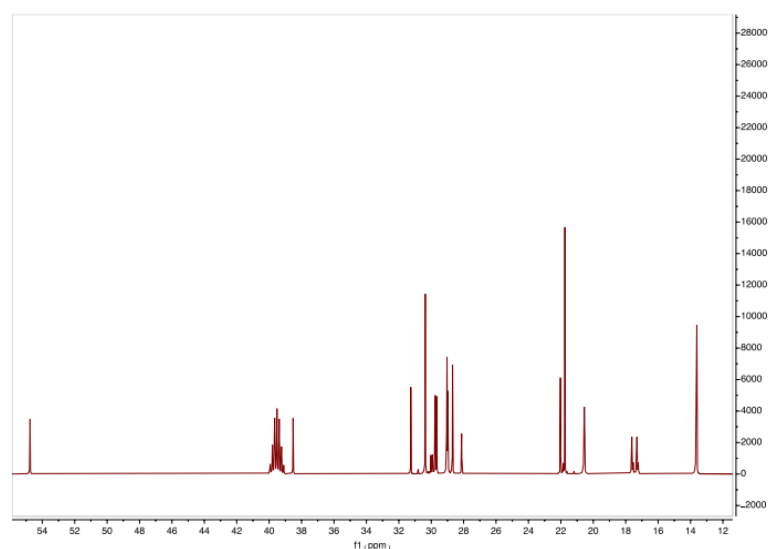


**Figure S5.17.**  $^{13}\text{C}$  NMR spectrum ( $d_6$ -DMSO, 150.90 MHz, 25 °C) of [P<sub>666,14</sub>][TAU].

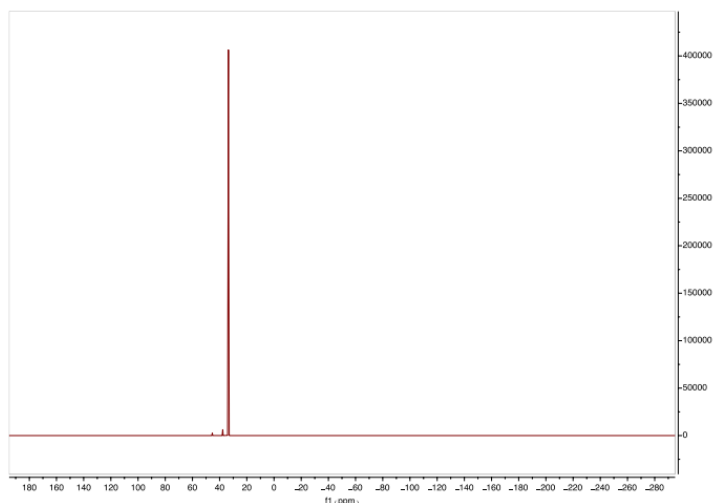


**Figure S5.18.**  $^{31}\text{P}$  NMR spectrum ( $d_6$ -DMSO, 242.94 MHz, 25 °C) of  $[\text{P}_{666,14}][\text{TAU}]$ .

**$[\text{P}_{666,14}][\text{BH}_4]$ .** Trihexyl(tetradecyl)phosphonium chloride  $[\text{P}_{666,14}]\text{Cl}$  (0.10 mol eq.) and sodium borohydride,  $\text{Na}[\text{BH}_4]$  (0.13 mol eq.) were separately added to 150  $\text{cm}^3$  of deionised water (18.2  $\text{M}\Omega\cdot\text{cm}$ ). Both solutions were combined (total of 300  $\text{cm}^3$ ) in a round-bottomed flask, resulting in the formation of a biphasic liquid system. The solution was left to react (48 h, room temperature, 600 rpm). The ionic liquid layer was dissolved in 300  $\text{cm}^3$  of chloroform ( $\text{CHCl}_3$ ) and collected using a separating funnel. The dense chloroform layer was washed ten times with 100  $\text{cm}^3$  of salt solution (1.0 equivalent of  $\text{NaBH}_4$  in 1000  $\text{cm}^3$  of deionised water (18.2  $\text{M}\Omega\cdot\text{cm}$ )). Chloroform was removed via rotary evaporation (30 min, 35 °C) and the solution was dried overnight under high vacuum (12 h, 70 °C,  $10^{-2}$  mbar). XRF analysis of  $[\text{P}_{666,14}][\text{BH}_4]$  recorded a chloride content of 47900 ppm with a lower detection limit (LLD) of 3.57 ppm. Chloride removal was carried out in three subsequent polishing steps.

Firstly, ionic liquid  $[\text{P}_{666,14}][\text{BH}_4]$  was redissolved in 300  $\text{cm}^3$  of chloroform and additional washes were performed to lower the chloride content. 1.0 equivalent of  $\text{NaBH}_4$  was dissolved in 150  $\text{cm}^3$  of deionised water (18.2  $\text{M}\Omega\cdot\text{cm}$ ) and added to the solution. The reaction mixture was stirred for 4 h, then allowed to stand for 30 min for chloroform–water phase separation. Centrifugation was performed to encourage phase disentanglement. The dense chloroform layer was washed seven times with 100  $\text{cm}^3$  of deionised water (18.2  $\text{M}\Omega\cdot\text{cm}$ ) to remove traces of  $\text{NaCl}$  by-product residing within the organic layer. Chloroform was removed via rotary evaporation (30 min, 35 °C) and the solution was dried overnight under high vacuum (12 h, 70 °C,  $10^{-2}$  mbar). XRF analysis of  $[\text{P}_{666,14}][\text{BH}_4]$  recorded a chloride content of 9270 ppm with a lower detection limit (LLD) of 3.97 ppm.

Secondly, the ionic liquid  $[\text{P}_{666,14}][\text{BH}_4]$  was again redissolved in 300  $\text{cm}^3$  of chloroform and additional washes were performed to lower the chloride content. 1.0 equivalent of

NaBH<sub>4</sub> was dissolved in 150 cm<sup>3</sup> of deionised water (18.2 MΩ.cm) and added to the solution. The reaction mixture was stirred for 4 h, then allowed to stand for an additional 30 min. Centrifugation was performed to encourage phase disentanglement. The dense chloroform layer was washed seven times with 100 cm<sup>3</sup> of deionised water (18.2 MΩ.cm). Chloroform was removed via rotary evaporation (30 min, 35 °C) and the solution was dried overnight under high vacuum (12 h, 70 °C, 10-2 mbar). XRF analysis of [P<sub>666,14</sub>][BH<sub>4</sub>] recorded a chloride content of 7230 ppm with a lower detection limit (LLD) of 3.96 ppm.

In the final step, the ionic liquid [P<sub>666,14</sub>][BH<sub>4</sub>] was redissolved in 300 cm<sup>3</sup> of chloroform and additional washes were performed. 1.0 equivalent of NaBH<sub>4</sub> was dissolved in 150 cm<sup>3</sup> of deionised water (18.2 MΩ.cm) and added to the solution. The reaction mixture was stirred for 4 h and allowed to stand for 30 min. The dense chloroform layer was washed seven times with 100 cm<sup>3</sup> of salt solution (1.0 equivalent of NaBH<sub>4</sub> in 700 cm<sup>3</sup> of deionised water (18.2 MΩ.cm). Final three washes were performed with 100 cm<sup>3</sup> of deionised water (18.2 MΩ.cm). Chloroform was removed via rotary evaporation (30 min, 35 °C) and the ionic liquid was dried overnight under high vacuum (12 h, 70 °C, 10<sup>-2</sup> mbar). XRF analysis of [P<sub>666,14</sub>][BH<sub>4</sub>] was recorded three times to give an average chloride content of 1326 ppm with an average lower detection limit (LLD) of 3.49 ppm. <sup>1</sup>H, <sup>13</sup>C, <sup>11</sup>B and <sup>31</sup>P NMR spectra of the ionic liquid were recorded in *d*<sub>6</sub>-DMSO.

<sup>1</sup>H NMR (600.13 MHz, *d*<sub>6</sub>-DMSO) δ: -0.72(-0.27) (q, 4H) 0.44-0.60 (m, 12H), 0.60-0.92 (m, 18H), 0.92-1.01 (m, 14H), 1.04-1.16 (m, 8H), 1.17-1.38 (m, 8H), 1.92-2.48 (m, 8H).

<sup>13</sup>C{<sup>1</sup>H} NMR (150.90 MHz, *d*<sub>6</sub>-DMSO) δ: 13.15 (s, P-(CH<sub>2</sub>)<sub>5</sub>-CH<sub>3</sub>), 13.18 (s, P-(CH<sub>2</sub>)<sub>13</sub>-CH<sub>3</sub>), 18.07 (d, <sup>1</sup>J<sub>CP</sub> = 186 Hz, P-CH<sub>2</sub>-(CH<sub>2</sub>)<sub>4</sub>-CH<sub>3</sub> and P-CH<sub>2</sub>-(CH<sub>2</sub>)<sub>12</sub>-CH<sub>3</sub>), 20.98 (s, P-(CH<sub>2</sub>)<sub>12</sub>-CH<sub>2</sub>-CH<sub>3</sub>), 21.06 (s, P-(CH<sub>2</sub>)<sub>11</sub>-CH<sub>2</sub>-CH<sub>2</sub>-CH<sub>3</sub>), 21.62 (s, P-(CH<sub>2</sub>)<sub>10</sub>-CH<sub>2</sub>-(CH<sub>2</sub>)<sub>2</sub>-CH<sub>3</sub>), 21.75 (s, P-(CH<sub>2</sub>)<sub>9</sub>-CH<sub>2</sub>-(CH<sub>2</sub>)<sub>3</sub>-CH<sub>3</sub>), 21.84 (s, P-(CH<sub>2</sub>)<sub>8</sub>-CH<sub>2</sub>-(CH<sub>2</sub>)<sub>4</sub>-CH<sub>3</sub>), 27.54 (d, <sup>2</sup>J<sub>CP</sub> = 258 Hz, P-CH<sub>2</sub>-CH<sub>2</sub>-(CH<sub>2</sub>)<sub>3</sub>-CH<sub>3</sub>), 28.29 (s, P-(CH<sub>2</sub>)<sub>7</sub>-CH<sub>2</sub>-(CH<sub>2</sub>)<sub>5</sub>-CH<sub>3</sub>), 28.57 (s, P-(CH<sub>2</sub>)<sub>6</sub>-CH<sub>2</sub>-(CH<sub>2</sub>)<sub>6</sub>-CH<sub>3</sub>), 28.75 (s, P-(CH<sub>2</sub>)<sub>5</sub>-CH<sub>2</sub>-(CH<sub>2</sub>)<sub>7</sub>-CH<sub>3</sub>), 28.87 (s, P-(CH<sub>2</sub>)<sub>4</sub>-CH<sub>2</sub>-(CH<sub>2</sub>)<sub>8</sub>-CH<sub>3</sub>), 28.96 (s, P-(CH<sub>2</sub>)<sub>4</sub>-CH<sub>2</sub>-CH<sub>3</sub>), 29.64 (d, <sup>2</sup>J<sub>CP</sub> = 54 Hz, P-CH<sub>2</sub>-CH<sub>2</sub>-(CH<sub>2</sub>)<sub>11</sub>-CH<sub>3</sub>), 30.00 (d, <sup>3</sup>J<sub>CP</sub> = 60 Hz, P-(CH<sub>2</sub>)<sub>2</sub>-CH<sub>2</sub>-(CH<sub>2</sub>)<sub>10</sub>-CH<sub>3</sub>), 30.17 (d, <sup>3</sup>J<sub>CP</sub> = 54 Hz, P-(CH<sub>2</sub>)<sub>2</sub>-CH<sub>2</sub>-(CH<sub>2</sub>)<sub>2</sub>-CH<sub>3</sub>), 30.36 (s, P-(CH<sub>2</sub>)<sub>3</sub>-CH<sub>2</sub>-(CH<sub>2</sub>)<sub>9</sub>-CH<sub>3</sub>), 31.11 (s, P-(CH<sub>2</sub>)<sub>3</sub>-CH<sub>2</sub>-CH<sub>2</sub>-CH<sub>3</sub>).

<sup>11</sup>B NMR (64.48 MHz, *d*<sub>6</sub>-DMSO) δ: -36.98 (p).

<sup>31</sup>P{<sup>1</sup>H} NMR (242.94 MHz, *d*<sub>6</sub>-DMSO) δ: 32.72.

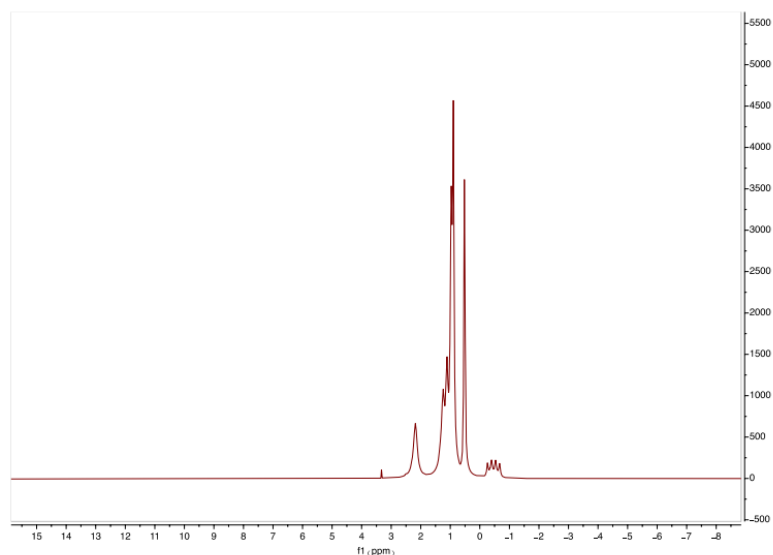


**Figure S5.19.**  $^1\text{H}$  NMR spectrum ( $d_6$ -DMSO, 600.13 MHz, 25 °C) of  $[\text{P}_{666,14}][\text{BH}_4]$ .

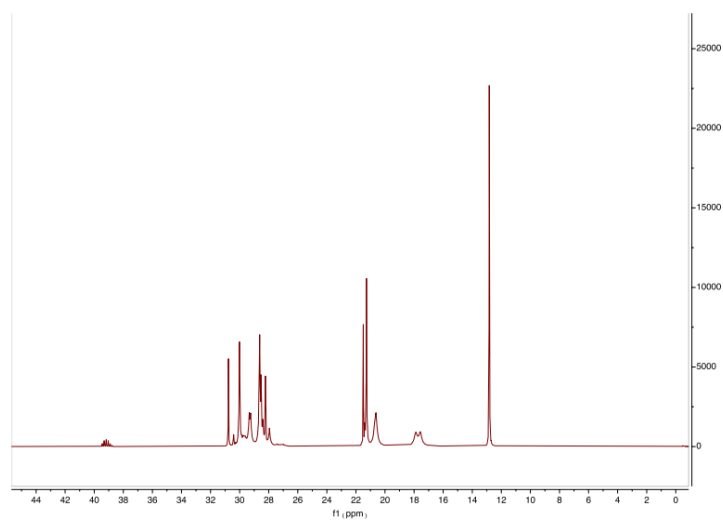


**Figure S5.20.**  $^{13}\text{C}$  NMR spectrum ( $d_6$ -DMSO, 150.90 MHz, 25 °C) of  $[\text{P}_{666,14}][\text{BH}_4]$ .

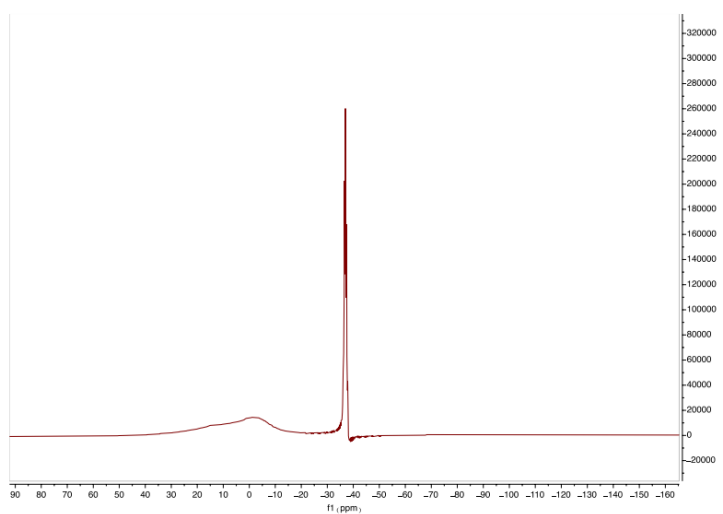


**Figure S5.21.**  $^{11}\text{B}$  NMR spectrum ( $d_6$ -DMSO, 64.48 MHz, 25 °C) of  $[\text{P}_{666,14}][\text{BH}_4]$ .

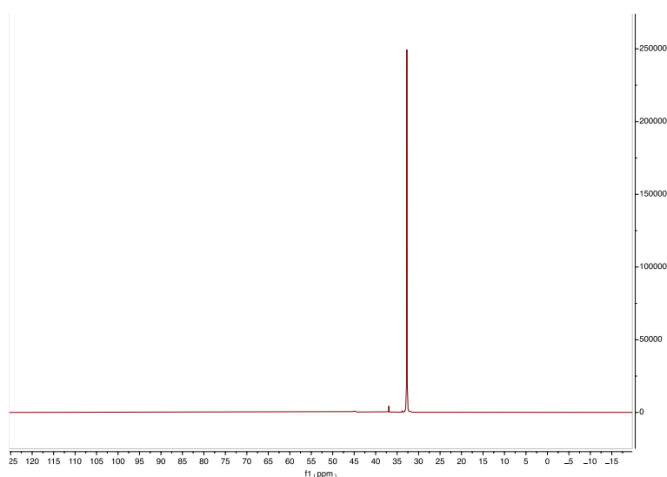


**Figure S5.22.**  $^{31}\text{P}$  NMR spectrum ( $d_6$ -DMSO, 242.94 MHz, 25 °C) of  $[\text{P}_{666,14}][\text{BH}_4]$ .

$[\text{P}_{666,14}][\text{BOB}]$  was synthesized in a two-step synthesis, following a recently-reported, improved procedure [47].

**Na[BOB].** Oxalic acid (0.03 mol eq.) and boric acid (0.01 mol eq.) were separately dissolved in water and then combined under constant stirring.  $\text{Na}_2\text{CO}_3$  (0.5 mol eq.) was slowly added to the mixture with vigorous stirring. The turbid solution was heated in an oil bath at 120 °C and water collected by distillation until a dry white powder was obtained. The crude product was dispersed in hot acetonitrile at 60 °C and stirred for one hour. The white powder formed was isolated using vacuum filtration. The product was further washed with cold ethanol and the powder was dried overnight under high vacuum (12 h, 60 °C,  $10^{-2}$  mbar).  $^{13}\text{C}$  and  $^{11}\text{B}$  NMR spectra of sodium bis(oxalato)borate ( $\text{Na}[\text{BOB}]$ ) were recorded in  $\text{CDCl}_3$ .

$^{13}\text{C}\{^1\text{H}\}$ NMR (150.90 MHz,  $\text{CDCl}_3$ )  $\delta$ : 158.59.

$^{11}\text{B}$  NMR (64.48 MHz,  $\text{CDCl}_3$ )  $\delta$ : 7.35.

**$[\text{P}_{666,14}][\text{BOB}]$ .** Trihexyl(tetradecyl)phosphonium chloride  $[\text{P}_{666,14}]\text{Cl}$  (0.01 mol eq.) and sodium bis(oxalato)borate (0.01 mol eq.) were mixed in 150  $\text{cm}^3$  of dichloromethane, DCM. The reaction mixture was stirred overnight at room temperature and then water was added under continuous stirring. The aqueous layer was separated, and the organic layer was collected and washed with 100  $\text{cm}^3$  deionized water (18.2  $\text{M}\Omega\cdot\text{cm}$ ). Subsequent washes were performed with solution of  $\text{Na}[\text{BOB}]$  in deionized water (18.2  $\text{M}\Omega\cdot\text{cm}$ ). Final three washes were performed with deionised water (18.2  $\text{M}\Omega\cdot\text{cm}$ ) water until no chloride could be detected with silver nitrate solution. Subsequently, DCM was removed via rotary evaporation (30 min, 35 °C) and the ionic liquid was dried overnight under high vacuum (12 h, 60 °C,  $10^{-2}$  mbar). XRF analysis of  $[\text{P}_{666,14}][\text{BOB}]$  recorded a chloride content of 158 ppm with a lower detection limit (LLD) of 2.22 ppm.  $^1\text{H}$ ,  $^{13}\text{C}$  and  $^{31}\text{P}$  NMR spectra of the ionic liquid were recorded in  $\text{CDCl}_3$ .

$^1\text{H}$  NMR (600.13 MHz,  $\text{CDCl}_3$ )  $\delta$ : 0.86-0.91 (m, 12H), 1.21-1.31 (m, 18H), 1.31-1.35 (m, 14H), 1.44-1.51 (m, 8H), 1.51-1.58 (m, 8H), 2.09-2.21 (m, 8H).

$^{13}\text{C}\{^1\text{H}\}$  NMR (150.90 MHz,  $\text{CDCl}_3$ )  $\delta$ : 13.98 (s, P-( $\text{CH}_2$ )<sub>5</sub>-**CH**<sub>3</sub>), 14.23 (s, P-( $\text{CH}_2$ )<sub>13</sub>-**CH**<sub>3</sub>), 18.99 (d,  $^1J_{\text{C/P}} = 186$  Hz, P-**CH**<sub>2</sub>-( $\text{CH}_2$ )<sub>4</sub>-**CH**<sub>3</sub>), 19.00 (d,  $^1J_{\text{C/P}} = 186$  Hz, P-**CH**<sub>2</sub>-( $\text{CH}_2$ )<sub>12</sub>-**CH**<sub>3</sub>), 21.63 (s, P-( $\text{CH}_2$ )<sub>12</sub>-**CH**<sub>2</sub>-**CH**<sub>3</sub>), 21.67 (s, P-( $\text{CH}_2$ )<sub>11</sub>-**CH**<sub>2</sub>-**CH**<sub>2</sub>-**CH**<sub>3</sub>), 21.71 (s, P-( $\text{CH}_2$ )<sub>10</sub>-**CH**<sub>2</sub>-( $\text{CH}_2$ )<sub>2</sub>-**CH**<sub>3</sub>), 22.37 (s, P-( $\text{CH}_2$ )<sub>9</sub>-**CH**<sub>2</sub>-( $\text{CH}_2$ )<sub>3</sub>-**CH**<sub>3</sub>), 22.80 (s, P-( $\text{CH}_2$ )<sub>8</sub>-**CH**<sub>2</sub>-( $\text{CH}_2$ )<sub>4</sub>-**CH**<sub>3</sub>), 27.92 (s, P-( $\text{CH}_2$ )<sub>7</sub>-**CH**<sub>2</sub>-( $\text{CH}_2$ )<sub>5</sub>-**CH**<sub>3</sub>), 28.35 (s, P-( $\text{CH}_2$ )<sub>6</sub>-**CH**<sub>2</sub>-( $\text{CH}_2$ )<sub>6</sub>-**CH**<sub>3</sub>), 28.94 (s, P-( $\text{CH}_2$ )<sub>5</sub>-**CH**<sub>2</sub>-( $\text{CH}_2$ )<sub>7</sub>-**CH**<sub>3</sub>), 29.47 (d,  $^2J_{\text{C/P}} = 72$  Hz, P-**CH**<sub>2</sub>-**CH**<sub>2</sub>-( $\text{CH}_2$ )<sub>3</sub>-**CH**<sub>3</sub>), 29.65 (d,  $^2J_{\text{C/P}} = 72$  Hz, P-**CH**<sub>2</sub>-**CH**<sub>2</sub>-( $\text{CH}_2$ )<sub>11</sub>-**CH**<sub>3</sub>), 29.75 (s, P-( $\text{CH}_2$ )<sub>4</sub>-**CH**<sub>2</sub>-**CH**<sub>3</sub>), 29.79 (s, P-( $\text{CH}_2$ )<sub>4</sub>-**CH**<sub>2</sub>-( $\text{CH}_2$ )<sub>8</sub>-**CH**<sub>3</sub>), 30.44 (d,  $^3J_{\text{C/P}} = 60$  Hz, P-( $\text{CH}_2$ )<sub>2</sub>-**CH**<sub>2</sub>-( $\text{CH}_2$ )<sub>2</sub>-**CH**<sub>3</sub>), 30.79 (d,  $^3J_{\text{C/P}} = 60$  Hz, P-( $\text{CH}_2$ )<sub>2</sub>-**CH**<sub>2</sub>-( $\text{CH}_2$ )<sub>10</sub>-**CH**<sub>3</sub>), 31.01 (s, P-( $\text{CH}_2$ )<sub>3</sub>-**CH**<sub>2</sub>-( $\text{CH}_2$ )<sub>9</sub>-**CH**<sub>3</sub>), 32.03 (s, P-( $\text{CH}_2$ )<sub>3</sub>-**CH**<sub>2</sub>-**CH**<sub>2</sub>-**CH**<sub>3</sub>), 159.03 (s, B( $\text{C}_2\text{O}_4$ )<sub>2</sub>).

$^{11}\text{B}$  NMR (64.48 MHz,  $\text{CDCl}_3$ )  $\delta$ : 7.66.

$^{31}\text{P}\{^1\text{H}\}$  NMR (242.94 MHz,  $\text{CDCl}_3$ )  $\delta$ : 33.18.

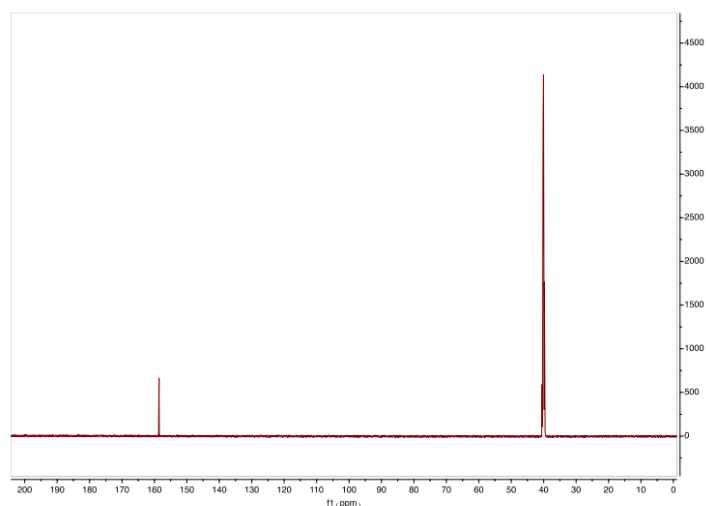


**Figure S5.23.**  $^{13}\text{C}$  NMR spectrum ( $\text{CDCl}_3$ , 150.90 MHz, 25 °C) of Na[BOB].

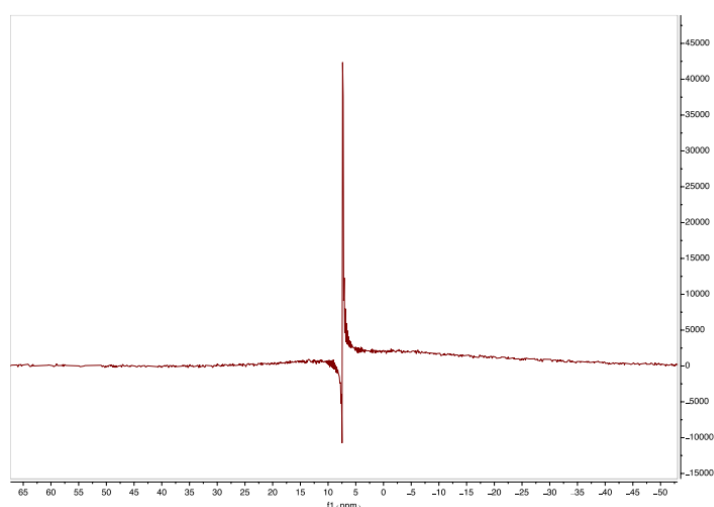


**Figure S5.24.**  $^{11}\text{B}$  NMR spectrum ( $\text{CDCl}_3$ , 64.48 MHz, 25 °C) of Na[BOB].

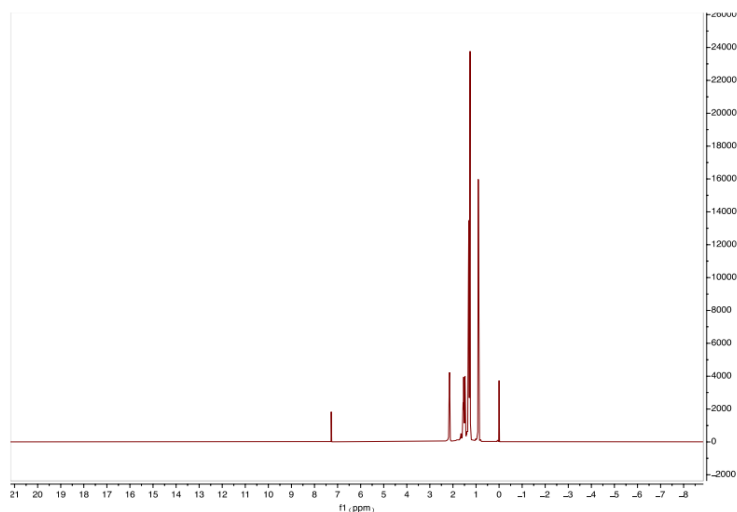


**Figure S5.25.**  $^1\text{H}$  NMR spectrum ( $\text{CDCl}_3$ , 600.13 MHz, 25 °C) of  $[\text{P}_{666,14}][\text{BOB}]$ .

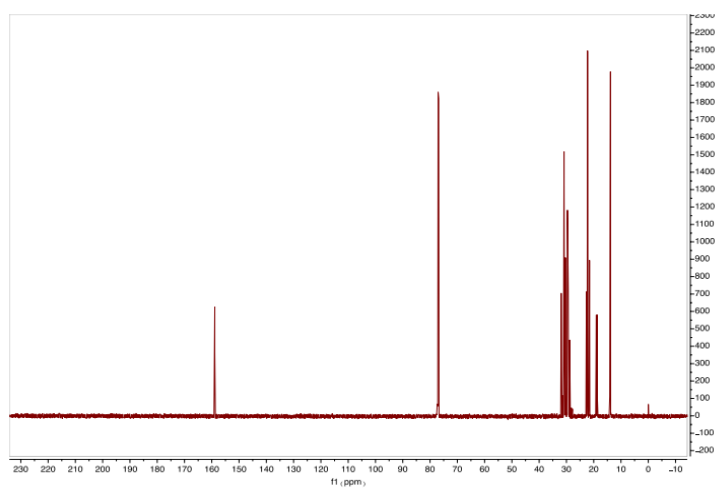


**Figure S5.26.**  $^{13}\text{C}$  NMR spectrum ( $\text{CDCl}_3$ , 150.90 MHz, 25 °C) of  $[\text{P}_{666,14}][\text{BOB}]$ .

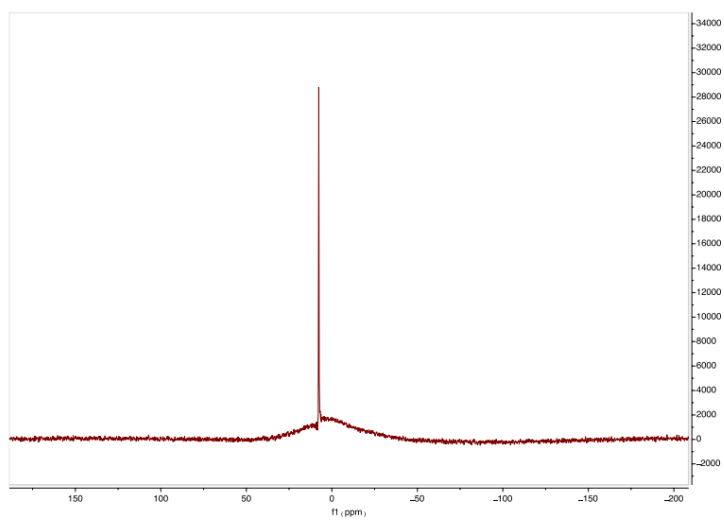


**Figure S5.27.**  $^{11}\text{B}$  NMR spectrum ( $\text{CDCl}_3$ , 64.48 MHz, 25 °C) of  $[\text{P}_{666,14}][\text{BOB}]$ .

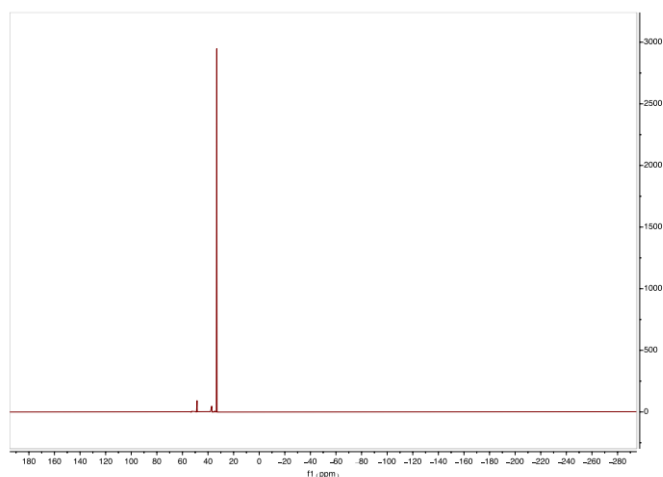


**Figure S5.28.**  $^{31}\text{P}$  NMR spectrum ( $\text{CDCl}_3$ , 242.94 MHz, 25 °C) of  $[\text{P}_{666,14}][\text{BOB}]$ .

Prior to the measurements, the samples were dried under vacuum at 90 °C for 24 h. The water content detected using the Karl Fischer method, was around 500 and 300 ppm before and after drying, respectively. The one exception is  $[\text{P}_{666,14}][\text{BH}_4]$  with the water content of 3% after drying.

### Supplementary Note 1

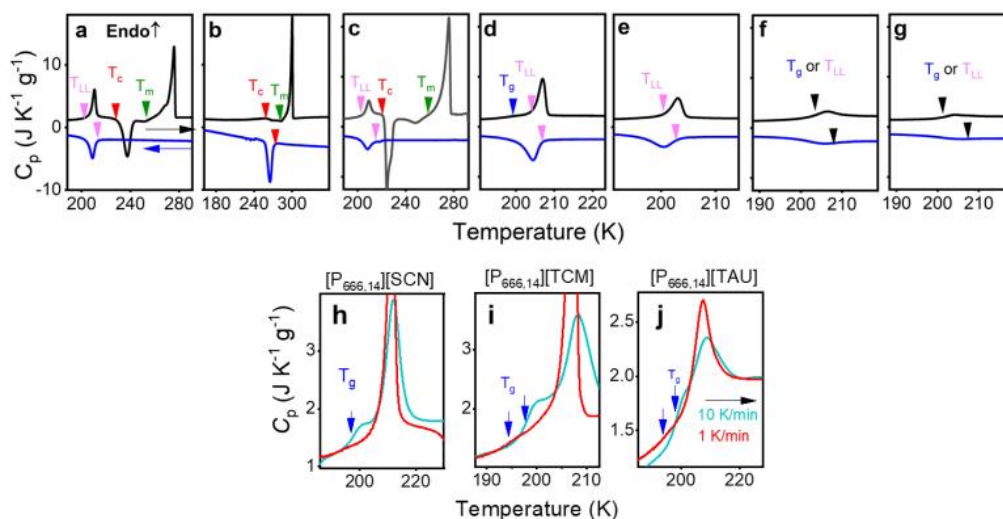


**Figure S5.29** Differential scanning calorimetry (DSC) traces of  $[\text{P}_{666,14}]^+$ -based ILs. The DSC data collected on cooling (blue curve) and subsequent heating (black curve) with the rate of  $1 \text{ K}\cdot\text{min}^{-1}$  of **a**  $[\text{P}_{666,14}][\text{SCN}]$ , **b**  $[\text{P}_{666,14}][\text{BF}_4]$ , **c**  $[\text{P}_{666,14}][\text{BH}_4]$ , **d**  $[\text{P}_{666,14}][\text{TCM}]$ , **e**  $[\text{P}_{666,14}][\text{TFSI}]$ , **f**  $[\text{P}_{666,14}][\text{TAU}]$ , **g**  $[\text{P}_{666,14}][\text{BOB}]$ . Arrows indicate the onset of: LLT (pink one), melting point (green one), cold crystallization (red one) and  $T_g$  (blue one). Panels **h**, **i** and **j** shows DSC thermograms obtained on heating of aged glass with the rate of 1 K per min (red curve) and 10 K per min (turquoise curve).  $T_g$  shifts left on a slower scanning rate as indicated by blue arrows; however, at the same time, a slow release of enthalpy occurs and overshoot peak is no longer visible.

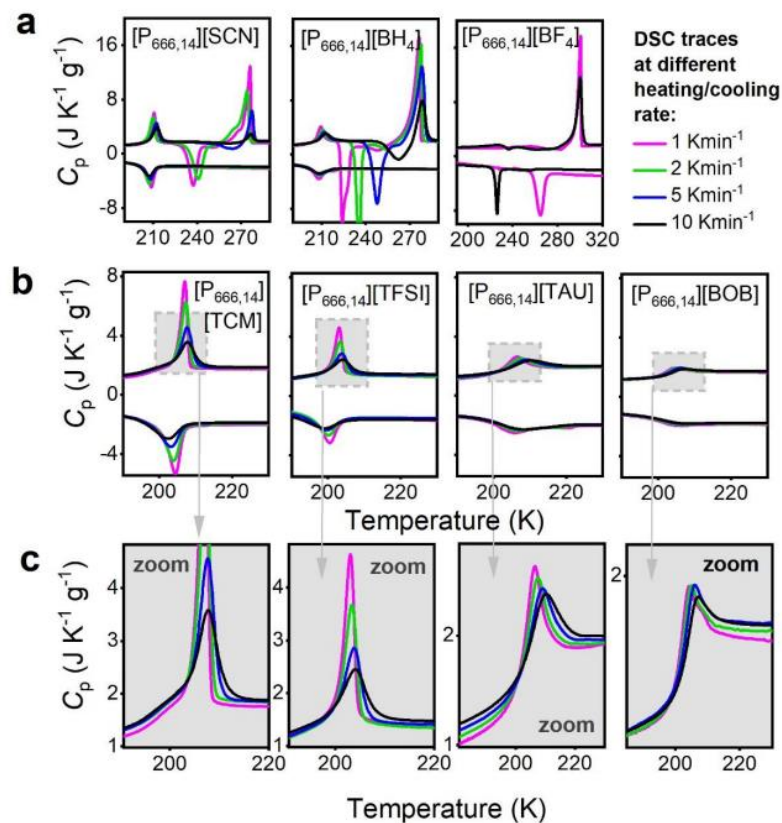


**Figure S5.30.** a and b Heat capacity measured on different heating and cooling rate:10 (black), 5 (blue), 2 (green), and 1 (pink) K per min for [P<sub>666,14</sub>]-based ionic liquids (the name of IL is described in the panel). Panel c presents the zoom of data presented in panel b.

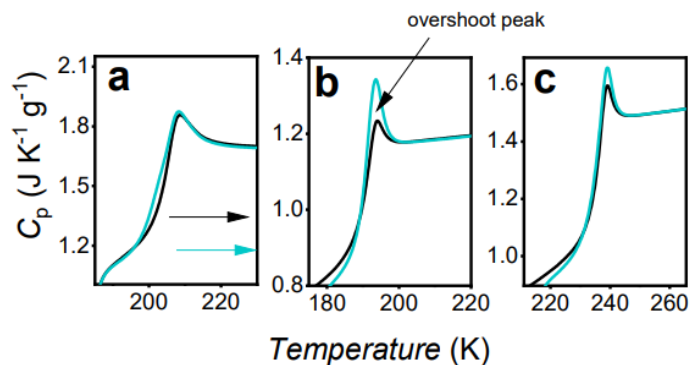


**Figure S5.31.** Comparison between DSC traces obtained during the standard heating with rate 10 K/min (black curved) and after the 6 hours-aging process performed in the glassy state (turquoise curve) for a [P<sub>666,14</sub>][BOB], b [BMIm][BETI] and c [BMP][BOB]. In the latter two cases, clear overshoot peak of aged glass is visible.

## Supplementary Note 2

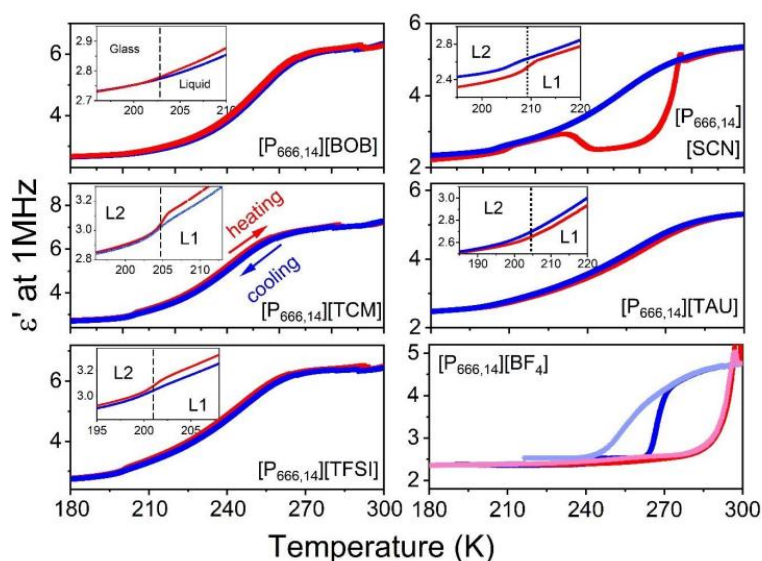


**Figure S5.32.** The change of  $\epsilon'$  as a function of temperature at fixed frequency ( $f=1\text{MHz}$ ) during cooling (blue) and heating (red) with a rate of 1 K per min for  $[\text{P}_{666,14}][\text{BOB}]$ ,  $[\text{P}_{666,14}][\text{TCM}]$ ,  $[\text{P}_{666,14}][\text{TFSI}]$ ,  $[\text{P}_{666,14}][\text{SCN}]$ ,  $[\text{P}_{666,14}][\text{TAU}]$  and  $[\text{P}_{666,14}][\text{BF}_4]$ . The light blue and light red curves in the graph of  $[\text{P}_{666,14}][\text{BF}_4]$  denote the cooling and heating processes with a rate of 5 K per min, respectively.

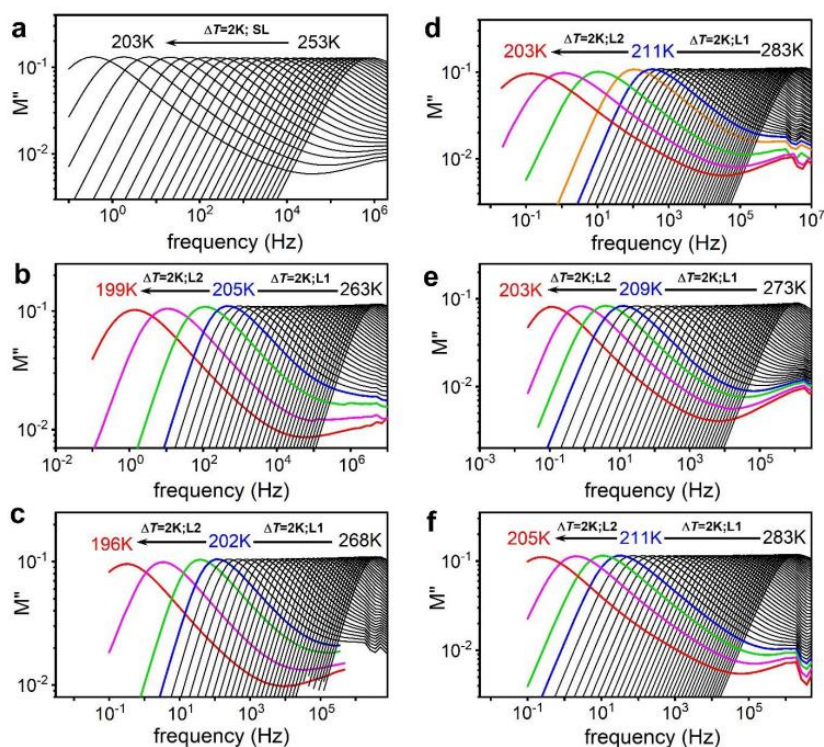


**Figure S5.33.** All the dielectric modulus spectra collected for  $[\text{P}_{666,14}]$ -based IL at ambient pressure conditions. **a**  $[\text{P}_{666,14}][\text{BOB}]$ , **b**  $[\text{P}_{666,14}][\text{TCM}]$ , **c**  $[\text{P}_{666,14}][\text{TFSI}]$ , **d**  $[\text{P}_{666,14}][\text{SCN}]$ , **e**  $[\text{P}_{666,14}][\text{TAU}]$ , **f**  $[\text{P}_{666,14}][\text{BF}_4]$ .

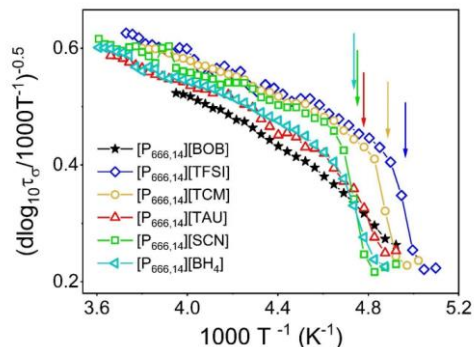


**Figure S5.34.** Stickel analysis of studied samples. Arrows indicate the LLT.

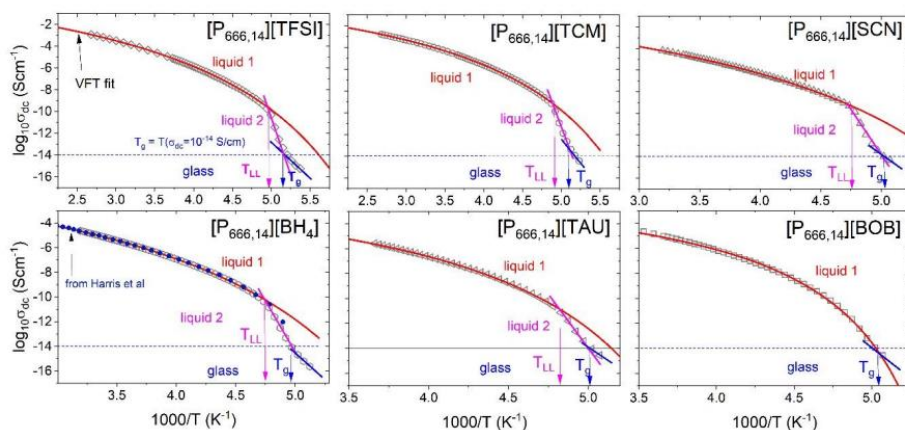


**Figure S5.35.** The dc-conductivity of [P<sub>666,14</sub>]-based ionic liquids as a function of inverse temperature. The solid circles for [P<sub>666,14</sub>][BH<sub>4</sub>] represent the data taken from ref.[30].  $T_{LL}$  denotes temperature of liquid-liquid transition.

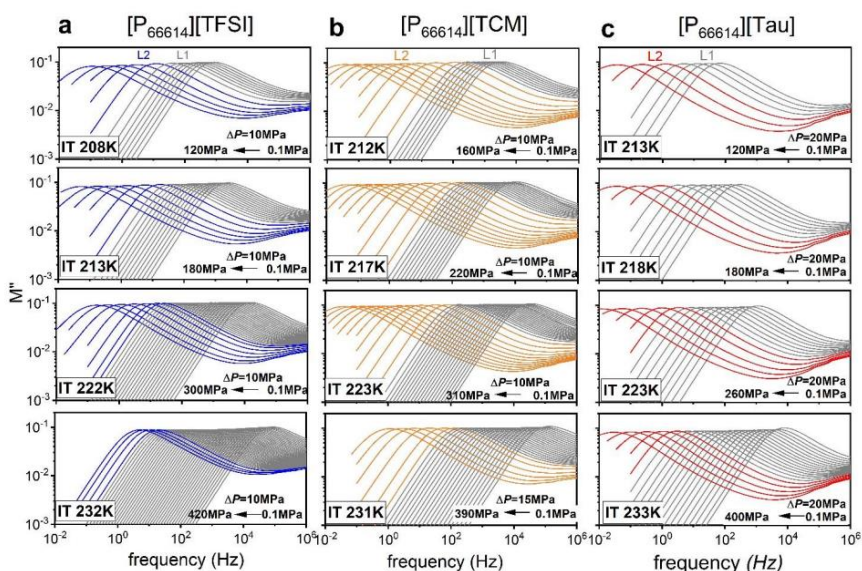


**Figure S5.36.** Dielectric modulus data recorded at high-pressure conditions and for different temperatures for **a** [P<sub>666,14</sub>][TFSI], **b** [P<sub>666,14</sub>][TCM] and **c** [P<sub>666,14</sub>][TAU]. IT denotes temperature of isotherm. The data collected in liquid 1 (L1) are marked in grey, while data collected in liquid 2 (L2) are marked in color.

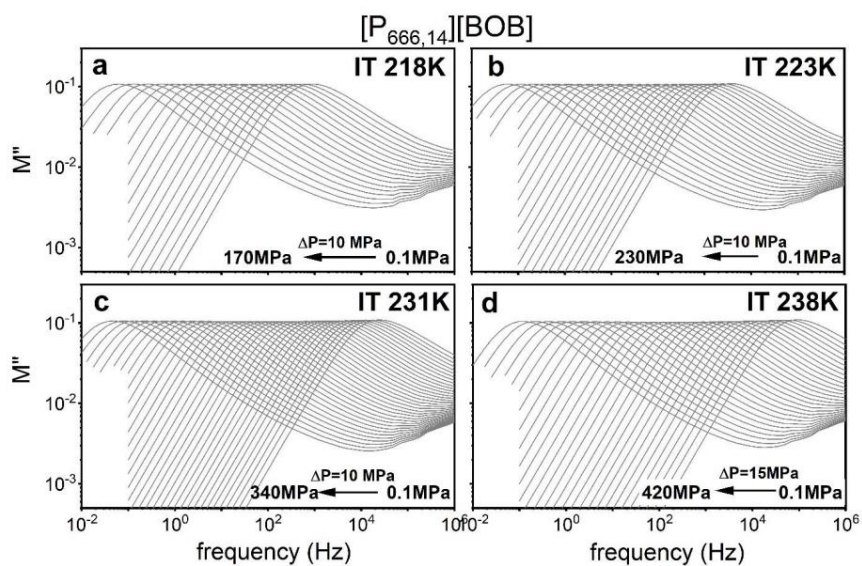


**Figure S5.37.** Dielectric modulus data of  $[P_{666,14}][BOB]$  recorded at high-pressure conditions at **a** 218 K, **b** 223 K, **c** 231 K, **d** 238 K. IT=isotherm.

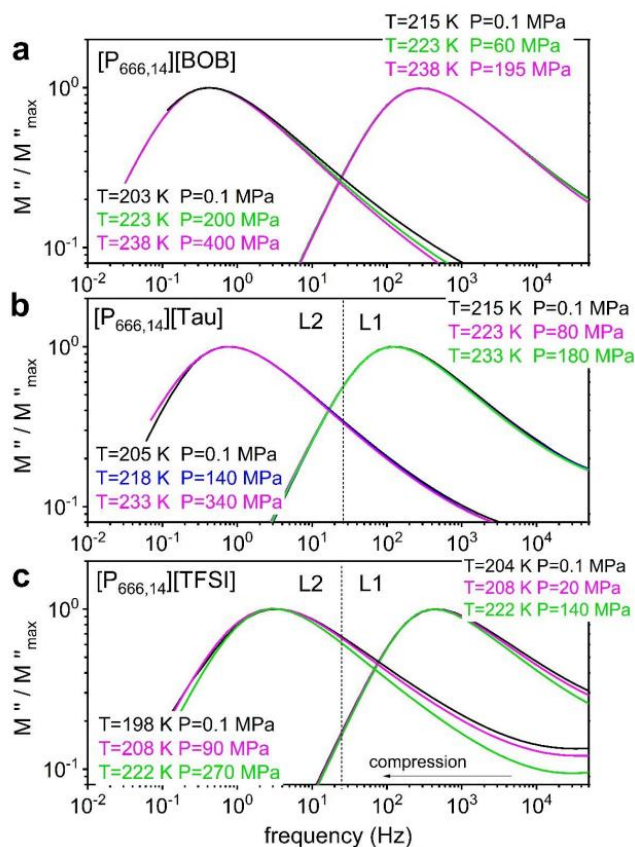


**Figure S5.38.** The representative  $M''(f)$  spectra of **a**  $[P_{666,14}][BOB]$ , **b**  $[P_{666,14}][TAU]$  and **c**  $[P_{666,14}][TFSI]$  recorded at various  $T$ - $P$  conditions; however the same  $\tau_\sigma$  superimposed to each other at two different frequencies in liquid 1 (L1) and liquid 2 (L2).

### Supplementary Note 3

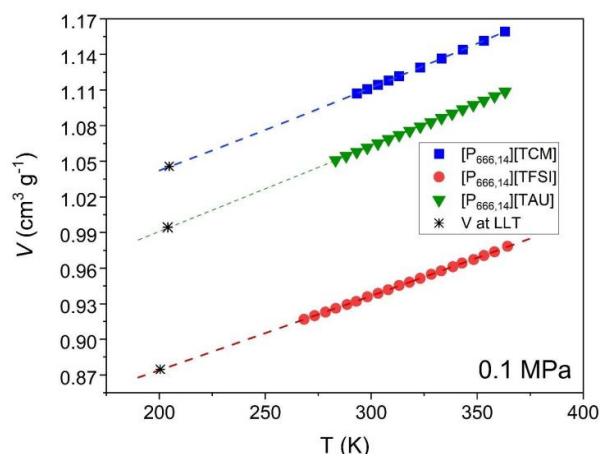


**Figure S5.39.** Temperature dependence of specific volume for [P<sub>666,14</sub>][TCM], [P<sub>666,14</sub>][TAU] and [P<sub>666,14</sub>][TFSI]. The data for [P<sub>666,14</sub>][TFSI] were taken from ref.[48].

## 5.7 References

- [1] C. A. Angell, *Science* **267**, 1924 (1995).
- [2] G. Adam and J. H. Gibbs, *J. Chem. Phys.* **43**, 139 (1965).
- [3] Y. Katayama, T. Mizutani, W. Utsumi, O. Shimomura, M. Yamakata, and K. Funakoshi, *Nature* **403**, 170 (2000).
- [4] S. Sastry and C. Austen Angell, *Nat. Mater* **2**, 739 (2003).
- [5] I. Saika-Voivod, P. H. Poole, and F. Sciortino, *Nature* **412**, 514 (2001).
- [6] J. N. Glosli and F. H. Ree, *Phys. Rev. Lett.* **82**, 4659 (1999).
- [7] H. W. Sheng, H. Z. Liu, Y. Q. Cheng, J. Wen, P. L. Lee, W. K. Luo, S. D. Shastri, and E. Ma, *Nat. Mater* **6**, 192 (2007).
- [8] W. Xu, M. T. Sandor, Y. Yu, H.-B. Ke, H.-P. Zhang, M.-Z. Li, W.-H. Wang, L. Liu, and Y. Wu, *Nat. Commun.* **6**, 7696 (2015).
- [9] G. N. Greaves, M. C. Wilding, S. Fearn, D. Langstaff, F. Kargl, S. Cox, Q. V. Van, O. Majérus, C. J. Benmore, R. Weber, C. M. Martin, and L. Hennem, *Science* **322**, 566 (2008).
- [10] S. Wei, F. Yang, J. Bednarcik, I. Kaban, O. Shuleshova, A. Meyer, and R. Busch, *Nat. Commun.* **4**, 2083 (2013).
- [11] C. A. Angell, *Science* **319**, 582 (2008).
- [12] K. Ito, C. T. Moynihan, and C. A. Angell, *Nature* **398**, 492 (1999).
- [13] R. Kurita and H. Tanaka, *Science* **306**, 845 (2004).
- [14] H. Tanaka, R. Kurita, and H. Mataka, *Phys. Rev. Lett.* **92**, 025701 (2004).
- [15] M. Kobayashi and H. Tanaka, *Nat. Commun.* **7**, 13438 (2016).
- [16] R. Kurita and H. Tanaka, *J. Phys.: Condens. Matter* **17**, L293 (2005).
- [17] M. Zhu, J.-Q. Wang, J. H. Perepezko, and L. Yu, *J. Chem. Phys.* **142**, 244504 (2015).
- [18] H. Tanaka, *Phys. Rev. E* **62**, 6968 (2000).

- [19] X. Liu, S. Liu, E. Chen, L. Peng, and Y. Yu, *J. Phys. Chem. Lett.* **10**, 4285 (2019).
- [20] H. Otsuka, A. Hamasaki, T. Iiyama, and S. Ozeki, *J. Phys. Chem. Lett.* **11**, 21 (2020).
- [21] J. Wang, Y. He, J. Li, R. Hu, H. Kou, and E. Beaugnon, *Mater. Chem. Phys.* **149–150**, 17 (2015).
- [22] J. Wang, J. Li, R. Hu, H. Kou, and E. Beaugnon, *Mater. Lett.* **145**, 261 (2015).
- [23] Q. Zeng, Y. Ding, W. L. Mao, W. Yang, Stas. V. Sinogeikin, J. Shu, H. Mao, and J. Z. Jiang, *Phys. Rev. Lett.* **104**, 105702 (2010).
- [24] L. Liu, S.-H. Chen, A. Faraone, C.-W. Yen, and C.-Y. Mou, *Phys. Rev. Lett.* **95**, 117802 (2005).
- [25] M. Armand, F. Endres, D. R. MacFarlane, H. Ohno, and B. Scrosati, *Nat. Mater* **8**, 621 (2009).
- [26] C. A. Angell, W. Xu, M. Yoshizawa-Fujita, A. Hayashi, J.-P. Belieres, P. Lucas., M. Videa, Z.-F. Zhao, K. Ueno, Y. Ansari, J. Thomson, and D. Gervasio, in *Electrochemical Aspects of Ionic Liquids* (John Wiley & Sons, Ltd, **2011**), pp. 5–31.
- [27] R. S. Anareddy and S. K. Shaw, *J. Phys. Chem. C* **123**, 8975 (2019).
- [28] R. S. Anareddy and S. K. Shaw, *Langmuir* **32**, 5147 (2016).
- [29] R. S. Anareddy and S. K. Shaw, *J. Phys. Chem. C* **122**, 19731 (2018).
- [30] M. A. Harris, T. Kinsey, D. V. Wagle, G. A. Baker, and J. Sangoro, *Proc. Natl. Acad. Sci.* **118**, e2020878118 (2021).
- [31] K. J. Fraser and D. R. MacFarlane, *Aust. J. Chem.* **62**, 309 (2009).
- [32] M. Schmeisser and R. van Eldik, *Dalton Trans.* **43**, 15675 (2014).
- [33] I. M. Hodge, *Science* **267**, 1945 (1995).
- [34] F. Kremer and A. Schönhal, editors, *Broadband Dielectric Spectroscopy* (Springer Berlin Heidelberg, Berlin, Heidelberg, **2003**).
- [35] J. R. Sangoro and F. Kremer, *Acc. Chem. Res.* **45**, 525 (2012).
- [36] M. Paluch, editor, *Dielectric Properties of Ionic Liquids* (Springer International Publishing, Cham, **2016**).
- [37] K. L. Ngai, G. N. Greaves, and C. T. Moynihan, *Phys. Rev. Lett.* **80**, (1998).
- [38] Z. Wojnarowska and M. Paluch, *J. Phys.: Condens. Matter* **27**, 073202 (2015).
- [39] R. Kurita and H. Tanaka, *Phys. Rev. Lett.* **95**, 065701 (2005).
- [40] G. Monaco, S. Falconi, W. A. Crichton, and M. Mezouar, *Phys. Rev. Lett.* **90**, 255701 (2003).
- [41] G. D. Mukherjee and R. Boehler, *Phys. Rev. Lett.* **99**, 225701 (2007).
- [42] G. Floudas, M. Paluch, A. Grzybowski, and K. Ngai, *Molecular Dynamics of Glass-Forming Systems*, Vol. 1 (Springer Berlin Heidelberg, Berlin, Heidelberg, **2011**).
- [43] A. Dzienia, P. Maksym, M. Tarnacka, I. Grudzka-Flak, S. Golba, A. Zięba, K. Kaminski, and M. Paluch, *Green Chem.* **19**, 3618 (2017).
- [44] S. Aasland and P. F. McMillan, *Nature* **369**, 633 (1994).

- [45] J. L. Ferguson, J. D. Holbrey, S. Ng, N. V. Plechkova, K. R. Seddon, A. A. Tomaszowska, and D. F. Wassell, *Pure Appl. Chem.* **84**, 723 (2011).
- [46] B. F. Goodrich, J. C. de la Fuente, B. E. Gurkan, Z. K. Lopez, E. A. Price, Y. Huang, and J. F. Brennecke, *J. Phys. Chem. B* **115**, 9140 (2011).
- [47] M. R. Shimpi, P. Rohlmann, F. U. Shah, S. Glavatskih, and O. N. Antzutkin, *Phys. Chem. Chem. Phys.* **23**, 6190 (2021).
- [48] J. Klomfar, M. Součková, and J. Pátek, *J. Chem. Eng. Data* **59**, 2263 (2014).

# 6 Effect of Bulky Anions on the Liquid-Liquid Phase Transition in Phosphonium Ionic Liquids: Ambient and High-Pressure Dielectric Studies



Reprinted with permission from Scientific Reports volume 13, Article number: 3040 (2023)

<https://doi.org/10.1038/s41598-023-29518-8> Copyright © 2023, The Author(s) Published by Scientific Reports

## Author Declaration:

*“Effect of bulky anions on the liquid-liquid phase transition in phosphonium ionic liquids: Ambient and high-pressure dielectric studies”, Sci. Rep., 13, 3040 (2023)*

B. Yao conceived the study, planned and carried out the experimental work, analyzed the data, prepared figures, and co-wrote the manuscript.

Signature:

M. Paluch co-wrote the manuscript.

Signature:

Z. Wojnarowska co-wrote the manuscript and supervised the project.

Signature:

## 6.1 Abstract

Although the first-order liquid–liquid phase transition (LLT) has been reported to exist in various systems (i.e., phosphorus, silicon, water, triphenyl phosphite, etc.), it is still one of the most challenging problems in the field of physical science. Recently, we found that this phenomenon occurs in the family of trihexyl(tetradecyl)phosphonium  $[P_{66,14}]^+$  based ionic liquids (ILs) with different anions (Wojnarowska et al in *Nat Commun* 13:1342, 2022). To understand the molecular structure–property relationships governing LLT, herein, we examine ion dynamics of two other quaternary phosphonium ILs containing long alkyl chains in cation and anion. We found that IL with the anion containing branched  $-O-(CH_2)_5-CH_3$  side chains does not reveal any signs of LLT, while IL with shorter alkyl chains in the anion brings a hidden LLT, i.e., it overlaps with the liquid-glass transition. Ambient pressure dielectric and viscosity measurements revealed a peculiar behavior of ion dynamics near  $T_g$  for IL with hidden LLT. Moreover, high-pressure studies have shown that IL with hidden LLT has relatively strong pressure sensitivity compared to the one without first-order phase transition. At the same time, the former exposes the inflection point indicating the concave-convex character of  $\log\tau_\sigma(P)$  dependences.

## 6.2 Introduction

In the past decades, the interest in ionic liquids (ILs), fluids composed solely of ions, has risen tremendously, especially in the fields of chemistry, materials science, and energy research [1]. This is because a change of cation or anion can significantly tune the physicochemical properties of IL. Good chemical and thermal stability, high ionic conductivity ( $> 10^{-4} \text{ S cm}^{-1}$ ), negligible vapor pressure, and non-flammability make ILs promising electrolyte [2] and green solvents for applications in electrochemistry [3], biology, and pharmacology [4],[5].

Compared to cyclic ILs containing imidazolium, pyrrolidinium, or piperidinium cations, quaternary phosphonium (P) ILs have many valuable physicochemical properties, e.g., enhanced hydrophobicity and significantly wider electrochemical window [6]. Furthermore, they exhibit relatively low viscosity and thus enhanced ionic conductivity at RT conditions [7],[8]. The origin of these essential features has been examined over the years by several groups. Among the molecular factors which may contribute to the lower viscosity of phosphonium ILs the size of the phosphorous atom, the charge distribution, and the flexibility of bond and dihedral angles were examined. Furthermore, a large volume of phosphonium cations that result from the shielding of phosphonium

core by charge-neutral alkyl groups and bring lower electrostatic friction between counterions was also considered [9],[10].

Extensive investigations of charge transport in phosphonium ionic liquids have shown that the dc conductivity ( $\sigma_{dc}$ ) is closely coupled to their structural ( $\alpha$ ) relaxation [11], which is related to the viscosity ( $\eta$ ) by the Maxwell equation,  $\eta = G_{\infty}/\tau_{\alpha}$  [12]. Thus, the classical vehicle mechanism characterizes the ion transport in phosphonium ILs. Furthermore, these materials have been reported in the literature as good glass-formers, i.e., they can form an amorphous solid if sufficiently fast cooling is applied [13]. Over a relatively narrow temperature range, from RT to the temperature of liquid-glass transition ( $T_g$ ), the viscosity of P-ILs increases dramatically, even by ten orders of magnitude. At the same time,  $\sigma_{dc}$  decreases in the same manner, commonly described by a single Vogel-Fulcher-Tamman (VFT) equation  $\sigma_{dc} = \sigma_0 \exp(DT_0/(T-T_0))$ , where  $\sigma_0$  is a pre-exponential factor, and D quantifies the departure of experimental data from the Arrhenius law. An alternative measure of the non-Arrhenius conductivity and fluidity behavior is the fragility index  $m_P$  defining the steepness of the temperature dependence of various transport properties at  $T_g$ . The phosphonium ionic liquids studied so far fall into the intermediate range of fragilities ( $m_P = 46-60$ ) compared to other ionic liquids and glassformers in general [14].

Such a well-defined physical picture of ion dynamics of P-RTILs has been updated by recent studies of trihexyl(tetradecyl)phosphonium  $[P_{666,14}]^+$  based ionic liquids. In particular, it has been shown that at a certain temperature, dc-conductivity and conductivity relaxation times  $\tau_{\sigma} = \epsilon_0 \epsilon_s \sigma_{dc}^{-1}$ , reveal a substantial departure from VFT law accompanied by an abrupt increase in apparent activation energy [15],[16] (note that during the liquid-glass transition, an apparent activation energy decreases [17]). This peculiar behavior, reported for five different  $[P_{666,14}]^+$ -based ILs, has been recognized as the dielectric signature of the first-order liquid-liquid phase transition (LLT). Strictly speaking, two isotropic liquid states of different dc-conductivity behavior were found to exist within a single IL. As a molecular origin of this unique phenomenon, enhanced ordering of cation alkyl chains in non-polar domains was postulated from XRD and IR experiments [16]. Furthermore, it has been shown that LLT occurs at elevated pressure. Namely, isothermal compression triggers the LLT, with the  $\tau_{\sigma}$  at LLT being independent of temperature and pressure conditions. The time scale of ion dynamics at LLT was found anion-specific, i.e., dependent on anion size, geometry, conformational flexibility, and the strength of interionic interactions [15]. Furthermore, it was postulated that large anions most likely complicate the ordering of the alkyl chains in the non-polar domains and consequently prevent the LLT [15].

To further advance the issue of liquid–liquid phase transition in ionic systems, herein we focus on ion dynamics of two ILs containing  $[P_{666,14}]^+$  cation and phosphorus-based anions with long alkyl chains as well. The results of dielectric experiments performed over a wide temperature range revealed that both examined ILs display the conventional dc-conductivity behavior without a clear sign of LLT. However, a more detailed analysis of experimental data indicated that one of the chosen ILs exhibits a hidden LLT. High-pressure dielectric experiments performed for both ILs, have shown distinct differences in their pressure sensitivity of ion dynamics. Furthermore, another unique phenomenon called “inflection point” has been observed for one of examined herein ILs.

### 6.3 Results and discussion

The ILs examined in this work are two quaternary phosphonium ionic liquids with hydrophobic  $[P_{666,14}]^+$  cation and anions: bis(2-ethylhexyl) phosphate ( $[BEHP]^-$ ) and bis(2,4,4-trimethylpentyl) phosphinate ( $[BTMPP]^-$ ). The chemical structures are displayed in Fig. 6.1a. In analogy to cation, the anions reveal non-cyclic nature with two long and branched alkyl chains connected to a phosphorus core. Specifically, in the  $[BEHP]^-$  structure, two six-carbon chains are attached to phosphorus through the oxygen atom. On the other hand, five carbon chains characterize the  $[BTMPP]^-$  anion. The van der Waals volume of anions, determined by the Bondi method [18], is equal to  $V_{[BEHP]}^{vdW} = 0.339 \text{ nm}^3$  and  $V_{[BTMPP]}^{vdW} = 0.321 \text{ nm}^3$ . Consequently, the former provides more sterical hindrance that might affect the alignment of the nonpolar alkyl chains of  $[P_{666,14}]$  cation, suggested as the origin of the liquid–liquid transition. Moreover, oxygen atoms in  $[BEHP]^-$  make the side chains polar, which can also influence the LLT.

Differential scanning calorimetry (DSC) measurements have been performed for initial characterization of  $[P_{666,14}][BTMPP]$  and  $[P_{666,14}][BEHP]$ . Importantly, before the experiments, both examined samples were extensively dried at 343 K under vacuum for 12 h. The DSC thermograms obtained at a cooling rate of  $10 \text{ Kmin}^{-1}$  of examined ILs are given in Fig. 6.1b. It can be seen that both ILs exhibit a step-like increase in heat capacity during the cooling process, which is a typical manifestation of the liquid-glass transition. However, on the heating scan, there are also some unidentified endothermic effects of small intensity (see Fig. S6.1). Since they are not observed on the cooling trace, one can exclude the LLT as the origin of these thermal events. At the same time, one can suppose that the other peaks visible on the heating scan are due to the crystallization of impurities in examined samples. Thus, at this point, the calorimetric results only indicated the occurrence of the typical glass transition in examined ILs and did not provide any signs of the first-order liquid–liquid transition.

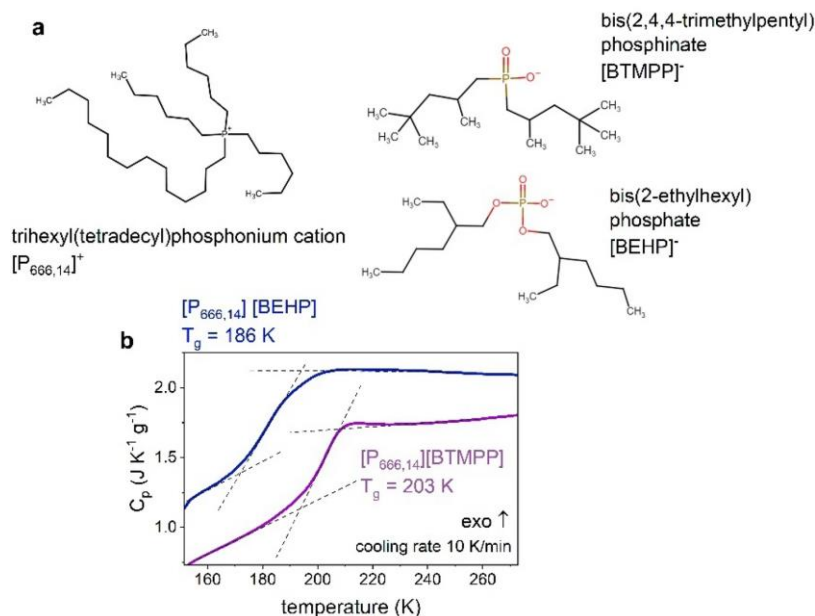


**Fig. 6.1** Initial characterization of studied ILs. **(a)** Chemical structure of trihexyl(tetradecyl)-phosphonium cation  $[P_{666,14}]^+$  and anions: bis(2-ethylhexyl) phosphate  $[BEHP]^-$ , bis(2,4,4-trimethylpentyl) phosphinate  $[BTMPP]^-$ . **(b)** Differential scanning calorimetry (DSC) traces of  $[P_{666,14}][BEHP]$  and  $[P_{666,14}][BTMPP]$  obtained on cooling with the rate of  $10 \text{ Kmin}^{-1}$ .

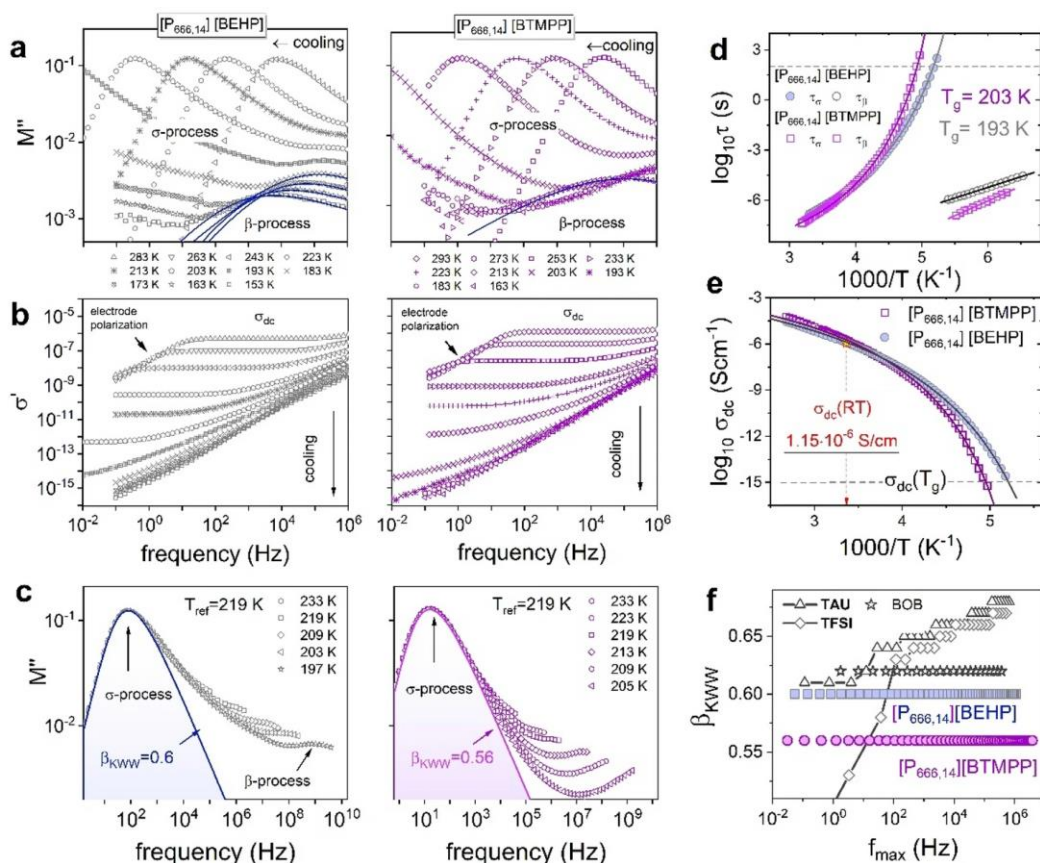


**Fig. 6.2** Dielectric response of examined ILs measured at ambient pressure. **(a)** Imaginary part of the complex electric modulus  $M''$  and **(b)** real part of complex conductivity  $\sigma'$  as a function of frequency at various temperatures for  $[P_{666,14}][BEHP]$  and  $[P_{666,14}][BTMPP]$ . **(c)** Superimposition of  $M''$  spectra of  $[P_{666,14}][BEHP]$ ,  $[P_{666,14}][BTMPP]$  at 0.1 MPa and several temperatures. **(d)** Temperature

dependence of conductivity relaxation times above and below  $T_g$ . **(e)** Temperature dependence of dc-conductivity. Solid lines in **(d)** and **(e)** denote the fits of the VFT equation to experimental data above  $T_g$  and the fits of Arrhenius law for the secondary relaxation process below  $T_g$ . Adj. R-Square of VFT fits is equal to 0.9999 and 0.9992 for  $[P_{666,14}][\text{BEHP}]$ ,  $[P_{666,14}][\text{BTMPP}]$ , respectively. **(f)**  $\beta_{KWW}$  as a function of  $M''(f)$  peak maximum for  $[P_{666,14}][\text{BEHP}]$ ,  $[P_{666,14}][\text{BTMPP}]$  and three others IL, i.e.  $[P_{666,14}][\text{BOB}]$ ,  $[P_{666,14}][\text{TAU}]$  and  $[P_{666,14}][\text{TFSI}]$ .

To characterize the ion dynamics of  $[P_{666,14}][\text{BTMPP}]$  and  $[P_{666,14}][\text{BEHP}]$  ILs through the liquid-glass transition, temperature-dependent dielectric experiments have been performed. Herein, we employed two formalisms, complex electric modulus  $M^*(f)$  and complex conductivity  $\sigma^*(f)$ , to present the obtained data. Both of them are commonly adopted to express the charge transport properties of conducting materials [19],[20],[21]. The representative dielectric spectra of  $[P_{666,14}][\text{BEHP}]$  and  $[P_{666,14}][\text{BTMPP}]$  measured over eight decades of frequency ( $10^{-2}$ – $10^6$  Hz) in a wide temperature range are illustrated in Fig. 6.2a,b, in modulus and conductivity formalism, respectively. In both examined cases, the imaginary part of the complex modulus  $M''(f)$  recorded in a supercooled liquid state takes the form of a well-resolved peak, so-called a conductivity relaxation (denoted as  $\sigma$ -process), which shifts toward lower frequencies upon cooling. This behavior reflects the suppressed mobility of ions and is in keeping with the cooling effects revealed in all kinds of ionic glass formers [22]. Further decreasing temperature below the calorimetric  $T_g$  brings the modulus peak out of the experimental window, and a well-distinguished secondary mode ( $\beta$ ) becomes visible. Similar to the conductivity relaxation, the  $\beta$ -process move toward lower frequencies on cooling; however it is far less temperature-dependent. At the same time, the real part of complex conductivity  $\sigma'(f)$  is characterized by three clearly visible regions: (i) a frequency-independent dc-conductivity ( $\sigma_{dc}$ ) that is proportional to the number of ions and their mobility, (ii) a power-law behavior obeyed on the high-frequency side, (iii) a decrease of  $\sigma'$  from  $\sigma_{dc}$  denoting the electrode polarization effect. Note that both formalisms,  $M''(f)$  and  $\sigma'(f)$ , adopted herein for data analysis, provide information on the ion mobility in a supercooled liquid state; however, compared to modulus representation, dc-plateau is well visible above room temperature. Therefore, the temperature dependence of  $\sigma_{dc}$  over 11 orders of magnitude can be examined. At the same time, only the modulus representation offers a characterization of dynamics in a glassy state.

Taking the last mentioned advantage, we have examined the dynamics of glassy  $[P_{666,14}][\text{BEHP}]$  and  $[P_{666,14}][\text{BTMPP}]$  in more detail. For this purpose, a numerical fitting analysis of  $M''(f)$  data, in terms of the Havriliak–Negami function (Eq. 6.1) [23], has to be carried out.

$$M^*(\omega) = 1/\varepsilon^*(\omega) = \left( \varepsilon_\infty + \frac{\Delta\varepsilon}{[1+(i\omega\tau_{HN})^{\alpha_{HN}}]^{\beta_{HN}}} \right)^{-1} \quad (6.1)$$

where  $\Delta\varepsilon$  is the dielectric strength,  $\varepsilon_\infty$  denotes the high-frequency limit permittivity,  $\tau_{HN}$  is the characteristic relaxation time and the exponents  $\alpha_{HN}$  and  $\beta_{HN}$  represent the symmetric and asymmetric broadenings of the dielectric loss curve. Having the values of fitting parameters, we calculated the characteristic relaxation times of  $\beta$ -mode observed in modulus spectra below  $T_g$ :

$$\tau_\beta = \tau_{HN} \left[ \sin\left(\frac{\alpha_{HN}\cdot\pi}{2+2\beta_{HN}}\right) \right]^{-1/\alpha_{HN}} \left[ \sin\left(\frac{\alpha_{HN}\cdot\beta_{HN}\cdot\pi}{2+2\beta_{HN}}\right) \right]^{1/\alpha_{HN}} \quad (6.2)$$

The obtained temperature variations in  $\tau_\beta$  are depicted in Fig. 6.2d. As can be seen,  $\log\tau_\beta(T^{-1})$  data of both examined ILs obeys the Arrhenius law  $\tau_\beta = \tau_\infty \exp(E_a/RT)$  with the energy barrier equal to  $24.4 \pm 0.2$  kJ/mol and  $33.9 \pm 0.5$  kJ/mol, for [P<sub>666,14</sub>][BEHP] and [P<sub>666,14</sub>][BTMPP], respectively. Considering the relatively low activation energy of these modes, one can assume their intramolecular origin—specifically, rotations of anion or cation alkyl chains. The higher  $E_a$  determined for relaxation of 5-carbon anion's chains can be rationalized by more extended branching compared to the side groups of [BEHP]<sup>-</sup> anion. The coupling model (CM) predictions have been performed to confirm the intramolecular origin of secondary modes. As can be seen in Fig. S6.2, the temperature dependence of  $\tau_{IG}$  (denoting the potential position of a secondary mode of intermolecular origin) for [P<sub>666,14</sub>][BTMPP] and [P<sub>666,14</sub>][BEHP] does not match with the relaxation times of the  $\beta$ -process, indicating their intramolecular nature.

To describe the ion dynamics of [P<sub>666,14</sub>][BEHP] and [P<sub>666,14</sub>][BTMPP] in a supercooled liquid state thoroughly, first, we focus on the shape of the conductivity relaxation process. At first sight in Fig. 6.2a, the shape of the  $\sigma$ -peak does not change across the broad temperature range. Several dielectric modulus spectra have been superimposed to verify this observation. As presented in Fig. 6.2c, the time–temperature superposition (TTS) principle is indeed fulfilled for both examined ILs. Thus, the phosphonium ILs with [BEHP]<sup>-</sup> and [BTMPP]<sup>-</sup> anions follow the behavior of typical ionic glass-formers [24] rather than [P<sub>666,14</sub>]-based ILs with the liquid–liquid phase transition (see Fig. 6.2f). To quantify the shape of the conductivity relaxation process of [P<sub>666,14</sub>][BEHP] and [P<sub>666,14</sub>][BTMPP], the Kohlrausch–Williams–Watts (KWW) function,  $\Phi(t) = \exp[-(t/\tau_\alpha)^{\beta_{KWW}}]$  has been employed. It is well known that the stretching parameter  $\beta_{KWW}$  takes the value between 0 and 1, and it is lower for the broader and more asymmetric peaks [25]. As presented in Fig. 6.2c, the KWW function with  $\beta_{KWW} = 0.6$  and 0.56 describes the  $M''(f)$  spectra of [P<sub>666,14</sub>][BEHP] and [P<sub>666,14</sub>][BTMPP], respectively. When compared to other [P<sub>666,14</sub>]-based ILs, the examined herein fluids reveal quite broad  $M''(f)$  peaks, i.e., they are characterized by a relatively broad distribution of the relaxation times (see Fig. 6.2f). It means that in the supercooled state of ILs containing [P<sub>666,14</sub>]<sup>+</sup>

cation and small anions like  $[\text{SCN}]^-$ ,  $[\text{TAU}]^-$  or  $[\text{TFSI}]^-$ , the ions are more dynamically correlated (i.e., components relax with similar  $\tau_\sigma$ ), whereas an increase of anion size to  $[\text{BEHP}]^-$  or  $[\text{BTMPP}]^-$  brings higher heterogeneity (i.e., some components are more mobile and some are less mobile).

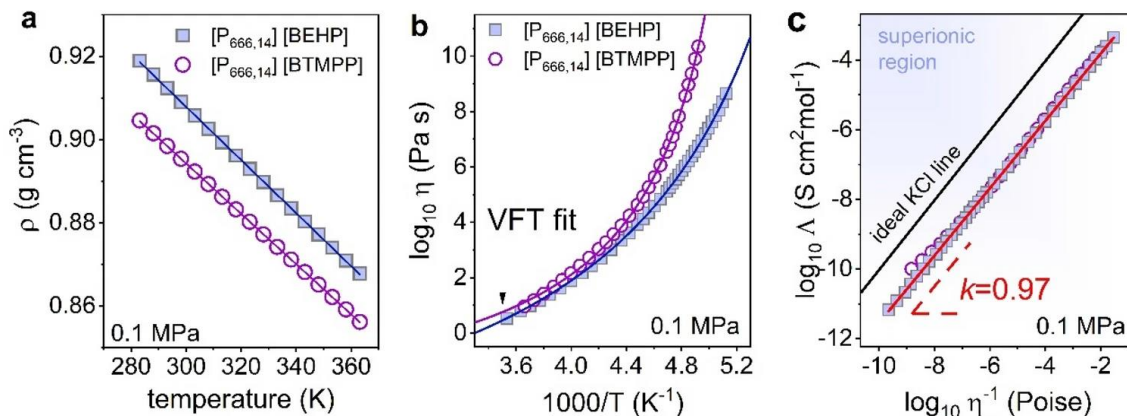


**Fig. 6.3** (a) Temperature dependence of density for  $[\text{P}_{666,14}][\text{BEHP}]$  and  $[\text{P}_{666,14}][\text{BTMPP}]$  measured at 0.1 MPa. The solid lines are linear fits. (b) Temperature dependence of viscosity for studied ILs. Solid lines denote the fit of the VFT equation. (c) Walden plot constructed for studied ILs comparing with ideal KCl line.

The next important aspect of ion dynamics in a supercooled state is the temperature behavior of dc-conductivity  $\sigma_{dc}$  and conductivity relaxation times  $\tau_\sigma$ . The former is determined directly from the frequency-independent part of  $\sigma'(f)$  while  $\tau_\sigma$  is calculated as the inverse of  $M''(f)$  peak maximum ( $\tau_\sigma = (2\pi f_{max})^{-1}$ ). The obtained results are presented in Fig. 6.2d,e. At first sight, one can see that the data meet each other at high temperatures, diverge more and more during the cooling and achieve the time scale of 100 s at two temperatures different by 10 K. Thus, both samples reveal the same dc-conductivity at RT conditions; however various  $T_g$ . Note that  $\sigma_{dc}(\text{RT}) = 1.15 \cdot 10^{-6} \text{ Scm}^{-1}$  is around 1.5 decades below the values reported in the past for phosphonium ILs with shorter alkyl tails of a cation [11]. Furthermore, we found that the glass transition temperature defined conventionally as  $T(\tau_\sigma = 100 \text{ s or } \sigma_{dc} = 10^{-15} \text{ S/cm})$  quite well agrees with calorimetric  $T_g$ , thereby suggesting that the charge transport is controlled by viscosity in  $[\text{P}_{666,14}][\text{BEHP}]$  and  $[\text{P}_{666,14}][\text{BTMPP}]$ . The temperature dependence of viscosity has been determined and analyzed in terms of the fractional Walden rule,  $\Lambda \eta^{-k} = \text{const}$  [26]. to verify this assumption. For this purpose, dc-conductivity needs to be converted to molar conductivity according to the relation,  $\Lambda = \sigma_{dc} M_{mol} \rho^{-1}$ . The temperature evolution of density  $\rho$  and viscosity  $\eta$  obtained experimentally for  $[\text{P}_{666,14}][\text{BEHP}]$  and  $[\text{P}_{666,14}][\text{BTMPP}]$  are presented in Fig. 6.3a,b. On the other hand, Fig. 6.3c shows molar conductivity vs. fluidity on a double logarithmic scale. The solid line represents the ideal Walden behavior assigned to a 0.01 mol dm<sup>-3</sup> KCl aqueous solution that is a fully

dissociated electrolyte with equally mobile ionic species [27],[28]. As presented, the fractional exponent  $k$  is slightly lower than the unity ( $k = 0.97$ ) for both studied ILs. This means that charge transport is indeed strongly coupled to structural dynamics at any  $T$  in the supercooled liquid state. From Fig. 6.3c, it is also evident that the experimental data obtained for [P<sub>666,14</sub>][BEHP] and [P<sub>666,14</sub>][BTMPP] fall below the ideal line indicating that, in analogy to other phosphonium ILs [29], ionization is not complete in these materials.

From closer inspection of dielectric and viscosity data, one can notice that the Vogel-Fulcher-Tammann equation  $\tau_{\sigma}(T) = \tau_{\infty} \exp(DT_0/(T-T_0))$  provides proper interpolation of non-Arrhenius  $\sigma_{dc}(T^{-1})$  and  $\eta(T^{-1})$  dependences of [P<sub>666,14</sub>][BEHP], while for [P<sub>666,14</sub>][BTMPP], the VFT fit deviates slightly from experimental points. For typical glass-forming liquids, such a result designates the existence of the intermediate temperature,  $T_b$ , identified with the onset of complex dynamics [30]. Strictly speaking, there are two regions of complex ( $T < T_b$ ) and simple ( $T > T_b$ ) dynamics, characterized by different VFT behavior. Interestingly, considering ILs, only the materials containing imidazolium cation and [TCM] anion revealed a clear  $T_b$  point [31]. To confirm or exclude the presence of  $T_b$  for [P<sub>666,14</sub>][BEHP] and [P<sub>666,14</sub>][BTMPP], the Stickel operator has been employed for dielectric and mechanical data. According to the literature, derivative analysis of temperature variations of the relaxation time (or any other dynamic quantity),  $\Phi = [d(\log(\tau_{\sigma})/d(1000/T))^{-1/2}]$ , transforms single VFT behavior into a linear dependence [32]. On the other hand, when two VFT equations are required to parameterize the experimental data, two linear regions intersect at  $T_b$ . The results of the Stickel analysis of  $\tau_{\sigma}(T^{-1})$  for studied ILs are presented in Fig. 6.4a. It clearly shows that [P<sub>666,14</sub>][BTMPP] displays a different behavior than [P<sub>666,14</sub>][BEHP]. Namely, for the latter one, the Stickel plot reveals a single slope while clear deviation from linear behavior is observed for [P<sub>666,14</sub>][BTMPP]. However, in contrast to the Stickel graph of any other glass-forming liquid revealing  $T_b$  [31], the slope of  $[d(\log(\tau_{\sigma})/d(1000/T))^{-1/2}]$  dependence is getting larger in the vicinity of the liquid-glass transition; specifically, it grows twice. The analogous analysis performed for viscosity data also confirms such untypical behavior. In this regard, the ion transport in [P<sub>666,14</sub>][BTMPP] follows the behavior of [P<sub>666,14</sub>]-based ILs revealing a liquid-liquid phase transition. The observed effect is not as significant as for [P<sub>666,14</sub>][TCM] or [P<sub>666,14</sub>][TAU], where the LLT was detectable as an abrupt decrease of the Stickel operator, but surprisingly it fully mimics the  $\Phi$  trend reported for [P<sub>666,14</sub>][BOB], which undergoes a hidden LLT (see Fig. 6.4b and inset therein). Thus, one can conclude that in [P<sub>666,14</sub>][BTMPP], LLT occurs in the close vicinity of the liquid-glass transition. At the same time, the first-order phase transition of the same nature does not exist in [P<sub>666,14</sub>][BEHP]. In this context, it is interesting to ask whether these differences bring various pressure sensitivity to examined systems. To

explore this issue, a set of isothermal measurements of  $[P_{666,14}][\text{BTMPP}]$  and  $[P_{666,14}][\text{BEHP}]$  has been performed. The representative loss modulus spectra collected at 244 K are shown in Fig. 6.5a for both examined ILs. We see that isothermal compression has basically the same effect on the ion dynamics as isobaric cooling. Namely, the  $M''$  peak shifts systematically toward lower frequencies with increasing pressure. However, despite the same pressure step, the shift of  $M''(f)$  is much more extensive for  $[P_{666,14}][\text{BTMPP}]$ . Consequently,  $M''(f)$  maximum moves out of the experimental window already at 300 MPa, while for  $[P_{666,14}][\text{BEHP}]$  480 MPa is not enough. This effect is better visualized when the conductivity relaxation times  $\tau_\sigma$  are plotted vs. pressure. From Fig. 6.5b, it can be noted that isothermal squeezing makes the conductivity relaxation time longer; however, the  $\tau_\sigma(P)$  dependences of  $[P_{666,14}][\text{BTMPP}]$  follow the non-Arrhenius behavior, while  $\log\tau_\sigma$  grows linearly with increasing pressure for  $[P_{666,14}][\text{BEHP}]$ . The same is observed for  $\sigma_{dc}(T,P)$  dependences (see Fig. S6.3 in the supporting information file). Interestingly, the isotherms of  $[P_{666,14}][\text{BTMPP}]$  expose the same performance as high-pressure data of  $[P_{666,14}][\text{BOB}]$  [15], which again confirms similarities between these two ILs.

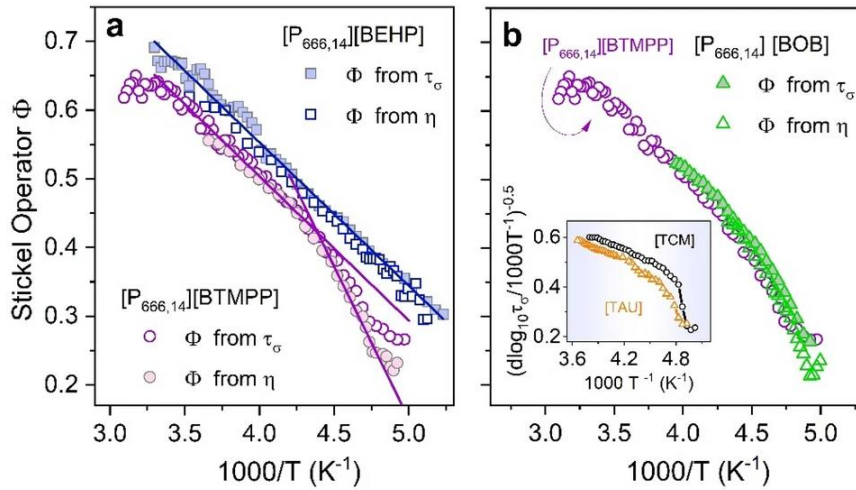


**Fig. 6.4** (a) The Stickel plots of conductivity relaxation times  $\tau_\sigma$  and viscosity  $\eta$  for  $[P_{666,14}][\text{BEHP}]$  and  $[P_{666,14}][\text{BTMPP}]$ . (b) The comparison of Stickel analysis for  $[P_{666,14}][\text{BTMPP}]$  with  $[P_{666,14}][\text{BOB}]$ . The inset shows the Stickel analysis of ILs with the LLT phenomenon. Data are taken from ref.[15].

The  $dT_g/dP$  coefficient is usually employed to describe the pressure sensitivity of ion dynamics quantitatively. For this purpose, the liquid glass transition pressure  $P_g$  needs to be determined at various temperature conditions. In analogy to ambient pressure data, we defined  $P_g$  as  $P(\tau_\sigma = 100 \text{ s})$ . Since within the available pressure range, only a few isotherms of  $[P_{666,14}][\text{BEHP}]$  reach the time scale of 100 s, the experimental data have been fitted by using the pressure version of the Arrhenius relation:  $\tau_\sigma = \tau_0 \exp(P\Delta V/RT)$  and then extrapolated to desired conductivity relaxation time. At the same time, to interpolate

isotherms of  $[P_{666,14}][\text{BTMPP}]$  pressure counterpart of VFT law ( $\tau_\sigma = \tau_0 \exp(D_P P / (P_0 - P))$ ) has been employed (fits quality will be discussed later). The obtained pressure dependence of liquid-glass transition temperature is presented in Fig. 6.5c. Due to its non-linear character, the empirical Andersson-Andersson equation:  $T_g = k_1(1 + (k_2/k_3)P)^{1/k_2}$  was used to parameterize the data and calculate the  $dT_g/dP$  coefficient ( $k_1/k_3$ ) [33]. As expected, markedly different values of  $dT_g/dP$  (in the limit of ambient pressure) are obtained for  $[P_{666,14}][\text{BTMPP}]$  and  $[P_{666,14}][\text{BEHP}]$ ; that is 174 K/GPa and 90 K/GPa, respectively. Interestingly,  $dT_g/dP$  of  $[P_{666,14}][\text{BOB}]$  is between these two limits. The obtained results suggest that in  $[P_{666,14}][\text{BEHP}]$ , there are strong van der Waals interactions between alkyl chains of cations and anions. Such a constituted structure becomes hard to break and thus is weakly sensitive to compression. The same is impossible for  $[P_{666,14}][\text{BTMPP}]$  due to the branched 5-carbon chains of the anion. Consequently, squeezing seems to strongly reduce the free volume between the alkyl chains and brings significant pressure sensitivity of  $T_g$ .

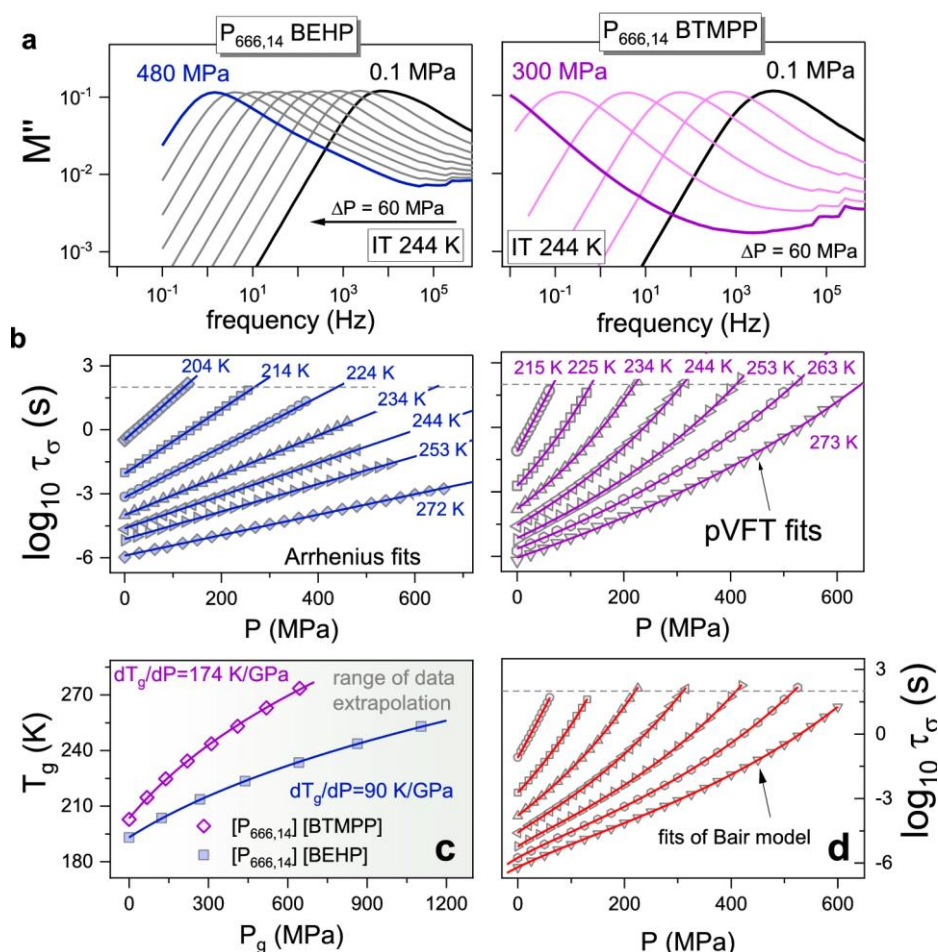


**Fig. 6.5** (a) The imaginary part of the dielectric loss modulus  $M''$  versus frequency registered during the compression of  $[P_{666,14}][\text{BEHP}]$  and  $[P_{666,14}][\text{BTMPP}]$  at  $T = 244$  K. (b) Pressure dependence of the conductivity relaxation times  $\tau_\sigma$  measured at different isothermal conditions for  $[P_{666,14}][\text{BEHP}]$  and  $[P_{666,14}][\text{BTMPP}]$ . The solid lines denote the corresponding fits, i.e., Arrhenius fit for

[P<sub>666,14</sub>][BEHP] and  $p$ VTF fit for [P<sub>666,14</sub>][BTMPP]. (c) Pressure dependence of the glass transition temperature  $T_g$  for studied ILs. The solid lines are fits of the Andersson-Andersson equation to the experimental data. (d) Pressure dependence of  $\log_{10} \tau_\sigma(P)$  of [P<sub>666,14</sub>][BTMPP] for the same isotherms. The solid lines represent the fits with the hybrid model (Eq. 6.4).

Coming back to the discussion on  $\tau_\sigma(T,P)$  dependences, one can notice that volume-activated law quite well parameterizes the data of [P<sub>666,14</sub>][BEHP]. However,  $p$ VFT deviates from experimental points, especially at high temperatures and low pressures. Therefore, in the next step, we employed Avramov entropic model [34] for data analysis. The mathematical expression of this model is

$$\log \tau_\sigma(T, P) = \log \tau_\infty + \left(\frac{T_r}{T}\right)^{\alpha_0 \left[1 - k \ln\left(1 + \frac{P}{\Pi}\right)\right]} \left(1 + \frac{P}{\Pi}\right)^\beta \log \frac{\tau_g}{\tau_\infty} \quad (6.3)$$

where the pre-exponential factor  $\tau_\infty$  denotes the conductivity relaxation times at high temperatures,  $T_r$  is a reference temperature (e.g.,  $T_g$ ),  $\log \tau_\sigma = 2$  since we previously defined  $T_g$  as the temperature at which  $\tau = 100$  s, and  $\Pi$ ,  $k$ ,  $\alpha_0$ , and  $\beta$  are fitting parameters. A significant advantage of this model is that it accounts for isothermal and isobaric conductivity relaxation times simultaneously. Although it was introduced to predict the viscosity of glass-formers at various temperature and pressure conditions, the Avramov model has been satisfactorily applied to describe the ion dynamics of aprotic ionic liquids, where viscosity controls ion transport [35]. As displayed in Fig. S6.4, the isothermal and isobaric dielectric relaxation data form a two-dimensional plot. The wire surface, in turn, represents the result of global fitting analysis using Eq. (6.3). It is clearly visible that the generated surface shows good agreement with the experimental  $\tau_\sigma(T,P)$  data for both studied ILs. However, when the fitting curves have been transferred to conventional representation (see Fig. S6.4b), a poor agreement between fits and the experimental points is again visible for [P<sub>666,14</sub>][BTMPP] at high temperatures. Therefore, the derivative analysis has been performed to look closer at  $\tau_\sigma(T,P)$  dependences. Precisely, the apparent activation volume  $\Delta V = 2.303RT(d\log_{10}\tau_\sigma/dP)_T$  that provides information on the volume required for local molecular motion has been calculated. Note that for linear  $\tau_\sigma(P)$  dependences, constant  $\Delta V$  is expected, while for non-Arrhenius  $\log \tau_\sigma(P)$ , it continuously increases with pressure.  $\Delta V(P)$  determined at various  $T$  conditions for [P<sub>666,14</sub>][BEHP] and [P<sub>666,14</sub>][BTMPP] are depicted in Fig. 6.6a. Keeping the same scale of Y-axis, it becomes obvious that  $\Delta V$  of [P<sub>666,14</sub>][BEHP] is markedly lower and weakly dependent on pressure, especially at high temperatures. Furthermore, it decreases with increasing temperature, which is typical for glass-forming liquids. Compared to activation volume determined for imidazolium-based ionic liquids, it is markedly larger [36], which reflects the big size of relaxing ions. On the other hand, unusual behavior of  $\Delta V(P)$  is observed for [P<sub>666,14</sub>][BTMPP]. In particular, the activation volume decreases upon compression at the lower pressure range and increases with pressure in the higher pressure region.

Consequently,  $\Delta V(P)$  reveals a clear minimum called an inflection point that indicates the concave-convex character of  $\log\tau_\sigma(P)$  dependences.

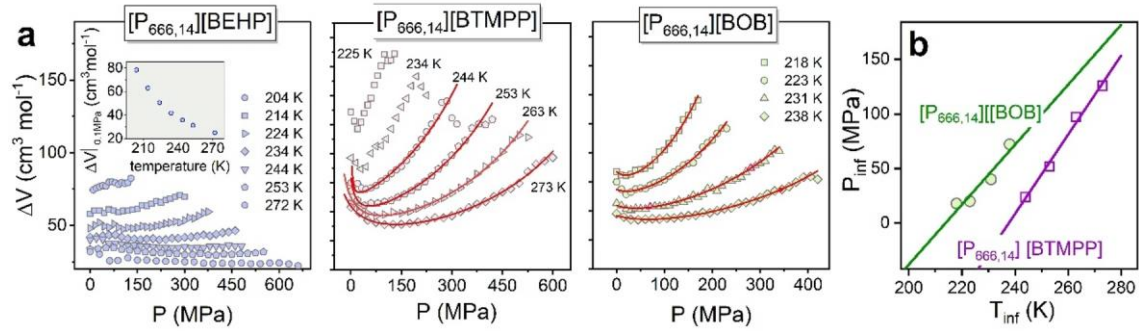


**Fig. 6.6** (a) Pressure dependences of activation volume for  $[P_{666,14}][BEHP]$ ,  $[P_{666,14}][BTMPP]$  and  $[P_{666,14}][BOB]$ . The lines are fits according to Eq. (6.4). In the inset, the temperature dependence of activation volume of  $[P_{666,14}][BEHP]$  at ambient pressure is shown. (b) Temperature dependence of inflection pressure for  $[P_{666,14}][BTMPP]$  and  $[P_{666,14}][BOB]$ . Solid lines are linear fits, extrapolating to the inflection temperature at 0.1 MPa.

In 1993, Herbst et al. [37] proposed that this inflection point might arise from a non-linearity of the volume with a change of pressure. On the other hand, Casalini and Bair [38] suggested that it should be attributed to the pressure dependences of the compressibility and the apparent activation energy at constant volume. In order to analyze this phenomenon in more detail, a phenomenological model proposed by Bair [39], employed initially to describe inflections in pressure dependence of viscosity, can be used here to parametrize the pressure dependence of conductivity relaxation times. This model combines the  $pVFT$  equation with the McEwen equation  $\eta(P) = \eta_0(1 + \frac{\alpha_0}{q}P)^q$ , and can be appropriate for low and high-pressure ranges, respectively,

$$\tau_\sigma = \tau_0(1 + \frac{\alpha_0}{q}P)^q \exp(\frac{D_P P}{P_0 - P}) \quad (6.4)$$

Here,  $q$  and  $\alpha_0$  are the McEwen exponent and parameter, respectively. The fits of this hybrid model to  $\tau_\sigma(P)$  isothermal data of  $[P_{666,14}][BTMPP]$  are presented in Fig. 6.5d. As can be seen, the fitting curves follow the experimental points perfectly and consequently correctly interpolate the  $\Delta V(P)$  dependences of  $[P_{666,14}][BTMPP]$ . From Fig. 6.6b, one can note that the inflection point is observed at higher pressures as the temperature increases, and a linear dependence describes well the obtained data. Namely, the inflection pressure increases with temperature at a slope of 3.6 MPa/K. Extrapolation of this linear fit to ambient pressure gives  $T_{inf}(P=0.1 \text{ MPa})$  equal to 238 K, which is above the dynamic glass transition temperature.

Interestingly, so far, only a few glass formers have been compressed strongly enough to observe the inflection point experimentally [40]. Among them, one can mention protic ionic liquid  $[C_8Him][NTf_2]$  [41], glycerol [42] and 2-butyl-1-octanol. Interestingly, all of

them can form supermolecular structures due to the strong H-bonding network. In this context, one could expect that [P<sub>666,14</sub>][BTMPP], as well as [P<sub>666,14</sub>][BOB], reveal some ordering tendencies that affect their ion dynamics at ambient and elevated pressure and finally become the origin of the LLT.

## 6.4 Conclusions

In summary, we examined the dielectric properties of trihexyl(tetradecyl)-phosphonium bis(2-ethylhexyl) phosphate ([P<sub>666,14</sub>][BEHP]) and trihexyl(tetradecyl)-phosphonium bis(2,4,4-trimethylpentyl) phosphinate ([P<sub>666,14</sub>][BTMPP]) over a wide temperature and pressure range. These materials can be classified as good glass-forming liquids, as confirmed by DSC scans. However, at the same time, there is no clear calorimetric evidence of the liquid–liquid phase transition being observed previously for other [P<sub>666,14</sub>]-based ILs. Furthermore, the dynamics of examined ILs shows the features typical for ionic conductors, that is non-exponential behavior of conductivity relaxation peak  $M''(f)$  and non-Arrhenius temperature dependence of  $\tau_\sigma(T^{-1})$ . Although the dielectric parameters (i.e.,  $\tau_\sigma$ ,  $\sigma_{dc}$ , and  $\beta_{KWW}$ ) did not reveal any signs of LLT, a detailed analysis of  $\tau_\sigma(T^{-1})$  and  $\eta(T^{-1})$  dependences revealed an unusual curvature of Stickel plot for [P<sub>666,14</sub>][BTMPP]. Such a peculiar behavior of ion dynamics near  $T_g$  has not been observed before for any other phosphonium IL, instead of [P<sub>666,14</sub>][BOB], for which the LLT was postulated to overlap the liquid-glass transition. Thus, one can conclude that LLT and  $T_g$  occur in close vicinity for IL with [BTMPP]<sup>-</sup> anion. At the same time, an increase in the Stickel slope at  $T_b$  can be identified as the fingerprint of changes in ion dynamics accompanying LLT. The high-pressure dielectric measurements revealed that the ion dynamics of [P<sub>666,14</sub>][BTMPP] is much more similar to [P<sub>666,14</sub>][BOB] than to [P<sub>666,14</sub>][BEHP]. In particular,  $\tau_\sigma(P)$  of the latter follows the volume-activated law, while non-Arrhenius behavior characterizes the isotherms of the first two ILs. Specifically, the concave-convex character of  $\log\tau_\sigma(P)$  dependences has been observed for [P<sub>666,14</sub>][BTMPP] and [P<sub>666,14</sub>][BOB]. Consequently, a unique phenomenon called an inflection point was found to characterize the high-pressure dynamics of ionic systems with hidden LLT.

## 6.5 Methods

### Materials

Investigated ionic liquids trihexyl(tetradecyl)phosphonium bis(2-ethylhexyl) phosphate ([P<sub>666,14</sub>][BEHP],  $M_w = 805.27 \text{ g mol}^{-1}$ ) and trihexyl(tetradecyl)phosphonium bis(2,4,4-trimethylpentyl) phosphinate ([P<sub>666,14</sub>][BTMPP],  $M_w = 773.27 \text{ g mol}^{-1}$ ) were purchased from io-li-tec Ionic Liquids Technologies as transparent liquids

(([P<sub>666,14</sub>][BTMPP]-bright yellow, [P<sub>666,14</sub>][BEHP]-colorless). The purity tests, including NMR, have been made, and they agree with those provided by Iolitec. The bright yellow color can indicate the halide impurities in [P<sub>666,14</sub>][BTMPP]. Before the experiments, samples were dried overnight in a Vacutherm oven (1000 mbar, 12 h, 70 °C). The color of the samples did not change after drying. The water content of both ILs is less than 0.1%, determined by Metrohm 899 coulometer.

### **Differential scanning calorimetry measurements**

Thermodynamic properties of studied ILs were examined using a Mettler-Toledo DSC instrument equipped with a HSS8 ceramic sensor with 120 thermocouples and a liquid nitrogen cooling accessory. The calibrations for temperature and enthalpy were performed by using indium and zinc standards. The samples (approx. 20 mg) were sealed in aluminum crucibles (40  $\mu$ L) with pierced lid. Each IL was measured from 123.15 to 303.15 K with a 10 K min<sup>-1</sup> heating rate. A new sample was prepared for the same temperature cycles three times to ensure reproducibility and high accuracy.

### **Dielectric measurements**

We have used a glove box to prepare samples for dielectric measurements. The dielectric measurements in a wide frequency range of 10<sup>-2</sup>–10<sup>7</sup> Hz were performed at ambient pressure using a Novo-Control GMBH Alpha dielectric spectrometer. The same stainless steel electrodes (diameter = 15 mm) with a fixed distance (0.1 mm) provided by the quartz ring were used for both studied ILs. During the measurements, the temperature was controlled by a Quatro system using a nitrogen gas cryostat with an accuracy of 0.1 K. The Karl Fisher test made after the dielectric experiments did not show moisture uptake. The dielectric measurements at elevated pressure were carried out by means of a high-pressure system developed by Unipress over a frequency range from 10<sup>-2</sup> to 10<sup>6</sup> Hz with a specially designed capacitor. The capacitor was filled with the studied sample and sealed by a Teflon capsule during the measurements. Then the whole part was placed in the high-pressure chamber and compressed using silicone oil. The pressure was controlled with a resolution of 1 MPa by means of the Unipress setup, and a Weiss fridge adjusted the temperature within 0.1 K.

### **Viscosity measurements**

The viscosity was measured employing an ARES G2 Rheometer. In the supercooled liquid region, aluminum parallel plates of diameter 4 mm were used. The rheological experiments were performed in the frequency range from 0.1 to 100 rad s<sup>-1</sup> (10 points per decade) with strain equal to 0.01% in the vicinity of the liquid glass transition. The strain was increased by one order of magnitude with every 10 K. The relative uncertainty of the reported viscosity measurements  $u_r(\eta)$  from calibration, temperature and pressure control did not exceed 7%.

## Density measurements

Density was measured in the temperature range from 283.15 to 363.15 K using a vibrating-tube densimeter DMA 4500 M (Anton Paar, Austria). The apparatus was calibrated directly before measurements with dry air and bi-distilled water. The water was freshly degassed (by boiling) before use. The viscosity-related errors were automatically corrected in full range.

## 6.6 Acknowledgements

This research was funded in a whole by National Science Centre, Poland [Opus 21, 2021/41/B/ST5/00840]. For the purpose of Open Access, the author has applied a CC-BY public copyright license to any Author Accepted Manuscript (AAM) version arising from this submission.

## 6.7 Supplementary information

### Supplementary Figures

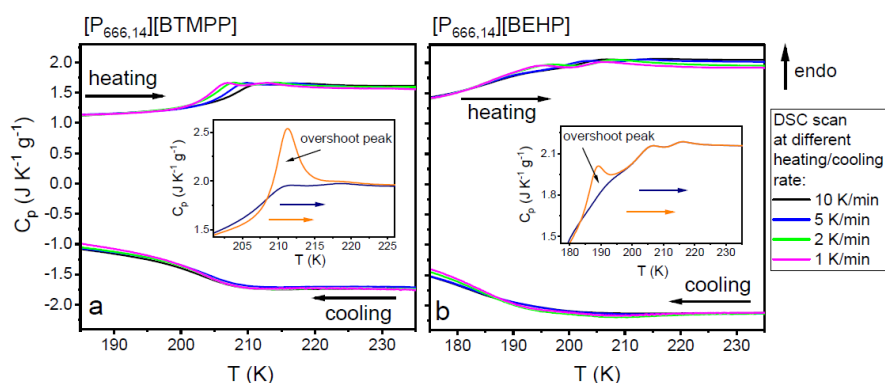


**Figure S6.1** The temperature dependence of heat capacity on different cooling and heating rate: 10 (black), 5 (blue), 2 (green), 1 (magenta) K/min for  $[\text{P}_{666,14}][\text{BTMPP}]$  **a** and  $[\text{P}_{666,14}][\text{BEHP}]$  **b**. Inset: Comparison between DSC scans obtained during the standard heating rate 10 K/min (navy) and after 6 hours-aging process performed in the glassy state (orange) at 193 K for  $[\text{P}_{666,14}][\text{BTMPP}]$  and at 173 K for  $[\text{P}_{666,14}][\text{BEHP}]$ .

Generally, the secondary relaxations in glass formers can be classified depending on how strongly they are correlated to the primary relaxation. Namely, secondary relaxations are identified as the Johari-Goldstein (JG) relaxation, which involves a certain (intermolecular) motion of the entire molecule, and non-JG relaxation, which involves a part of the molecule (intramolecular) motion. Hence, JG relaxation is considered an indispensable precursor for cooperative structure relaxation and is characterized by sensitivity to density changes. Non-JG relaxations, by contrast, originate from intramolecular local motion, are pressure insensitive and have lower activation energy. To fast-check the origin of the secondary mode, the coupling model (CM) can be used:

$$\tau_{JG} \approx t_c^{1-\beta_{KWW}} \tau_\alpha^{\beta_{KWW}} \quad (S6.1)$$

where  $t_c = 2$  ps is a temperature-independent constant,  $\beta_{KWW}$  is the stretching parameter. It has been confirmed that the CM is still valid by replacing  $\tau_\alpha$  with  $\tau_\sigma$  in Eq. (S6.1) for ionic glass formers. We can see from Fig S6.2, as expected, the determined values of  $\tau_{JG}$  for [P<sub>666,14</sub>][BTMPP] and [P<sub>666,14</sub>][BEHP] are not agreement with the relaxation times of the  $\beta$ -process.

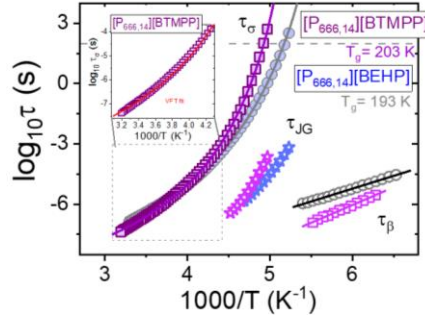


**Figure S6.2** The comparison of the temperature dependence of  $\tau_\beta$  and  $\tau_{JG}$  for [P<sub>666,14</sub>][BEHP] and [P<sub>666,14</sub>][BTMPP].

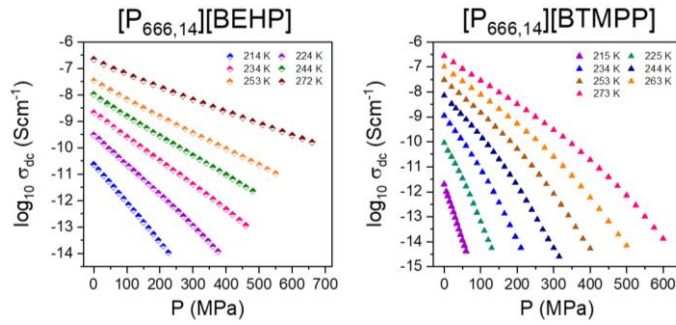


**Figure S6.3** The dc-conductivity as a function of pressure for [P<sub>666,14</sub>][BEHP] and [P<sub>666,14</sub>][BTMPP] at several isothermal conditions.

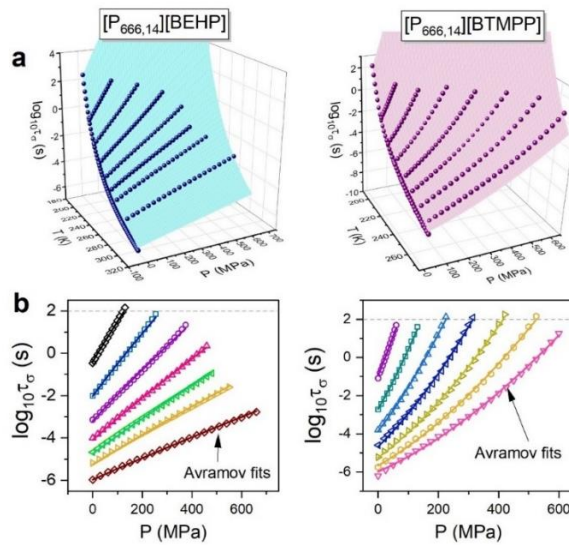


**Figure S6.4 a** The conductivity relaxation times are plotted as a function of both temperature and pressure in a 3D plane for studied ILs. The surface is determined by fitting the experimental data to

the Avramov model with the following parameters: 1)  $\log_{10}(\tau_{\infty})=-7.55\pm 0.03$ ,  $k=0.101\pm 0.004$ ,  $\alpha_0=5.26\pm 0.03$ ,  $\beta=0.72\pm 0.02$ , and  $\Pi=271.8\pm 10.9$  MPa for [P<sub>666,14</sub>][BEHP] with  $T_r=T_g=193.0$  K; 2)  $\log_{10}(\tau_{\infty})=-7.07\pm 0.06$ ,  $k=-0.019\pm 0.014$ ,  $\alpha_0=7.20\pm 0.11$ ,  $\beta=1.68\pm 0.07$ , and  $\Pi=267.42\pm 14.87$  MPa for [P<sub>666,14</sub>][BTMPP] with  $T_r=T_g=202.9$  K. **b** Test of the Avramov model for pressure dependence of conductivity relaxation times for both samples. Solid lines indicate fits of the Avramov model.

## 6.8 References

- [1] M. Armand, F. Endres, D. R. MacFarlane, H. Ohno, and B. Scrosati, *Nat. Mater* **8**, 621 (2009).
- [2] C. A. Angell, W. Xu, M. Yoshizawa-Fujita, A. Hayashi, J.-P. Belieres, P. Lucas., M. Videa, Z.-F. Zhao, K. Ueno, Y. Ansari, J. Thomson, and D. Gervasio, in *Electrochemical Aspects of Ionic Liquids* (John Wiley & Sons, Ltd, **2011**), pp. 5–31.
- [3] P. Simon and Y. Gogotsi, *Nat. Mater* **7**, 845 (2008).
- [4] Z. Wojnarowska, K. Grzybowska, L. Hawelek, A. Swiety-Pospiech, E. Masiewicz, M. Paluch, W. Sawicki, A. Chmielewska, P. Bujak, and J. Markowski, *Mol. Pharmaceutics* **9**, 1250 (2012).
- [5] Z. Wojnarowska, J. Knapik, M. Rams-Baron, A. Jedrzejowska, M. Paczkowska, A. Krause, J. Cielecka-Piontek, M. Jaworska, P. Lodowski, and M. Paluch, *Mol. Pharmaceutics* **13**, 1111 (2016).
- [6] K. J. Fraser and D. R. MacFarlane, *Aust. J. Chem.* **62**, 309 (2009).
- [7] N. Karodia, S. Guise, C. Newlands, and J.-A. Andersen, *Chem. Commun.* 2341 (1998).
- [8] P. J. Carvalho, S. P. M. Ventura, M. L. S. Batista, B. Schröder, F. Gonçalves, J. Esperança, F. Mutelet, and J. A. P. Coutinho, *J. Chem. Phys.* **140**, 064505 (2014).
- [9] H. Shirota, H. Fukazawa, T. Fujisawa, and J. F. Wishart, *J. Phys. Chem. B* **114**, 9400 (2010).
- [10] L. K. Scarbath-Evers, P. A. Hunt, B. Kirchner, D. R. MacFarlane, and S. Zahn, *Phys. Chem. Chem. Phys.* **17**, 20205 (2015).
- [11] P. J. Griffin, A. P. Holt, K. Tsunashima, J. R. Sangoro, F. Kremer, and A. P. Sokolov, *J. Chem. Phys.* **142**, 084501 (2015).
- [12] S. V. Nemilov, *Glass Phys. Chem.* **36**, 253 (2010).
- [13] T. Cosby, Z. Vicars, E. U. Mapesa, K. Tsunashima, and J. Sangoro, *J. Chem. Phys.* **147**, 234504 (2017).
- [14] P. Sippel, P. Lunkenheimer, S. Krohns, E. Thoms, and A. Loidl, *Sci. Rep.* **5**, 13922 (2015).
- [15] Z. Wojnarowska, S. Cheng, B. Yao, M. Swadzba-Kwasny, S. McLaughlin, A. McGrogan, Y. Delavoux, and M. Paluch, *Nat. Commun.* **13**, 1342 (2022).
- [16] M. A. Harris, T. Kinsey, D. V. Wagle, G. A. Baker, and J. Sangoro, *Proc. Natl. Acad. Sci.* **118**, e2020878118 (2021).
- [17] Z. Wojnarowska and M. Paluch, *J. Phys.: Condens. Matter* **27**, 073202 (2015).

- [18] A. Bondi, *J. Phys. Chem.* **68**, 441 (1964).
- [19] A. Rivera-Calzada, K. Kaminski, C. Leon, and M. Paluch, *J. Phys. Chem. B* **112**, 3110 (2008).
- [20] Z. Wojnarowska, J. Knapik, M. Díaz, A. Ortiz, I. Ortiz, and M. Paluch, *Macromolecules* **47**, 4056 (2014).
- [21] M. Paluch, editor, *Dielectric Properties of Ionic Liquids* (Springer International Publishing, Cham, **2016**).
- [22] J. R. Sangoro and F. Kremer, *Acc. Chem. Res.* **45**, 525 (2012).
- [23] S. Havriliak and S. Negami, *Polymer* **8**, 161 (1967).
- [24] K. L. Ngai, G. N. Greaves, and C. T. Moynihan, *Phys. Rev. Lett.* **80**, (1998).
- [25] F. Kremer and A. Schönhals, editors, *Broadband Dielectric Spectroscopy* (Springer Berlin Heidelberg, Berlin, Heidelberg, **2003**).
- [26] P. Walden, *Bull. Acad. Imper. Sci. (St. Petersburg)* **1800**, 405-422 (1914).
- [27] C. Schreiner, S. Zugmann, R. Hartl, and H. J. Gores, *J. Chem. Eng. Data* **55**, 1784 (2010).
- [28] K. R. Harris, *J. Phys. Chem. B* **123**, 7014 (2019).
- [29] M. D. Green, C. Schreiner, and T. E. Long, *J. Phys. Chem. A* **115**, 13829 (2011).
- [30] F. Stickel, E. W. Fischer, and R. Richert, *J. Chem. Phys.* **102**, 6251 (1995).
- [31] M. Musiał, S. Cheng, Z. Wojnarowska, and M. Paluch, *J. Mol. Liq.* **317**, 113971 (2020).
- [32] G. Floudas, M. Paluch, A. Grzybowski, and K. Ngai, *Molecular Dynamics of Glass-Forming Systems*, Vol. 1 (Springer Berlin Heidelberg, Berlin, Heidelberg, **2011**).
- [33] S. P. Andersson and O. Andersson, *Macromolecules* **31**, 2999 (1998).
- [34] I. Avramov, A. Grzybowski, and M. Paluch, *J. Non. Cryst. Solids* **355**, 733 (2009).
- [35] Z. Wojnarowska, K. Grzybowska, A. Grzybowski, M. Paluch, K. Kaminski, P. Włodarczyk, K. Adrjanowicz, and J. Pionteck, *J. Chem. Phys.* **132**, 094506 (2010).
- [36] K. R. Harris and M. Kanakubo, *Phys. Chem. Chem. Phys.* **24**, 14430 (2022).
- [37] C. A. Herbst, R. L. Cook, and H. E. King Jr, *Nature* **361**, 518 (1993).
- [38] R. Casalini and S. Bair, *J. Chem. Phys.* **128**, 084511 (2008).
- [39] S. Bair, L. Martinie, and P. Vergne, *Tribol. Lett.* **63**, 37 (2016).
- [40] M. Musiał, S. Bair, S. Cheng, Z. Wojnarowska, and M. Paluch, *J. Mol. Liq.* **331**, 115772 (2021).
- [41] E. Thoms, Z. Wojnarowska, P. Goodrich, J. Jacquemin, and M. Paluch, *J. Chem. Phys.* **146**, 181102 (2017).
- [42] R. L. Cook, H. E. King Jr., C. A. Herbst, and D. R. Herschbach, *J. Chem. Phys.* **100**, 5178 (1994).

# 7 Self-Assembled Nanostructures in Aprotic Ionic Liquids Facilitate Charge Transport at Elevated Pressure

## Self-assembled nanostructures in aprotic ionic liquids facilitate charge transport at elevated pressure

Journal:	<i>ACS Applied Materials &amp; Interfaces</i>
Manuscript ID	am-2023-08606j
Manuscript Type:	Article
Date Submitted by the Author:	14-Jun-2023
Complete List of Authors:	Yao, Beibei; University of Silesia in Katowice Institute of Physics named after August Chełkowski, Institute of Physics Paluch, Marian; Uniwersytet Śląski w Katowicach, Institute of Physics Paturej, Jarosław; University of North Carolina at Chapel Hill, Chemistry McLaughlin, Shannon ; Queen's University Belfast, QUILL McGrogan, Ann; Queen's University Belfast, QUILL Swadzba-Kwasny, Malgorzata; Queen's University Belfast, QUILL Shen, Jie; Institut Neel, 38000 Grenoble, France Ruta, Beatrice; Institut Neel, 38000 Grenoble, France Rosenthal, Martin; ESRF, DUBBLE-CRG @ ESRF Liu, Jiliang; ESRF Kruk, Danuta; 4University of Warmia and Mazury, Faculty of Mathematics and Computer Science Wojnarowska, Zaneta; Uniwersytet Śląski w Katowicach, Institute of Physics

Status: under review

## Author Declaration:

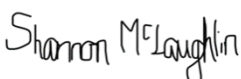
*"Self-assembled nanostructures in aprotic ionic liquids facilitate charge transport at elevated pressure"*, *ACS Applied Materials & Interfaces*, ID: am-2023-08606j

B. Yao planned and carried out the experimental work, analyzed the data, prepared figures, and co-wrote the manuscript.

Signature: 

J. Paturej carried out molecular simulations.

S. McLaughlin characterized and synthesized the ionic liquids.

Signature: 

A. McGrogan characterized and synthesized the ionic liquids.

Signature: 

M. Swadzba-Kwasny supervised the characterization and synthesis of ionic liquids.

Signature: 

J. Shen carried out the small-angle X-ray scattering (SAXS) and wide-angle X-ray scattering (WAXS) measurements and analyzed the data.

Signature: 

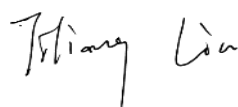
B. Ruta carried out the small-angle X-ray scattering (SAXS) and wide-angle X-ray scattering (WAXS) measurements and analyzed the data.

Signature: 

M. Rosenthal carried out the small-angle X-ray scattering (SAXS) and wide-angle X-ray scattering (WAXS) measurements and analyzed the data.

Signature: 

J. Liu carried out the small-angle X-ray scattering (SAXS) and wide-angle X-ray scattering (WAXS) measurements and analyzed the data.

Signature: 

D. Kruk carried out the Nuclear Magnetic Resonance (NMR) experiments and analyzed data.

Z. Wojnarowska prepared figures, carried out the rheological measurements, and co-wrote the manuscript.

Signature: 

M. Paluch supervised the project.

Signature: 

## 7.1 Abstract

Ionic liquids (ILs), revealing a tendency to form self-assembled nanostructures have emerged as promising materials in various applications, especially in energy storage and conversion. Despite multiple reports discussing the effect of structural factors and external thermodynamic variables on ions organization in a liquid state, little is known about the charge-transport mechanism through the self-assembled nanostructures and how it changes at elevated pressure. To address these issues, we chose three amphiphilic ionic liquids containing the same tetra(alkyl)phosphonium cation and anions differing in size and shape, i.e., thiocyanate [SCN]<sup>-</sup>, dicyanamide [DCA]<sup>-</sup>, and tricyanomethanide [TCM]<sup>-</sup>. From ambient pressure dielectric and mechanical experiments, we found that charge transport of all three examined ILs is viscosity-controlled at high temperatures. On the other hand, ion diffusion is much faster than structural dynamics in a nanostructured supercooled liquid (at  $T < 210 \pm 3$  K), which constitutes the first example of conductivity independent from viscosity in neat aprotic ILs. High-pressure measurements and MD simulations reveal that the created nanostructures depend on the anion size and can be modified by compression. For small anions, increasing pressure shapes immobile alkyl chains into lamellar-type phases, leading to increased anisotropic diffusivity of anions through channels. Bulky anions drive the formation of interconnected phases with continuous 3D curvature, which render ion transport independent of pressure. This work offers insight into the design of high-density electrolytes with percolating conductive phases providing efficient ion flow.

## 7.2 Introduction

Ionic liquids (ILs) are a novel class of fluids showing rich structural diversity in the nature of ions, their interactions, and the organization of ionic species in the liquid phase.[1],[2] Almost unlimited combinations of cations and anions enable tailoring ILs for numerous applications across multiple disciplines in science and engineering e.g., pharmacy[3], chemical synthesis[4], or electrochemistry[5],[6]. However, in most instances, the physical arrangement of ions in bulk strongly affects the mechanical and conducting properties of IL, thereby determining process efficiency.[7] There is growing evidence that the ability to support self-assembly is widespread among ILs providing another common trait of ionic fluids.[8] Therefore, a deep understanding of ILs self-assembly is essential to control their properties and, thus, functions comprehensively.

The nanostructure of IL is driven by the spontaneous solvophobic segregation of charged and uncharged groups into polar and apolar domains.[7] Thus, amphiphilic ions with both polar and apolar moieties, like localized and exposed charges or long alkyl

chains, have a stronger tendency to self-assemble. If the ions are weakly amphiphilic, the bulk structure is determined mainly by Coulombic forces and simple packing.[9] Hence, the degree of nanostructure in ILs usually scales with the elongation of a cation alkyl chain, while anions control local structure in the polar domains. For instance, imidazolium and pyrrolidinium-based ILs develop amphiphilic nanostructure (like micelles) above n-butyl chains.[10],[11] However, the geometry of trialkyl-methylammonium ( $[N_{1,nnn}]^+$ ) cation is sufficient to facilitate the nanostructure formation even with short ethyl tails.[12] These studies emphasize the importance of the volume ratio of charged and uncharged groups ( $V_{\text{alkyl}}:V_{\text{polar}}$ ) and the relative position of the alkyl groups on the cation. In principle, a larger  $V_{\text{alkyl}}:V_{\text{polar}}$  ratio, stronger segregation of polar and apolar domains is observed.[13] Ions forming hydrogen-bonded networks also support amphiphilic self-assembly.[14] Thereby, nanostructures are observed in both protic and aprotic ILs.[15]

Over the years, numerous experimental techniques and theoretical studies have been focused on the effect of temperature on the nanoscale morphology of ILs.[16],[17],[18] It has been reported that thermal fluctuations make ILs homogeneous fluids without any self-assembly behavior at high temperatures. On the other hand, cooling brings competition between hydrophobic and hydrophilic interactions accompanied by changes in ions conformation. Various nanoscale phases arise as the molecules rearrange in a supercooled liquid state.<sup>11</sup> In this context, it should be noted that isobaric cooling decreases the kinetic energy and increases the ions' packing (density), making the self-assembly complex and puzzling. Therefore, the combined effect of thermal and density fluctuations must be separated to thoroughly understand IL (nano)structure formation. It can only be achieved by performing high-pressure experiments.[19] Since simple packing constraints determine the general arrangement of polar and non-polar domains, the effect of pressure on ions rearrangement is naturally expected. Since the pressure-dependent experiments are far more complex than their temperature counterpart, there are no reports on the behavior of ILs self-assembled nanostructure under pressure. A methodology that can address this challenge employs high-pressure dielectric spectroscopy.[20] In addition to insight into dc-conductivity behavior and relaxation dynamics at various T-P conditions, isothermal dielectric measurements offer a unique possibility to recognize the dominating charge transport mechanisms in low-molecular ILs and their polymer counterparts.[ 21 ],[ 22 ],[ 23 ],[ 24 ] Thereby, high-pressure dielectric experiments can capture two missing crucial aspects: ion dynamics through the self-assembled nanostructures and how it changes at elevated pressure.

The current paper discusses the conductivity mechanism as a function of the structural organization of three trihexyl(tetradecyl)phosphonium  $[P_{666,14}]^+$ -based aprotic

ionic liquids over a wide temperature and pressure range. Specifically, the  $[P_{666,14}]^+$  cation has been combined with three structurally different anions: thiocyanate,  $[SCN]^-$ , dicyanamide  $[DCA]^-$  and tricyanomethanide  $[TCM]^-$ . According to X-ray diffraction and FT-IR spectroscopic studies of borohydride IL  $[P_{666,14}][BH_4]$ , presented in ref. [25] enhanced ordering of alkyl chains occurs in the supercooled liquid state accessible through the first-order liquid-liquid phase transition (LLT). Our ambient pressure dielectric and mechanical measurements covering both supercooled liquids and glassy states reveal high similarities in the relaxation dynamics of all three studied systems. Specifically, at high temperatures ( $T > T_{LL}$ ), the charge transport is fully controlled by viscosity (so-called vehicle mechanism), while in a supercooled state revealing self-assembly behavior ( $T < T_{LL}$ ), ion diffusion is much faster than the structural dynamics. Furthermore, the conducting properties of self-assembled glass differ from typical IL and depend on the thermal history of sample. To disclose the details of the charge transport mechanism in  $[P_{666,14}]^+$  materials, high-pressure dielectric spectroscopy has been employed. High-pressure experiments combined with MD simulations show that the nanostructure of  $[P_{666,14}]^+$ -ILs depends on the anion size and reveals different pressure sensitivity for each material.

### 7.3 Materials and Methods

The synthesis of examined  $[P_{666,14}][SCN]$  and  $[P_{666,14}][TCM]$  is provided in Supporting Materials.  $[P_{666,14}][DCA]$  with a purity of 99% was supplied by Iolitec.

**Differential Scanning Calorimetry (DSC).** Calorimetric experiments of studied ILs were performed by means of a Mettler Toledo DSC1STAR System equipped with a liquid nitrogen cooling accessory and an HSS8 ceramic sensor (a heat flux sensor with 120 thermocouples). During the experiments, the flow of nitrogen was kept at  $60 \text{ ml min}^{-1}$ . Enthalpy and temperature calibrations were performed using indium and zinc standards. Low-temperature verification was made using n-heptane ( $182.15 \text{ K}$ ,  $140.5 \text{ Jg}^{-1}$ ) at different scanning rates ( $0.7$ ,  $1$ ,  $5$ , and  $10 \text{ Kmin}^{-1}$ ). The baseline was constructed as a straight line from the onset to the endpoint. A dedicated software Mettler Toledo DSC1STAR allows various calculations (onset, heat, peak temperature, etc.) from the original recorded DSC curves. Before the measurement, the samples were annealed 30 min at  $373 \text{ K}$ . Temperature ramps involved cooling to  $143 \text{ K}$  and heating to  $373 \text{ K}$  with a rate of  $10 \text{ K per min}$ . Samples were cycled at least 3 times to ensure reproducibility and high accuracy. The 6-hour aging experiment was performed at  $187 \text{ K}$  after cooling with the rate of  $10 \text{ K}\cdot\text{min}^{-1}$ .

**Dielectric Measurements.** The dielectric measurements at ambient pressure for studied ILs were carried out over a frequency range from  $10^{-1} \text{ Hz}$  to  $10^7 \text{ Hz}$  by means of

a Novo-Control GMBH Alpha dielectric spectrometer. The Novocool system controlled the temperature with an accuracy of 0.1 K. During this measurement, the sample was placed between two stainless steel electrodes (diameter = 15 mm). The quartz ring provided the distance between plates. We used the capacitor filled with the studied sample for the pressure-dependent dielectric measurements, which was next placed in the high-pressure chamber and compressed using silicone oil. Note that the sample was only in contact with stainless steel during the measurement. The Unipress setup measured the pressure with a resolution of 1 MPa. The temperature was controlled within 0.1 K by means of a Weiss fridge. To avoid cold crystallization and maintain the same history for each sample, each [P<sub>666,14</sub>]-based IL was quenched to 201 K and then compressed to the glassy state. Afterward, the temperature was increased, and the dielectric data were collected on isothermal decompression. This procedure enables studies of ion dynamics in the glassy and supercooled liquid 2 state. Further decompression to liquid 1 resulted in cold crystallization of [P<sub>666,14</sub>][SCN] and [P<sub>666,14</sub>][DCA] and required melting of the sample in the subsequent step.

**Viscosity measurements.** The viscosity was measured employing an ARES G2 Rheometer. In the supercooled liquid region, aluminum parallel plates of diameter 4 mm were used. The rheological experiments were performed in the frequency range from 0.1 to 100 rad·s<sup>-1</sup> (10 points per decade) with strain equal to 0.1% in the vicinity of the liquid glass transition. The strain was increased by one order of magnitude with every 10 K. The relative uncertainty of the reported viscosity measurements from calibration, temperature and pressure control, as well as sample purities, did not exceed 7%.

**Small-angle and wide-angle X-ray scattering (SAXS, WAXS).** To investigate the microscopic structural changes during LLT on a larger scale, we employed X-ray diffraction (XRD) characterization with an energy of 12 keV. Small-angle X-ray scattering (SAXS) measurements were performed in the  $q$  range of 0.13 to 0.8 Å<sup>-1</sup>, while wide-angle X-ray scattering (WAXS) measurements were conducted in the  $q$  range of 0.6 to 4.9 Å<sup>-1</sup>. The measurements were performed on cooling and subsequent heating, and the two-dimensional data were acquired using independent detectors. The one-dimensional data were obtained by azimuthal integration using the pyFAI program. The temperature of the system was controlled by Linkam, and the cooling/heating rate was set to 10 K/min.

**NMR Relaxometry Studies.** The <sup>1</sup>H spin–lattice relaxation data of [P<sub>666,14</sub>][DCA] were collected by a STELAR fast field cycling (FFC) relaxometer in the frequency range of 10 kHz to 25 MHz at 204 and 201 K. Data analysis has been performed with the following parameters:  $\rho=0.907\text{g/cm}^3$ ,  $M=549.90\text{ g/mol}$ ,  $N_H=6.75\times 10^{28}/\text{m}^3$ .

**MD Simulations.** Molecular dynamics simulations of ionic liquids comprised of amphiphile molecules were performed using a bead-spring model at coarse-grained

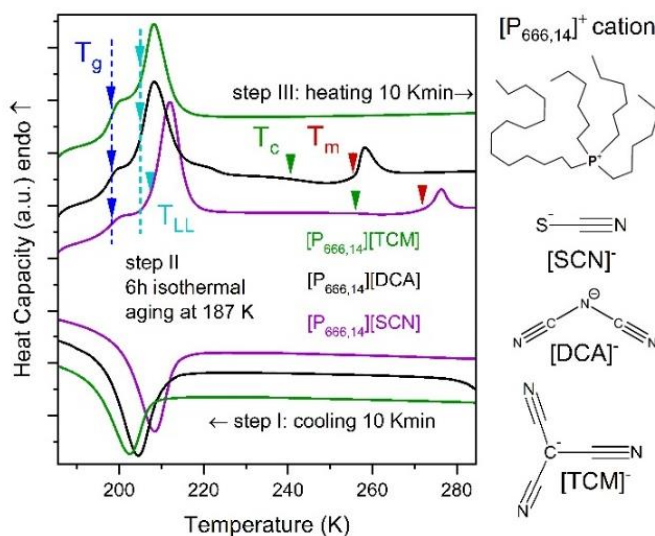
resolution. Details on the adopted numerical model are included in Supplementary Materials.

## 7.4 Results & Discussion

### 7.4.1 Samples characterization.

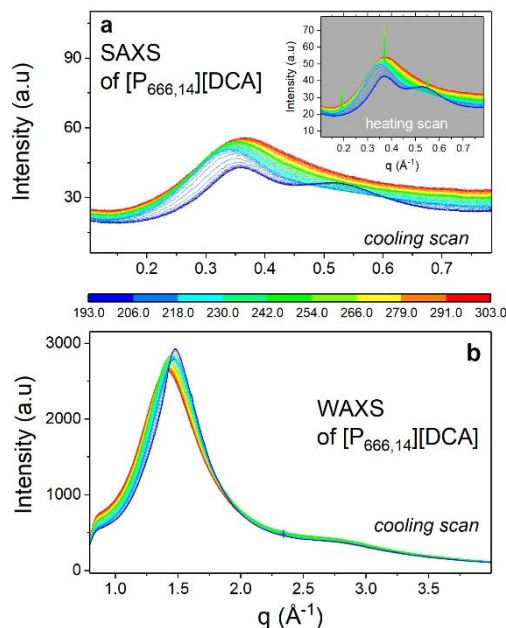
The materials examined herein were chosen as model systems to understand the effect of molecular architecture and external thermodynamic variables (temperature and pressure) on the charge transport mechanism in amphiphilic aprotic ionic liquids, revealing self-assembly behavior. Specifically,  $[P_{666,14}]^+$  cation with long alkyl chains has been combined with three anions of different sizes and shapes: a relatively small linear thiocyanate,  $[\text{SCN}]^-$ , a larger dicyanamide with bent geometry,  $[\text{DCA}]^-$ , and the largest, trigonal planar tricyanomethanide,  $[\text{TCM}]^-$ . Due to the amphiphilic nature of  $[P_{666,14}]^+$  cation the chosen ILs are expected to reveal self-assembly behavior. Recent X-ray diffraction and FT-IR spectroscopic studies of borohydride salt  $[P_{666,14}][\text{BH}_4]$ , confirmed the enhanced ordering of long alkyl chains in a supercooled liquid state accessible through the first-order liquid-liquid phase transition. Consequently, two liquid phases have been found within single component material. First, at  $T > T_{LL}$  (liquid 1) and the second with nanoscale structuration at  $T < T_{LL}$  (liquid 2). The LLT has also been reported for  $[P_{666,14}][\text{SCN}]$  and  $[P_{666,14}][\text{TCM}]$ [26]; however, the physical properties of  $[P_{666,14}][\text{DCA}]$  were studied only at room temperature conditions (thermal stability, viscosity, and dc-conductivity).[27] To bridge this gap, firstly, differential scanning calorimetry (DSC) studies of  $[P_{666,14}][\text{DCA}]$  have been carried out, and collected thermograms were compared to data recorded for  $[P_{666,14}][\text{SCN}]$  and  $[P_{666,14}][\text{TCM}]$  in Fig. 7.1. As presented, cooling at the rate of  $10 \text{ K}\cdot\text{min}^{-1}$  results in a broad exotherm with an onset at 207.4, 209, and 213.3 K for  $[P_{666,14}][\text{TCM}]$ ,  $[P_{666,14}][\text{DCA}]$  and  $[P_{666,14}][\text{SCN}]$ . Subsequent heating performed after the time-dependent isothermal step at 187 K (the so-called aging process) revealed the step-like change of heat capacity, followed by a well-resolved endothermic peak; the first indicating liquid-glass transition ( $T_g=197 \text{ K}$  the same for all examined here ILs), while the latter, reversible with respect to cooling scan, denoting the first-order liquid-liquid transition (LLT). More thermal effects were observed upon further heating of  $[P_{666,14}][\text{DCA}]$  and  $[P_{666,14}][\text{SCN}]$ : the onset of cold crystallization ( $T_c$ ) and subsequent melting ( $T_m$ ). However, due to the small enthalpy of these events, one can conclude that only partial crystallization of these two ILs occurred upon heating at a standard rate of  $10 \text{ K}\cdot\text{min}^{-1}$ . Extending the time for nucleation and crystal growth by decreasing the heating rate makes both  $T_c$  and  $T_m$  better detectable, while the onset of LLT remains the same (see

Figure S7.1 and Table S7.1). The same experimental protocol applied to  $[P_{666,14}][TCM]$  shows strong resistance to crystallization.



**Fig. 7.1** Differential scanning calorimetry (DSC) traces of  $[P_{666,14}]^+$ -based ILs. Arrows indicate the onset of: LLT (cyan), melting point (red), cold crystallization (green) and  $T_g$  (blue). The values of liquid-liquid transition temperature ( $T_{LL}$ ), onset of cold crystallization ( $T_c$ ), melting temperature ( $T_m$ ) and enthalpy of these processes  $\Delta H$  are collected in Table S1. The chemical structure of  $[P_{666,14}]^+$  cation and  $[TCM]^-$ ,  $[DCA]^-$  and  $[SCN]^-$  anions are also presented.

To investigate the structural changes accompanying LLT, XRD measurements were performed. Fig. 7.2 shows the temperature-dependent structure functions obtained from experiments for  $[P_{666,14}][DCA]$ . As can be seen, the examined IL shows three characteristic peaks at values of  $q$  below  $2 \text{ \AA}^{-1}$ . According to literature reports [28], the most intense diffraction peak near  $1.4 \text{ \AA}^{-1}$  arises from a short-range separation between counterions combined with a carbon-carbon interaction from cation alkyl chains. The latter indicates that hydrophobic tails of  $[P_{666,14}]^+$  have significant contact. This intermolecular peak shifts towards higher  $q$  values with cooling due to the increase in density, and becomes noticeably narrow when IL enters the liquid 2 state. At the same time, the intensity of the first diffraction peak, the so-called pre-peak ( $0.36 \text{ \AA}^{-1}$  at RT) identified with long-range anion-anion correlations, becomes smaller with decreasing temperature and the other peak starts to appear on its high- $q$  side when the liquid 2 state is achieved. The latter one, observed finally at around  $0.53 \text{ \AA}^{-1}$  can be due to the separation of ions of the same charge. The subsequent heating brings opposite changes in the XRD pattern. However, when the temperature rises above  $T_{LL}$ , the Bragg peaks indicating cold crystallization of  $[P_{666,14}][DCA]$  appear (see inset to Fig. 7.2a). These results correspond well with the DSC thermograms discussed above.



**Fig. 7.2** X-ray scattering intensity of [P<sub>666,14</sub>][DCA] at various temperatures recorded on cooling and subsequent heating (inset).

#### 7.4.2 Charge transport mechanism above and below the $T_{LL}$

In the further step, dielectric measurements were performed to examine the charge transport mechanism across the LLT and near the liquid-glass transition. Two experimental protocols have been applied to realize this task. In the first one, the dielectric data were collected on cooling, which allows for monitoring changes in ion dynamics during the transition from a simple liquid state to a nanostructured one. In the second procedure, the ionic liquids were quenched to 187 K (corresponding to a glassy state) in the dielectric setup, and then frequency scans ( $10^{-2}$ – $10^6$  Hz) were recorded upon heating at  $\Delta T = 1$  K intervals, i.e., with the rate of  $1 \text{ K min}^{-1}$ . A complex electric modulus,  $M^*(f) = \varepsilon^*(f)^{-1} = M'(f) + iM''(f)$ , has been adopted to analyze the dielectric response of examined systems. Representative results for [P<sub>666,14</sub>][DCA], in the form of the imaginary part of  $M^*(f)$  function, over a broad range of temperatures, are depicted in Fig. 7.3a. The modulus peak position,  $f_{\text{max}}$ , is strongly temperature-dependent and shifts towards lower frequencies with cooling, which is a typical behavior of ILs. This indicates slower ion mobility and a longer time scale of charge transport in a given system at lower temperatures. At a specific temperature close to  $T_{LL}^{\text{DSC}}$ , the amplitude of the  $M''(f)$  function decreases slightly and then maintains a new level.

At the same time, the  $M''(f)$  peak becomes broader (see also Fig. 7.3b). Below 195 K, the  $M''(f)$  peak, frequently called  $\sigma$ -relaxation, moves out of the experimental window. Then, a secondary mode characterizing the dynamics of the glassy state appears. Analogous results have been observed on the heating scan (see Fig. S7.2); however, an

increase in temperature above  $T_{LL}^{DSC}$  caused cold crystallization. Using the same experimental protocol, that is, heating of quenched IL, we observed cold crystallization of  $[P_{666,14}][SCN]$  in phase 1, whereas phase 2 was stable. At the same time, both liquid states of  $[P_{666,14}][TCM]$  were thermodynamically stable (Fig. S7.3). These results stay in agreement with previously described DSC data.

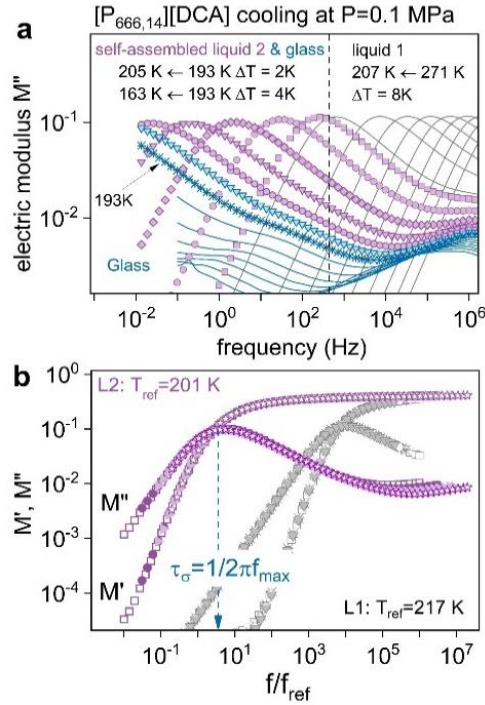


**Fig. 7.3** Dielectric response of  $[P_{666,14}][DCA]$  at ambient pressure conditions. **a** The representative dielectric data of  $[P_{666,14}][DCA]$  in glass (blue scatters and lines), liquid 2 (violet scatters) and liquid 1 (solid lines) phases were obtained on cooling. **b** The representative dielectric data of  $[P_{666,14}][DCA]$  measured in the supercooled liquid 1 state (grey symbols) and self-assembled liquid 2 state (violet symbols) superimposed to each other.

To characterize the physical stability of supercooled liquid 1 and liquid 2 states of  $[P_{666,14}][DCA]$  thoroughly, the time-dependent dielectric scans within the  $T$  range 199–215 K were taken after quench-cooling from room temperature. The procedure of isothermal dielectric measurements is schematically presented in Fig. 7.4a. Subsequently, single-frequency (0.1 MHz) time-dependent scans of  $[P_{666,14}][DCA]$  were performed. As shown in Fig. 7.4b, at least 1.5 hours of induction time is required to start a cold crystallization process at any studied  $T$  in the liquid 1 state. Later on, a decrease of  $M''$  over time takes place. Contrary, phase 2 of  $[P_{666,14}][DCA]$  is a stable liquid without crystallization tendency (see violet lines in Fig. 7.4b). To characterize the crystallization of phase 1 quantitatively, the normalized electric modulus  $M''_{norm}(f)$  has been analyzed in terms of the Avrami-Avramov model. The representative Avrami-Avramov plot for crystallization kinetics at  $T = 209$  K is shown in Fig. 7.4c.

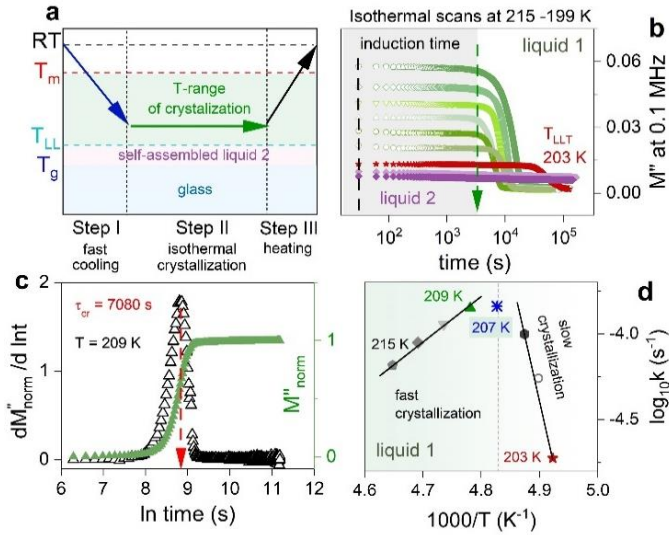


**Fig. 7.4.** **a** The isothermal time-dependent dielectric measurements were performed in the crystallization range; each scan was started after a quench from RT. **b** The time evolution of  $M''$  at 0.1 MHz and various temperatures in liquid 1 and liquid 2 states of  $[P_{666,14}][DCA]$ . **c** The representative kinetic curve of  $[P_{666,14}][DCA]$  obtained from data presented in panel b and normalized using the  $M''_{norm}(f) = \frac{M''(0) - M''(t)}{M''(0) - M''(\infty)}$  (right axis). Avrami-Avramov plot constructed for  $[P_{666,14}][DCA]$  at 209 K (left axis). **d** The constant rate  $k$  of the crystallization process as a function of inverse temperature.

According to the Avramov model, the maximum value of  $dM''_{norm}/d(\ln t)$  vs.  $\ln t$  gives the characteristic time of crystallization,  $\tau_{cr}$  that is inversely related to crystallization rate  $k = 1/\tau_{cr}$ . The latter, plotted in log scale vs.  $T^{-1}$ , indicates two distinct regions of differing propensity to crystallize in liquid 1 state; first with the activation energy of ca.  $100 \text{ kJmol}^{-1}$  close to the LLT and second with  $E_a=45 \text{ kJ/mol}$  far from the LLT (see Fig. 7.4d).

To describe the dynamics in both supercooled liquids and glassy state, we chose a frequency point where the  $M'(f)$  and  $M''(f)$  crossed each other ( $f_{cross}$ ) and determined the time scale of conductivity ( $\sigma$ ) relaxation ( $\tau_{\sigma} = 1/2\pi f_{cross}$ ) over a wide temperature range, covering both liquid 1 and liquid 2. Note that  $f_{cross}$  corresponds perfectly to  $f_{max}$ . To extract the value of conductivity relaxation,  $\tau_{\sigma}$ , in the  $T_g$  region,  $\sigma$ -peak recorded at 197 K has been shifted horizontally to the temperatures  $T < T_g$ , so that its high-frequency side superimposes with the spectra collected in the glassy state. This operation could be employed since all conductivity relaxation modes in liquid 2 retain the same shape, i.e., the time-temperature superposition (TTS) rule is satisfied (Fig. 7.3b).

As illustrated in Fig. 7.5a, all three physical states are well identified on the relaxation map of  $[P_{666,14}][DCA]$ ,  $[P_{666,14}][SCN]$  and  $[P_{666,14}][TCM]$ . Liquid 1 reveals a VFT-type behavior that changes towards Arrhenius law,  $\tau_{\sigma} \propto \exp[-E_a/(k_B T)]$ , at  $T_{LL}^{DSC}$ . A substantial increase in activation energy accompanies this behavior (see Fig. 7.5b).

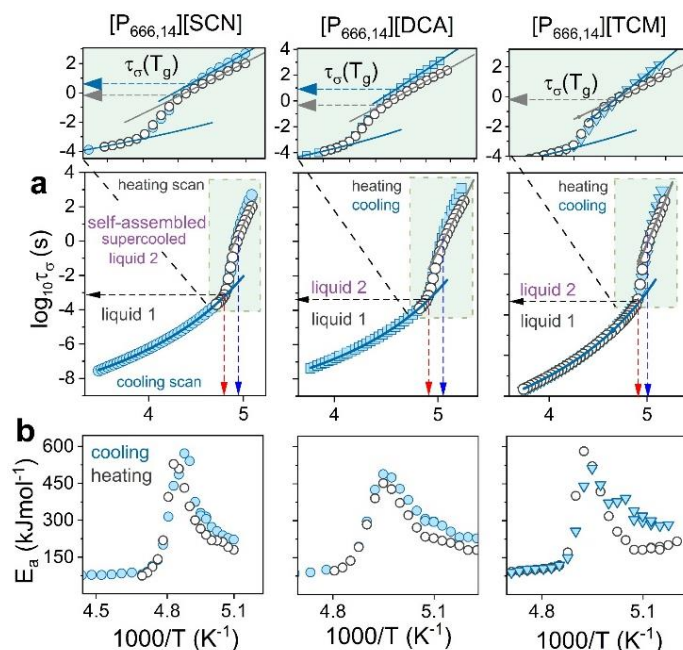


**Fig. 7.5.** **a** Comparison between the temperature dependence of conductivity relaxation time for  $[P_{666,14}][SCN]$ ,  $[P_{666,14}][DCA]$ ,  $[P_{666,14}][TCM]$  (from left to right respectively) obtained cooling and heating scans. Heating has been performed after the quench cooling to the glassy state. Scatters-experimental data, solid lines in liquid 1 state denote the fit of VFT function  $\tau_{\sigma} = \tau_{\infty} \exp\left(\frac{DT_0}{T-T_0}\right)$  to experimental data. Dashed lines indicate  $T_g$  and temperature of LLT (blue and red arrows). Zooms highlight different  $\tau_{\sigma}(T_g)$  obtained on cooling (blue arrow) and heating (grey arrow) scans. **b** Apparent activation energy  $E_a = 2.303R \frac{d \log \tau_{\sigma}}{dT^{-1}}$  calculated from dielectric data obtained on cooling and heating for  $[P_{666,14}][SCN]$ ,  $[P_{666,14}][DCA]$ ,  $[P_{666,14}][TCM]$ .

Upon vitrification of supercooled liquid 2 taking place at  $T_g^{DSC}$ , the  $\tau_{\sigma}(T^{-1})$  continues the Arrhenius dependence but with much lower activation energy (see the zoom). The crossover of  $\tau_{\sigma}(T^{-1})$  visible at  $T_g$  is an inherent part of the liquid-glass transition and reflects the slowing down of charge transport in a disordered solid state.[29] However, close inspection of Fig. 7.5a reveals that the time scale of charge diffusion in amorphous  $[P_{666,14}][DCA]$ ,  $[P_{666,14}][SCN]$  and  $[P_{666,14}][TCM]$  is thousands of times faster when compared to 1000s ( $\log \tau_{\sigma}(T_g)=3$ ) observed for all aprotic ILs examined so far.[30] Specifically,  $\log \tau_{\sigma}(T_g)=-0.14^{SCN}$ ,  $-0.36^{DCA}$  and  $-0.38^{TCM}$ , (for heating scans) and importantly, it is sensitive to the thermal history of the sample. That is, different values of  $\log \tau_{\sigma}(T_g)$  are obtained for slowly cooled and quenched IL. As shown in zoomed Fig. 7.5a, when liquid 2 of  $[P_{666,14}][DCA]$  and  $[P_{666,14}][SCN]$  is cooled slowly, it enters a glassy state at  $\tau_{\sigma}$  much longer than it is for quenched material. Furthermore, the slow cooling of these ILs brings a glass of much higher apparent activation energy (see Fig. 7.5b). Thus, two different glassy states can be obtained within a single-component

material. This phenomenon, called polyamorphism, gives a unique possibility to tune the properties of disordered electrolytes. However, it has never been observed before for ionic systems. From this point of view, it is interesting to note that in contrast to ILs containing [DCA] and [SCN] anions, the liquid-glass transition occurs at single  $\log\tau_\sigma(T_g)$  for quenched and slowly cooled [P<sub>666,14</sub>][TCM]. This suggests that the self-assembly of alkyl chains in [P<sub>666,14</sub>]-ILs depends on anion and brings differences in conductivity mechanisms between examined systems. However, fast charge transport, to some extent independent of structural rearrangements, is expected in supercooled liquid 2 and in the vicinity of liquid-glass transition of [P<sub>666,14</sub>][DCA], [P<sub>666,14</sub>][SCN] and [P<sub>666,14</sub>][TCM]. To verify this hypothesis, there is a need for a direct comparison between the time scale of charge transport and the structural dynamics,  $\tau_\alpha$ , under the same conditions.

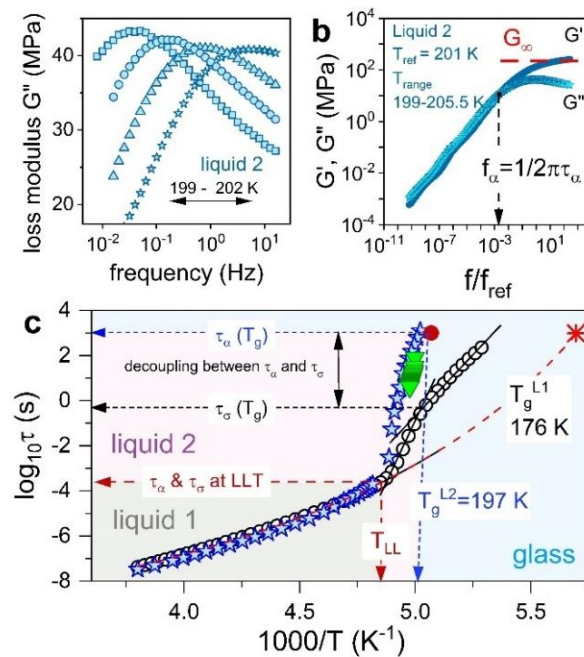


**Fig. 7.6.** **a** The mechanical response of [P<sub>666,14</sub>][DCA] recorded in supercooled liquid 2 and presented in the form of loss modulus peaks  $G''(f)$ . In panel **b**, the mechanical data recorded at various temperatures in liquid 2 have been superimposed to each other and form so-called masterplot. **c** Direct comparison between conductivity relaxation times (open circles) obtained on heating and structural relaxation times determined from rheology (blue stars) and TMDSC (green triangles) in supercooled liquid 1, 2 and glass for [P<sub>666,14</sub>][DCA]. The red point denotes  $T_g$  from standard DSC. The red star presents the predicted value of  $T_g$  for liquid 1 state.

Two experimental techniques were used to determine the time of structural motions: temperature-modulated DSC (TMDSC) and rheology. The experiments have been performed for [P<sub>666,14</sub>][DCA], and the representative results of mechanical measurements are illustrated in Fig. 6a. In analogy to dielectric data, the frequency dependence of shear loss modulus  $G''$  forms a well-resolved peak; the intersection of  $G'(f)$  and  $G''(f)$  gives the structural relaxation time,  $\tau_\alpha$  (Fig. 6b). Since the  $G''(f)$  peaks are well-identified only

within four decades from the liquid-glass transition, Maxwell relation  $\tau_\alpha = \eta/G_\infty$  was employed to convert  $\eta(T^{-1})$  data to  $\tau_\alpha(T^{-1})$  and thereby probe the structural dynamics of liquid 1. From Fig. 7.6c, it becomes evident that the mechanical  $\alpha$ -relaxation of [P<sub>666,14</sub>][DCA] follows the VFT law in liquid 1 and steeply increases at the temperature of LLT: over 8 K, there is a six-decade change in the value of  $\tau_\alpha$ . Consequently, recalling condensed matter physics terminology, one can state that liquid 2 is much more fragile than liquid 1. Notably, an opposite conclusion was drawn by H. Tanaka for molecular liquid TPP,[31] who explicitly identified LLT as fragile-to-strong transition.

An important conclusion is drawn from the direct comparison of temperature dependencies of  $\tau_\alpha$  and  $\tau_\sigma$ , obtained for [P<sub>666,14</sub>][DCA]. In supercooled liquid 1, these two time scales are nearly identical, implying that the charge transport requires the diffusion of entire molecular units. Such a vehicle mechanism characterizes all aprotic ILs studied so far.[32] Upon cooling below  $T_{LLT}$ , the timescales of  $\tau_\alpha$  and  $\tau_\sigma$  start to diverge: the structural motions become slower than the time scale of conductivity relaxation, and the most significant difference (decoupling) between these two variables, noted as  $R$ , is seen at  $T_g$ , where  $R = \log\tau_\alpha(T_g) - \log\tau_\sigma(T_g) = 3.1$ . Thus, when the structural relaxation time of the glassy phase is in the order of 1000 s, which gives [P<sub>666,14</sub>][DCA] mechanical properties of a solid, fast charge transport still occurs and takes around 1 s ( $\log\tau_\sigma(T_g) = 0$ ). This decoupling occurs for all three [P<sub>666,14</sub>]<sup>+</sup>-based ILs, and only slightly depends on the anion size. Such a phenomenon has never been reported for aprotic ILs or any other material revealing self-assembly or LLT, which raises an intriguing question about the mechanism behind this observation.

Taking into account the chemical structure of examined ILs and their self-assembly behavior, one can expect that in liquid 2, long alkyl chains of cations form a skeleton that contributes substantially to structural dynamics. At the same time, anions are free to move through created channels and thus are responsible for charge transport. Such a scenario has been previously described for polymerized ionic liquids, in which anions travel easily within channels of the covalently bonded, cationic polymer backbone.[33],[34] From this point of view, [P<sub>666,14</sub>][DCA], [P<sub>666,14</sub>][SCN] and [P<sub>666,14</sub>][TCM] in their liquid 2 state seem to act as single-ion conductors. To verify this hypothesis, we used [P<sub>666,14</sub>][DCA] as a reference system and determined the translational diffusion of cations in liquid 2 state using <sup>1</sup>H NMR relaxometry. We found that the  $D_{trans}$  of [P<sub>666,14</sub>]<sup>+</sup> cations slows below  $T_{LL}$  and practically does not change with further temperature decrease.  $D_{trans}$  at 204 K was found to be equal  $7.32 \cdot 10^{-14}$  m<sup>2</sup>/s and fluctuates within the error of  $2.82 \cdot 10^{-15}$  m<sup>2</sup>/s in liquid 2 state.

To provide more detailed insight into charge transport in studied systems, we have performed high-pressure experiments.

### 7.4.3 Compression through the liquid-liquid and liquid-glass transitions.

The experimental protocol of high-pressure measurements has been described in the Methods section. The representative spectra recorded for  $[P_{666,14}][DCA]$  in the pressure range 0.1-200 MPa are shown in Fig. S7.4, while the isothermal conductivity relaxation times plotted as a function of pressure are presented in Fig. 7.7a. In analogy to ambient pressure results, every  $\tau_\sigma$ - $P$  dependence obtained for  $[P_{666,14}][TCM]$ ,  $[P_{666,14}][SCN]$ , and  $[P_{666,14}][DCA]$  reveals two kinks: first at  $\tau_\sigma \approx 3.5$  ms separating two supercooled liquids, and second, being a manifestation of liquid-to-glass transition. Defining  $P_{LL}$  and  $P_g$  as the pressure at which the  $\log\tau_\sigma$  rapidly changes the behavior, the  $T_{LL}(P_{LL})$  and  $T_g(P_g)$  dependences were obtained for the three studied ILs (Fig. 7.7b). In addition, the  $T$ - $P$  conditions of cold crystallization have been included for  $[P_{666,14}][SCN]$  and  $[P_{666,14}][DCA]$ . Finally, the melting line  $T_m(P_m)$  for  $[P_{666,14}][DCA]$  has been determined (Fig. S7.5).

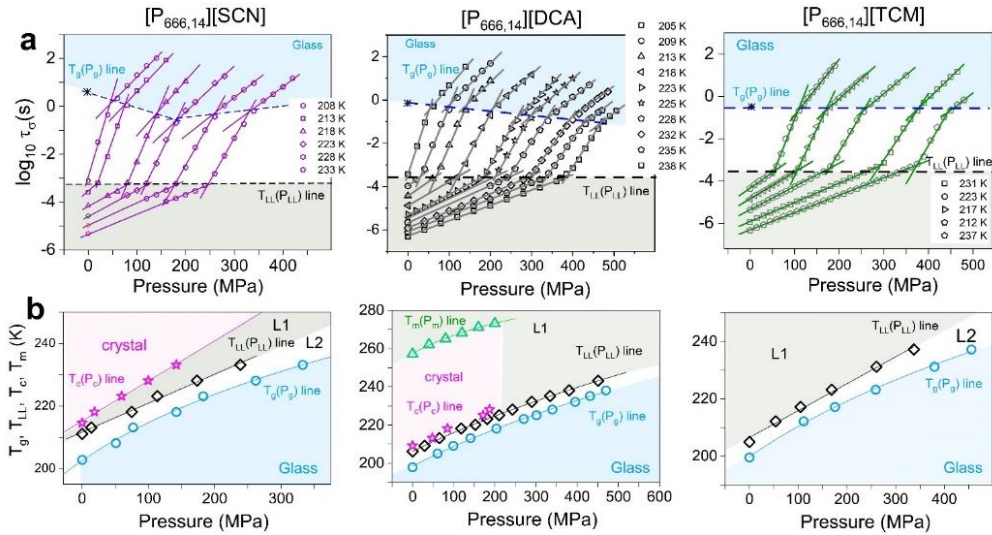


**Fig. 7.7** High-pressure data of  $[P_{666,14}][SCN]$ ,  $[P_{666,14}][DCA]$  and  $[P_{666,14}][TCM]$  (from left to right respectively). **a** presents the pressure dependence of conductivity relaxation time measured at various  $T$ . Solid lines denote fit of Arrhenius equation to experimental data. Dashed lines separate liquid 1 from liquid 2 (black dashed line) and liquid 2 from glass (blue dashed line). **b**  $T_{LL}$  and  $T_g$  as a function of  $P$  is presented. The color area on **a** and **b** panels denotes the liquid 1 phase (gray) and glass region (blue), crystalline state (pink). L1 denotes liquid 1 while L2 liquid 2.

A closer inspection of Fig. 7.7a reveals different pressure behavior of ion dynamics in each examined IL. In  $[P_{666,14}][TCM]$ , both liquid-liquid and liquid-glass transitions occur at isochronal conditions:  $\log\tau_\sigma(T_{LL}, P_{LL}) = -3.5$  and  $\log\tau_\sigma(T_g, P_g) = -0.5$ . In  $[P_{666,14}][DCA]$ , there is a continuous shift of  $\tau_\sigma(P_g)$  towards shorter relaxation times with increasing pressure. Finally, in  $[P_{666,14}][SCN]$ , there is a clear minimum in  $\tau_\sigma(P_g) = f(P)$  dependence, around 170 MPa. Furthermore, for every  $P_g$  value,  $\tau_\sigma$  is larger than 1000 s.

Note that the time scale of structural relaxation is isochronal ( $\tau_\alpha \approx 1000$ s) regardless of  $T$ - $P$  thermodynamic conditions.[35] Thus, the examined phosphonium ILs are characterized by pressure-tunable fast charge transport, decoupled from structural relaxation and governed by anion size. It can be speculated that, for relatively small anions,  $[\text{SCN}]^-$  and  $[\text{DCA}]^-$ , an increase in pressure results in better packing of cation alkyl chains and consequently provides more channels for anion motions. In this scenario, the diffusion of anions becomes faster at elevated pressures, which is visualized as shorter  $\log\tau_\sigma(T_g, P_g)$ . However, above the pressure limit of 180 MPa, the  $[\text{SCN}]^-$  slows down due to the reduced free volume,  $V_{\text{free}}$ . The same effect is expected for  $[\text{P}_{666,14}][\text{DCA}]$ ; however, it probably occurs above the experimentally available pressure range. Further increase in anion size, in turn, makes the alkyl chain arrangements more difficult, which results in irregular channels for anion transport. In this case, anions still move faster than cations making the system decoupled; however, squeezing does not affect it much, making  $\log\tau_\sigma(T_g, P_g)$  pressure independent.

#### 7.4.4 MD simulations of the charge transport mechanism

MD simulations have been performed to verify the proposed mechanism of charge transport (see SI for details). To mimic the architecture of the phosphonium ILs, a simple bead-spring coarse-grained model was employed, consisting of an amphiphilic molecule containing a positively charged head connected to a stiff, neutral tail and a negatively charged free counterion (Fig. 7.8a). Since recently, we found that the 14-carbon chain is critical to observe LLT and shortening the other three tails makes the LLT better detectable we have been omitted the latter in MD simulations.[36] The morphologies at high and low reduced temperatures and various pressures have been considered for two different anion-to-cation size ratios. At high temperatures, independently of  $R_-/R_+$  ratio, thermal fluctuations were dominant, yielding an isotropic structure of ILs. Upon decrease in temperature, the cations tend to form nanostructures with different morphology depending on applied pressure  $P$  and anion size. For small anions, an increase in pressure induces a morphological transition from weakly ordered aggregates composed of ionic pairs or triplets, to lamellar-type phases[16]. In contrast, for bulky anions, interconnected phases with continuous 3D curvature emerge, regardless of  $P$ . Notably, the diffusivity of cations  $D_+$  is negligible in all examined cases (they are almost immobile,  $D_+ \approx 0$ ), while anion dynamics is strictly related to the IL phase and applied pressure. Larger anions favor isotropic diffusivity, decreasing with pressure, whereas  $D_-$  varies nonmonotonically with pressure for smaller anions. Namely, the random distribution of small cation clusters leads to isotropic diffusivity of anions at low pressure, while lamellar-type phases, obtained at higher pressures, favor anisotropic diffusivity making the anions transport

five times faster along the lamellar plane. A pressure increase brings a further decrease in  $D$ . (Fig. S7.6).

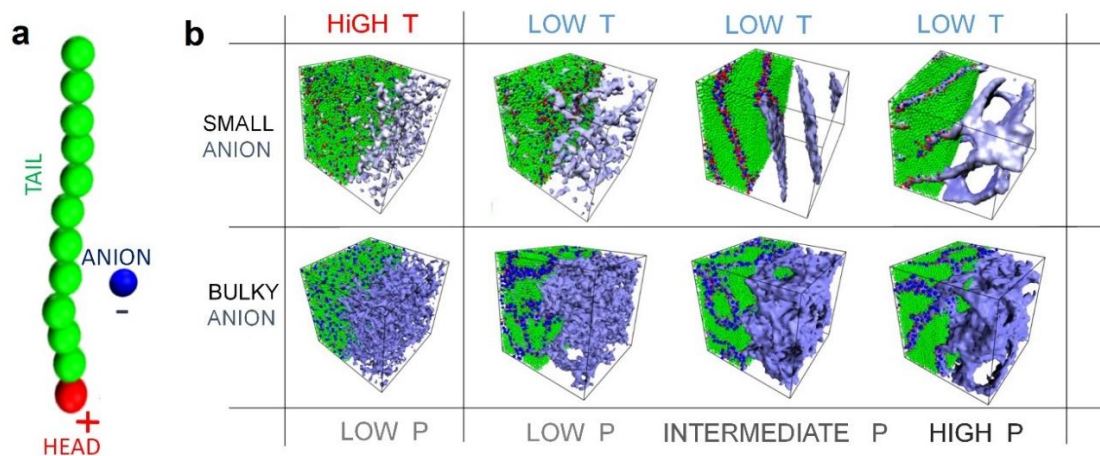


**Fig. 7.8** MD simulations snapshots. Panel **a** presents a single amphiphilic cation molecule with its counterion. Panel **b** illustrates IL morphologies at various  $T$ - $P$  conditions. Columns present molecular structure of IL obtained at high ( $T=5$ ) and low ( $T=2$ ) reduced temperature, correspondingly, and its variation with increased reduced pressure  $P$  (from low  $P=2$ , through intermediate  $P=5$ , to high  $P=10$ ). Rows display results for two different anion-to-cation size ratios  $R_a/R_c$  (small anion with  $R_a/R_c = 1$  and bulky anion with  $R_a/R_c = 2$ ). Isosurface representation of ionic channels density consisting of head groups and anions are displayed in blue

## 7.5 Conclusions

Here, we focused on the charge transport mechanism of three phosphonium ionic liquids comprising the same large amphiphilic cation with long, intertwined non-polar alkyl chains, and much smaller anions, charge-balanced by the cationic phosphonium centers. Our studies reveal that upon isothermal compression, and isobaric cooling, the examined phosphonium ILs:  $[P_{666,14}][SCN]$ ,  $[P_{666,14}][DCA]$ , and  $[P_{666,14}][TCM]$ , transform from one liquid state to another, both differing in self-assembly behavior, viscosity and charge transport mechanism. The comparative analysis between the time scales of ion diffusion ( $\tau_\sigma$ ) and structural dynamics ( $\tau_\alpha$ ) shows that charge transport is fully controlled by viscosity in liquid 1, that is, at  $T > T_{LL}$  and  $P < P_{LL}$ . In contrast, liquid 2 has a nanostructure that facilitates charge transport decoupled from structural dynamics. Long alkyl chains of the cations are partially frozen in non-polar domains while anions move swiftly through the created channels. From this point of view, the supercooled liquid 2 phase in  $[P_{666,14}]^+$  ILs seems to mimic single-ion conductors, such as polymerized ionic liquids. The self-assembled nanostructures of liquid 2, allowing fast ion transport, can be fine-tuned by sample thermal history, anion size, and compression. When quenching and slow cooling are applied, two different glasses differing in the time scale

of ion motions can be obtained from the liquid 2 state. That is, in both disordered solids, the charge transport is independent of structural dynamics, however, in the one obtained by quenching, the decoupling is more pronounced compared to the slowly cooled system. This phenomenon, called polyamorphism, observed for the first time in ILs, gives a unique possibility to tune the properties of disordered electrolytes. Furthermore, a decrease in anion size brings nonmonotonic behavior of decoupling at elevated pressure. That is,  $\tau_{\sigma}(P_g)$  reveals a minimum accompanied by diffusivity changes from isotropic to an anisotropic character, and the latter facilitates anion transport along the lamellar-type plane. For bulky anions, inter-connected phases with 3D continuous curvature emerge regardless of  $P$  and make  $\tau_{\sigma}(P_g)$  constant. These results pave the way for a better understanding of self-organization in ILs and hence control the charge transport mechanism in ion-containing systems. The self-assembly-based charge transport mechanism discovered here offers a new approach for fine-tuning transport properties of ILs and other fluids with ordered nanostructures, which could profoundly impact emerging technologies associated with ionic liquids as soft conductive materials.

## 7.6 Acknowledgement

This research was funded in whole by National Science Centre, Poland [Opus 21, 2021/41/B/ST5/00840]. For the purpose of Open Access, the author has applied a CC-BY public copyright licence to any Author Accepted Manuscript (AAM) version arising from this submission.

## 7.7 Supplementary information

### Supplementary Methods

Trihexyl(tetradecyl)phosphonium chloride,  $[P_{666,14}]Cl$ , was kindly provided by Solvay. Sodium tricyanomethanide was bought from TCI Chemicals. All other chemicals were purchased from Sigma-Aldrich and used as received. XRF analysis was performed on a Rigaku NEX QC+ QuantEZ High-Resolution Energy Dispersive X-ray Fluorescence (EDXRF) Spectrometer. NMR spectra were recorded on either a Bruker Avance III 400 MHz spectrometer or a Bruker Avance II DPX 600 MHz spectrometer.  $[P_{666,14}][DCA]$  was supplied from Ionitec.

$[P_{666,14}][SCN]$ . Trihexyl(tetradecyl)phosphonium chloride  $[P_{666,14}]Cl$  (0.010 mol eq.) and  $K[SCN]$  (0.013 mol eq.) were separately added to 25 cm<sup>3</sup> deionised water (18.2 M $\Omega$ .cm) deionised water (total 50 cm<sup>3</sup>) and then combined in a round-bottomed flask (250 cm<sup>3</sup>), resulting in the formation of a biphasic liquid system; the mixture was left to react (1 h, room temperature, 600 rpm). The aqueous layer was separated, and the organic layer was collected and washed, firstly with deionised water (10 cm<sup>3</sup>) and then dichloromethane,

DCM (10 cm<sup>3</sup>). Subsequent washes were performed with solution of K[SCN] in deionised water (18.2 MΩ.cm). Final three washes were performed with deionised water (18.2 MΩ.cm) until no chloride could be detected with XRF. Subsequently, DCM was removed *via* rotary evaporation (30 min, 35 °C) and the ionic liquid was dried under high vacuum (12h, 70 °C, 10<sup>-2</sup> mbar). XRF analysis of [P<sub>666,14</sub>][SCN] confirmed chloride content was below the detectable limit. <sup>1</sup>H, <sup>13</sup>C and <sup>31</sup>P NMR spectra of the ionic liquid were recorded in *d*<sub>6</sub>-DMSO.

**[P<sub>666,14</sub>][TCM].** Trihexyl(tetradecyl)phosphonium chloride [P<sub>666,14</sub>]Cl (0.010 mol eq.) and sodium tricyanomethanide, Na[TCM] (0.013 mol eq.) were separately added to 25 cm<sup>3</sup> deionised water (18.2 MΩ.cm) (total 50 cm<sup>3</sup>) and then combined in a round-bottomed flask (250 cm<sup>3</sup>), resulting in the formation of a biphasic liquid system; the mixture was left to react (1 h, room temperature, 600 rpm). The aqueous layer was separated, and the organic layer was collected and washed, firstly with deionised water (18.2 MΩ.cm) (10 cm<sup>3</sup>) and then dichloromethane, DCM (10 cm<sup>3</sup>). Six subsequent washes were performed with solution of Na[TCM] in deionised water (18.2 MΩ.cm). Final three washes were performed with deionised water (18.2 MΩ.cm) until no chloride could be detected with silver nitrate solution. Subsequently, DCM was removed *via* rotary evaporation (30 min, 35 °C) and the ionic liquid was dried under high vacuum (12h, 70 °C, 10<sup>-2</sup> mbar). XRF analysis of [P<sub>666,14</sub>][TCM] recorded a chloride content of 89.3 ppm with a lower detection limit (LLD) of 2.80 ppm. <sup>1</sup>H, <sup>13</sup>C and <sup>31</sup>P NMR spectra of the ionic liquid were recorded in *d*<sub>6</sub>-DMSO.

Prior to the measurements, the samples were dried under vacuum at 90 °C for 24 h. The water content detected using the Karl Fischer method, was around 500 and 300 ppm before and after drying, respectively.

### **Coarse-grained model, simulation methodology and numerical results.**

Molecular dynamics simulations of ionic liquids comprised of amphiphile molecules were performed using a bead-spring model at coarse-grained resolution. We adopted the numerical model that was used in the previous study of conductivity in dry ionic liquids [16]. An individual amphiphile molecule is composed of a positively charged head (cation) linked to a stiff tail of  $N_t = 11$  adjacently connected neutral beads. The system electroneutrality was maintained by adding negatively-charged counterion beads to compensate for each charged cation on the amphiphile. The non-bonded interactions between beads  $i$  and  $j$ , separated by a distance  $r$ , are accounted by the truncated and shifted expanded Lennard-Jones (LJ) potential [37]

$$V^{LJ}(r) = \begin{cases} 4\epsilon \left[ \left( \frac{\sigma}{r-\Delta_{ij}} \right)^{12} - \left( \frac{\sigma}{r-\Delta_{ij}} \right)^6 \right] + \delta_{ij} & r \leq r_{ij}^{\text{cut}} + \Delta_{ij}, \\ 0 & r > r_{ij}^{\text{cut}} + \Delta_{ij}. \end{cases} \quad (\text{S7.1})$$

In the above equation,  $\epsilon = k_B T$  is the parameter that controls strength of the LJ potential, where  $k_B$  is the Boltzmann constant and  $T$  is the absolute temperature. The potential of (Eq. S7.1) is a standard 12-6 LJ potential shifted to the right by the parameter  $\Delta_{ij}$  which allows to account for interactions between beads of different size. In (Eq. S7.1) the potential shift for tail-tail  $\Delta_{tt}$ , tail-cation  $\Delta_{tc}$ , and cation-cation  $\Delta_{cc}$  pairs is  $\Delta_{tt} = \Delta_{tc} = \Delta_{cc} = 0$ . This yields the equal size of tail  $R_t$  and cation  $R_c$  beads which is set to:  $R_t = R_c = \sigma$ . The potential shift for tail-anion  $\Delta_{ta}$ , cation-anion  $\Delta_{ca}$ , and anion-anion  $\Delta_{aa}$  pairs is:  $\Delta_{ta} = \Delta_{ca} = (R_a - \sigma)/2$  and  $\Delta_{aa} = R_a - \sigma$ , where  $R_a$  is the size of anion. In this study we consider two diameters of anions, i.e.  $R_a = \sigma$  (denoted as small anions) and  $2\sigma$  (denoted as bulky anions). The cutoff distance  $r_{tt}^{\text{cut}}$  in (Eq. S7.1) is adjusted to model hydrophobic and hydrophilic interactions between beads. To account for hydrophobicity between tail beads we take  $r_{tt}^{\text{cut}} = 6\sigma$ . The same cutoff was used for the interactions between cation heads  $r_{cc}^{\text{cut}} = 6\sigma$ . All other pairs of beads interact through the LJ potential with a cutoff  $r_{tc}^{\text{cut}} = r_{ta}^{\text{cut}} = r_{ca}^{\text{cut}} = r_{aa}^{\text{cut}} = 2^{1/6}\sigma$ . This choice provides a repulsive LJ force between hydrophobic tails and hydrophilic head groups and anions. The quantity  $\delta_{ij}$  in (Eq. S7.1) is chosen such that  $V^{eLJ}(r_{ij}^{\text{cut}} + \Delta_{ij}) = 0$ .

The connectivity between two adjacent chain monomers is maintained by the finite extension nonlinear elastic (FENE) potential. [38],[39]

$$V^{FENE} = -\frac{1}{2}k_F r_F^2 \ln \left[ 1 - \left( (r - \Delta_{ij})/r_F \right)^2 \right]. \quad (\text{S7.2})$$

where  $k_F = 30\epsilon/\sigma^2$  is the bond spring-constant and  $r_F = 1.5\sigma$  is the maximum bond length. Depending on the bead size the spring extends up to  $r_F + \Delta_{ij}$ .

In our experiments tails are expected to be stiff. To account for large persistence length of tails, in simulations we introduced bond-bending potential which acts on three consecutive tail beads. The bending potential reads

$$V^B = k_\theta (\theta - \theta_0)^2 \quad (\text{S7.3})$$

where  $k_\theta = 10\epsilon/\text{rad}^2$  is the bending stiffness which yields persistence length on the order of the tail size. In (Eq. S7.3)  $\theta$  is the angle between two subsequent tail bond vectors and  $\theta_0 = 180^\circ$  is the reference angle.

The Coulombic interactions were introduced by assigning to each cation head a rescaled charge of  $q = +e/\sqrt{4\pi\epsilon_0\sigma\epsilon}$  where  $e$  stands for the elementary charge and  $\epsilon_0$  is the electric permittivity of the vacuum. Each anion carries an opposite charge of  $-q$ . The short-range electrostatic interactions between any two charged particles are calculated via:

$$V^C(r) = \pm \epsilon \frac{l_B}{r}, \quad r < r_e \quad (\text{S7.4})$$

where the Bjerrum length  $l_B \equiv q^2\sigma/\epsilon_p$  determines the strength of electrostatic interactions and  $\epsilon_p$  is the relative dielectric constant of the medium. In our simulations we set  $l_B = 10\sigma$  corresponding to  $\epsilon_p = 80$  which is in accordance with dielectric constant reported for dense polymeric melts [16],[40]. The electrostatic cut-off distance  $r_e$  in Eq. (S7.3) was set to  $r_e = 10\sigma$ . Above  $r_e$  longer-range electrostatic interactions are calculated via Particle-Particle-Particle Mesh (PPPM) Ewald method and the error tolerance for force was set to  $10^{-4}\epsilon/\sigma$ .

The LAMMPS package [41] was utilized to perform molecular dynamics simulations in NPT ensemble using Nosé-Hoover barostat. Simulations were carried out in a cubic box with periodic boundary conditions. Simulations were run with a timestep of  $\delta t = 0.005\tau$ , where  $\tau = \sigma\sqrt{m/\epsilon}$  is the time unit. Bead masses were set to  $m = 1$  for all tail monomers including cation head. The mass of anion was set proportional to its diameter, i.e. through relationship:  $m_a = m(R_a/\sigma)^3$ .

Each system was comprised of 5400 amphiphile molecules and equal amount of counterions. For each individual system we firstly carried out simulations at high temperature  $T = 5$  to obtain isotropic phase. The morphologies of ionic liquids at low temperature were produced using step-annealing procedure in which we slowly cooled down the system from high ( $T = 5$ ) to low ( $T = 2$ ) temperature at prescribed pressure  $P$ . The temperature step size during annealing was  $\Delta T = 0.25$  K. We consider three values of  $P$  in this study denoted as low ( $P = 2.5$ ), intermediate ( $P = 5.0$ ) and high ( $P = 10 \sigma^3/\epsilon$ ) pressure, respectively. Each system was simulated at least  $5 \cdot 10^7$  time steps to ensure thermodynamic stability of the observed phase. We also tested different starting configurations of ionic melts at high temperature to exclude possible effects of the initial configurations on the final assembled morphologies. We found no influence of starting configuration on the resulting ionic liquid assemblies.

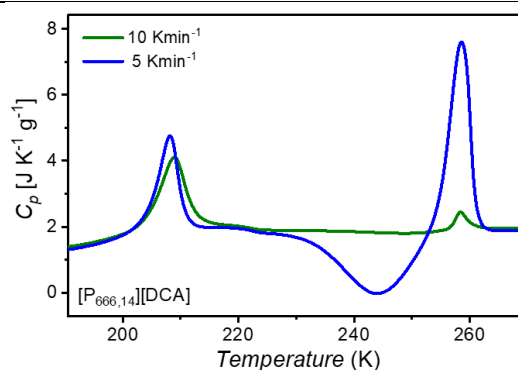
In Fig. S7.6 we display MD data for diffusivity  $D_a$  of small anions with anion-to-cation size ratio  $R_a/R_c = 1$  (depicted as squares) and bulky anions with  $R_a/R_c = 2$  (displayed as circles) measured for ionic liquid morphologies obtained at different pressure conditions. The values of  $D_a$  were calculated from the mean-squared displacement of anions. The relative size of anions strongly influences pressure-dependent diffusivity profiles. For anions of the same size as cations ( $R_a/R_c = 1$ ) nonmonotonic behavior is observed. Here, the increase in  $D_a$  between pressure  $P = 2.5$  and  $5 \sigma^3/\epsilon$  is due to morphological transition of ionic liquid from weakly ordered aggregates composed of ionic pairs or triplets to ordered lamellar phases. The lamellar phases obtained for  $P > 5 \sigma^3/\epsilon$  have highly anisotropic diffusivity which is signaled by an increase in the ratio  $D_{||}/D_{\perp}$  of parallel to perpendicular components of  $D_a$  (see inset of

Fig. S7.6). The decrease in  $D_a$  visible between  $P = 5$  and  $10 \sigma^3/\epsilon$  is caused by an increase in the overall bead density in the whole system ( $\approx 0.9\sigma^{-3}$ ) which significantly hinders anion dynamics. Larger size polarity between anion and cation (i.e. for  $R_a/R_c = 2$ ) induces 3D inter-connected morphological phases of ionic liquids and leads to monotonic decrease of  $D_a$  with increasing  $P$ . Here diffusivity is isotropic ( $D_{||}/D_{\perp} \approx 1$ ) irrespectively of applied  $P$  (see inset of Fig. S7.6).

**Table S1.** Thermodynamic properties of studied ILs.

	Anion		
	[SCN] <sup>-</sup>	[DCA] <sup>-</sup>	[TCM] <sup>-</sup>
$T_{LLT}^c$ (K)	213.3	209.04 <sup>*</sup> ; 209.1	207.4
$-\Delta H_{LLT}^c$ (Jg <sup>-1</sup> )	11.4	10.3 <sup>*</sup> ; 9.2	8.1
$T_{LLT}^h$ (K)	207.1	204 <sup>*</sup> ; 203.8	204.8
$-\Delta H_{LLT}^h$ (Jg <sup>-1</sup> )	11.6	11.5 <sup>*</sup> ; 9.9	8.6
$T_g$ (K)	197.7 <sup>a</sup> ; 199.1 <sup>b</sup>	197.3 <sup>a</sup>	197.7 <sup>a</sup> ; 196.3 <sup>b</sup>
$T_{LL}^{BDS}$ (K)	210.3	203	203.6
$T_c$ (K)	254.3	231.7 <sup>*</sup> ; 240.6	-
$-\Delta H_c$ (Jg <sup>-1</sup> )	1.9	23.3 <sup>*</sup> ; 1.3	-
$T_m$ (K)	272.3	254.2 <sup>*</sup> ; 256.2	-
$\Delta H_m$ (Jg <sup>-1</sup> )	5.0	24.1 <sup>*</sup> ; 1.3	-
$\nu$ (nm <sup>3</sup> )	0.048	0.064	0.093
$dT_g/dP$ (KGPa <sup>-1</sup> )	144	112	118
$dT_{LL}/dP$ (KGPa <sup>-1</sup> )	109	104	93
$dT_m/dP$ (KGPa <sup>-1</sup> )	-	130	-

a: The glass transition temperature was determined from DSC measurements after 6h aging at -183.15K with the heating rate 10 K/min;  
b: The glass transition temperature determined from dielectric measurements  
\* 5 K/min; Others: 10 K/min  
The van der Waals volume was calculated by using the Bondi method.



**Fig. S7.1** The DSC thermograms of  $[P_{666,14}][DCA]$  were obtained on heating with the rates of 5 and 10 Kmin<sup>-1</sup>.

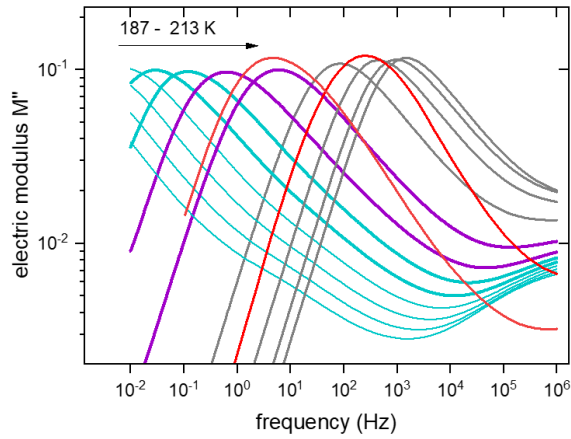


**Fig. S7.2** The dielectric data of  $[P_{666,14}][DCA]$  obtained on heating from 187 to 213 K with the step of 2 K. Cyan lines are obtained in the glassy state, violet in liquid 2, grey in liquid 1 and the red lines denote crystalline state of examined sample.

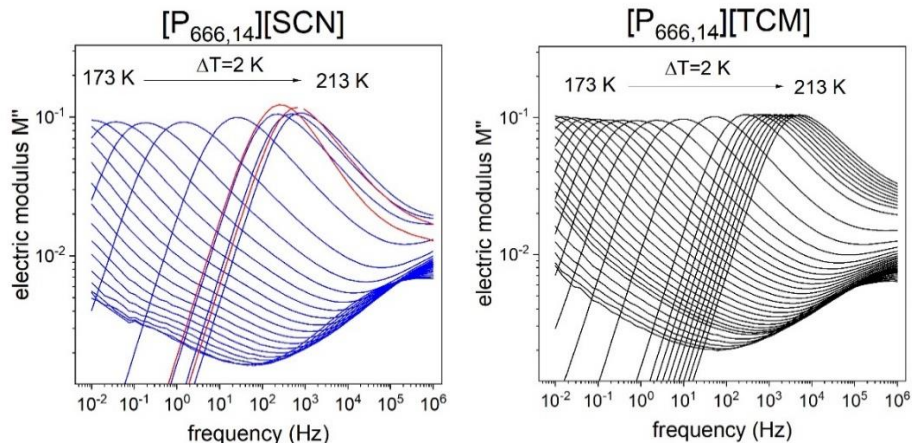


**Fig. S7.3** The dielectric data of  $[P_{666,14}][SCN]$  and  $[P_{666,14}][TCM]$  obtained on heating from 173 to 213 K with the step of 2 K. Red lines denote crystalline state of examined sample.

To quantitatively compare dielectric data of  $[P_{666,14}][DCA]$ ,  $[P_{666,14}][SCN]$  and  $[P_{666,14}][TCM]$ , the same experimental protocol, i.e., measurement on heating after preceding quenching, has been employed (see Fig. S7.3).

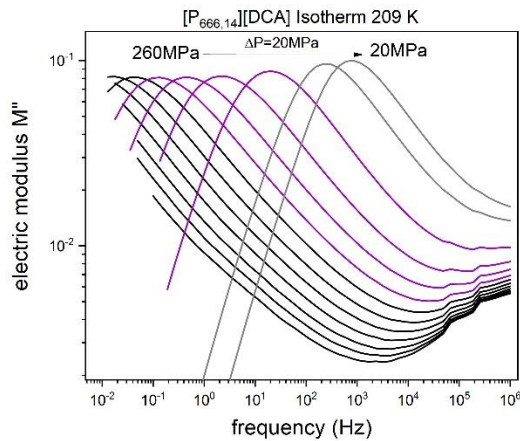


**Fig. S7.4** The dielectric spectra of  $[P_{666,14}][DCA]$  obtained during decompression at 209 K. Black lines denote glassy state, violet-liquid 2 state, grey-liquid 1 state.

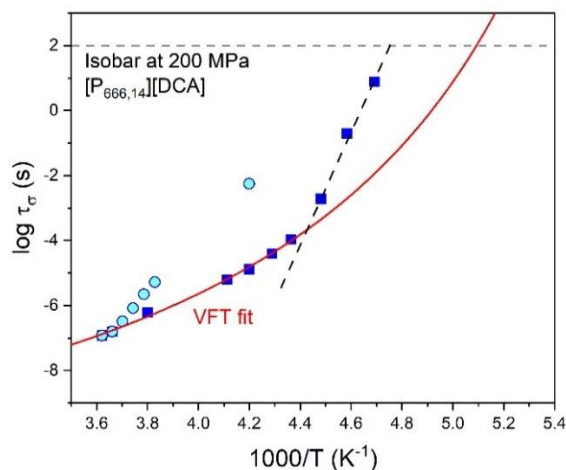


**Fig. S7.5** The conductivity relaxation times of  $[P_{666,14}][DCA]$  at 200 MPa (blue squares). The data in liquid 1 are parametrized by the VFT equation. Blue circles are obtained during the heating after crystallization at 228 K and 200 MPa. The melting point at 200 MPa was determined as the temperature where experimental data meet the VFT line.

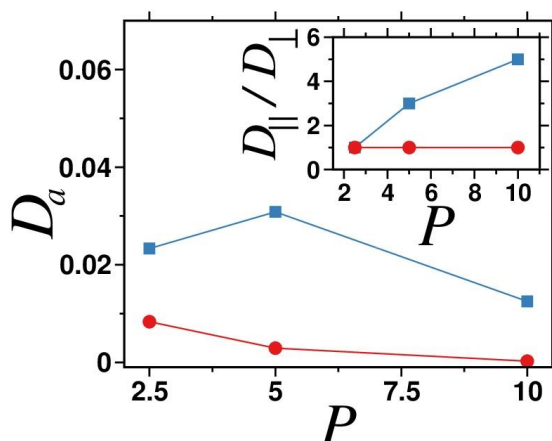


**Fig. S7.6** MD simulation data for diffusivity of anions  $D_a$  in ionic liquids at temperature  $T = 2$  plotted as a function of imposed pressure  $P$ . Data displayed for different anion-to-cation size ratios  $R_a/R_c = 1$  (squares) and  $R_a/R_c = 2$  (circles). The inset shows the ratios  $D_{||}/D_{\perp}$  of parallel to perpendicular components of diffusivity vs.  $P$ .

## 7.8 Reference

- [1] D. R. MacFarlane, M. Forsyth, P. C. Howlett, M. Kar, S. Passerini, J. M. Pringle, H. Ohno, M. Watanabe, F. Yan, W. Zheng, S. Zhang, and J. Zhang, *Nat. Rev. Mater.* **1**, 1 (2016).
- [2] P. Simon and Y. Gogotsi, *Nat. Mater.* **7**, 845 (2008).
- [3] Z. Wojnarowska, K. Grzybowska, L. Hawelek, A. Swiety-Pospiech, E. Masiewicz, M. Paluch, W. Sawicki, A. Chmielewska, P. Bujak, and J. Markowski, *Mol. Pharmaceutics* **9**, 1250 (2012).
- [4] T. Welton, *Chem. Rev.* **99**, 2071 (1999).

- [5] M. Armand, F. Endres, D. R. MacFarlane, H. Ohno, and B. Scrosati, *Nat. Mater.* **8**, 621 (2009).
- [6] T. L. Greaves and C. J. Drummond, *Chem. Rev.* **115**, 11379 (2015).
- [7] R. Hayes, G. G. Warr, and R. Atkin, *Chem. Rev.* **115**, 6357 (2015).
- [8] X. Mao, P. Brown, C. Červinka, G. Hazell, H. Li, Y. Ren, D. Chen, R. Atkin, J. Eastoe, I. Grillo, A. A. H. Padua, M. F. Costa Gomes, and T. A. Hatton, *Nat. Mater.* **18**, 1350 (2019).
- [9] C. Hardacre, J. D. Holbrey, S. E. J. McMath, D. T. Bowron, and A. K. Soper, *J. Chem. Phys.* **118**, 273 (2002).
- [10] H. K. Kashyap, C. S. Santos, N. S. Murthy, J. J. Hettige, K. Kerr, S. Ramati, J. Gwon, M. Gohdo, S. I. Lall-Ramnarine, J. F. Wishart, C. J. Margulis, and E. W. Jr. Castner, *J. Phys. Chem. B* **117**, 15328 (2013).
- [11] A. Triolo, O. Russina, H.-J. Bleif, and E. Di Cola, *J. Phys. Chem. B* **111**, 4641 (2007).
- [12] T. L. Greaves, D. F. Kennedy, S. T. Mudie, and C. J. Drummond, *J. Phys. Chem. B* **114**, 10022 (2010).
- [13] E. Bodo, L. Gontrani, A. Triolo, and R. Caminiti, *J. Phys. Chem. Lett.* **1**, 1095 (2010).
- [14] H. J. Jiang, S. Imberti, R. Atkin, and G. G. Warr, *J. Phys. Chem. B* **121**, 6610 (2017).
- [15] R. Hayes, S. Imberti, G. G. Warr, and R. Atkin, *J. Phys. Chem. C* **118**, 13998 (2014).
- [16] A. Erbaş and M. O. de la Cruz, *Phys. Chem. Chem. Phys.* **18**, 6441 (2016).
- [17] C. S. Santos, H. V. R. Annapureddy, N. S. Murthy, H. K. Kashyap, E. W. Castner Jr., and C. J. Margulis, *J. Chem. Phys.* **134**, 064501 (2011).
- [18] H. Tanaka, *Faraday Discuss.* **167**, 9 (2014).
- [19] G. Floudas, M. Paluch, A. Grzybowski, and K. Ngai, *Molecular Dynamics of Glass-Forming Systems*, Vol. 1 (Springer Berlin Heidelberg, Berlin, Heidelberg, **2011**).
- 20 Z. Wojnarowska, M. Paluch, High pressure dielectric spectroscopy for studying the charge transfer in ionic liquids and solids in *Dielectric Properties of Ionic Liquids* (Springer, Berlin, **2016**).
- 21 Z. Wojnarowska, K. J. Paluch, E. Shoifet, C. Schick, L. Tajber, J. Knapik, P. Włodarczyk, K. Grzybowska, S. Hensel-Bielowka, S. P. Verevkin, and M. Paluch, *J. Am. Chem. Soc.* **137**, 1157 (2015).
- 22 Z. Wojnarowska, H. Feng, M. Diaz, A. Ortiz, I. Ortiz, J. Knapik-Kowalczyk, M. Vilas, P. Verdía, E. Tojo, T. Saito, E. W. Stacy, N.-G. Kang, J. W. Mays, D. Kruk, P. Włodarczyk, A. P. Sokolov, V. Bocharova, and M. Paluch, *Chem. Mater.* **29**, 8082 (2017).
- [23] Z. Wojnarowska, Y. Wang, J. Pionteck, K. Grzybowska, A. P. Sokolov, and M. Paluch, *Phys. Rev. Lett.* **111**, 225703 (2013).
- [24] Z. Wojnarowska, C. M. Roland, A. Swiety-Pospiech, K. Grzybowska, and M. Paluch, *Phys. Rev. Lett.* **108**, 015701 (2012).

- [25] M. A. Harris, T. Kinsey, D. V. Wagle, G. A. Baker, and J. Sangoro, *Proc. Natl. Acad. Sci.* **118**, e2020878118 (2021).
- [26] Z. Wojnarowska, S. Cheng, B. Yao, M. Swadzba-Kwasny, S. McLaughlin, A. McGrogan, Y. Delavoux, and M. Paluch, *Nat. Commun.* **13**, 1342 (2022).
- [27] K. J. Fraser and D. R. MacFarlane, *Aust. J. Chem.* **62**, 309 (2009).
- [28] H. K. Kashyap, C. S. Santos, H. V. R. Annapureddy, N. S. Murthy, C. J. Margulis, and J. Edward W. Castner, *Faraday Discuss.* **154**, 133 (2011).
- [29] Z. Wojnarowska and M. Paluch, *J. Phys.: Condens. Matter* **27**, 073202 (2015).
- [30] J. R. Sangoro and F. Kremer, *Acc. Chem. Res.* **45**, 525 (2012).
- [31] R. Kurita and H. Tanaka, *Phys. Rev. Lett.* **95**, 065701 (2005).
- 32 M. Paluch, editor, *Dielectric Properties of Ionic Liquids* (Springer International Publishing, Cham, **2016**).
- [33] J. R. Sangoro, C. Iacob, A. L. Agapov, Y. Wang, S. Berdzinski, H. Rexhausen, V. Strehmel, C. Friedrich, A. P. Sokolov, and F. Kremer, *Soft Matter* **10**, 3536 (2014).
- [34] F. Fan, W. Wang, A. P. Holt, H. Feng, D. Uhrig, X. Lu, T. Hong, Y. Wang, N.-G. Kang, J. Mays, and A. P. Sokolov, *Macromolecules* **49**, 4557 (2016).
- [35] Z. Wojnarowska, M. Rams-Baron, J. Knapik-Kowalczyk, A. Połatyńska, M. Pochylski, J. Gapinski, A. Patkowski, P. Włodarczyk, and M. Paluch, *Sci. Rep.* **7**, 7084 (2017).
- [36] B. Yao, M. Paluch, M. Dulski, C. Quinn, S. McLaughlin, A. McGrogan, M. Swadzba-Kwasny, and Z. Wojnarowska, *J. Phys. Chem. Lett.* 2958 (2023).
- [37] J. S. Smith, D. Bedrov, and G. D. Smith, *Comput. Sci. Technol.* **63**, 1599 (2003).
- [38] K. Kremer and G. S. Grest, *J. Chem. Phys.* **92**, 5057 (1990).
- [39] G. S. Grest and K. Kremer, *Phys. Rev. A* **33**, 3628 (1986).
- [40] D.R. Lide, *CRC Handbook of Chemistry and Physics*, **2004**.
- [41] S. Plimpton, *J. Comput. Phys.* **117**, 1 (1995).
- Humphrey, W.; Dalke, A.; Schulten, K. VMD: Visual Molecular Dynamics, *J. Molec. Graph. Model.* **1996**, *14* (1), 3

## 8 Conclusion

This dissertation aims to provide some experimental proof to support the liquid-liquid phase transition phenomenon occurring in ion-containing systems and to identify key factors governing the structure-property relationships of LLT. Several aprotic ionic liquids based tetra(alkyl)phosphonium cations have been selected to explore the thermodynamic and dynamic properties in the vicinity of LLT and glass transition. Herein, I will summarize the dissertation by answering the following questions.

*1. What is the experimental evidence of liquid-liquid phase transition in these ionic liquids?*

In this dissertation, differential scanning calorimetric (DSC), Raman, and small-angle X-ray scattering (SAXS) measurements have been performed to provide experimental evidence of LLT in studied ILs. Specifically, the clear reversible enthalpic peaks corresponding to the first-order phase transition have been found in [P<sub>444,14</sub>][TFSI], [P<sub>444,14</sub>]Cl, and [P<sub>666,14</sub>]<sup>+</sup>-based AILs with seven anions ([BH<sub>4</sub>]<sup>-</sup>, Cl<sup>-</sup>, [SCN]<sup>-</sup>, [DCA]<sup>-</sup>, [TCM]<sup>-</sup>, [TAU]<sup>-</sup>, and [TFSI]<sup>-</sup>). Importantly, their glass transition temperature  $T_g$  has been detected by performing the physical aging for six hours to separate the glass transition and LLT. The aging experiment consisted of three steps: decreasing the temperature to approximately 20 K below the  $T_{LL}$ , followed by time-dependent isothermal experiments at  $T_{ag}$ , and heating to room temperature. Taking [P<sub>666,14</sub>][TFSI] as an example, the thermograms measured on a standard cooling/heating rate of 10 K/min and after the aging experiment are presented in Fig. 8.1a. The broad exothermic and endothermic peaks were observed around 200 K upon cooling and subsequent heating, respectively, demonstrating the reversibility of LLT. Simultaneously, the enthalpy change during LLT was found to be consistent upon cooling and heating cycles, indicating the stability of the observed phase transition. In addition, after keeping at  $T_{ag}=183$  K for 6 hours, a step-like change of heat capacity became visible at  $T < T_{LL}$ , which denotes the glass transition process occurring below  $T_{LL}$ .

Raman measurements have been performed for information about the alkyl chain conformational order during LLT in the case of [P<sub>666,14</sub>][TFSI] and [P<sub>444,14</sub>][TFSI]. The results indicate enhanced chain coupling and an increase in their conformational order. Notably, our features of structural rearrangements associated with LLT are consistent with results reported for [P<sub>666,14</sub>][BH<sub>4</sub>] [1].

The characterization of structural reorganization in LLT of [P<sub>666,14</sub>][DCA] was achieved by the temperature dependence SAXS measurements. As shown in Fig. 8.1b, the results clearly show that there is no crystallization during the cooling process, and the structural difference between supercooled liquid 1 and liquid 2 states can be easily

detected. In the liquid 2 phase, the charge-alternation correlation structure is visible as a shoulder around  $0.53 \text{ \AA}^{-1}$  on the high- $q$  side of the polarity-alternation structure around  $0.36 \text{ \AA}^{-1}$ .

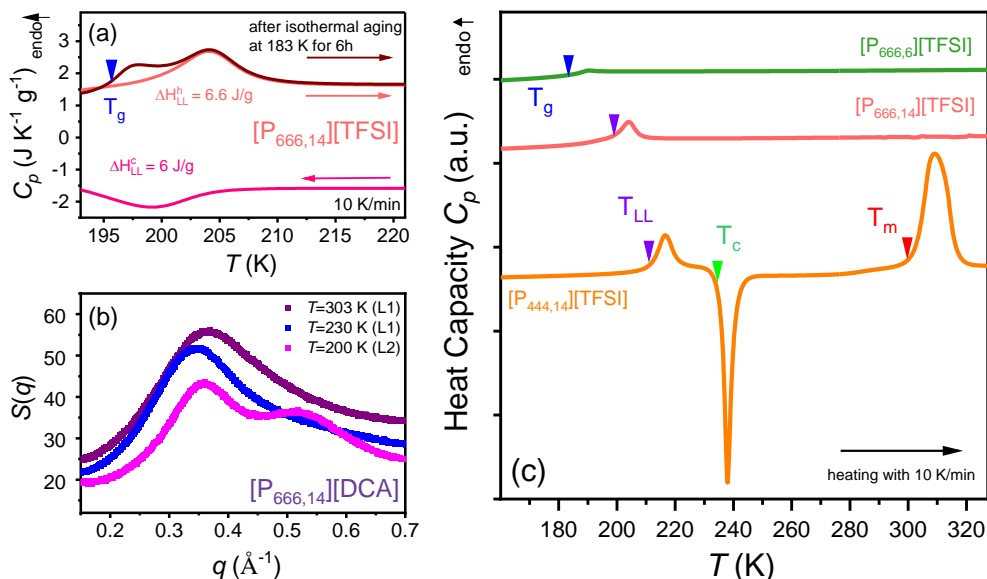


**Fig. 8.1** **a** The temperature dependence of heat capacity  $C_p$  ( $T$ ) for  $[\text{P}_{666,14}][\text{TFSI}]$  on cooling and subsequent heating, as well as data after the aging process. **b** Small-angle X-ray scattering intensity,  $S(q)$ , at different temperatures, covering liquid 1 and liquid 2 states for  $[\text{P}_{666,14}][\text{DCA}]$ . **c** DSC traces of  $[\text{P}_{666,6}][\text{TFSI}]$ ,  $[\text{P}_{666,14}][\text{TFSI}]$ ,  $[\text{P}_{444,14}][\text{TFSI}]$  on heating scan with standard rate 10 K/min. The arrows denote the characteristic temperatures: glass transition (blue), onset of liquid-liquid transition upon heating (violet), onset of crystallization (green), and melting (red).

## 2. How does the alkyl chain length of $[\text{P}_{666,14}]^+$ cation affect LLT?

Most ILs used in this work belong to a family of ILs containing the  $[\text{P}_{666,14}]^+$  cation and exhibit the LLT phenomenon. By tailoring the alkyl chain length of  $[\text{P}_{666,14}]^+$  cation, we found that the longest aliphatic chain ( $\text{C}_{14}$ ) is crucial for enabling the ILs to undergo LLT. In particular, shortening the other three substituents while keeping the  $\text{C}_{14}$  alkyl chain (i.e.,  $[\text{P}_{444,14}]^+$ ) retain the ability of ILs exhibiting LLT. The DSC traces of  $[\text{P}_{444,14}]\text{Cl}$  and  $[\text{P}_{444,14}][\text{TFSI}]$  show a well-resolved endothermic peak in the heating process, revealing the occurrence of LLT. However, the enthalpy of LLT increased and  $T_{LL}$  shifted to a higher temperature. The high enthalpy of LLT reported in  $[\text{P}_{444,14}]\text{-ILs}$  implies that the alkyl chains self-assembly inducing LLT is better constituted than in  $[\text{P}_{666,14}]\text{-ILs}$ , and therefore they crystallize above  $T_{LL}$  (see Fig. 8.1c for  $[\text{P}_{444,14}][\text{TFSI}]$ ). Furthermore, the crystalline Raman spectrum of  $[\text{P}_{444,14}][\text{TFSI}]$  strongly indicated the difference between the crystalline and liquid 2 states. In addition, the ion dynamics of  $[\text{P}_{444,14}]\text{-ILs}$  exhibit the same anomalous behaviors as that of  $[\text{P}_{666,14}]\text{-ILs}$  during LLT.

On the other hand, shortening the longest alkyl chain of  $[P_{666,14}]^+$  cation prevents the occurrence of LLT in ILs, demonstrating that only one supercooled liquid state was observed in the ILs with trihexyl(alkyl)phosphonium cations, i.e.,  $[P_{666,n}]^+$  ( $n = 2, 6, 8, 12$ ). Only a step-like change in heat capacity denoting the glass transition has been found in the DSC traces of these ILs (for example,  $[P_{666,6}][TFSI]$  in Fig. 8.1c) At the same time, their glass transition temperature significantly decreased compared with  $[P_{666,14}]^+$ -based ILs. Interestingly, not only that, the glass transition region becomes broader, indicating a broad distribution of structural relaxation times (a higher dynamic heterogeneity, i.e., only a few of particles are contained in the same cooperative motion). It is noteworthy that the calculated number of dynamically correlated particles,  $N_a^D(T_g)$ , for  $[P_{666,n}]$ -ILs is extremely small (less than ten). This finding is in agreement with the aforementioned higher heterogeneity. Although there is no intuitive representation of LLT, the more ordered nanoscale molecular packing is still captured by Raman spectroscopy, and the Stickel analysis of their ion dynamics near the glass transition indicates similar behavior to LLT.

### 3. What are the dielectric fingerprints accompanying LLT in ionic liquids?

The ion dynamics of studied ILs was investigated by dielectric spectroscopy over a wide frequency ( $10^2$ - $10^7$  Hz) and temperature range. The dynamic signature of LLT in ILs can be summarized into three distinct aspects. First, the shape of the conductivity relaxation processes ( $M''(f)$  peak) in liquid 2 state is much broader than that in liquid 1 state. It means that the distribution of conductivity relaxation becomes broader from liquid 1 to liquid 2, which is quantified by the decreasing of  $\beta_{KWW}$  parameter. Fig. 8.2 shows the exponent  $\beta_{KWW}$  plotting as a function of the frequency of modulus peak maximum ( $f_{max}$ ) for all examined ILs. Usually, the shape of conductivity relaxation processes in ionic glass-forming systems is invariant in a supercooled liquid state. As shown by  $[P_{666,14}][BOB]$ ,  $[P_{666,14}][BEHP]$ ,  $[P_{666,14}][BTMPP]$ , and  $[P_{666,n}][TFSI]$  ( $n=2-12$ ), their  $\beta_{KWW}$  parameters are constant over the entire available frequency range. Namely, they obey the time-temperature superposition (TTS) rule. In turn, for the ILs exhibiting LLT, the  $\beta_{KWW}$  characterizing liquid 1 remains approximately constant and falls within a range of  $0.58 < \beta_{KWW} < 0.68$ . However, the value of  $\beta_{KWW}$  decreases across the transition, revealing a broader and more asymmetric distribution of conductivity relaxation times in liquid 2 phase. Interestingly, the degree of  $\beta_{KWW}$  decreasing is associated with anions. Specifically, the most pronounced drop occurs in ILs with  $[SCN]^-$ , while the slightest drop occurs in ILs with  $[TAU]^-$  and chloride anion. In addition, the exponents of  $[P_{444,14}][Cl]$  and  $[P_{444,14}][TFSI]$  in liquid 1 could not be obtained because of the subsequent crystallization process after liquid 2, indicating a strong ordering tendency.

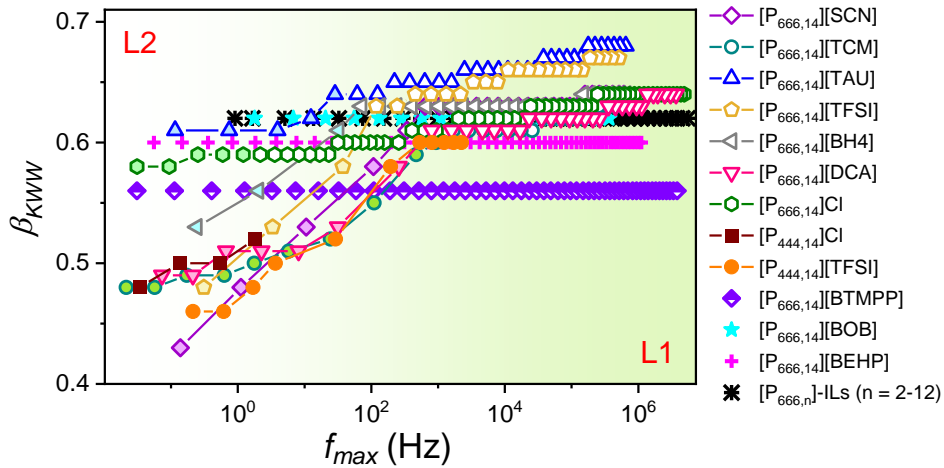


**Fig. 8.2** Plot of exponent  $\beta_{KWW}$  as a function of frequency at modulus peak maximum for all examined ILs. L1 denotes liquid 1, and L2 denotes liquid 2.

The second dynamic signature of LLT observed is the significant increase in the conductivity relaxation time  $\tau_\sigma$ . In supercooled liquid 1,  $\tau_\sigma(T^{-1})$  are described by the Vogel-Fulcher-Tammann (VFT) law, while they exhibit Arrhenius behavior in supercooled liquid 2. A considerable heightened increase in activation energy accompanies the LLT. The onset of the phase transition temperature,  $T_{LL}$ , coincides nicely with the calorimetric LLT temperature ( $T_{LL}^{DSC}$ ). Notably, the same peculiar signature of LLT can be detected in dc-conductivity ( $\sigma_{dc}$ ) behavior as well. In contrast, in the cases of other examined ILs (i.e.,  $[P_{666,14}][BOB]$ ,  $[P_{666,14}][BTMPP]$ ,  $[P_{666,14}][BEHP]$ , and  $[P_{666,n}]-ILs$ ), that do not reveal calorimetric LLT, the temperature evolution of  $\tau_\sigma$  and  $\sigma_{dc}$  reveals a typical non-Arrhenius dependence over the wide temperature range.

Finally, the increased slope in the Stickel operator  $\Phi = [d(\log(\tau_\sigma)/d(1000/T))]^{-1/2}$  from the supercooled liquid 1 to liquid 2 can be treated as the third dielectric fingerprint of LLT in ILs. From this perspective, one may declare that liquid 2 is much more fragile than liquid 1. However, it is worth emphasizing that H. Tanaka et al. found an opposite result in the molecular liquid TPP [2], where liquid 1 is much more fragile than liquid 2. On the other hand, although one VFT equation can be used to describe the temperature dependence of conductivity relaxation time  $\log_{10} \tau_\sigma(1000/T)$  for  $[P_{666,n}]-ILs$ , their Stickel analysis still departs from linear behavior. Consequently, although the shortening of aliphatic chains reduces the possibility of LLT, the potential for the partial nanoscale organization of  $[P_{666,n}]-ILs$  is still retained, which has been proven by our Raman measurements.

#### 4. How do various anions of ILs influence LLT?

Considering the  $[P_{666,14}]-$ based ILs, several anions were selected reflecting different sizes, spatial arrangement, flexibility, and coordination ability. Our results suggest that

not all anion pairing with the  $[P_{666,14}]^+$  enable LLT. In other words,  $[P_{666,14}]^+$  cation allows ILs to induce LLT, while anions finally determine whether they exhibit LLT or not. Specifically, the LLT occurs in  $[P_{666,14}]$ -ILs with  $[BH_4]^-$ ,  $Cl^-$ ,  $[SCN]^-$ ,  $[DCA]^-$ ,  $[TCM]^-$ ,  $[TAU]^-$ , and  $[TFSI]^-$  anions, which are typically small in size and weakly coordinating. Interestingly, for all examined ILs  $T_{LL}$  is around  $205 \pm 2$  K and  $T_g = 197 \pm 1$  K. That is, the anion species has a negligible effect on the liquid-liquid transition and glass transition temperature. However, for higher the van der Waals volume of anion, e.g.,  $[BOB]^-$  and  $[BTMPP]^-$ , we found that the LLT can be overlapped with glass transition, and it completely disappears for bulky anion, e.g.,  $[BEHP]^-$ . Unfortunately, for certain anions, cooling induces crystallization, which disrupts LLT, for example, the small and non-coordinating anion  $[BF_4]^-$  and the amphiphilic chain-like anion  $[Dec]^-$ . Specific thermodynamic characteristics of each sample on the standard heating process are summarized in Table 8.1, which explicitly indicates the presence or absence of LLT in the examined systems.

**Tab. 8.1** Thermodynamic properties of examined ILs

ILs	$T_{LL}$ (K)	$\Delta H_{LL}$ (J/g)	$T_g$ (K)	$T_c$ (K)	$T_m$ (K)	$\beta_{KWW}$
${}_{666,2}[TFSI]$	-	-	184.2	-	-	0.62
$[P_{666,6}][TFSI]$	-	-	184.1	-	-	0.62
$[P_{666,8}][TFSI]$	-	-	184.2	-	-	0.62
$[P_{666,12}][TFSI]$	-	-	182.3	-	-	0.62
$[P_{666,6}][Cl]$	-	-	206.6	232.6	288.9	0.62
$[P_{666,12}][Cl]$	-	-	199.1	-	-	0.62
$[P_{666,14}][BEHP]$	-	-	186	-	-	0.6
$[P_{666,14}][BOB]$	-	-	202.1	-	-	0.62
$[P_{666,14}][BTMPP]$	-	-	203	-	-	0.56
$[P_{444,14}][Cl]$	227.1	5.73	221.2	233.8	309.8	$0.6^{L1}$
$[P_{444,14}][TFSI]$	211.5	11.14	208.5	236.1	301.7	$0.6^{L1}$
$[P_{666,14}][TFSI]$	200.1	6.6	195.9	-	-	$0.66^{L1}$
$[P_{666,14}][Cl]$	205.9	5.23	197.9	-	-	$0.63^{L1}$
$[P_{666,14}][SCN]$	207.1	11.6	197.7	254.3	272.3	$0.63^{L1}$
$[P_{666,14}][DCA]$	203.6	9.6	197.3	240.6	256.2	$0.62^{L1}$
$[P_{666,14}][TCM]$	204.8	8.6	197.7	-	-	$0.62^{L1}$
$[P_{666,14}][TAU]$	203.9	3.9	197.5	-	-	$0.67^{L1}$
$[P_{666,14}][BH_4]$	207.6	5.0	198.5	250.9	271.9	$0.63^{L1}$
$[P_{666,14}][BF_4]$	-	-	-	229	295	-
$[P_{666,14}][Dec]$	-	-	-	241	265.7	-

### 5. What is the charge transport mechanism in ILs with LLT?

So far, the charge transport in neat aprotic ILs is suggested as a vehicular mechanism, namely, the conductivity is fully controlled by its viscosity. However, the decoupling of ionic conductivity from structural dynamics has been discovered in our ILs with LLT. The timescales of  $\tau_\alpha$  and  $\tau_\sigma$  start to diverge at the temperature of LLT and reach the most pronounced difference (decoupling) at  $T_g$ . Specifically, the charge transport is much faster than structural relaxation after the LLT. Additionally, the time scale of charge transport at  $T_g$  is significantly shorter than 1000 s, which is a typical structural relaxation time for freezing ions in aprotic ILs at the glassy state. The sharp increase in structural relaxation time indicates a sudden slowing down of structural motion, while the anions remain highly mobile thereby contributing to ionic conductivity.

For a deeper understanding of the decoupling behavior in aprotic ILs with LLT, the degree of decoupling has been quantified by the decoupling index defined as  $R_\tau(T_g) = \log \tau_\alpha(T_g) - \log \tau_\sigma(T_g)$ . [3],[4],[5], The decoupling indexes of examined ILs are collected in Fig. 8.3, which clearly shows an increase of decoupling in  $[P_{444,14}]^+$ -based ILs than in  $[P_{666,14}]^+$ -based ILs with the same anion. Remarkably,  $[P_{666,14}][TAU]$  and  $[P_{666,14}][Cl]$  exhibits the smallest decoupling index, and at the same time, they also reveal a minor decrease in exponent  $\beta_{KWW}$  from liquid 1 to liquid 2.

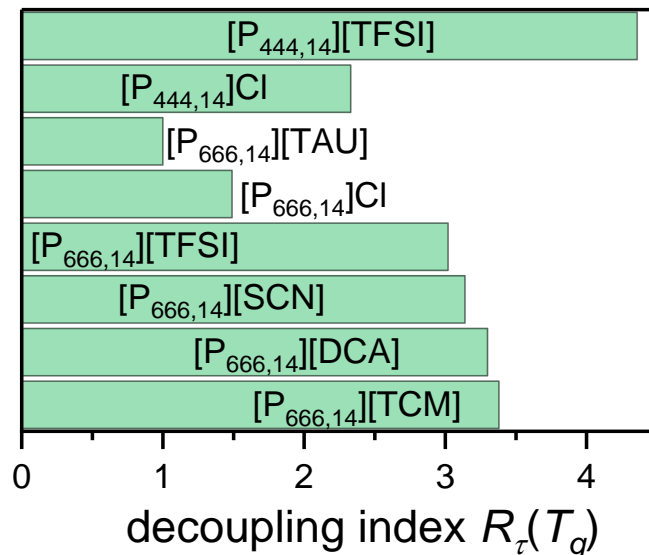


**Fig. 8.3** Bar chart of decoupling index  $R_\tau(T_g)$  for examined ILs with LLT.

So far, the decoupling phenomenon of ion conductivity from structural relaxation at glass transition has been reported in various protic ILs [6] and polymerized ILs [7]. Nevertheless, such behavior has never been found in aprotic ILs and any other systems with LLT. Therefore, exploring the mechanism underlying this phenomenon is of great significance for understanding the nature of LLT and the application of aprotic ionic

liquids. The examined aprotic ILs exhibiting LLT contain bulky tetra(alkyl)phosphonium cations with a non-polar C<sub>14</sub>-alkyl chain and relatively small anions. Such a combination raises the possibility of forming nanoscale structures in which alkyl chains of cations serve as the main framework dominating structural dynamics, while anions are free to move inside, controlling the charge transport. The same scenario has been previously declared as the origin of decoupling for polymerized ILs. [8],[9] From this point of view, the ion transport of studied ILs in liquid 2 basically comes from the anions, which is verified by high-pressure experiments and molecular dynamics simulations.

*6. How does thermal history affect dynamic properties in the vicinity of LLT and glass transition?*

We already know from DSC results that the LLT in ILs is reversible, so the ion dynamics can be obtained from the cooling and heating process. However, slow cooling and quenching produce different dynamic properties for ILs near  $T_g$ . Specifically, the slow cooling of the sample results in higher apparent activation energy of the glass compared to quenched one. Thus, obtaining two distinct glassy states within a single-component ionic system is possible. Notably, quenched heating and slow cooling cause two distinct glasses differing in the time scale of ion transfer. The observation of such a so-called polyamorphism phenomenon in terms of ILs is a groundbreaking discovery that opens new avenues for tailoring the characteristics of disordered electrolytes.

*7. Can we monitor LLT in ILs by mechanical measurements?*

The answer is yes. The LLT in ILs can be monitored by performing mechanical measurements. Taking [P<sub>666,14</sub>][DCA] as an example, the viscosity in liquid 1 and the shear modulus in liquid 2 can be measured directly. By employing the Maxwell relation  $\tau_\alpha = \eta/G_\infty$ , the temperature dependence of structural relaxation time in liquid 1 state can be obtained from viscosity data and suddenly departs from the VFT behavior at calorimetric LLT temperature ( $T_{LL}^{DSC}$ ). The abrupt increase in structural relaxation time indicates the sudden slowing of structural motion, implying the more coordinated local structures in liquid 2 than in liquid 1.

*8. Does the LLT occur at elevated pressure in ILs?*

In addition to isobaric cooling, isothermal compression is another available route to induce LLT. It has been reported that high pressure can induce the first-order liquid-liquid phase transition but with extreme conditions, for example, 1050 °C and 1GPa for phosphorus [10] and 1920 K and 50 GPa for nitrogen [11]. In contrast, our results suggest that such extreme pressures are not required for LLT to occur in ILs. Actually, 600 MPa

is enough to induce LLT in ILs at 233 K, and even 150 MPa is already enough if the temperature is lower, i.e., 213 K.

The ion dynamics of ILs with LLT at elevated pressure exhibit the same peculiar behaviors as observed at ambient pressure, i.e., the pressure dependences of conductivity relaxation times are dramatically elongated at a certain pressure called the liquid-liquid transition pressure,  $P_{LL}$ , and their distribution in liquid 2 undergoes a notable broadening with respect to liquid 1. Furthermore, the transition from liquid 1 to liquid 2 under compression substantially increases activation volume  $\Delta V$ , suggesting the amount of space required for local molecular motion grows.

Additionally, isothermal compression demonstrates another intriguing feature of LLT. The conductivity relaxation time of LLT is independent of  $T$ - $P$  conditions for a given IL system but appears in various values for different anions. Namely,  $\log \tau_{\sigma}(T_{LL}, P_{LL})$  remains constant but sample dependent. Fig. 8.4 presents the pressure evaluation of  $\log \tau_{\sigma}$  at the onset of LLT and glass transition for examined ILs. It clearly shows that the time scale of  $\tau_{\sigma}$  of LLT (open symbols) remains constant at around 3.5 ms detaching two supercooled liquid phases for  $[P_{666,14}][DCA]$ ,  $[P_{666,14}][TCM]$ , and  $[P_{666,14}][SCN]$ , while longer conductivity relaxation times are required, e.g., 5.6 ms and 30 ms, to separate liquid 1 and liquid 2 for  $[P_{666,14}][TFSI]$  and  $[P_{666,14}][TAU]$ , respectively. This feature highlights the isochronous behavior of LLT. However, the ion dynamics  $\tau_{\sigma}(T_{LL}, P_{LL})$  are not universal and can be impacted by intermolecular interactions.

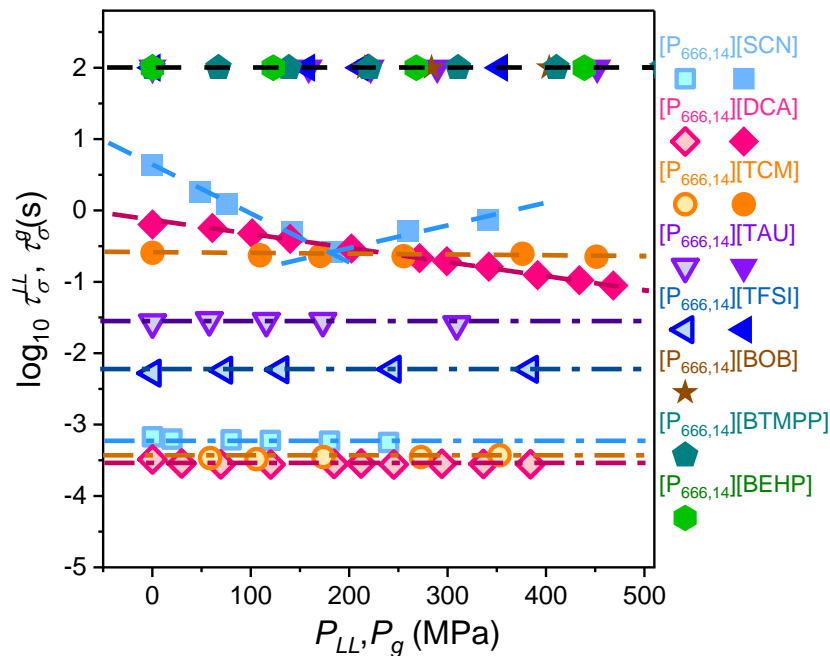


**Fig. 8.4** The characteristic relaxation times of glass (closed symbols) and liquid-liquid (open symbols) transition at various temperatures are plotted as a function of pressure. The dash-dot lines are  $\tau_{\sigma}(T_{LL}, P_{LL})$  and the dashed lines are  $\tau_{\sigma}(T_g, P_g)$ .

### 9. How does the pressure affect the charge transport in ILs with LLT?

As mentioned previously, in the case of ILs with LLT, the charge transport in the liquid 2 phase is not fully controlled by viscosity due to the occurrence of nanostructures. Moreover, the pressure dependences of conductivity relaxation time for examined ILs reveal similar patterns to those observed at ambient pressure. For [P<sub>666,14</sub>][SCN], [P<sub>666,14</sub>][DCA], and [P<sub>666,14</sub>][TCM], the glass transition can also be recognized in the detectable pressure range and demonstrate unique behaviors, as shown in Fig. 8.4 (closed symbols). Specifically, an obvious minimum of  $\tau_\sigma(P_g)$  at 180 MPa has been found in [P<sub>666,14</sub>][SCN], and  $\log \tau_\sigma(P_g)$  decreases one decade with pressure increase for [P<sub>666,14</sub>][DCA]. Furthermore, their conductivity relaxation time  $\tau_\sigma$  at glass transition is markedly faster than the structural relaxation time 100 s ( $\log \tau_\alpha(P_g) = 2$ ), which is a typical value at glass transition pressure for most ionic glass formers. Such anomalous behavior indicates that the decoupling between charge transport and ion motion can be induced by pressure in the case of phosphonium ILs with LLT. One can suppose that an increase in pressure results in a more organized packing of alkyl chains within [P<sub>666,14</sub>]<sup>+</sup> cations, creating additional channels through which smaller anions can diffuse. Therefore, higher pressure facilitates anion motions, which is reflected by a decrease of  $\log \tau_\alpha(T_g, P_g)$  and an increased degree of decoupling. However, the movement of [SCN]<sup>-</sup> is hindered at pressures above 180 MPa, which can be observed in Fig. 8.4, since the reduced availability of free volume causes a slowdown of anions. As a result, the gap between the timescales of conductivity and structural relaxation is reduced. Similar effects are expected for [P<sub>666,14</sub>][DCA]; however, they likely occur at pressures beyond the range that can be experimentally accessed. On the other hand, as the anion size increases, the formation of open channels for charge diffusion becomes more challenging. Despite the fact that anions move faster than cations, the effect of pressure on molecular packing is weak, leading to the constant value of  $\log \tau_\alpha(T_g, P_g)$  at various temperatures and pressures for [P<sub>666,14</sub>][TCM].

In order to verify the proposed mechanism of charge transport in ILs with LLT, MD simulations have been performed. Our results reveal that isotropic structure dominates in ILs at high temperatures considering the thermal fluctuations, and the [P<sub>666,14</sub>]<sup>+</sup> cations tend to form nanostructures with varying degrees of order as the temperature decreases, depending on the applied pressure  $P$  and anion size. Increased pressure induces a morphological transition of cation from weakly ordered aggregates composed of ionic pairs or triplets to ordered lamellar phases for small anions at low temperatures. In contrast, independent of  $P$ , interconnected phases with continuous 3D curvature form in the case of bulky anions. Therefore, compared to liquid 1 phase, liquid 2 possesses a self-

assembled nanostructure promoting fast ion transport through channels created by amphiphilic cations with long non-polar alkyl chains.

### 10. How does the volume change at the LLT in ILs?

Given the nature of first-order phase transitions, density changes with LLT in ILs are a matter of course that we should take into account. The Clausius-Clapeyron equation  $\Delta V_{LLT} = \frac{\Delta S_{LL}}{dP_{LL}/dT_{LL}} = \frac{\Delta H_{LL}}{T_{LL}} \frac{dT_{LL}}{dP_{LL}}$  offers an excellent opportunity to estimate the alterations in volume accompanying the LLT ( $\Delta V_{LL}$ ). The volume change can be easily calculated by combining the enthalpy change during LLT ( $\Delta H_{LL}$ ) obtained from the DSC experiments and the sensitivity of liquid-liquid transition temperature to pressure ( $dT_{LL}/dP$ ) obtained from high-pressure experiments. The values of  $\Delta V_{LL}$  for examined ILs are collected in Fig. 8.5a (green columns). One can see that the volume change during LLT for examined ILs does not exceed 0.01 cm<sup>3</sup>/g. Furthermore, the temperature evaluation of specific volume in the temperature range of 283 K to 363 K from density measurements provides a possibility to obtain  $V_{LL}$  at  $T_{LL}$  by extrapolating the experiment data (see Fig. 8.5b open symbols). To help understand the significance of these numbers, the ratio of volume fluctuation to specific volume at  $T_{LL}$ ,  $n = \Delta V_{LL}/V_{LL}$ , has been plotted in Fig. 8.5a (magenta columns). As indicated, it is apparent that a volume change of roughly 0.5% occurs at the LLT, which is within the error range of dilatometric measurements. Such minor fluctuations in specific volume may not be easily observable in direct  $V(T,P)$  measurements, highlighting that density is not the dominant order parameter driving the LLT in ILs.

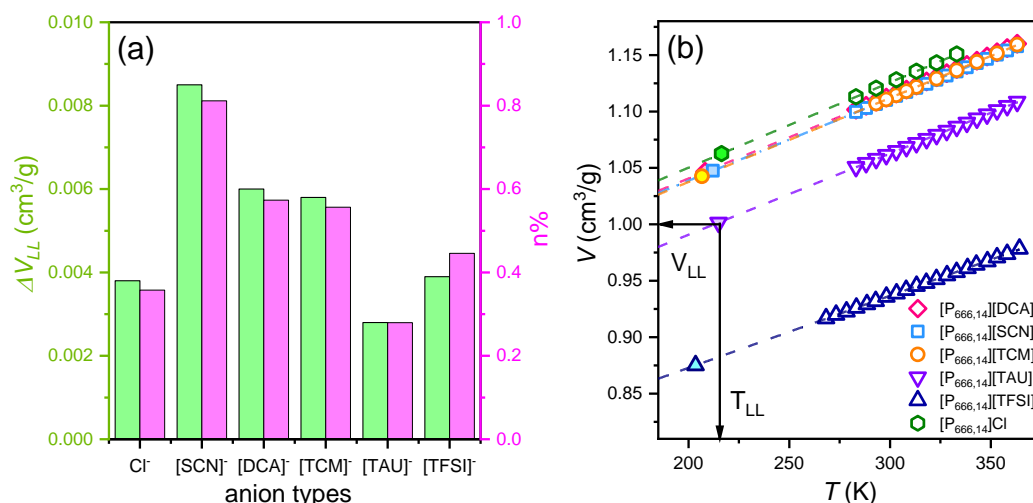


**Fig. 8.5 a** The volume fluctuation for [P<sub>666,14</sub>]<sup>+</sup>-based ILs with different anions during LLT, the right Y-axis is the corresponding percentage of the volume fluctuation to specific volume ratio at  $T_{LL}$ . **b** The specific volume as a function of temperature for the ILs plotted in panel **a**, where the data of [P<sub>666,14</sub>][Cl] are taken from reference [12]. The dashed lines are linear fits.

### 11. How does the pressure affect the ion dynamics of [P<sub>666,14</sub>]-based ILs without LLT?

In this dissertation, the IL without any features of LLT is [P<sub>666,14</sub>][BEHP], which has the biggest van der Waals volume over all examined ILs. Our isothermal measurements show that the  $\tau_\sigma(P)$  dependence of [P<sub>666,14</sub>][BEHP] follows the Arrhenius law with increasing pressure and [P<sub>666,14</sub>][BEHP] exhibits the weakly pressure sensitivity, i.e., the smallest value of  $dT_g/dP$ . Simultaneously the constant  $\Delta V(P)$  was expected due to the linear relation of  $\log \tau_\sigma(P)$ . Interestingly, despite the striking similarity in anion structures of [P<sub>666,14</sub>][BEHP],  $\log \tau_\sigma(P)$  of [P<sub>666,14</sub>][BTMPP] exhibits non-Arrhenius behavior, as in [P<sub>666,14</sub>][BOB]. They expose more similar performance especially when the apparent activation volume  $\Delta V$  has been determined. A noticeable minimum called inflection point revealing the concave-convex nature of the  $\tau_\sigma(P)$  dependence has been observed in  $\Delta V(P)$  dependence of [P<sub>666,14</sub>][BTMPP] and [P<sub>666,14</sub>][BOB], in which the LLT has overlapped by the glass transition.

## 8.1 Outlook

In summary, our findings provide the groundwork for revealing the nature of LLT phenomenon and take a crucial step toward a comprehensive understanding of liquids. In particular, this first-order LLT without volume discontinuity offers a rare chance to probe the subtle structural and ion dynamic changes in a supercooled liquid. Furthermore, the self-assembly-based charge transport mechanism observed here provides a distinct window into precisely adjusting the ionic diffusion of ILs and similar nanostructured fluids. These results may profoundly impact the emerging technologies and the advanced materials industry associated with ionic liquids. Of course, the research on the LLT phenomenon in ILs is still interesting, and many theoretical frameworks, experiments, and simulations are still needed for further verification. For example it would be interesting to: (i) characterize self-assembled nanostructure distributions by using transmission electron microscopy or neutron scattering, (ii) directly access the locally favored structure in liquid 2 state experimentally, especially at low temperature, (iii) explore the transformations between polymorphism and polyamorphism over a wide temperature and pressure conditions, for which numerical simulation is a pretty promising approach.

## 8.2 Reference

- [1] M. A. Harris, T. Kinsey, D. V. Wagle, G. A. Baker, and J. Sangoro, *Proc. Natl. Acad. Sci.* **118**, e2020878118 (2021).
- [2] R. Kurita and H. Tanaka, *Phys. Rev. Lett.* **95**, 065701 (2005).
- [3] I. M. Hodge, K. L. Ngai, and C. T. Moynihan, *J. Non-Cryst. Solids* **351**, 104(2005).

- [4] M. D. Ingram, *Philos. Mag. B*, **60**, 729 (1989).
- [5] C. A. Angell, *Chem. Rev.* **90**, 523 (1990).
- [6] Z. Wojnarowska, Y. Wang, K. J. Paluch, A. P. Sokolov, and M. Paluch, *Phys. Chem. Chem. Phys.* **16**, 9123 (2014).
- [7] J. R. Sangoro, C. Iacob, A. L. Agapov, Y. Wang, S. Berdzinski, H. Rexhausen, V. Strehmel, C. Friedrich, A. P. Sokolov, and F. Kremer, *Soft Matter* **10**, 3536 (2014).
- [8] Z. Wojnarowska, H. Feng, M. Diaz, A. Ortiz, I. Ortiz, J. Knapik-Kowalczyk, M. Vilas, P. Verdía, E. Tojo, T. Saito, E. W. Stacy, N.-G. Kang, J. W. Mays, D. Kruk, P. Wlodarczyk, A. P. Sokolov, V. Bocharova, and M. Paluch, *Chem. Mater.* **29**, 8082 (2017).
- [9] Z. Wojnarowska, H. Feng, Y. Fu, S. Cheng, B. Carroll, R. Kumar, V. N. Novikov, A. M. Kisliuk, T. Saito, N.-G. Kang, J. W. Mays, A. P. Sokolov, and V. Bocharova, *Macromolecules* **50**, 6710 (2017).
- [10] G. Monaco, S. Falconi, W. A. Crichton, and M. Mezouar, *Phys. Rev. Lett.* **90**, 255701 (2003).
- [11] G. D. Mukherjee and R. Boehler, *Phys. Rev. Lett.* **99**, 225701 (2007).
- [12] L. I. N. Tomé, R. L. Gardas, P. J. Carvalho, M. J. Pastoriza-Gallego, M. M. Piñeiro, and J. A. P. Coutinho, *J. Chem. Eng. Data* **56**, 2205 (2011).

# 9 Appendix

I have been also involved in the following works during my Ph.D. studies.

## Publications

1. M. Rams-Baron, B. Yao, S. Cheng, M. Dulski, and M. Paluch, Complex Reorientation Dynamics of Sizable Glass-Formers with Polar Rotors Revealed by Dielectric Spectroscopy. *J. Phys. Chem. Lett.* **12** (46), 11303–11307, (2021).  
<https://doi.org/10.1021/acs.jpcllett.1c03088>.
2. M. Paluch, B. Yao, J. Pionteck, Z. Wojnarowska, Predicting the density-scaling exponent of a glass-forming liquid from complex dielectric permittivity measurements. *Phys. Rev. Lett.* Under review.
3. K. Łucak, R. Wrzalik, J. Grelska, K. Jurkiewicz, N. Soszka, B. Hachuła, D. Kramarczyk, K. Grzybowska, B. Yao, K. Kaminski, S. Pawlus, Experimental and Computational Approach to Studying Supramolecular Structures in Propanol and Its Halogen Derivatives, *J. Phys. Chem.* under review (ID jp-2023-02092d)

I am also a co-author of following papers.

4. B. Yao, Z. Wojnarowska, and M. Paluch, Effect of Structure on Molecular Dynamics in Glass-Forming Liquids. The Case of Aromaticity. *J. Mol. Liq.* **344**, 117757 (2021).  
<https://doi.org/10.1016/j.molliq.2021.117757>.
5. M. Musiał, S. Cheng, Z. Wojnarowska, B. Yao, K. Jurkiewicz, and M. Paluch, Thorough Studies of Tricyanomethanide-Based Ionic Liquids – the Influence of Alkyl Chain Length of the Cation. *Soft Matter*, **16** (41), 9479–9487. (2020)  
<https://doi.org/10.1039/D0SM01433H>.

## Conference Contributions

### Oral Presentation

11th Conference on Broadband Dielectric Spectroscopy and its Applications, International Dielectric Society, San Sebastián, Spain, September 4th to 9th 2022. Title: *Ion dynamics of trihexyltetradecyl-phosphonium-based ionic liquids with big anions at ambient and elevated pressure.*

YOUNG MULTIS - Multiscale Phenomena in Condensed Matter - a conference for young researchers, The Henryk Niewodniczański Institute of Nuclear Physics Polish Academy of Sciences, Zoom platform, July 3rd - 5th 2023. Title: *Liquid-liquid phase transition promotes the decoupling of ion dynamics from structural dynamics in aprotic ionic liquids.*

**Poster**

IDS Online Workshop 2021, Silvina Cervený, Ranko Richert, Catalin Gainaru, Online Zoom, September 6th to 9th ,2021, *Effect of Aromaticity on Molecular Dynamics of Glass-forming Liquids.*